RADIO FREQUENCY PULSE DESIGNS FOR MAGNETIC RESONANCE IMAGING AT HIGH FIELD

By

Jason E. Moore

Dissertation

Submitted to the Faculty of the
Graduate School of Vanderbilt University
in partial fulfillment of the requirements
for the degree of
DOCTOR OF PHILOSOPHY
in
Physics

May, 2011

Nashville, Tennessee

Approved:

Professor John C. Gore

Professor Adam W. Anderson

Professor Volker E. Oberacker

Professor Cynthia B. Paschal

Professor Todd E. Peterson

In loving memory of my grandfather

William Harrison Sellers

1913 – 2010

ABSTRACT

The increased signal-to-noise ratio (SNR) that accompanies the use of stronger static fields in magnetic resonance imaging (MRI) has driven the use of increasingly higher fields ever since the technology's inception over thirty years ago. Currently, the potential clinical use of 7 Tesla (7 T) MRI scanners is under investigation. At such high fields, a number of complications prohibit practical realization of the potential gains in SNR and reduce image quality. One major problem is the inhomogeneity of radio frequency (RF) fields that originates when transmitted RF wavelengths are comparable to the dimensions of the human body. When this condition is fulfilled, significant RF attenuation and interference result, leading to spatially varying MR signal intensities.

This thesis addresses the challenge of nonuniform RF fields through the design of RF pulses that induced magnetization responses largely independent of underlying RF field variations. The advantages of this approach are that pulse designs are not patient-specific and can even be implemented across a range of static field strengths. Drawbacks to such strategies involve the limited degree to which uniform magnetization responses can be achieved given the practical restrictions of RF pulse power and duration. Pulse designs rely upon numerical optimization of RF modulation patterns composed of series of discrete sub-pulses. Such composite pulses have been designed for excitation, inversion, refocusing, and saturation and largely tolerate the field variations observed in the human brain at 7 T. In all cases, appropriate comparisons are made with established field-insensitive pulse designs, and performance as a function of pulse power and duration is considered in detail. Results indicate that use of numerically optimized composite pulses can greatly reduce the effects of nonuniform RF fields in almost any pulse sequence employed in the human brain at 7 T. In addition to field-insensitive composite pulses, this thesis includes an evaluation of RF field mapping protocols, the numerical optimization of adiabatic pulses, and the design of frequency-selective composite pulses for a number of applications at both low and high field strengths.

PREFACE

My time as a graduate student has been characterized by cycles of excitement and disappointment. At times I was full of enthusiasm for the experiments I was conducting or the knowledge I was acquiring, and, at other times, I thought I was not going to make it and that everything was pointless. On countless occasions, I thought I had discovered a new way of doing things only to learn that someone else had come across the same idea 10 or 100 years ago. Also, there were many times I had worked very hard in programming MR scanners to perform certain tasks, and the results seemed to indicate that everything was functioning properly. Time and time again I would learn that the reason everything seemed to be working so well was because it was not working in the way I had intended. Many times I had oversimplified the problem and was overlooking something fundamental. At first, I would feel so depressed when these roadblocks would surface. Sometimes I felt that there was no hope for me—that I was just too stupid to succeed. After some time, I would inevitably regain excitement about what I was working on and would start to get ideas about how to do it differently, but, invariably, I would discover another pitfall. Eventually, after witnessing this cycle enough times, I began to realize that it really was just a cycle, and, moreover, it was the process by which I was learning. I also began to understand that science can be a very tedious process, but, with patience and determination, progress can really be made, even if in the smallest of steps.

I remember as a young boy reading my dad's copy of the book *Cosmos* by Carl Sagan (69). On the first page, in reference to mankind's discoveries over the last few millennia, Sagan writes,

> Those explorations required skepticism and imagination both. Imagination will often carry us to worlds that never were. But without it, we go nowhere. Skepticism enables us to distinguish fancy from fact, to test our speculations. The Cosmos is rich beyond measure—in elegant facts, in exquisite interrelationships, in the subtle machinery of awe.

It makes sense to me now that the cycles of exuberance and discouragement that I experience closely parallel the scientific process. They are my emotional responses to the process of discovery. As described in *Cosmos*, Johannes Kepler also was familiar with similar states of despair and euphoria. In recalling his excitement of investigating the relationship of planetary orbits to the five Euclidean solids, Kepler wrote,

> I shunned no calculation no matter how difficult. Days and nights I spent in mathematical labors, until I could see whether my hypothesis would agree with the orbits of Copernicus or whether my joy would vanish into thin air.

Kepler was heartbroken upon his realization that planetary orbits were not circles, but ellipses. Although he initially felt he had been left with "only a single cartful of dung," he later rejoiced in his own perils of discovery writing,

> The truth of nature, which I had rejected and chased away, returned by stealth through the back door, disguising itself to be accepted... Ah, what a foolish bird I have been!

Today, I strive to embrace the scientific process in the manner of Kepler rather than to fear it as I once did. I now know that to learn anything new, I will first likely be surprised or disappointed or both. Making mistakes is an integral part of the scientific mechanism and not a part that should hamper one's courage to seek the truth. These perhaps most important lessons of graduate school can be consolidated in a single thought—never be afraid of feeling stupid.

Besides Carl Sagan and Johannes Kepler, many people have helped me realize that science is worth the trouble and have helped to make my time in graduate school rewarding. I have a long list of people whose help and support I wish to acknowledge. Firstly, I'd like to thank my adviser, John Gore, for giving me an opportunity. I walked into his office in 2006 and professed my interest in trying my hand at MRI research. Up until that time, my graduate school research had been focused on attempting to digest the workings of high-energy physics, and I was more than a little discouraged with my abilities to do so. John did not want to see a *curriculum vitae* or letters of reference. He had no idea who I was or what I was capable of, but he opened his doors to me and shared with me his hard-earned resources without hesitation. This attitude struck me as remarkable. Today, I see it as a hallmark of John's success—an open mind and a willingness to explore new ideas and new opportunities, often times with total disregard for the prevailing consensus. Over the last five years, John has been a very busy person. Nevertheless, he has found a way to make time for me and to help steer me away from dead-end streets. He has also given me complete freedom to explore the facets of MR science that most interest me. He seems to understand that new insights can be discovered in unpredictable contexts and that every question (well, most questions) deserve an answer—thus, he recognizes value in almost any investigation. I am indebted to John not only for his open-mindedness, his kind and patient support, and his sharing with me the opportunity to conduct research on state-of-the-art instruments but for his demonstration of how it is possible to be a successful scientist and administrator while still embracing one's own values. He has shown me a way to maintain uniqueness and courage in the face of a corporate machine.

Thank you to the other members of my Ph.D. committee for giving their valuable time to help direct me and give useful feedback to my studies. I thank Adam Anderson for finding time to answer my questions despite the myriad of other students vying for his attention and for his clear explanations to someone who knew nothing about magnetic resonance. When I returned from the 7 T MR scanner for the first time, with images that were mostly noise, he patiently went through the list of sequence parameters describing the many things I had done wrong. This must be an example of why so many students flock to him—because he really is so helpful, so kind, and so patient. I think Adam has not forgotten what it is like to be a student, a fact that makes him an excellent teacher. It makes perfect sense that he is heavily sought as an advisor and a mentor. I thank Volker Oberacker for being without question the most outstanding physics teacher I have ever taken a class from. He too has not forgotten the plight of the graduate student and has a true gift for decomposing daunting theories into a collection of comprehensible ideas such that true understanding is possible. I believe his ability to do this is critically important in instilling physics students will the self-confidence they need to succeed. The subject of physics can seem intimidating and discouraging when presented in a complicated way; however, when the teacher makes priorities out of clarify and simplicity, the subject can seem manageable and inspiring. I appreciate the willingness of Cynthia Paschal to remain on this committee despite her new responsibilities as a dean. I would like to thank her for supervising the writing of my first scientific paper, for teaching me so many basics of MR science, and for being such an approachable and caring mentor. I also wish to thank Todd Peterson for lending his physics expertise to the review of this thesis and for his willingness to spend time digesting research that is largely unrelated to his own. This is another example of how he patiently tolerates an MR dominated workplace in order to achieve a greater good.

I would like to thank Marcin Jankiewicz for being a friend through most of my graduate school days. Our daily conversations about RF pulses over the course of several years have led to and refined many of the ideas presented in this thesis. The way we feel comfortable admitting ignorance to each other has proved invaluable in gaining understanding of a subject we knew nothing about five years ago. This process has shown me that realizing how little you know is sometimes necessary in order to learn anything more.

I would like to thank Medford Webster for mentioning to me back toward the beginning of graduate school that “The things John Gore is doing in imaging science are nothing short of astounding.” Med, thank you also for demonstrating to me the way that the subject of physics can bring fulfillment and fascination to someone over the course of an entire lifetime. Your enthusiasm and determination are inspiring.

I want to acknowledge support of those who worked for Philips Healthcare during the majority of my time in graduate school. Brian Welch has been most helpful in keeping me up-to-date with respect to Philips software releases and virtual machines and source code repositories. His willingness to answer never-ending droves of questions about Philips programming, ExamCards, and MR scan parameters has been invaluable. Engineer Chuck Nockowski has made himself available at a moment's notice to investigate the various misfirings of a complicated and experimental machine. I am indebted to him for the long hours spent in making sure the scanner and the godforsaken couch were functional. I would also like to acknowledge the helpful advice of Stefan Fisher concerning RF pulse implementation on the Philips 7 T system.

The team of MR technicians has been indispensable in ensuring the smooth daily operation in the VUIIS Center for Human Imaging. Thanks to Donna Butler, Robin Avison, Debbie Boner, Leslie McIntosh, and Dave Pennell for always being there to help.

Kevin Waddell has been a very supportive friend over the last two years. I have very much enjoyed our conversations about things such as Thomas the Tank Engine and the native trees of Tennessee. I also appreciate Kevin coming to me with his ideas about low-field RF pulse applications and introducing me to this area of research, and I thank Raul Colón for spending so much time at the workbench trying to turn these pulse designs into something tangible. Including Sasidhar Tadanki, the four of us have made what I think is exciting progress in this arena.

I am grateful to Subechhya Pradhan for taking time out to reflect on life with me.

I believe we are kindred spirits, and your friendship is comforting. Thanks to Martha Holmes for appreciating the good and not-so-good moments of graduate school with me. It would be hard to make it out alive without embracing the humor in otherwise frustrating circumstances. I would like to thank Jim Joers and Indrajit Saha for attempting to bestow on me some of their knowledge of spectroscopy. Thanks to Don Nolting and Jason Buck for showing me around the chemistry lab. I appreciate conversations with Richard Dortch and Mark Does for mentioning the Version-S pulse during the VUIIS retreat of 2010. It it were not for them, I might have thought I had done something interesting for even longer.

Both literally and figuratively, I would not be here without my parents, Gayle and Paul Moore. Together, they have worked tirelessly to ensure that that my life is full of opportunity and potential and in doing so have shown me unconditional love. My mom has taken great care to instill in me self-confidence and has never let down her guard in making sure I feel loved and appreciated. My dad is characterized by selflessness, understanding, compassion, and creativity and has demonstrated the importance of these qualities to me. Everyday, thoughts of my dad motivate me in trying to make this world a better place, but not with anticipation of acknowledgement. For as long as I can remember, there has been an old, ragged copy of *Tao Te Ching* (80) on my dad's nightstand. The words remind me of him.

> The ten thousand things rise and fall without cease,
> Creating, yet not possessing,
> Working, yet not taking credit.
> Work is done, then forgotten.
> Therefore it lasts forever.

My brother, Will, has been my dear friend since the day I was born. I am indebted to him for his comradeship over the last thirty-something years. Since the beginning, we have sailed the course of life together and will always share that unique perspective. It has always been comforting to know he is with me.

Even though I'm not sure it was a conscious effort, my children, Evelyn and Nigel, have provided me with an extra incentive to finish graduate school. In the last few years, they have also revealed to me that school and work are only parts of life. They have helped me understand that doing something for another person can be one of life's greatest joys.

My heart is full of gratitude for my loving wife, Alisha. She has been so patient and supportive over these many years of graduate school. She has contributed so much to the self-confidence that I required to survive such an extended training program during which I questioned my abilities and self-worth on more than a few occasions. When it seems not so easy to go on, I always know that she is there. The comfort and security she provides gives me a place to which I can retreat from the world. Bob Dylan sang about a similar sentiment in 1975 (20).

> 'twas in another lifetime, one of toil and blood,
> When blackness was a virtue, and the road was full of mud,
> I came in from the wilderness, a creature void of form.
> "Come in," she said, "I'll give you shelter from the storm."

Everyone mentioned above has given up part of his or her own life and shared it with me. I am truly and forever grateful for your sacrifice, support, encouragement, guidance, and compassion.

TABLE OF CONTENTS

Appendices

LIST OF TABLES

LIST OF FIGURES

LIST OF SYMBOLS AND ABBREVIATIONS

RF	radio frequency	1
NMR	nuclear magnetic resonance	1
ω_0	resonant frequency	2
B_0	static magnetic field strength	2
γ	gyromagnetic ratio	2
MRS	magnetic resonance spectroscopy	2
MRI	magnetic resonance imaging	2
2-D	two-dimensional	3
M_0	equilibrium magnetization	4
$\mathbf{E}$	electric field	5
Φ_B	magnetic flux	5
M_T	transverse magnetization	118
S	signal	5
emf	electromotive force	6
SNR	signal-to-noise ratio	6
σ_T	thermal noise	6
σ_P	physiological noise	6
σ_S	Johnson noise	6
σ	total noise	6
a_s	sample size	7

a_c	coil size	7
λ	wavelength	8
ϵ	electrical permittivity	9
μ	magnetic permeability	9
c	speed of light	9
$^1\mathrm{H}$	hydrogen nucleus or proton	10
SAR	specific absorption rate	9
$\mathbf{M}$	bulk magnetization vector	11
B_1^+	RF transmission field	11
B_1^-	RF reception field	11
T_1	longitudinal relaxation constant	11
T_2^*	collective transverse relaxation constant	11
ϕ_M	transverse magnetization phase	12
ΔB_0	static magnetic field offset	12
1-D	one-dimensional	13
3-D	three-dimensional	13
δz	imaging slice thickness	107
BW	bandwidth	13
G_z	slice-selective gradient strength	13
$\mathbf{M_F}$	final magnetization vector	15
T_2'	transverse relaxation constant for reversible processes	16
T_2	transverse relaxation constant for irreversible processes	16

T_E	echo time	16
α	flip angle	16
$A(t)$	amplitude modulation function	17
$B_{1,\mathrm{nom}}^{+}$	nominal RF transmission field strength	17
R	rotation matrix	19
$\mathbf{B}_{\mathrm{eff}}$	effective field	21
BIR	B_1-insensitive rotation	22
DA	double angle	37
PSS	pulsed steady state	37
PSS+	pulsed steady state with optimized spoiling	37
GEs	gradient echo series	37
ssEPI	single-shot echo planar imaging	37
T_R	repetition time	38
A_G	gradient area	41
β	$M_0 B_1^{-}$	42
λ	$B_1^{+}/B_{1,\mathrm{nom}}^{+}$	42
$\overline{P}$	average power	55
$T_{R,\mathrm{min}}$	minimum repetition time	55
AFI	actual flip-angle imaging	56
GRE	gradient-recalled echo	56
α_0	nominal flip angle	56
N_s	number of sub-pulses	61

Δt_s	sub-pulse duration	61
ϕ	phase	61
δ	cost function value	62
F	B_1^+-dependent factor of signal equation	68
c_v	coefficient of variation	81
Δz	imaging slice thickness	107
M_T	transverse magnetization	118
γ_{eff}	effective gyromagnetic ratio	221
$^{13}\mathrm{C}$	carbon-13 nucleus	221

CHAPTER I

INTRODUCTION: THE ROLES AND CHALLENGES OF RADIO FREQUENCY PULSES IN HIGH-FIELD MAGNETIC RESONANCE

1.1 Historical Perspective

The research on radio frequency (RF) pulses presented in this thesis can not be properly motivated without a brief account of the history of nuclear magnetic resonance (NMR) and its application to medical imaging. Although certainly reliant upon early 20th century discoveries in the field of quantum mechanics by pioneers such as Stern, Gerlach, Pauli, and Bohr, the discovery of NMR can be traced to Isidor Rabi who, in 1938, first observed an electrical signal arising from the precession of nuclear magnetic moments in an external magnetic field (64). While Rabi's observations were in the context of molecular beams, Felix Bloch and Edward Purcell independently observed the same phenomenon in condensed matter in 1946 (6; 63). The detection of nuclear precession was possible since rotation of a nuclear magnetic moment gives rise to a changing magnetic flux which can then induce an electrical current in a conducting coil—a phenomenon described by Faraday's Law of classical electrodynamics[†]. Such experiments as the ones of Bloch and Purcell relied upon the continuous transmission of radio waves with the frequency being varied until signal was detected from a sample. By this method, known today as continuous-wave NMR,

---

[†] A more detailed description of the physical origin of NMR is provided in Appendix A, the intention of which is to bridge the knowledge of a typical physics student to the realm of NMR.

the radio frequency to which a certain nuclear species responded could be determined and thus the *resonant frequency* identified. The relationship between this resonant frequency (ω_0) and the ambient magnetic field strength (B_0) is characterized by the nuclear gyromagnetic ratio (γ) such that

$$\omega_0 = \gamma B_0 \, . \tag{1.1.1}$$

Continuous-wave NMR experiments performed with a known chemical sample can be used to determine the unique value of γ for any atomic nucleus. Once these γ values have been determined for the nuclei of interest, similar experiments can be used to acquire the spectra of the various resonant frequencies associated with an array of nuclear species in a complex chemical sample—a process known as NMR spectroscopy (MRS).

In the early 1970's, a major breakthrough in the application of NMR came when Paul Lauterbur, at New York's Stony Brook University, developed a technique for determining the originating location of an NMR signal (41). Lauterbur's method used spatially varying magnetic fields (now referred to as field gradients) to encode an NMR signal such that the spatial location of the signal's origin could be determined (41). Thus, images in which intensity reflects the NMR signal originating from a given spatial region or *voxel* were producible. This advance signified the birth of magnetic resonance imaging (MRI). While Lauterbur's image reconstruction technique involved projection of the imaging volume along various directions (as is the case in

X-ray computed tomography, or CT), Peter Mansfield and others at the University of Nottingham later employed two-dimensional (2-D) Fourier transform operations to form images from NMR signals (47), thereby establishing the basic method of image reconstruction still in use today. Allen Garroway, working with Mansfield at the University of Nottingham, pioneered the use of magnetic field gradients during the application of radio frequency pulses to restrict the NMR signal to a planar volume (22), a process now widely used to produce MR images of prescribed slices through the imaging volume. Raymond Damadian was also an instrumental figure in the early days of MRI. In 1971, while at the State University of New York (SUNY) Downstate Medical Center, he investigated the differences in nuclear magnetic properties of cancerous and healthy tissues as means for differentiating pathologies (18). In 1972, he filed a patent for an NMR scanning technique for use in diagnosing cancer and thus is sometimes also recognized as the co-discoverer of MRI. Damadian also produced *in vivo* NMR images as early as 1976 (17) and was the first to do so in the human body in 1977 (19). In the same year, Waldo Hinshaw and Raymond Andrew at Nottingham imaged the *in vivo* human wrist (29). Following the success of these first human MRI scans, the technology was quickly embraced by researchers at Hammersmith Hospital in London[†] (working with EMI, Ltd.) and the University of California San Diego (UCSF). Within only a few years, MRI technology had proven useful for clinical applications and was poised for commercial proliferation.

[†] John Gore was a medical physicist undertaking research in diagnostic imaging at Hammersmith Hospital when the first MRI system was constructed there in 1978. He led the research developments at this facility until moving to Yale University in 1982.

1.2 High-field MRI

While Lauterbur's imaging study of 1973 was conducted at 1.4 Tesla (1.4 T) and the human wrist study of Hinshaw was performed at half that field strength[†], the first whole-body human MRI scanners, such as those at Nottingham, Hammersmith, and UCSF, operated between 0.10 and 0.35 T. Since the early 1980's, technological refinement of large-scale superconducting magnets has allowed for the use of increasingly higher static field strengths in human scanners. A major step forward occurred in 1986 with General Electric's introduction of a 1.5 T clinical system. Today, 1.5 T is still commonplace for clinical use with 3.0 T systems becoming more widespread. About 40 research sites worldwide now have 7.0 T human scanners, with a few 9.4 T systems in operation. Figure 1 exhibits a timeline of the static field strengths used in clinical and research MRI since 1978.

The driving motivation for higher field strength is an increased NMR signal associated with the larger induced bulk magnetization (i.e., the macroscopic sum of individual nuclear magnetic moments) in the imaging volume. The bulk magnetization at equilibrium, typically symbolized as M_0, can be shown to be directly proportional to the static field strength, typically denoted by B_0 (see Appendix A). However, the electro-motive force that allows for detection of NMR signal depends on the rate of

---

[†] Hinshaw's experiment used a smaller solenoid that could accommodate a human arm. Construction of whole-body magnets is considerably more challenging and typically relies upon superconductivity to achieve fields greater than 0.1 T.

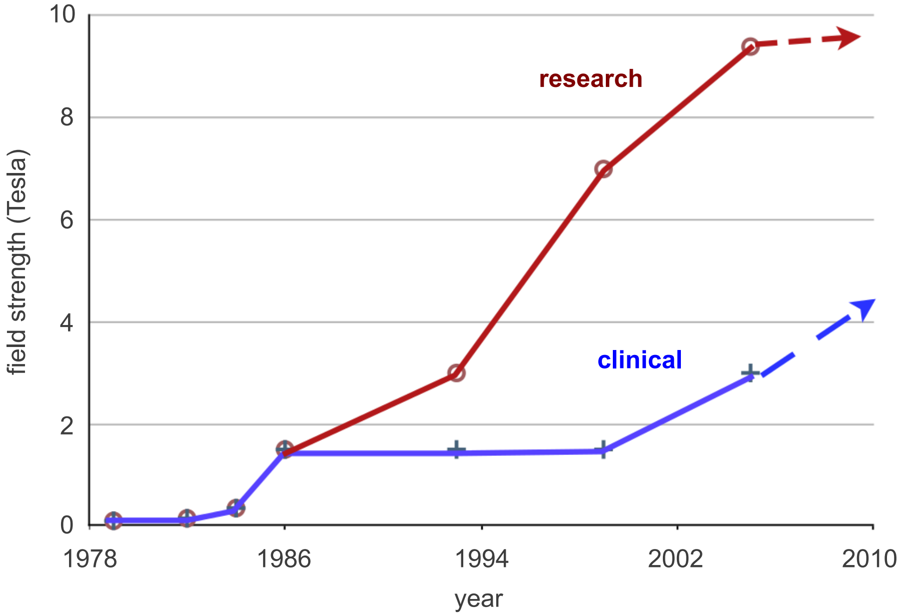

Figure 1: Highest field strengths of research and clinical human MRI scanners since the first whole-body systems in 1978. The 1.5 T fields first introduced in 1986 are still the worldwide clinical standard some twenty-five years later. Graphic courtesy of John Gore.

change of magnetic flux through the receiver coil and is expressible as

$$\text{emf} = \oint_{\text{line}} \mathbf{E} \cdot d\mathbf{s} = -\frac{d\Phi_B}{dt}\,, \tag{1.2.1}$$

with $\mathbf{E}$ being the electric field in the conducting coil, $d\mathbf{s}$ being the line element along the coil, and Φ_B being the magnetic flux through the coil. Φ_B depends on both the magnitude of the transverse component of magnetization (M_T) resulting from application of radio frequency radiation and the rate of precession of this magnetization as dictated by the nuclear resonant frequency (ω_0), so the NMR signal (S) can be written in terms of the static field strength via the following series of relations:

$$S \quad \propto \quad \mathrm{emf} = -\frac{d\Phi_B}{dt} \quad \propto \quad \omega_0 M_T \quad \propto \quad \omega_0 M_0 \quad \propto \quad B_0^2\,. \tag{1.2.2}$$

Thus, the signal is found to increase with the square of the static field.

The field-strength dependence of various noise contributions must also be considered to determine gains in the signal-to-noise ratio (SNR) and, thus, the actual practical advantage of higher B_0. Noise sources include thermal noise (σ_T) from random motions of molecules in the imaging volume, so-called physiological noise (σ_P) arising from such biological processes as tissue perfusion and the cardiac and respiratory cycles, and scanner Johnson noise (σ_S) originating in hardware such as the transmission/reception coils, pre-amplifiers, and associated electronics. The collective noise (σ) from these contributions can then be described through a typical error propagation relationship such that

$$\sigma = \sqrt{\sigma_T^2 + \sigma_P^2 + \sigma_S^2}\,. \tag{1.2.3}$$

To relate this collective noise to B_0, the dependence on static field strength of each noise component must be considered. σ_T scales with the size of the object and B_0. It has been demonstrated that σ_P depends directly on B_0 while σ_S largely depends on the frequency of the transmitted and received radiation (ω_0). Combining all contributions, noise can then be written in terms of ω_0 using Equation 1.2.3:

$$\sigma \quad \propto \quad \sqrt{a_c^2 \omega_0^{1/2} + a_s^5 \omega_0^2} \quad \propto \quad \omega_0 \quad \propto \quad B_0\,, \tag{1.2.4}$$

where a_c and a_s characterize the dimensions of the coil and the object, respectively. Combining this result with Equation 1.3.6 gives the field-strength dependence of SNR to be

$$\mathrm{SNR} = \frac{S}{\sigma} \quad \propto \quad \frac{B_0^2}{B_0} = B_0. \tag{1.2.5}$$

Thus, for large objects such as the human body, SNR is found to be directly proportional to the strength of the static field.

Higher SNR in MRI can be beneficial in two main ways—higher resolution images or shorter scan times. In the first case, higher SNR allows for the collection of images with higher spatial resolution such that the signal arising from individual voxels remains well above the background noise. Without higher SNR, such a high resolution image could be obtained but might appear “noisy” or “grainy” if acquired in the same amount of time. Only if scan time were lengthened could the same image quality be achieved at lower field strength. For example, a 2-fold increase in SNR could either be used to achieve voxel volumes of half the previous size or to reduce scan time by 75%.

High SNR is useful in MRS for similar reasons, but MRS at high field further benefits from a larger separation of resonant frequencies for different chemical species (i.e., a larger *chemical shift*). This allows for separation of NMR signals arising from two species with very similar resonant frequencies. For example, hydrogen protons in the molecule glutamate (a prominent neurotransmitter) have a slightly different resonant frequency than in the structurally similar molecule glutamine. The difference, due to interactions between hydrogen protons and the specific electromagnetic fields arising from other components of the given molecule, is always about 0.1 ppm (with respect to B_0). Thus, the ^{1}H NMR signals from glutamate and glutamine are separated by ~ 6 Hz ($\gamma_{1\mathrm{H}} \times B_0 \times 0.1 \times 10^{-6}$) at a field strength of 1.5 T but by ~ 30 Hz at 7 T.

There exist significant technical challenges that accompany the push to higher field strength. Perhaps the most consequential of these challenges are the attenuation and interference of radio waves and the increased energy absorption of radiation in tissue, both of which arise from the linear dependence of ω_0 on field strength (Equation 1.1.1). As ω_0 increases, so too must the frequency of the transmitted RF radiation in order to maintain nuclear resonance. The degree of RF attenuation in a dielectric medium such as the human body depends directly on the frequency of the radiation. The depth of RF penetration therefore becomes increasingly problematic at higher field strengths since, ideally, radiation would permeate the entire imaging volume with equal intensity. RF interference becomes important when the wavelength of radiation in the dielectric medium (λ_{RF}) is near or below the physical dimensions of the imaging volume. When this condition is satisfied, standing waves with prominent nodes and anti-nodes can arise in the sample, thereby causing the effective RF amplitude to vary with spatial location. For ^{1}H, λ_{RF} in biological tissues is roughly 50 cm at 1.5 T

($\omega_0 = 64\,\mathrm{MHz}$)[†‡], and standing wave effects are not necessarily troublesome when imaging the human torso and are even less worrisome when imaging the brain; at 3.0 T ($\omega_0 = 128\,\mathrm{MHz}$), λ_{RF} is reduced to 25 cm, and standing wave effects become pronounced in the human torso; at 7.0 T ($\omega_0 = 128\,\mathrm{MHz}$), λ_{RF} shrinks to almost 10 cm, and standing wave effects become prominent in volumes as small as the human brain (70). A graphical depiction of these relationships is presented in Figure 2. Both the phenomena of RF attenuation and RF interference result in spatially dependent RF fields that translates to MR images with pronounced regions of bright and dark (83). The clinical usefulness of such images is thus severely compromised, and the SNR advantage of higher field strength is limited to spatial locations at which these RF effects happen to be minimal. The primary purpose of the RF designs presented in this thesis is to mitigate such undesirable RF effects that arise when imaging the human body at high field.

The higher RF frequencies used at high field also result in more effective absorption of the radiation in tissue for the same physical reason that RF penetration depth is reduced. More RF absorption means more heating of tissue—an effect that becomes a safety issue at high enough amplitude or frequency. Safety regulation of the U.S. Food and Drug Administration (FDA) call for specific absorption rates (SAR) of

---

[†] In the context of physics, ω generally refers to an angular frequency; however, in NMR, ω is commonly adopted to symbolize any frequency regardless of the units of Hz or rad/s.

[‡] While $\lambda_{\mathrm{RF}} = c/\omega = 1/\left(\omega\sqrt{\epsilon_0\mu_0}\right)$ for electromagnetic radiation in a vacuum, $\sqrt{\epsilon_0\mu_0}$ is replaced by $\sqrt{\epsilon\mu}$ when considering radiation in a “poorly” conducting medium such as biological tissue (33), with c being the speed of light, ϵ the electrical permittivity, and μ the magnetic permeability. It is primarily the deviation of ϵ from ϵ_0 that is responsible for the reduction in wavelength that occurs when radiation travels from air to the human body.

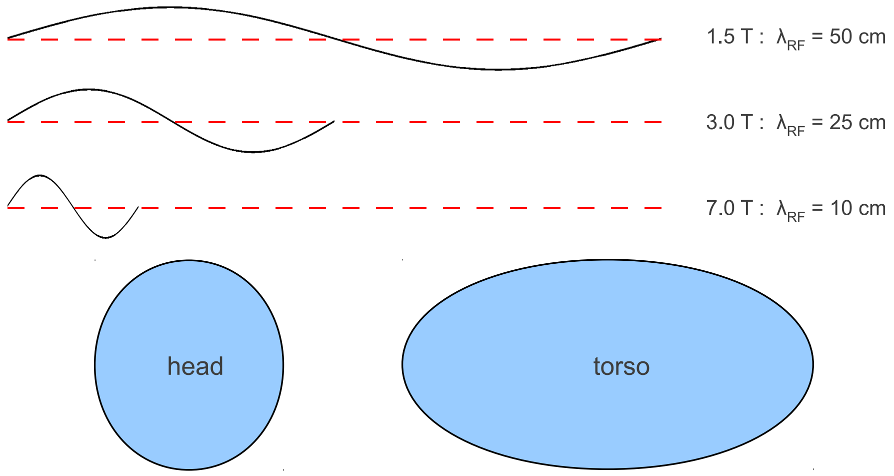

Figure 2: The relative RF wavelengths used in ^{1}H MRI at the given field strengths in relation to typical axial cross-sections of the human head and torso. When the RF wavelength is near or below the size of the imaging volume, standing wave patterns can arise that lead to significant variations in MR image intensity. The effect becomes quite severe in the torso at 3.0 T and in both the head and torso at 7.0 T.

radiation to not exceed 3 W/kg in the head, 4 W/kg in the body, and 8 W/kg in the extremities (13). At high field, compliance with these regulations often necessitates the lengthening of MRI scan times if the duration and amplitude of RF transmissions can not be adjusted accordingly. In practice, SAR restrictions thus complicate the design of RF waveforms for use at high field; therefore, SAR (or, equivalently, RF power) figures prominently in the practicality of the RF waveform designs presented in this thesis.

1.3 Manipulating Magnetization with RF Pulses

Central to any magnetic resonance experiment is the application of RF radiation that allows for control of the orientation of bulk magnetization. Without application of RF energy, bulk magnetization would remain aligned with the static magnetic field. Only when this magnetization is rotated into the *transverse* plane (i.e., perpendicular to the static field) by RF radiation does the orientation of the magnetization vector become time dependent and thus detectable with a receiver coil via Faraday induction. This section begins with a brief description of the response of magnetization to RF radiation as described by the Bloch equation and then proceeds with a discussion of various ways RF radiation can be transmitted to manipulate the orientation of magnetization and thus the NMR signal.

1.3.1 The Bloch equation

If the main field is oriented along the $\hat{z}$ direction, the behavior of a bulk magnetization vector $\mathbf{M} = (M_x, M_y, M_z)$ in an external field can be described in terms of the magnitude of the static field (B_0), the transmitted RF field ($\mathbf{B}_1^+$)†, the magnitude of $\mathbf{M}$ at equilibrium (M_0), and the decay constants T_1 and T_2^* through the empirical relationship

$$\frac{d\mathbf{M}}{dt} = \gamma \mathbf{M} \times \left(\Delta B_0 \hat{z} + \mathbf{B}_1^+\right) + \frac{1}{T_1}\left(M_0 - M_z\right)\hat{z} - \frac{1}{T_2^*}\left(M_x \hat{x} + M_y \hat{y}\right) \tag{1.3.1}$$

known as the Bloch equation. It is evident through the cross product in Equation 1.3.1 that application of an RF field will result in rotation of the magnetization. Time constants T_1 and T_2^* then characterize the return to equilibrium of a perturbed magnetization along the $\hat{z}$ and transverse directions, respectively, a process known as *relaxation*. The transverse magnetization components, M_x and M_y, undergo the same changes

---

† $\mathbf{B}_1^-$ usually denotes the RF field associated with the receiver.

due to T_2^* relaxation and are often referred to collectively as the transverse magnetization ($\mathbf{M}_T$) with a magnitude $M_T = \sqrt{M_x^2 + M_y^2}$ and a phase $\phi_M = \arctan\left(M_y/M_x\right)$. Equation 1.3.1 is expressed in a frame of reference that rotates with respect to the laboratory frame with an angular frequency equal to the nuclear resonance frequency ω_0. In the laboratory frame, ΔB_0—representing static field offsets with respect to the field strength for which the given nucleus in on-resonance—would be replaced by B_0 in Equation 1.3.1 . Further details of the Bloch equation and the formulations used for the numerical modeling results presented in this thesis are provided in Appendix B.

1.3.2 Radio frequency pulses

In the original NMR experiments described in Section 1.1, signals were obtained using continuous transmission of RF radiation; however, the application of short bursts of RF energy (known as RF *pulses* and pioneered by Erwin Hahn at the University of Illinois around 1950 (25; 26)) allows for far greater control of the bulk magnetization response†. While the rotation angle (or *flip angle*) of the bulk magnetization is controllable through the amplitude and duration of the RF pulse alone (defining a rectangular or block-shaped amplitude modulation), more sophisticated RF modulation patterns allow for targeting specific frequency bandwidths in NMR spectroscopy. For example, an amplitude modulation defined by the `sinc` function results in a rectangularly shaped frequency spectrum, as this is the one-dimensional

---

†Such RF pulses were employed in the original imaging experiments of the 1970's and are utilized by virtually all modern MR imagers and spectrometers.

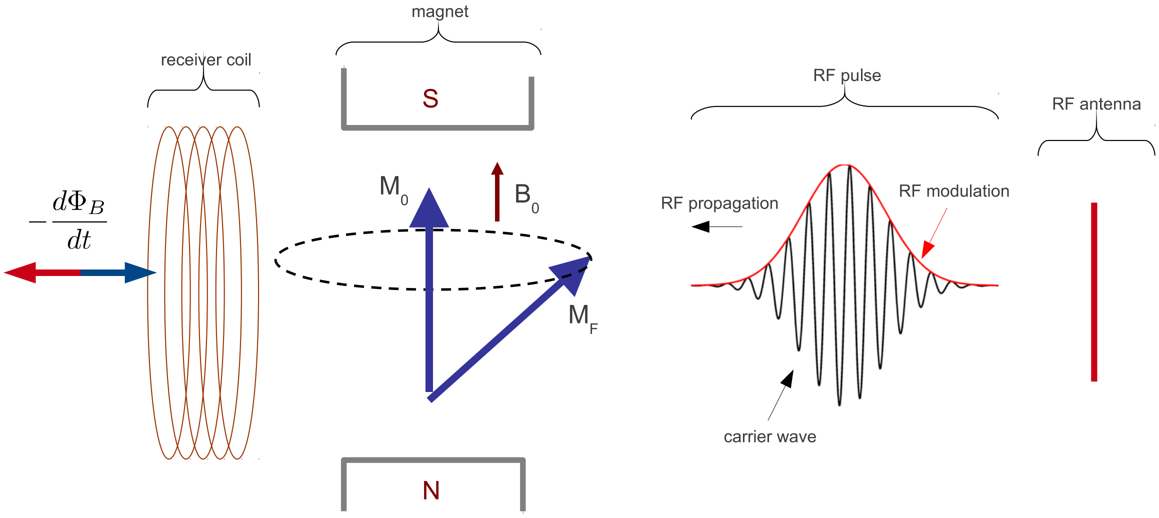

Figure 3: The basic elements of an NMR experiment. A static magnetic field (B_0) represented by North and South poles establishes a net magnetization (M_0) in a sample. Application of an RF pulse rotates the magnetization perpendicular to the static field according to Equation 1.3.1. The precession of the magnetization about the direction of the static field (also described by Equation 1.3.1) induces a time-varying magnetic flux through a conducting receiver coil which in turn produces a voltage as described by Equation 1.2.1. The observation of such voltages constitute the NMR signal.

(1-D) Fourier transform of the waveform (see Appendix A). In the context of MRI, such a `sinc` pulse can be transmitted in the presence of a linear magnetic field gradient applied across the imaging sample such that magnetization is affected only within a 3-D planar volume or imaging *slice*. The thickness of the imaging slice (Δz) can be controlled by the bandwidth of the RF pulse (BW) and the strength of the linear field gradient (G_z). The relationship between these quantities is given by

$$\Delta z = \frac{\mathrm{BW}}{\gamma G_z}\,. \tag{1.3.2}$$

This approach to slice-selective MRI is the basic technique first employed by Garroway and Mansfield in 1974 (Section 1.1) (22).

RF pulses have been described thus far in the context of *excitation*—the rotation of magnetization from its equilibrium so as to introduce a transverse component and thus a detectable NMR signal. However, RF pulses can be employed to manipulate the orientation and magnitude of the magnetization vector in a myriad of other ways. Two other broad categories of RF pulses to be discussed below are defined by the goals of magnetization *inversion* and *refocusing*.

Inversion pulses change the sign of M_z. The simplest example of this is analogous to an excitation pulse but with a flip-angle of 180°, thus rotating the vector $\mathbf{M} = M_0\hat{z}$ to $-\mathbf{M}$. In MRI, inversion pulses are typically used to generate image contrast among different tissue types. This effect is achieved by the application of an inversion pulse followed by a time delay. Due to the recovery of the disturbed magnetization toward equilibrium, which in this case is solely described by the longitudinal time constant T_1 in Equation 1.3.1, the magnitude of $\mathbf{M}$ depends on this time delay. Moreover, since T_1 is dictated by energy exchange with neighboring molecules and therefore the local magnetic environment, T_1 values, and therefore $\mathbf{M}$ magnitudes, may differ significantly from one tissue to another depending on tissue composition and structure. For example, T_1 values for white and grey matter in the human brain at a field strength of $7\,\mathrm{T}$ have been reported to be $1.22\,\mathrm{s}$ and $2.13\,\mathrm{s}$, respectively (66). The contrasting magnitudes of M_0 occurring in different tissues after a given time delay can then be translated into MR signal contrast through application of an excitation pulse that rotates longitudinal (i.e., $\hat{z}$) magnetization into the transverse

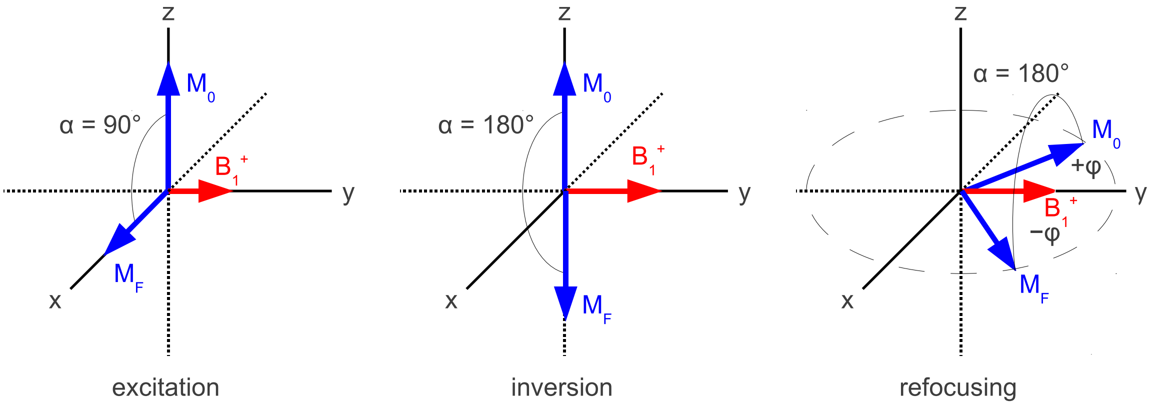

Figure 4: Examples of rotations induced by excitation, inversion, and refocusing pulses. In all examples, the direction of the $\mathbf{B}_1^+$ field is the same—along the $+y$ axis. In the excitation example, initial magnetization ($\mathbf{M}_0$) is in the $+z$ direction with $\mathbf{B}_1^+$ inducing a 90° rotation of the magnetization. In this case, all magnetization has been rotated into the transverse plane as indicated by the final magnetization vector ($\mathbf{M}_F$). The inversion example is identical to the excitation example except that the magnitude of $\mathbf{B}_1^+$ is twice as large, thus inducing twice the flip angle. The result is a change in the direction of the z component of magnetization. For the refocusing example, $\mathbf{M}_0$ lies in the x-y plane with a phase $+\phi$ relative to the $+y$ axis. $\mathbf{B}_1^+$ is identical to that of the inversion example, again inducing a 180° flip angle about the $+y$ axis; however, due to the different orientation of $\mathbf{M}_0$, it is the x component of magnetization (or, equivalently, the transverse phase) that is reversed. The dashed circle is to aid in the visual perception of $\mathbf{M}_0$ and $\mathbf{M}_F$ both lying in the x-y plane.

plane. This ordering of RF pulses and time delays is referred to as an inversion recovery sequence and is a widely employed method of generating T_1 tissue contrast in MRI. Additionally, an inversion recovery sequence can be used to null unwanted signal contributions based on the T_1 of the targeted tissue. To achieve this effect, a delay time is chosen such that $\mathbf{M} = 0$ for the tissue to be nulled. Such delay times can be analytically determined by solving the Bloch equation (Equation 1.3.1) for the case when ΔB_0, $\left|\mathbf{B}_1^+\right|$, and T_2^* are all zero. RF pulses applied for the purpose of canceling signal from specific chemical species are known as *saturation* pulses.

It is the role of refocusing pulses to reverse the phase of transverse magnetization so as to partially avoid signal losses arising from the decay of transverse magnetization. The transverse decay constant T_2^* in Equation 1.3.1 can be characterized by the sum of reversible (T_2') and irreversible (T_2) components such that

$$\frac{1}{T_2^*} = \frac{1}{T_2} + \frac{1}{T_2'} \,. \tag{1.3.3}$$

Coherent magnetization dephasing related to the time constant T_2' (i.e., the dephasing of transverse magnetization due to local variations in B_0) can thereby be recouped through application of a refocusing pulse such that contributions to the total transverse magnetization are again in phase at a time after the excitation pulse known as the *echo time* (T_E). Loss of transverse magnetization due to random processes involving exchange of energy with neighboring spins (i.e., T_2 decay) is not recoverable via application of RF pulses.

1.3.3 MR signal

In the simplest sense, MR signal is a function of the magnitude of the equilibrium magnetization (M_0), the magnitude of the RF field associated with the receiving coil (B_1^-), and the effects of one or more RF pulses. When considering a pulse sequence in which the only RF pulse is an excitation pulse (such as in a gradient-recalled echo or *GRE* sequence[†]), the actual flip angle (α) of the magnetization is determined by

---

[†] A GRE sequence brings transverse magnetization to a coherent phase, thus maximizing signal, through application of linear gradients that reverse phase dispersion induced by slice-selection and

the time integral of the product of the RF amplitude modulation function $A(t)$ and the relative magnitude of the B_1^+ field such that

$$\alpha = \gamma \int_0^{\Delta T} A(t) \frac{B_1^+}{B_{1,\text{nom}}^+} \, dt \,, \tag{1.3.4}$$

where ΔT is the RF pulse duration and $B_{1,\text{nom}}^+$ is the nominal B_1^+ field strength. If B_1^+ is not time-dependent, the associated term may be removed from the integration resulting in the expression

$$\alpha = \left(\gamma \int_0^{\Delta T} A(t) \, dt \right) \cdot \frac{B_1^+}{B_{1,\text{nom}}^+} = \alpha_0 \frac{B_1^+}{B_{1,\text{nom}}^+} \,, \tag{1.3.5}$$

where α_0, the product of gamma and the integrated RF amplitude of the pulse, is referred to as the nominal flip angle. M_T is the component of magnetization responsible for producing MR signal, so α can be related to signal (S) through the relationship $S \propto |\sin \alpha|$. Thus, considering the effects of M_0 and B_1^-, the MR signal can be written as

$$S = M_0 B_1^- \left| \sin \left(\alpha_0 \frac{B_1^+}{B_{1,\text{nom}}^+} \right) \right| \,. \tag{1.3.6}$$

Together, equations 1.3.5 and 1.3.6 demonstrate an example of the relationship between MR signal, the transmitted RF field, the received RF field, and an RF modulation (in this case an amplitude modulation), thus setting the stage for a discussion of the ways modulation patterns can be designed to counteract variations in B_1^+.

---

read-out gradients.

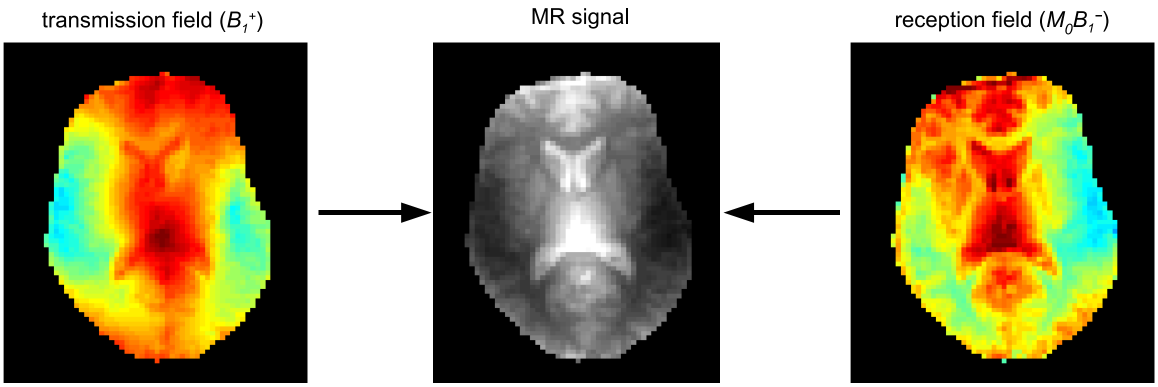

Figure 5: Effects of nonuniform RF fields on MRI signal intensity. The RF field maps at left and right are measurements of B_1^+ and $M_0B_1^-$ distributions in an axial slice of the human brain at 7 T. As described by Equation 1.3.6, MRI signal intensity (center) depends on both of these fields such that regions of reduced field strength give rise to low image intensity. The color scale for field maps is such field strength increases from blue to red.

1.4 Existing RF Pulse Designs that Address B_1^+ Inhomogeneity

As described in Section 1.2, undesirable variations in the B_1^+ and B_1^- fields[†] can arise in the human body at high B_0 due to increased levels of RF attenuation and interference. While the range of variations in B_1^- is typically similar to that in B_1^+ (since both are dictated by λ_{RF}, ϵ, and the dimensions of the imaging volume), the B_1^- field relevant to MR signal arises after application of RF radiation and, therefore, does not affect the performance of RF pulses. It is the B_1^+ field that forms during the transmission of radiation, and variations in this field are responsible for spatially inhomogeneous responses of the magnetization. Nevertheless, through the use of RF amplitude, phase, and/or frequency modulations, it is possible to design RF pulses that achieve a spatially uniform magnetization response, despite the presence

---

[†] While $\mathbf{B}_1^+$ and $\mathbf{B}_1^-$ represent vector fields, the magnitudes B_1^+ and B_1^- are referred to from this point on since the direction of the fields are not particularly relevant to the work presented in this thesis.

of spatial variations in the B_1^+ field†. Such pulses can be divided into two major classes: (1) B_1^+-insensitive pulses and (2) spectral-spatial pulses.

1.4.1 Existing B_1^+-insensitive pulse designs

B_1^+-insensitive pulses are designed to produce similar magnetization responses over certain ranges of B_1^+ variations. Such pulses can be designed for excitation, inversion, or refocusing. Over time, two main strategies have emerged for achieving the desired field-insensitive effects. The first strategy involves series of short RF pulses with varying phase and amplitude known as composite pulses. The second strategy relies upon RF modulations of slowly varying phase or frequency at high amplitude known as adiabatic pulses.

Composite pulses

RF pulses with some degree of immunity to variations in the B_1^+ field have been investigated extensively over the last 30 years. Malcolm Levitt and Ray Freeman were two of the first to explore such possibilities. Their studies of the early 1980's focused on the use of series of RF *sub-pulses* to collectively achieve a desired rotation while tolerating a certain level of B_1^+ inhomogeneity (44; 42; 43; 15). The authors referred to this class of RF pulses as *composite* pulses. An example of such a pulse still widely used today can be described by the notation $R_x(\pi/2)R_y(\alpha_0)R_x(\pi/2)$ where each R

[†] It is a common misconception that RF pulses can be designed to change the B_1^+ field. In fact, for a given transmission coil configuration, imaging volume, and resonant frequency, the B_1^+ field is always the same. RF pulses that mitigate inhomogeneous B_1^+ effects are designed to produce the desired magnetization response in the presence of the given B_1^+ field.

represents a sub-pulse (i.e., rotation), the subscripts indicate the axes of rotation, and the rotation angles are given in parentheses (44; 42). Thus, Levitt and Freeman discovered that the desired flip angle α_0 could be achieved despite $\sim 10\%$ fluctuations in the B_1^+ field as long as the nominal pulse was bracketed by two $\pi/2$ rotations with a 90° phase difference relative to the original pulse. This is an example of using amplitude and phase modulation to attain B_1^+-insensitivity..

While early composite pulse designs were based on the analytic theory of rotation operators, faster computer processing allowed for the investigation of numerical algorithms as an efficient means for determining suitable modulation patterns in the early 1990's. Such designs were pioneered by Michael Poon and Mark Henkelmann in the context of refocusing pulses (60; 61). Their work revealed the power of numerically optimized composite pulses to achieve prescribed degrees of insensitivity to variations in both the B_1^+ and B_0 fields. Like the analytically designed composite pulses of the 1980's, the main drawback to these numerically designed pulses is a noisy frequency spectrum outside the bandwidth of interest, thus making the pulses unsuitable for slice-selective imaging.

This thesis focuses on the development of numerically optimized composite pulses insensitive to the field variations observed in the human brain at 7 T, and, while the targeted B_0 is higher and the field inhomogeneities more pronounced than those considered by Poon and Henkelmann, some of the adopted strategies draw heavily upon these earlier efforts. Even the designs of Levitt and Freeman have proven highly relevant to high-field applications. For example, their $R_x(\pi/2)R_y(\alpha_0)R_x(\pi/2)$ refocusing design is examined extensively in Chapter V and exhibits noteworthy performance given the challenging context of 7 T imaging.

Adiabatic pulses

One of the first pulse designs to demonstrate B_1^+-insensitivity was the hyperbolic secant waveform proposed by Michael Silver, R. Joseph, and David Hoult in 1984. The pulse, which originates from an analytic solution to a relaxation-free formulation of the Bloch equation known as the Bloch-Riccati equation, is defined by a hyperbolic tangent amplitude modulation and a hyperbolic secant frequency modulation. The combination of these amplitude and frequency waveforms ensures magnetization inversion within a bandwidth dictated by the range of the frequency modulation. Moreover, as long as the magnitude of the *effective* field ($\mathbf{B}_{\text{eff}} = \mathbf{B}_1^+ + \Delta\mathbf{B}_0$) far exceeds the rate of change in the direction of $\mathbf{B}_{\text{eff}}$, a requirement known as the *adiabatic condition*, the same magnetization response can be expected. This behavior implies B_1^+-insensitivity given a certain minimum amplitude threshold in relation to the rate of change of RF frequency ($d\omega/dt$). While hyperbolic secant pulses are still in mainstream MRI use today, they do suffer in their utility in that B_1^+-insensitivity can only be achieved for inversion. Additionally, given the requirement of a minimum amplitude threshold with respect to $d\omega/dt$, the adiabatic condition can be difficult to satisfy when large B_1^+ variations are present unless the waveform is extended significantly in time—a process that can then introduce prohibitive SAR levels at high field.

Significant work has been undertaken since the inception of the hyperbolic secant pulse to adjust the modulation functions for improved performance with respect to field variations in specific contexts. These efforts have been spearheaded by Michael Garwood, Kâmil Uğurbil, and their colleagues and include methods of time-stretching modulations for targeting wider bandwidths (40; 78), investigations into the phenomenon of *offset-independent adiabaticity* (OIA) to improve off-resonance performance (39; 79), and modulation function determination from numerical optimization methods (NOM) to customize B_1^+-insensitivity (82; 36).

Uğurbil's work in the late 1980's proved instrumental in synthesizing composite and adiabatic pulse strategies. Through the use of 2- and 3-part composites of amplitude and frequency modulated sub-pulses, he was able to achieve B_1^+-insensitive excitation. The modulation waveforms were defined in terms of the `sin` and `cos` functions and were capable of producing uniform 90° excitations despite the presence of RF field inhomogeneities (81). These B_1^+-insensitive rotations are known as BIR-1 and BIR-2. In 1990, Scott Staewen, with Garwood and others, published a related 4-part pulse design (BIR-4) reliant upon `tanh` and `tan` modulation functions (76). Being capable of arbitrary flip angles, the BIR-4 pulse signified a notable advance in adiabatic pulse design. The year after BIR-4's introduction, Garwood demonstrated the generalization of the BIR-1 and BIR-2 pulses such that arbitrary flip angles could be attained through the proper adjustment of phase changes in these waveforms as well (23); however, the BIR-4 pulse has proven more practical due to a higher tolerance for B_0 variations and is still widely used today. While BIR pulses are extremely flexible in allowing for excitation, inversion, and refocusing, frequency spectra exhibit erratic behavior thus making the pulses unsuitable for slice-selective imaging. Very recently, a group at Stanford University headed by John Pauli found that using the BIR-4 modulation patterns as an envelope for a series of spectrally selective subpulses can result in a slice-selective waveform with similar B_1^+-insensitive properties to those of the parent BIR-4 (1). This formulation will certainly prove practical in many contexts, with the main drawback being the requisite fulfillment of the adiabatic condition. As mentioned previously, this requirement can prove prohibitive in high-field human applications.

In this thesis, work is presented in which hyperbolic secant and BIR-4 waveforms are numerically optimized to produce the desired insensitivities to field variations (Chapter VI). These efforts differ from those previously described in that the resulting magnetization flip angle is the subject of optimizations rather than fulfillment of the adiabatic condition. Additionally, Appendix C describes adiabatic pulses in more detail than is presented above, including the specific forms of the hyperbolic secant and BIR-4 modulation functions.

1.4.2 Existing spectral-spatial pulse designs

Spectral-spatial pulses are capable of depositing RF energy as a function of spatial location while also maintaining a desired spectral (i.e., frequency) response. In general, the potential of these pulses are realized in one of two arenas—either with a transmission coil for which all elements are driven with the same RF waveforms (i.e., with a single amplifier) or with a transmission coil for which individual elements are driven independently. The latter technology is typically referred to as *parallel transmission* or *multi-transmit* and has emerged in the last five years as the industry-adopted standard by which RF field inhomogeneities are addressed on high-field human scanners.

Single-channel transmission

Spectral-spatial RF pulses typically employ a series of sub-pulses in tandem with an oscillating gradient waveform. Early such designs relied upon the timing of sub-pulses relative to the oscillating gradient lobes to produce frequency selectivity, with spatial selectivity arising in the usual manner of finite bandwidth waveforms executed in the presence of a linear field gradient (57). These original studies were oriented toward targeting specific resonance frequencies in the context of a slice-selective imaging. For example, pulses were designed to excite fat within the imaging slice while minimizing signal from water or vice versa (50; 27). The incorporation of transverse gradients (i.e., field gradients imposed perpendicularly to the direction of slice selection) during or between the applied RF sub-pulses allowed for a focused magnetization response within predetermined regions of the imaging slice (65; 67). Eventually, these capabilities were recognized as a means of achieving uniform flip angles in the presence of B_1^+ inhomogeneities (68). This task can be accomplished through magnetization response being spatially allotted in accordance with the spatial distribution of the B_1^+ field. Spectral-spatial pulses in which relatively few discrete sub-pulses are interleaved with transverse field gradients have come to be known as *sparse spokes* (or simply *spokes*) designs, and it is this form of spectral-spatial pulses that is most commonly employed to address issues of RF field nonuniformity. Figure 6 illustrates the capability of a spokes design in compensating for the B_1^+ field variations observed in the human brain at 7 T. Clearly, the strategy is effective. Another application of spokes pulses involves limiting magnetization response to a confined region of the imaging field of view so as to allow for reduced scan times or practical, high-resolution imaging of specific anatomy. Regardless of the objective, spokes pulses are implementable on single-channel transmission systems with the potential disadvantage of long total pulse durations (with respect to T_2 and T_2^*) which may be required to achieve the desired effects. Additionally, the time-consuming subject-specific field mapping and RF calibrations that must be performed prior to implementation of spokes pulses for B_1^+ mitigation may prove prohibitive, especially in a clinical setting.

Parallel transmission

On a parallel transmission system, independent RF modulations can be executed simultaneously on each RF coil element. Knowledge of the B_1^+ fields associated with each coil element can be exploited through the design of channel-specific RF waveforms to counteract the unwanted effects of RF field variations. These RF strategies typically involve numerical optimization of the phase and amplitudes (and sometimes frequency) modulations to be transmitted on each channel. When only the physical separation of the coil elements (along with the optimized RF modulations) is em-

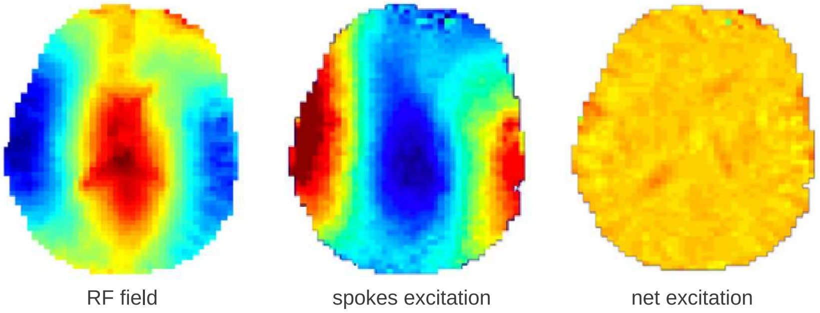

Figure 6: Simulation of a spokes experiment at 7 T showing an actual B_1^+ field measurement (left), the designed excitation pattern from a 25-spoke pulse (middle), and the net excitation pattern when the spokes pulse is executed in the presence of the nonuniform RF field (right). With a traditional RF pulse, the magnetization response would scale with the B_1^+ field such that a map of the resulting flip angles would reflect inhomogeneities in the B_1^+ distribution. Spokes pulses can be designed to circumvent this problem by concentrating RF effects in a pattern determined by the inverse of the B_1^+ field. Images reproduced with the permission of Marcin Jankiewicz (34).

ployed to achieve a spatially-varying magnetization response, the process is referred to as *RF shimming* (37; 48; 84; 49). With this technique, a single pulse is executed on each channel, and, most commonly, all pulses have the same form (e.g., Gaussian or `sinc`) with only constant phase and amplitude offsets. RF shimming has been shown effective in moderating B_1^+-related variations in magnetization phase and flip-angle, with efficacy generally corresponding to the number of RF channels. In practice, the number of independent channels is limited, and the performance of RF shimming is restricted due to the fixed locations of the transceiver elements.

When the spatially varying magnetization responses from RF shimming are inadequate, spokes pulses may be implemented for parallel transmission. The advantage of a parallel implementation of spokes pulses (as opposed to a single-channel implementation) is that fewer sub-pulses are necessary on each channel, thus resulting in total pulse duration times that are $\sim N$ times shorter where N is the number of channels. This increased efficiency relative to the single-channel implementation is due to an optimization in which the spatial separation of the transmitting elements is advantageous. Almost complete mitigation of B_1^+ inhomogeneities has been demonstrated in the human brain at 7 T using as few as 3 sub-pulses on each channel of an 8-channel system (71; 89).

MR systems equipped with multiple independent transmission channels are becoming increasingly widespread. The primary motivation is the same as for the use of single-channel spokes pulses—to produce uniform flip angles in the presence of severe B_1^+ variations. Multi-transmit pulse designs, however, are capable of achieving the desired magnetization responses in far less time, a critical factor given the shorter T_2^* values observed at high field. Despite the impressive performance of multi-transmit systems, there are some inherent limitations. Firstly, the requisite RF amplifiers are expensive, and compromise must be made between the number of channels and accepted performance levels. Also, while B_1^+-mitigation performance increases with the number of channels, so does the time needed to make the necessary field measurements, as separate field maps are required for each channel. Furthermore, the interactions of RF waves from independent coil elements can produce locally high SAR values in the imaging volume. These effects are a function of the coil geometry, the geometry of the imaging volume, and the set of RF waveforms (the latter two of which vary from subject to subject and from slice to slice), so SAR levels can potentially vary greatly from scan to scan, raising the question of whether subject-specific SAR modeling should be integrated with the pulse optimization process. Such measures, although perhaps justified, would add another step to an increasingly complicated subject-specific workflow—a factor that is not insurmountable but one that will have to be reconciled with clinical practicality in the face of rising healthcare costs.

As described in Section 1.4.1, the pulse designs presented in this thesis fall into the category of B_1^+-insensitive designs, rather than spectral-spatial designs, and are, in their current forms, intended for single-channel transmission.

1.5 Purpose and Overview

The inhomogeneous B_1^+ fields observed in the human brain at high field and the consequential nonuniform magnetization responses to applied RF fields form the motivation for the work presented in this thesis. The underlying purpose is, therefore, to explore the limits of RF pulse designs to counteract such ill-effects so as to better realize the full potential of high-field MRI. The studies of this thesis are focused on applications using a single-channel transmission system. This choice was motivated in part by the fact that no multi-transmit system was available on which to perform such research at the time of my graduate studies, and the pursuit of the implementation of such hardware and the subsequent application of new RF strategies in that context was perhaps beyond the scope of a graduate thesis project. An equally important factor was the acknowledgement that only by establishing the boundaries of existing technologies can we define the true benefits of new ones. Furthermore, the majority of pulse designs appearing in this work rely upon numerical optimization methods as applied to composite pulses. Through this approach, the power and efficiency of modern computing can be brought to bear upon a new challenge (i.e., the extreme RF inhomogeneities observed at high field) such that the appropriate limitations of previously proposed pulse structures can be established in this contemporary arena. The decision to largely pursue composite pulse designs rather than adiabatic ones has centered on the observation that the adiabatic condition is generally difficult to fulfill at 7 T given the observed range of field variations and the constraint that pulses can not be lengthened indefinitely due to SAR and relaxation effects.

Other related objectives surfaced while pursuing the design of B_1^+-insensitive pulses and have been included in the scope of this thesis. Most notably, perhaps, is the comparison of various methods of RF field mapping. To design B_1^+-insensitive pulses, a targeted range of field variations over which pulses are required to function must be established. To accomplish this, measurements of RF field magnitudes (RF field maps) can be made within the volume of interest. Initial findings suggested that widely adopted RF field mapping strategies differ dramatically in their resulting estimates of field strength and prompted a systematic evaluation of these differences. This objective turns out to be highly relevant to parallel transmission methods for mitigation of B_1^+ effects in which case the desired spatially varying magnetization response is determined by the inverse of the relevant B_1^+ map.

As colleagues became interested in the potential of composite pulse designs, other applications for these methods were brought to my attention. These include the optimization of adiabatic pulses for performance at 7 T, the incorporation of SAR limits in the optimization of composite pulses, and the design of frequency-selective composite pulses for an array of different applications. I ended up pursuing these projects concurrently with my main research objectives pursued, and relevant preliminary results are also presented in this thesis.

Following is a chapter-by-chapter summary of the work encompassed by this dissertation. Included are motivations and overviews of the major findings of each project.

RF field mapping (Chapter II)

This chapter describes studies to experimentally determine the variations in transmitted RF fields that are present in dielectric phantoms and the human brain at 7 T. Four leading RF mapping protocols are compared in the same context, with major discrepancies being identified amongst these strategies. Despite these differences, the general range of B_1^+ variations is established so as to identify the range of field variations to be targeted in the design of B_1^+-insensitive pulses. However, results are important to spectral-spatial B_1^+ mitigation strategies and suggest much work is warranted in the area of RF field mapping such that scan times can be shortened without significantly compromising the accuracy of measurements. This observation motivates an investigation into the use of one promisingly accurate mapping method in conjunction with fast, single-shot[†], echo-planar imaging (EPI). Results of this study suggest that use of single-shot EPI can provide very similar field maps while greatly accelerating

---

[†] All image data for a single slice is acquired after a single RF excitation, rather than over the course of multiple RF excitations. The penalty is loss of SNR and image distortion. The advantage is acquisition speed.

the data acquisition.

B_1^+-insensitive volume excitation (Chapter III)

In this chapter, a new class of composite RF pulses that perform well in the presence of specific ranges of B_0 and B_1^+ inhomogeneities is presented. This work was previously published in the *Journal of Magnetic Resonance* (56). Pulses are designed specifically for volume (non-selective) excitation in high-field MRI. The pulses consist of numerous (~ 100) short ($\sim 10\mu s$) block-shaped sub-pulses each with different phases and amplitudes derived from numerical optimization. Optimized pulses are designed to be effective over a specific range of frequency offsets and transmit field variations and are thus implementable regardless of field strength, transmit coil configuration, or the subject-specific spatial distribution of the static and RF fields. In the context of 7 T human brain imaging, both simulations and phantom experiments indicate that optimized pulses result in similar on-resonance flip-angle uniformity as BIR-4 pulses but with the advantages of superior off-resonance stability and significantly reduced average power. The pulse design techniques presented here are thus well-suited for practical application in ultra-high field human MRI.

B_1^+-insensitive slice-selective excitation (Chapter IV)

This work involves spatially selective excitation pulses designed to produce uniform flip angles in the presence of the RF and static field inhomogeneities observed in the human brain at 7 T. Pulse designs are based upon non-selective, composite pulses numerically optimized for the desired performance over prescribed ranges of field inhomogeneities. Non-selective pulses are subsequently transformed into spatially selective pulses with the same field-insensitive properties through modification of the spectral composition of the individual subpulses which are then executed in conjunction with an oscillating gradient waveform. An in-depth performance analysis of the resulting class of RF pulses is presented in terms of total pulse durations, slice profiles, linearity of in-slice magnetization phase, sensitivity to RF and static field variations, and signal loss due to T_2^* effects. Analysis involves both simulations and measurements in phantoms and the *in vivo* human brain for nominal flip angles of 45° and 90° and relies upon the performance of a single Gaussian pulse as a basis for evaluation. Target slice thickness in all cases is 2 mm and is achieved despite the hardware limitations of a commercial 7 T MRI system. Results indicate that the described class of field-insensitive RF pulses is capable of improving flip-angle uniformity in the context of 7 T human brain imaging. There appears to be a subset of pulses with durations $\lesssim$ 10 ms for which non-linearities in the magnetization phase are minimal and signal loss due to T_2^* decay is not prohibitive. Such pulses represent practical solutions for achieving uniform flip angles in the presence of the large field inhomogeneities common to high-field human imaging and help to better establish the performance limits of high-field imaging systems in the regime of single-channel transmission.

Evaluation of refocusing pulses (Chapter V)

There is a continuing need for improved RF pulses that achieve proper refocusing in the context of ultra-high field ($\geq 7\,\mathrm{T}$) human MRI. Simple block or `sinc` pulses are highly susceptible to RF field inhomogeneities, while adiabatic pulses are generally considered too SAR intensive for practical use at 7 T, but the performance of the array of pulses falling between these extremes has not been systematically evaluated. The aim of this work was to compare the performances of 16 different previously suggested non-selective refocusing pulses ranging in duration from ~ 1-13 ms. The evaluation includes measurements in both a phantom and *in vivo* human brain at 7 T. Tested designs included block, composite block, BIR-4, and numerically optimized refocusing pulses. These pulses were divided into three classes based on SAR, and practical recommendations on usage based on performance are made within each category. All evaluated pulses were found to produce greater volume-averaged signals relative to a 180° block pulse, and some pulses increased signal by more than a factor of three in localized areas. Through both simulation and experiment, this work demonstrates the signal gains and losses realizable with single-channel refocusing pulse designs and should assist in the selection of suitable refocusing pulses for practical 3-D spin-echo imaging at 7 T. It further establishes a reference against which future pulses and multi-channel designs can be compared.

Related pulse designs and applications (Chapter VI)

This chapter contains a sample of other applications for numerically optimized RF pulses. The first section describes findings related to the customizations of adiabatic pulses (specifically, hyperbolic secant and BIR-4 pulses) to the demands of 7 T imaging. Foremost, this investigation establishes appropriate bandwidths for hyperbolic secant inversion pulses used in the brain at 7 T—thus, maximizing the available B_1^+-insensitivity of these RF modulations. Furthermore, numerical optimization of BIR-4 waveforms is shown to significantly improve 7 T performance over that of the previously presented modulations. The second section of this chapter describes incorporation of SAR constraints in the optimization of non-selective composite pulses similar to those presented in Chapter III. Results indicate that pulse sequence repetition times as low as 200 ms can be accommodated with almost no loss in B_1^+-insensitivity and that significant immunity to field variations can still be achieved at repetition times of 50 ms. In the third section, studies of frequency selective, B_1^+-insensitive composite pulses are presented with particular focus on achieving slice selection in the presence of a linear field gradient. Results indicate that such pulse designs for saturation appear feasible but that maintaining a linear magnetization phase through the imaging slice is challenging when also requiring a high degree of B_1^+-insensitivity. The next section focuses on frequency selective composite pulses for B_1^+-insensitive saturation of lipids and water. Simulations of these endeavors have been successful thus far and initial experiments encouraging. Lastly, composite pulse designs relevant to single-channel polarization transfer at low-field are presented. In this context, RF field inhomogeneities are not considered, thus providing an arena in which other capabilities of composite pulses can be tested. While transmitting at a central frequency, RF pulses are designed for precise control of magnetization in prescribed off-resonance frequency bands. Designs include single- and dual-band excitation and refocusing. These novel pulses circumvent the need for an independent amplifier operating at each targeted frequency.

Appendices

Five appendices are included. Appendix A provides MR physics background and is written to help students relate a classroom understanding of physics to the discipline of NMR. Appendix B gives a detailed description of the methods employed in this thesis for the numerical simulation the Bloch equation, and may be helpful in assisting future students do the same. In Appendix C, modulation functions for hyperbolic secant and BIR-4 waveforms are provided along with identification of the parameters subject to numerical optimization in Chapter VI. Appendix D supplies additional simulation data relevant to Chapter III, and Appendix E describes the optimal control algorithm employed for the low-field, frequency-selective pulse designs discussed in Chapter VI.

CHAPTER II

RF FIELD MAPPING

2.1 Introduction

Accurate field mapping is integral to the success of ultra-high field MRI. Knowledge of the spatial variations in transmitted RF fields (B_1^+) allows for the calibration of RF pulse amplitude, guides the design of adiabatic and other B_1^+-insensitive pulses, and enables real-time pulse designs that capitalize on parallel transmission technologies (e.g., spectral-spatial excitations and RF shimming). Maps of the receive field (B_1^-) permit post-processing image intensity corrections and facilitate the design of RF coils for high-field applications. Static field variation (ΔB_0) maps are used in an array of applications from RF pulse calibration to post-processing image distortion correction.

One of the challenges currently facing high-field MRI research is the fast acquisition and calculation of RF (B_1^+ and B_1^-) field maps without sacrificing the accuracy of measurements. Development of new RF field-mapping techniques for this purpose is an area of active research. Presently, a handful of such methods are in common use; however, a systematic study has not been undertaken in which field maps resulting from the use of these protocols at high field are compared. Such a comparative study performed in the context of human brain imaging at 7 T is the focus of this chapter. Results of this study will aide in the selection of mapping protocols for specific tasks through providing knowledge of potential errors associated with each method. Since it is relatively straightforward to infer the B_1^- distribution from a measured B_1^+ distribution given that corresponding low flip-angle, gradient recalled echo (GRE) images are attained, the RF mapping evaluation of the present study focuses on the measurement of the B_1^+ field.

The methods evaluated in this study are a 2-D double-angle (DA) technique (77), a 3-D pulsed steady-state (PSS) sequence[†] (87), a 3-D PSS technique with optimized gradient and RF spoiling (PSS+) (88), and a 2-D multi flip-angle approach relying upon voxel-by-voxel data fitting (abbreviated as GEs for gradient-echo series) (30). Additionally, the latter method is performed with a single-shot EPI read-out (GEs-ssEPI), thus allowing for a much shorter acquisition time. This single-shot approach apparently has not been investigated before and thus represents a novel approach to high-speed RF field mapping.

2.2 Methods

The five RF field mapping protocols evaluated in this study (DA, PSS, PSS+, GEs, and GEs-ssEPI) are summarized in this section, and the way in which each was implemented is described. Following these explanations is a description of the comparative analyses. In the first analysis, the results from the DA, PSS, PSS+, and GEs protocols are compared. In the second analysis, results from the GEs and GEs-ssEPI protocols are compared. All data in this study was collected using a Philips 7 T whole-body MR scanner (Philips Healthcare, Best, The Netherlands) with a single-

---

[†] The pulsed steady-state method of Vasily Yarnykh has also become known as *actual flip-angle imaging*, or AFI.

channel volume head coil (Nova Medical, Wilmington, MA, USA) for RF transmission and reception.

2.2.1 DA technique

The DA approach to RF field mapping, like the PSS and PSS+ protocols, results in an estimation of the distribution of actual flip angles experienced by the magnetization. It is then typically assumed that the excitation pulses employed in mapping sequences result in actual flip angles that are determined by the integral of the amplitude modulation function in the presence of a constant relative B_1^+ ($B_1^+/B_{1,\mathrm{nom}}^+$) magnitude (See Equation 1.3.4). Under these circumstances, the flip angle (α) can be assumed proportional to the relative B_1^+ magnitude at a given spatial location, so that resulting flip-angle maps reflect the spatial distribution of the B_1^+ field[†].

The DA method relies on the ratio of two MR signals for calculation of the actual flip angle. For a gradient-recalled echo sequence with a long repetition time (T_R) and a short echo time such that $T_R \gg T_1$ and $T_E \ll T_2^*$, the MR signal (S) can be written as

$$S = M_0 B_1^- \left|\sin\alpha\right| \,, \tag{2.2.1a}$$

which is similar to Equation 1.3.6 but with α representing the actual flip angle. If two such signals (S_1 and S_2) are acquired with nominal flip angles α_0 and $2\alpha_0$, respectively,

---

[†] It is somewhat of a misnomer to refer to these techniques as B_1^+-mapping techniques as is commonly done—they are really flip-angle mapping techniques. On the other hand, it can be argued that the GEs method results in measurements of $B_1^+/B_{1,\mathrm{nom}}^+$, as this quantity is one of the fitting parameters. However, even in this case, the real measurement is an MR signal which depends on the magnitude of transverse magnetization as described by the flip angle.

the signal ratio is given by

$$\frac{S_2}{S_1} = \frac{\sin 2\alpha}{\sin \alpha}\,, \tag{2.2.1b}$$

with α again representing the actual rather than nominal flip angle. If a double-angle trigonometric identity is used to expand the denominator of the right-hand side, this expression becomes

$$\frac{S_2}{S_1} = \frac{2\sin\alpha\cos\alpha}{\sin\alpha} = 2\cos\alpha\,, \tag{2.2.1c}$$

which can be solved for α:

$$\alpha = \arccos\left(\frac{S_2}{2S_1}\right)\,. \tag{2.2.1d}$$

Thus, two GRE images acquired under the given conditions can be used to determine the actual flip angle for each voxel in the image corresponding to S_1.

In this study, such images were acquired for the central axial slice of a 17 cm spherical dielectric phantom (Functional Biomedical Information Research Network, FBIRN) and the human brain using $\alpha_0 = 60°$, $T_R = 5\,\mathrm{s}$, and $T_E = 3\,\mathrm{ms}$ with an in-plane imaging resolution of $3 \times 3\,\mathrm{mm}$ and a slice thickness of 5 mm. Total required scan time was 13 min 20 s for a 240 × 240 mm field of view.

2.2.2 PSS technique

The PSS method also relies on the ratio of two MR signals but in a somewhat more complex way due to the use of a steady-state signal acquisition. The primary motivation for this approach is the reduced acquisition time resulting from a shorter T_R. In the steady-state scenario, T_R may be on the order of T_1 such that longitudinal relaxation can no longer be ignored. Furthermore, the PSS method does not employ two different flip angles like the DA method but rather uses a single flip angle but two different T_R values. These T_R's are interleaved with S_1 being associated with the acquisition during $T_{R,1}$ and S_2 arising from acquisition during $T_{R,2}$. If the Bloch equation is solved under these conditions, the two signals can be expressed as

$$S_1 = M_0 \frac{1 - e^{-T_{R,2}/T_1} + \left(1 - e^{-T_{R,1}/T_1}\right) e^{-T_{R,2}/T_1} \cos\alpha}{1 - e^{-\left(T_{R,1}+T_{R,2}\right)/T_1} \cos^2\alpha} e^{-T_E/T_2^*} \sin\alpha \tag{2.2.2a}$$

and

$$S_2 = M_0 \frac{1 - e^{-T_{R,1}/T_1} + \left(1 - e^{-T_{R,2}/T_1}\right) e^{-T_{R,1}/T_1} \cos\alpha}{1 - e^{-\left(T_{R,1}+T_{R,2}\right)/T_1} \cos^2\alpha} e^{-T_E/T_2^*} \sin\alpha\,. \tag{2.2.2b}$$

The ratio of these signal expressions can then be taken and α solved for in a way analogous to that demonstrated for the DA technique. The resulting expression for the actual flip angle is

$$\alpha \approx \arccos\left[\frac{(S_2/S_1)\,(T_{R,1}/T_{R,2}) - 1}{(T_{R,1}/T_{R,2}) - (S_2/S_1)}\right]. \tag{2.2.2c}$$

The PSS method was implemented, and flip-angle maps were acquired for the central axial slice of a 17 cm dielectric phantom and the human brain using $\alpha_0 = 60°$, $T_{R,1} = 20\,\text{ms}$, $T_{R,2} = 100\,\text{ms}$, and $T_E = 5\,\text{ms}$ with an in-plane imaging resolution of $3 \times 3\,\text{mm}$ and a slice thickness of 5 mm. As is typical for a steady-state sequence, signal was acquired over a contiguous 3-D volume that encompassed the entire phantom/brain. Total required scan time was 2 min 44 s for a 240 × 240 × 85 mm field of view.

2.2.3 PSS+ technique

Steady-state sequences often employ strong field gradients following each period of signal acquisition in order to dephase the transverse magnetization. The purpose of these gradients is to prevent formation of magnetization coherencies that form as a function of local T_2^* values, thus lending T_2^* weighting to the resulting signal. For the same reason, the phase of transmitted radio waves is typically incremented from pulse to pulse. The former technique is known as *gradient spoiling* and the latter as *RF spoiling*. In 2010, Vasily Yarnykh, the inventor of the PSS method, published his findings related to the influence of incomplete magnetization dephasing and improper RF phase increments on the accuracy of PSS flip-angle measurements. Yarnykh's studies suggest: use of the largest possible spoiling gradients[†] (given practical limitations) is critical; the ratio of the spoiling gradient areas associated with signals S_1 and S_2 (i.e., $A_{G,1}$ and $A_{G,2}$, respectively) is chosen such that the condition

$$\frac{T_{R,2}}{T_{R,1}} = \frac{A_{G,2}}{A_{G,1}} \tag{2.2.3}$$

is maintained; the RF phase increment that most effectively prohibits the development of RF phase coherencies depends on the size of the spoiling gradients; a flip-angle of

---

[†] In this case, a *large* gradient means a gradient waveform with a large integrated area.

60° results in the most accurate flip-angle measurements.

PSS+ experiments were carried out in the same way as for the PSS protocol, with the recommended adjustments being made. Spoiling gradient areas of $A_{G,1}/A_{G,2} = 280/1400\,\mathrm{mT \cdot ms/m}$ were employed along with an RF phase increment of 34° as recommended by Yarnykh. All other sequence parameters were the same as in the PSS case, and measurements were again obtained in both the phantom and human brain.

2.2.4 GEs technique

In the GEs approach, RF field mapping is based upon a voxel-by-voxel, least-squares fitting of signal intensity from a multi flip-angle series of GRE images—a method previously adopted to generate B_1^+ maps for sparse spokes RF pulse designs (89; 34). Given a GRE signal intensity represented by

$$S_i = \beta \left|\sin\left(\lambda\, \alpha_{0i}\right)\right| \,, \tag{2.2.4}$$

with β representing the product of the received RF field (B_1^-) and the initial magnetization (M_0) and λ indicating the ratio of the actual transmitted RF field magnitude (B_1^+) to the corresponding field magnitude ($B_{1,\mathrm{nom}}^+$) associated with the nominal flip angle α_{0i} of the i-th image in the series, a least-squares fit of the parameters β and λ to the S vs. α_0 curve for each voxel in the imaging slice results in a measure of λ (i.e., the relative magnitude of the B_1^+ field) (89; 30). This method is believed to be the most accurate of the four major techniques evaluated in this study due to (1) the use of long T_R values that minimize the potential for magnetization coherencies and (2) the increased number of measurement points for each voxel. Additionally, this technique has the benefit of returning an estimate of the collective quantity $M_0B_1^-$ as one of the fitting parameters.

The GEs technique was implemented with the same scan protocol as was used for the DA technique. The flip-angle was varied from 10° to 210° in 20° steps for a total of 11 scans, and the voxel-by-voxel, least-squares fitting of the parameters β and λ was performed using custom written Matlab code (The MathWorks, Natick, MA, USA). An EPI factor of 3 was employed such that the total scan duration could be limited to 19 min 30 s.

2.2.5 GEs-ssEPI technique

The main disadvantage of the GEs approach to measuring B_1^+ and $M_0B_1^-$ is the lengthy scan duration required to accommodate ≥ 10 dynamics with varying flip angles while keeping T_R long enough that the resulting signal is independent of T_1 relaxation. To overcome this limitation, the GEs-ssEPI approach employs a single-shot EPI read-out. Given the B_0 variations in the brain at 7T, dramatic distortions result from the use of single-shot EPI; however, acquisition of a ΔB_0 can readily be used to make the necessary EPI distortion corrections (35).

In the GEs-ssEPI protocol, ΔB_0 is first measured using a 3-D GRE scan ($3\times3\times5$ mm resolution, 33 axial slices, $T_R = 4.0$ ms, $\alpha = 10°$) with a double echo acquisition

($T_{E,1} = 1.6\,\mathrm{ms}$, $T_{E,2} = 2.6\,\mathrm{ms}$) and second order static field shimming. Total scan time is 16 s. ΔB_0 is calculated from the phase difference of the two acquisitions and the known ΔT_E of 1 ms. Sequence parameters were the same as for the GEs scan except for the single-shot read-out and a multi-slice acquisition allowing for near whole-brain coverage. Also, the GEs scan was repeated with the same multi-slice acquisition such that whole-brain field distributions obtained with and without single-shot EPI could be compared. After data collection, distortion correction and the least-squares fitting were performed in Matlab, taking approximately 60 s. Whole-brain RF mapping data was acquired in 65 s for a total scan+processing time of $\sim 2.5\,\mathrm{min}$. Thus, the necessary time to perform RF mapping was reduced by a factor of ~ 8 with respect to the GEs protocol with an EPI factor of 3.

2.3 Results and Discussion

As described in Section 2.2.4, there are fundamental reasons why the GEs method is thought to result in accurate RF field measurements. Thus, this method was selected as the standard for comparison, and DA, PSS, and PSS+ maps were divided on a voxel-by-voxel basis by the corresponding GEs map so as to highlight differences among the various measurements. In the event that GEs measurements are the most accurate, these ratios represent an estimate of the error associated with each technique. GEs-ssEPI results were collected on a different human subject (along with a corresponding set of GEs measurements) and are, therefore, only compared to GEs results. In this case, no voxel-by-voxel division is performed. Rather, RF field measurements are reported in conjunction with the ΔB_0 measurements in the form of

ΔB_0-B_1^+ voxel-density grids. Such grids are a graphical representation of the overall distributions of the B_0 and B_1^+ fields.

2.3.1 Existing techniques

Actual flip-angle/B_1^+ maps in the central axial slice of the phantom as measured by the DA, PSS, PSS+, and GEs protocols are presented in Figure 7. Line profiles reflect flip-angle measurements along the indicated left-right lines. Also included in this figure are the calculated ratios of flip-angle measurements of the given method to those acquired with the GEs method. Differences among the results of the four techniques are striking. For example, in low B_1^+ regions, DA measurements differ from GEs measurements by up to 50%. The PSS map systematically overestimates flip angles by $\sim$ 25% as compared to the GEs results, suggesting that errors associated with the method are not spatially dependent. Error in the PSS+ map is significantly reduced with respect to that in the PSS map, thus insinuating that incomplete spoiling is greatly affecting the PSS results. Furthermore, the PSS+ errors don't correlate with regions of high and low B_1^+ as do the DA errors and, to a lesser degree, those of the PSS method; therefore, the PSS+ method appears to correctly determine the RF field geometry (assuming the GEs measurements are more or less correct), and only a modest offset between PSS+ and GEs methods is left unaccounted for. Results from all four protocols are somewhat consistent in confirming that B_1^+ field strength in the phantom spans a range equivalent to $\sim$ 70% of the nominal value. GEs measurements indicate that actual B_1^+ values range from $\sim$ 0.4–1.1 in units of the nominal field strength.

Field maps in the brain, shown in Figure 8, largely echo the phantom results; however, one noteworthy difference is a reduction in the total dynamic range of B_1^+ as compared to the phantom (at least for this particular slice). While this range was $\sim 70\%$ in the phantom, it is closer to $\sim 50\%$ in the brain. Moreover, the central "hot spot" is not as exaggerated in the brain, an effect that is likely due to the higher degree of geometric symmetry in the phantom and the conduciveness of that symmetry to RF standing wave patterns. Another noticeable difference between phantom and brain results are the larger PSS errors (i.e., values of ratios with respect to GEs maps) in the latter. These deviations appear to correlate with ripple artifacts in the PSS maps of the brian and could be indicative of the sensitivity of the PSS method to B_0 variations. These artifacts may not have surfaced in the phantom data due to the superior level of B_0 shimming that is possible in this volume. Another possible explanation of these artifacts is the fact that the PSS and PSS+ sequences employ a block-shaped excitation pulse whereas the DA and GEs sequences use sinc pulses. RF excitation occurring outside the imaging slab due to the non-selective characteristics of the block-pulse's frequency profile can be aliased back into the actual, thus producing artifact such as those exhibited by the PSS brain maps. Inspection of the GEs brain map reveals what appears to be subtle T_1 weighting of the RF field measurements. Since B_1^+ is not expected to vary according to tissue type in the brain (i.e., dielectric constants of grey and white matter are very similar), the presence of T_1 weighting indicates that the T_R of $5\,\mathrm{s}$ is insufficient to allow full magnetization recovery in long

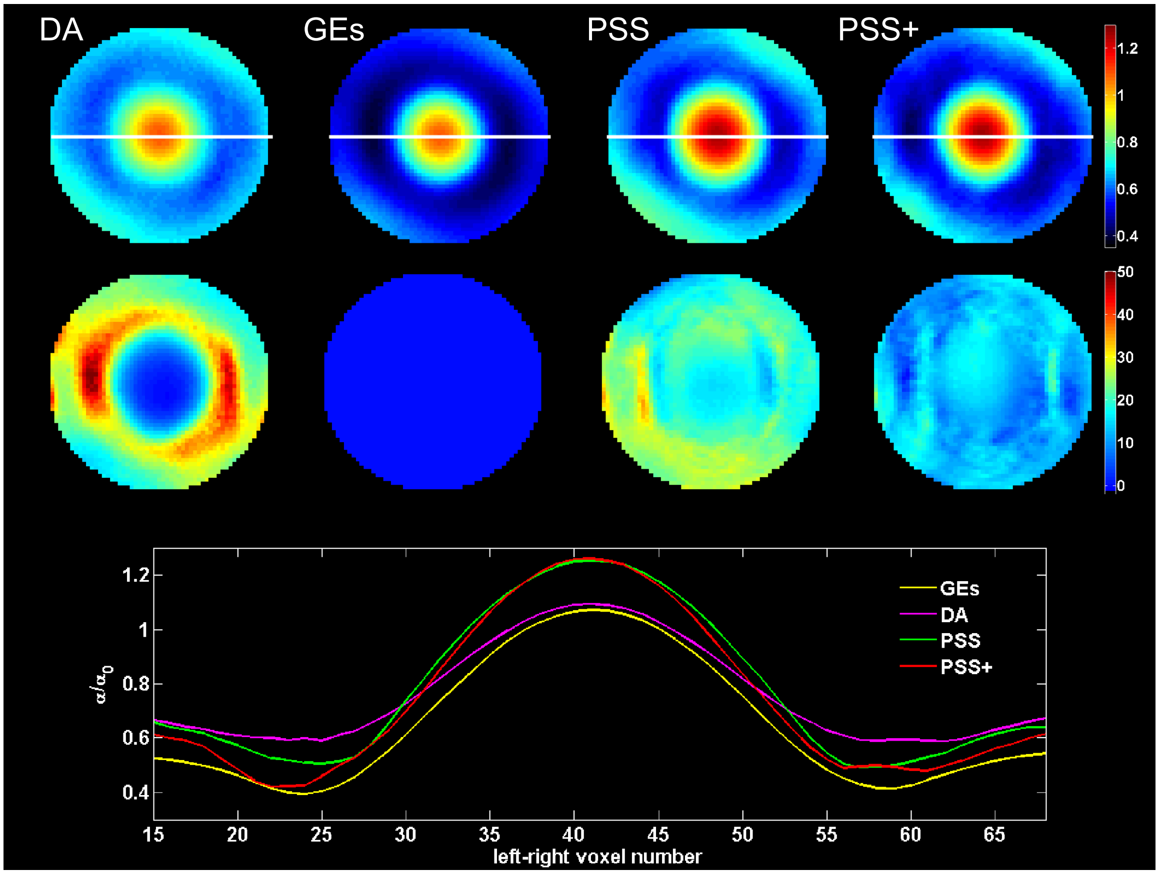

Figure 7: Axial flip-angle maps acquired via four different protocols in a 17 cm dielectric phantom at 7 T (first row); the ratio of those flip-angle maps to the GEs map (middle row); and line profiles across the maps at the indicated positions (bottom). These maps indicate a total dynamic range in the B_1^+ field of $\sim$ 70% relative to the nominal RF field strength. Measurements differences are significant among protocols, with the DA technique resulting in $\sim$ 50% variations in low B_1^+ regions as compared to the GEs map. The optimized spoiling scheme of the PSS+ technique appears to bring measurements from that protocol closer to those of the GEs method; however, a modest offset in the measured fields persists.

T_1 tissues, particularly the cerebrospinal fluid. For more accurate and non-tissue-dependent measurements, the T_R should be increased.

2.3.2 GEs-ssEPI technique

A sample of axial slices from all field maps—including ΔB_0, B_1^+, and $M_0 B_1^-$—is presented in Figure 9. Values of ΔB_0 largely fall in the $\pm 150\,\mathrm{Hz}$ range with the largest deviations occurring near the frontal sinuses and the ear canals. Single-shot EPI B_1^+ maps are qualitatively similar to those acquired with the low EPI factor; however, small-scale variations are apparent in regions of maximum ΔB_0 and likely reflect imperfections in the EPI distortion correction. Measurements of $M_0 B_1^-$ differ more noticeably between the single- and multi-shot scans, but, again, variations occur mostly on a small spatial scale. The highly localized nature of these differences suggests that single-shot RF field maps may benefit from the application of a 2D low-pass filter. Overall, the estimated geometry of both B_1^+ and $M_0 B_1^-$ maps is preserved under single-shot acceleration despite a $\sim$ 20-fold reduction in scan time. This fact is reflected in the 2D voxel histograms of Figure 10 which show the distributions of ΔB_0 and B_1^+ throughout the brain to be quite similar. Thus, the GEs-ssEPI technique presented here appears to be a practical tool given the existing demands for fast and accurate field mapping.

2.4 Conclusions

This RF field-mapping survey indicates that significant discrepancies exist among four major RF mapping techniques. Depending on the given application of RF field

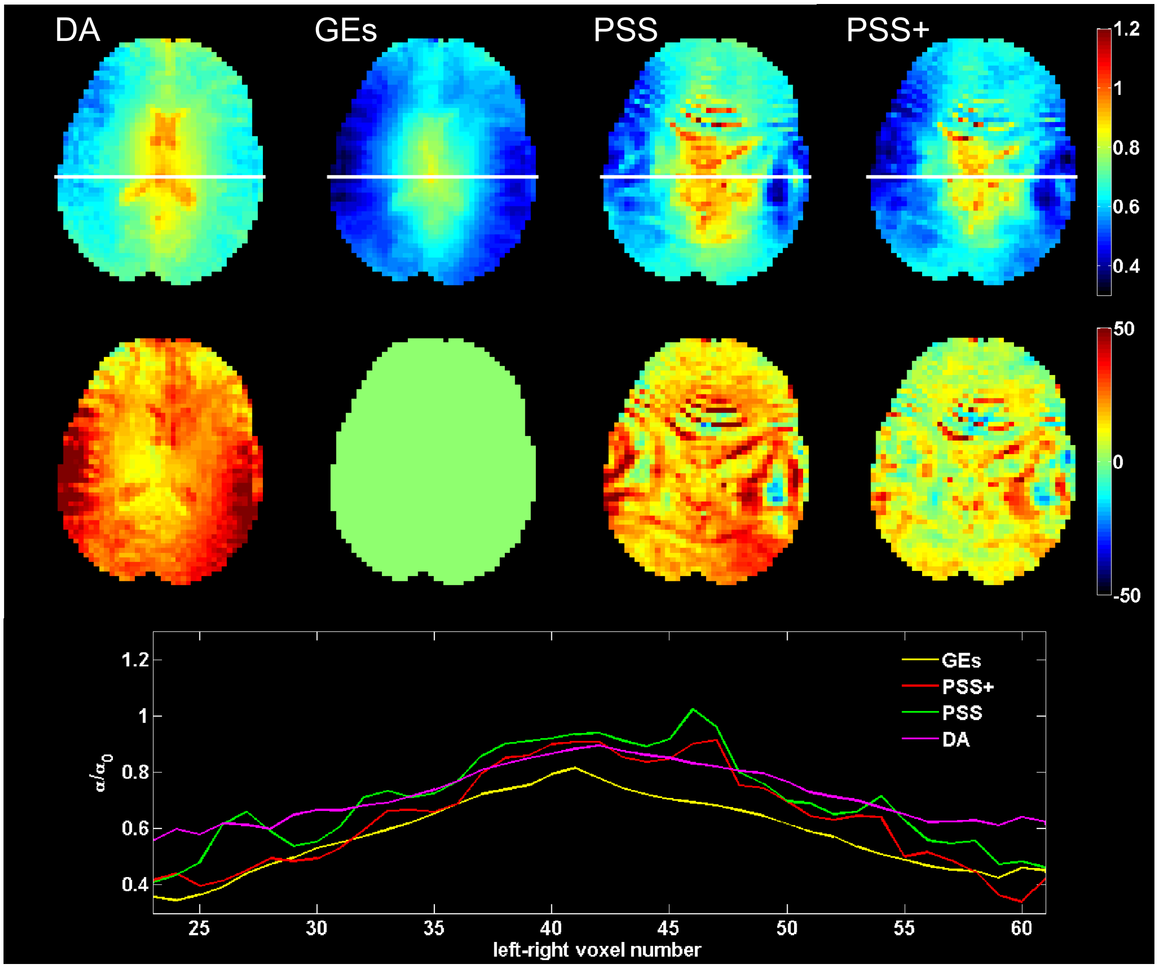

Figure 8: Axial flip-angle maps acquired via four different protocols in the human brain at 7 T (first row); the ratio of those flip-angle maps to the GEs map (middle row); and line profiles across the maps at the indicated positions (bottom). As with the phantom results, there exist significant discrepancies among results of the four mapping protocols. Maps indicate a total dynamic range in the B_1^+ field of $\sim 50\%$, somewhat lower than than observed in the phantom. PSS and PSS+ techniques result in a ripple artifact suggesting possible sensitivity to B_0 offsets. GEs results reveal the presence of subtle T_1 weighting indicating an insufficiently long T_R.

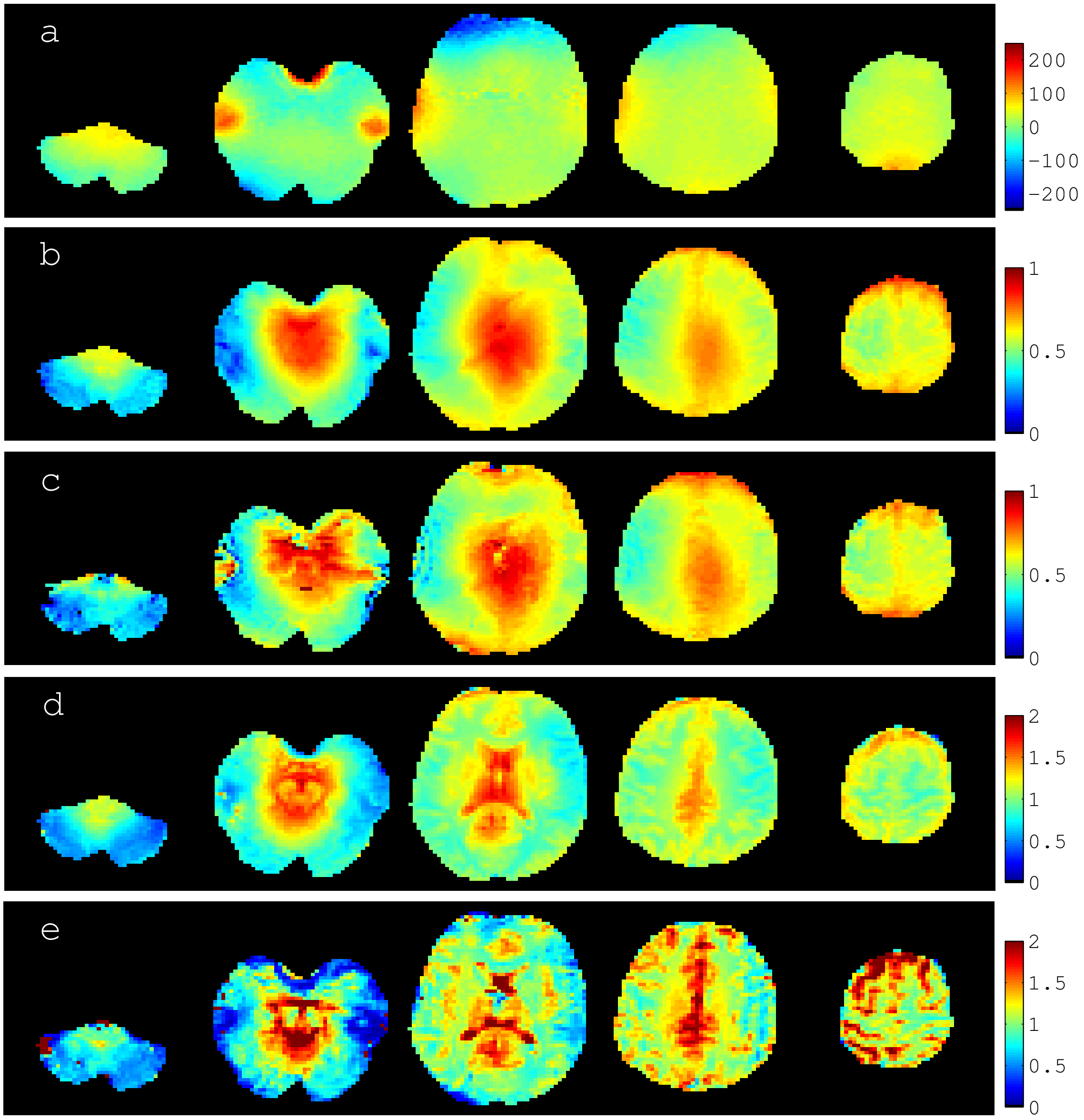

Figure 9: In-vivo field maps for 5 representative axial slices through the brain: (a) ΔB_0 maps (in units of Hz) used in EPI distortion correction; (b) and (c) $B_1^+/B_{1,\mathrm{nominal}}^+$ maps calculated from multi-shot and single-shot EPI data, respectively; (d) and (e) $M_0B_1^-$ maps (in arbitrary units) calculated from multi-shot and single-shot EPI data, respectively. High-frequency spatial noise apparent in (c) and (e) is due to the lower SNR of single-shot EPI as well as errors in the B_0 distortion corrections.

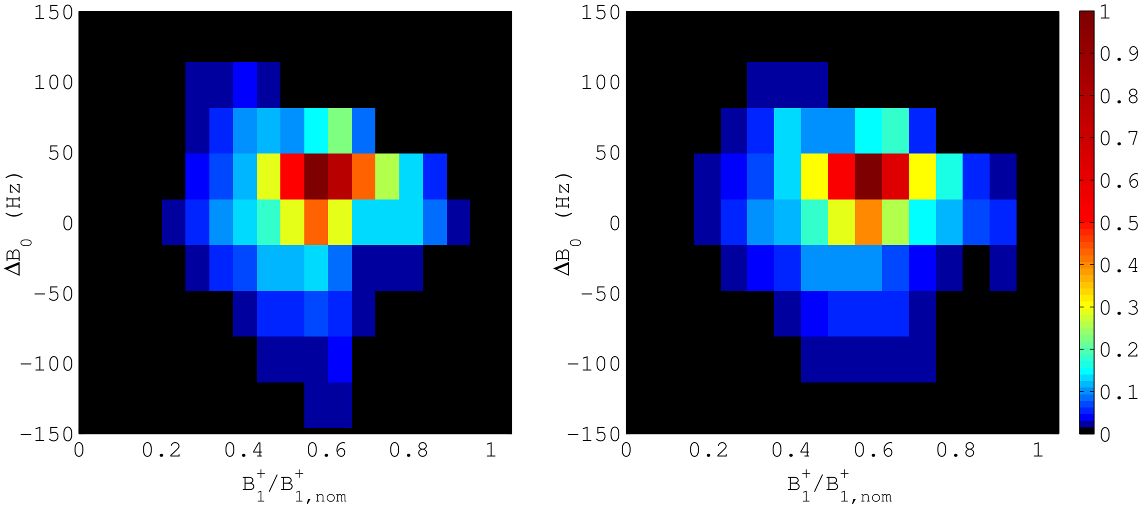

Figure 10: Relative voxel density of the 3-D B_1^+-ΔB_0 in-vivo data, acquired with multi-shot (left) and single-shot (right) EPI read-outs. The qualitative differences in the distributions are subtle, suggesting that single-shot EPI, while leading to some noticeable differences in localized field measurements, can be used to determine gross RF field characteristics (e.g., mean and standard deviation) without much loss of accuracy.

maps, such differences (i.e., potential errors) may lead to drastically improper calibrations of RF pulses or grossly incorrect post-processing intensity corrections. Further studies to better determine accuracy (as opposed to relative differences) are warranted. While this study has adopted the stance that the GEs method is likely the most accurate of the four protocols, confirmation of this assumption is needed and could be attained, at least in part, through numerical modeling of Maxwell's equations (i.e., FDTD modeling) for a prescribed phantom geometry and composition. The newly proposed single-shot GEs variant appears promising as a way to speed up the prohibitively time consuming GEs method; however, a multi-shot approach with a high EPI factor may be worthy of a similar investigation, as this adjustment might allow for more accurate EPI distortion corrections and therefore more accurate RF field estimates. Regardless of the conflicting results of the different techniques tested in this study, the work has established the approximate ranges of B_1^+ field variations in the human brain at 7 T. As opposed to the accurate RF maps needed for the design of spectral-spatial pulses for B_1^+ mitigation, these approximate ranges are all that are necessary for the effective design of the B_1^+-insensitive composite pulses that are the focus of subsequent chapters of this thesis.

CHAPTER III

COMPOSITE RF PULSES FOR B_1^+-INSENSITIVE VOLUME EXCITATION

3.1 Introduction

The problem of inhomogeneous transmitted RF (B_1^+) fields in ultra-high field MRI (83) has previously been addressed by various RF pulse designs (e.g., spectral-spatial excitations (89) and adiabatic pulses (72; 76; 23)) and hardware modifications (e.g., parallel transmit coils (86) and traveling-wave antennae (12)). Such techniques have practical limitations in that field maps must be acquired for a specific imaging slice prior to the design of the RF pulse, specific absorption rate (SAR) requirements hinder implementation at ultra-high field, pulse durations are impractical, or non-standard hardware configurations must be implemented. New methods that improve flip-angle uniformity in the presence of large B_1^+ inhomogeneities while simultaneously addressing or avoiding such shortcomings are therefore of interest.

The design scheme introduced here can be used to generate composite pulses for volume (non-selective) excitation that are executable on commercial quadrature transmit coils within the practical limits of maximum RF amplitude and pulse duration of current ultra-high field human MRI. Using numerical techniques, pulses are optimized to produce uniform flip angles over a range of B_1^+ and static (B_0) field variations designated during the design process. When such field inhomogeneities can be estimated to lie within a given range, pre-designed composite pulses can be used without the time-consuming acquisition of B_1^+ and B_0 field maps and the subsequent design of a tailored RF pulse.

The main objectives of this study were (1) to determine relevant B_1^+ and ΔB_0 ranges to be targeted for 7 T volume excitation of the human brain and a dielectric phantom of similar size; (2) to design optimized pulses as series of block-shaped sub-pulses with amplitudes and phases determined by numerical optimization; (3) to investigate the dependence of the performance of optimized composite pulses on such factors as average power, pulse duration, sub-pulse duration, and the number of component sub-pulses; (4) to compare the performance of selected optimized composite pulses to that of suitable block-shaped and adiabatic counterparts by way of simulations based on phantom and *in vivo* data acquired at 7 T; and (5) to validate the efficacy of optimized composite pulses in improving flip-angle homogeneity in phantom experiments at 7 T. Simulations and experiments demonstrate that this approach to pulse design is suitable for immediate practical application. Similar B_1^+- and ΔB_0-insensitive composite RF designs have been reported (43; 74; 38; 9; 10) but differ from this study in available RF time resolutions, maximum RF amplitude limits, and optimization methodologies. The present study therefore introduces new strategies for the design of B_1^+- and ΔB_0-insensitive pulses specifically for use in ultra-high field human imaging.

3.2 Methods

The design process for generation of the composite pulses in this study is summarized in the following steps:

1. perform experiments to determine the distribution of static and RF field magnitudes in volumes of interest (Section 3.2.1)
2. choose ranges of B_1^+ and ΔB_0 values for which pulses are targeted to perform (Section 3.2.2)
3. choose number and duration of component sub-pulses (Section 3.2.3)
4. optimize sub-pulse phases and amplitudes via a minimization algorithm (Section 3.2.4)
5. determine average power ($\overline{P}$) and minimum repetition time ($T_{R,\min}$) for each optimized pulse (Section 3.2.7)

Also in this section are descriptions of the block-shaped and adiabatic pulses used for performance comparisons (Sections 3.2.5 and 3.2.6) and details of methods used for simulation of the Bloch equations (Section 3.2.8). Lastly, the experimental procedures used for validation of optimized pulses are presented (Section 3.2.9).

3.2.1 Field mapping

A key design aim is the tailoring of pulses for a specific range of field inhomogeneities found in practice. Prior to determination of suitable ranges of B_1^+ and ΔB_0 values for which pulses are to be optimized, measurements were made of typical variations in these fields throughout particular volumes of interest—a 17 cm spherical dielectric phantom (Function Biomedical Information Research Network, FBIRN) and the human brain. Two volunteer subjects were recruited from the community, and written informed consent was obtained according to the guidelines of the local Institutional Review Board. All experimental data were acquired with a single-channel, volume quadrature transmit/receive head coil (Nova Medical, Wilmington, MA, USA) and a 7 T MR scanner (Philips Healthcare, Best, The Netherlands).

Protocols for estimating B_1^+ distributions were 1) a 3D spoiled steady-state actual flip-angle imaging (AFI) sequence (87) (referred to as PSS in Chapter II) and 2) a series of 11 single-slice gradient recalled echo (GRE) images acquired at flip angles ranging from 10° to 210° in 20° increments (referred to as GEs in Chapter II). Due to its superior data collection efficiency, the former technique was used to estimate the B_1^+ field throughout the 3D volume, while the latter technique was used to give a more accurate measure of the same quantity in a single imaging slice (55). The AFI data were referenced in choosing the range of B_1^+ values to be targeted by the optimized pulses as well as for multi-slice simulations, and the GRE series data were used for single-slice phantom and *in vivo* simulations.

Data for B_1^+ and ΔB_0 scans were acquired in 3 mm isotropic voxels within a 240×192 mm axial field of view, with the 3D scan spanning 153 mm in the cephalo-caudal direction. Both sequences also used identical second-order volume shimming with a targeted shim volume corresponding roughly to the largest cubic volume that could be inscribed within the imaging volume. The AFI sequence employs interleaved acquisitions with alternating T_R values of 20 ms and 100 ms, an echo time (T_E) of 1.70 ms, and a nominal flip angle (α_0) of 60°. The voxel-by-voxel ratio of signals acquired at the different values of T_R can be related to the actual flip angle (α) at a given spatial location. The value of α/α_0 then gives an estimate of the relative magnitude of the B_1^+ field. The series of GRE images was acquired for a single slice corresponding to the central axial slice of the 3D AFI scan, thus placing the slice location for the *in vivo* scans just superior of the corpus callosum. Imaging geometry was identical to that of the AFI sequence, with T_R and T_E respectively set to 5000 ms and 2.7 ms. Given a GRE signal intensity represented by

$$S_i = \beta \left|\sin\left(\lambda\, \alpha_{0i}\right)\right| \, , \tag{3.2.1}$$

with β representing the product of the received RF field (B_1^-) and the initial magnetization (M_0) and λ indicating the ratio of the actual transmitted RF field magnitude (B_1^+) to the corresponding field magnitude ($B_{1,\mathrm{nom}}^+$) associated with the nominal flip angle α_{0i} of the i-th image in the series, a least-squares fit of the parameters β and λ to the S vs. α_0 curve for each voxel in the imaging slice results in a measure of λ (i.e., the relative magnitude of the B_1^+ field) (89; 30). Axial B_1^+ maps obtained with this technique are shown in Figure 11b.

Static field variations (ΔB_0) were mapped via a 3D spoiled GRE sequence with a double-echo acquisition ($\Delta T_E = 0.5\,\mathrm{ms}$). Frequency offsets for all voxels were then calculated from the difference in magnetization phase at the two echo times ($\Delta B_0 = \Delta\phi/(2\pi\Delta T_E)$). The value of ΔT_E was chosen short enough that no phase wrapping existed in the phase difference data and that T_2 effects were minimized but long enough that phase differences remained large compared to the noise in the

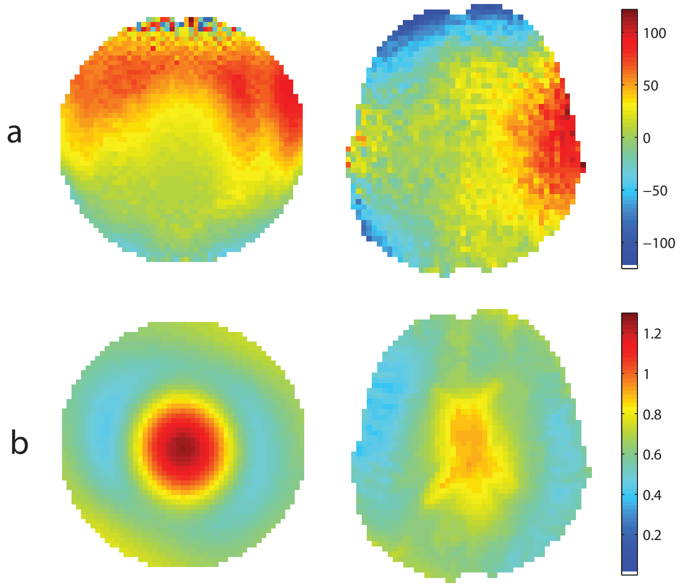

Figure 11: ΔB_0 (row a) and B_1^+ (row b) maps for the central axial slice of a phantom and the human brain at 7 T. ΔB_0 values are reported in Hz while B_1^+ magnitude is indicated as a ratio to that of $B_{1,\mathrm{nom}}^+$. B_1^+ maps are those obtained with the multi flip-angle technique (Equation 3.2.1).

phase images. Although the respective T_R and α_0 values of 5.3 ms and 10° resulted in considerable T_1-weighting in the magnitude images, the phase data, and therefore the ΔB_0 measurements, did not reflect tissue boundaries (see Figure 11a). Geometric imaging parameters were set identically to those of the AFI sequence such that corresponding measurements of ΔB_0 and α/α_0 were collected for all voxels in the 3D volume. Figure 12 shows ΔB_0 and corresponding AFI measurements throughout the spherical phantom and throughout the volume of the brain approximately superior to the red nucleus. Regions inferior to the midbrain are not included in Figure 12 since reduced coil sensitivity in the area significantly undermines the accuracy of AFI measurements. Central axial slices of phantom and *in vivo* ΔB_0 maps are presented

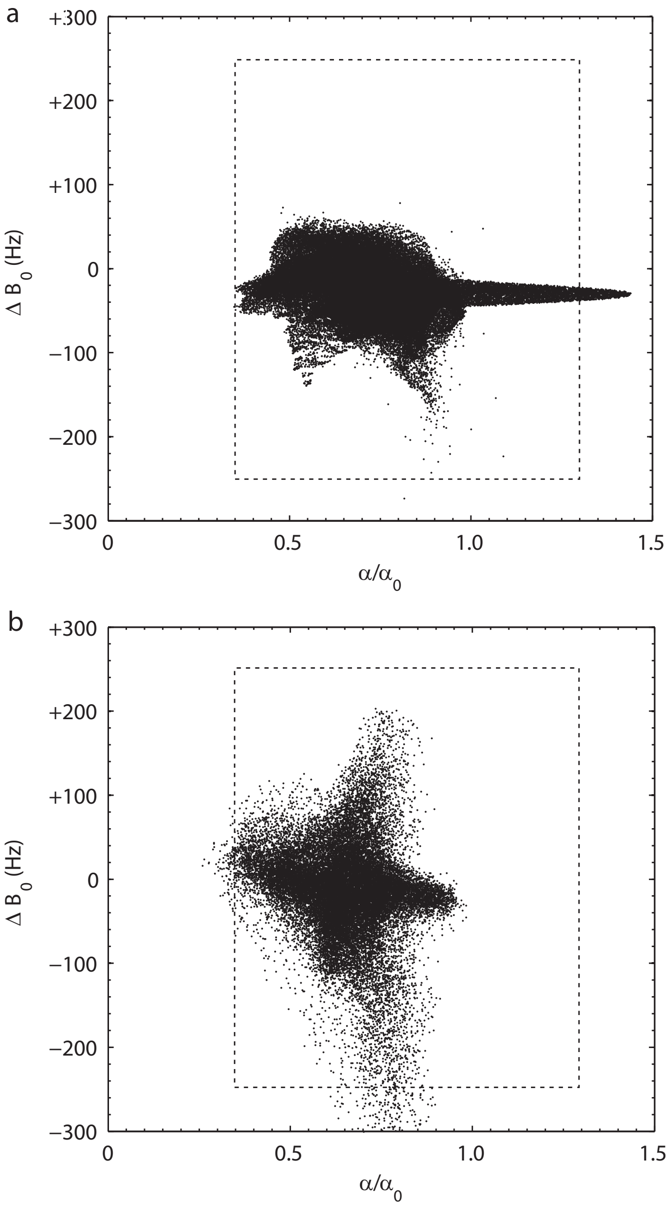

Figure 12: ΔB_0 values (y-axis) and corresponding actual flip-angle measurements (x-axis, given as the ratio of the actual flip angle α to the nominal flip angle α_0) throughout the volume of (a) a 17 cm dielectric spherical phantom and (b) the *in vivo* human cerebrum at 7 T. Each point represents a single imaging voxel and the entire distribution is plotted on the same coordinate system in which the composite pulses of this study are optimized. These data were used in selecting the ranges of B_1^+ and ΔB_0 values (indicated by dashed boxes) to be targeted by the optimized pulses.

in Figure 11a above the corresponding multi flip-angle B_1^+ data.

3.2.2 B_1^+-ΔB_0 grids

The next step in pulse design is the designation of a parameter space representing the ranges of the possible combinations of the B_1^+ and ΔB_0 values for which pulses are to be optimized (74; 60; 16). A target flip-angle map is generated by specifying the desired flip angle at each point in the B_1^+-ΔB_0 space. In the subsequent optimizations of this study, uniform flip angles of 30°, 60°, 90°, and 180° were targeted over the entire parameter space. For all examples presented in this work, respective $B_1^+/B_{1,\mathrm{nom}}^+$ and ΔB_0 ranges of 0.35–1.30 and $\pm 250\,\mathrm{Hz}$ were selected to represent typical variations throughout the human cerebrum and the spherical phantom at 7 T (Figure 12). Selected ranges reflect only an approximation to the total field variations of the brain and phantom but include the large majority of data points. B_1^+ and ΔB_0 ranges were respectively discretized into 20 and 21 evenly-spaced values, resulting in a grid of 420 points, a $B_1^+/B_{1,\mathrm{nom}}^+$ step size of 5%, and a ΔB_0 step size of 25 Hz. An odd number of ΔB_0 steps was selected so that the on-resonance response of the pulse could be specifically monitored. The chosen level of B_1^+ and ΔB_0 discretization reflects a compromise between the desired response of the pulse and the computing time associated with the optimization, and the practical validation of a given B_1^+-ΔB_0 grid comes with evaluating the experimental performance of the resulting optimized pulse.

3.2.3 Anatomy of optimized composite pulses

Prior to optimization, the basic structure of the amplitude and phase modulation waveforms must be defined. All pulses considered here are a composite of block-shaped sub-pulses executed in immediate succession with the amplitude and phase of each sub-pulse being subject to numerical optimization. Designations of the number (N_s) and duration (Δt_s) of sub-pulses, as well as the maximum and minimum allowed RF amplitudes, are prerequisites to pulse optimization. These choices effectively fix the number of free parameters and their constraints for the numerical optimization. Composite pulses with N_s = 16, 32, 48, 64, 80, 96, 112, and 128 were generated. In each case, Δt_s values were fixed to 6.4, 12.8, 19.2, 32.0, 64.0, 128.0, 192.0 and 320.0 μs, thus yielding a total of 64 optimized pulses for each target flip angle. The time increment of 6.4 μs, of which all sub-pulse durations are common multiples, reflects a typical electronics dwell time on commercial human MR scanners (i.e., the smallest time increment by which the output of the RF amplifier can be updated). Maximum and minimum parameter constraints were respectively set to 0 and 15 μT for sub-pulse amplitude and $\pm\pi$ for sub-pulse phase. The maximum amplitude of 15 μT was chosen in accordance with typical performance limits on commercial RF coils in practical imagers.

3.2.4 Optimization of composite pulses

Routines were written in MATLAB to optimize the sub-pulse amplitudes $\mathbf{A} = \{A_1, A_2, \ldots, A_k\}$ and phases $\boldsymbol{\phi} = \{\phi_1, \phi_2, \ldots, \phi_k\}$ of composite pulses via minimization of the function

$$\delta_\alpha(\mathbf{A}, \boldsymbol{\phi}) = \frac{1}{mn} \sum_{i,j=1}^{m,n} \left| \frac{\alpha_{i,j}^S(\mathbf{A}, \boldsymbol{\phi}) - \alpha_{i,j}^T}{\alpha_{i,j}^T} \right| , \tag{3.2.2}$$

where i is the B_1^+ index on the B_1^+-ΔB_0 grid, j is the ΔB_0 index on the B_1^+-ΔB_0 grid, and α is the flip angle given by $\cos^{-1}(M_z/M_0)$ with S and T denoting simulated and target values. The value of function δ_α represents the average deviation of simulated flip angles from the target flip angle over the entire B_1^+-ΔB_0 grid and is expressed as a fraction of the target flip angle. With the goal of finding a minimum of Equation 3.2.2, the non-linear constrained minimization algorithm (46; 62) (Matlab function `fmincon`) iteratively calculates a quasi-Newtonian estimate of the Hessian of the Lagrangian defined by the second partial derivatives of Equation 3.2.2 with respect to the k amplitudes and k phases of the RF waveform. The algorithm is seeded by a composite pulse in which the k amplitudes and phases conform to an even probability distribution within the prescribed limits of 0–15 μT and $\pm\pi$ rad, respectively. A termination condition is satisfied if the minimization algorithm fails to decrease the value of δ_α by at least a factor of 10^{-6} over the course of a single iteration. The phase of the magnetization is not considered in the cost function, since phase is not crucial to pulse performance. In the context of volume excitation, phase must only be a smoothly and slowly varying function of B_1^+ and ΔB_0 so as to avoid intravoxel dephasing. After the pulse design process, variations in phase were examined across the B_1^+-ΔB_0 grid to ensure minimal impact on the resulting signal.

Although the indices of $\alpha^T_{i,j}$ signify that composite pulses for which target flip-angles vary across the B_1^+-ΔB_0 grid could be designed without modification of the cost function (Equation 3.2.2), each of the pulse compositions described in Section 3.2.3 was optimized with target flip angles on the B_1^+-ΔB_0 grid uniformly set to 30°, 60°, 90°, and 180° as described in Section 3.2.2. A subset of four optimized pulses (see Figure 16) was selected for explicit comparison with block-shaped and adiabatic pulses with equivalent nominal flip angles.

3.2.5 Maximum-bandwidth block pulses

The central lobe of the frequency spectrum of a block-shaped pulse has a bandwidth inversely proportional to the pulse duration; therefore, block pulses can affect a range of ΔB_0 offsets limited only by the minimum possible pulse duration. The flip-angle (α) of a block pulse is determined solely by the pulse amplitude (A) and duration (ΔT) such that

$$\alpha = 2\pi\gamma \int_0^{\Delta T} \left| B_1^+ \right| dt = 2\pi\gamma A \Delta T\,, \tag{3.2.3}$$

with $\gamma = 42.57\,\mathrm{MHz/T}$ (for hydrogen), hence a block pulse with the largest possible bandwidth can be determined by choosing the shortest ΔT given the maximum allowed value of A ($A_{\max} = 15\,\mu\mathrm{T}$) and the desired flip-angle (α_0). Parameters for all block pulses in this study were chosen according to this condition of maximum bandwidth while simultaneously requiring ΔT to be an integer multiple of the electronics dwell time ($d = 6.4\,\mu$s). The integer number of dwell times (N_d) in a maximum-bandwidth block pulse is then uniquely given by

$$N_d = \texttt{ceil}\left(\frac{\alpha_0}{2\pi\gamma A_{\max} d}\right) , \tag{3.2.4a}$$

where `ceil` denotes the operation of rounding to the next highest integer. Actual values of A and ΔT were then defined via the relations

$$\Delta T_{\text{actual}} = N_d d \tag{3.2.4b}$$

and

$$A_{\text{actual}} = \frac{\alpha_0}{2\pi\gamma\Delta T_{\text{actual}}} . \tag{3.2.4c}$$

Using this protocol, block pulses serving as metrics for the performance of optimized pulses were generated for α_0 values of 30°, 60°, 90°, and 180°.

3.2.6 B_1^+-insensitive adiabatic pulses

Four-part B_1^+-insensitive rotations (BIR-4) are composites of four adiabatic pulse segments. Complete BIR-4 modulation functions can be found in Appendix C. These pulses are capable of producing arbitrary flip angles and have been shown to improve flip-angle uniformity in the context of volume (non-selective) excitation (76; 23); therefore, BIR-4 pulses provide a suitable basis for comparison when evaluating the performance of the optimized composite pulses produced in this study. Flip-angle maps for 4.096 ms BIR-4 pulses with nominal flip angles of 30°, 60°, 90°, and 180° were simulated for specific comparison with the subset of four 4.096 ms optimized pulses subject to additional analysis in Section 3.3.2. Simulation of the Bloch equations (Section 3.2.8) was carried out in an identical manner to that of optimized pulses; however, BIR-4 pulses were divided into as many $d = 6.4\mu\text{s}$ block-shaped sub-pulses as possible ($n = 640$) given the total pulse duration ($\Delta T = 4.096\,\text{ms}$). This reflects the typical way pulses with continuous waveforms are executed digitally on an amplifier for which $d = 6.4\mu\text{s}$. BIR-4 amplitude and frequency modulations were designated according to Staewen et al. (76), with $A_{\max} = 15\,\mu\text{T}$ and a frequency sweep of ±250 Hz.

3.2.7 Average power and minimum T_R

The specific context in which a given RF pulse is implemented usually dictates the optimal value of T_R, thus providing a restriction on the average power ($\overline{P}$) of the RF excitation. To maintain generality, $\overline{P}$ was therefore not directly incorporated into the design of the optimized pulses; however, $\overline{P}$ was indirectly limited by the maximum allowed (hardware restricted) RF amplitude and fixed duration of each pulse. With average power calculated as

$$\overline{P} = \frac{1}{\Delta T} \int_0^{\Delta T} |A(t)|^2 \, dt \tag{3.2.5a}$$

for an amplitude modulation $A(t)$ of length ΔT, practical limitations associated with RF power of each pulse were quantified by calculation of a minimum value of T_R via the relationship

$$T_{R,\mathrm{min}} = \frac{C\,\overline{P}\,\Delta T}{\mathrm{SAR}_{\mathrm{max}}}\,, \tag{3.2.5b}$$

where $C = 1.41\,\mathrm{W/kg/\mu T^2}$ is a coil-specific constant representing the rate of energy dissipation of 298 MHz radiation in human brain tissue, $\mathrm{SAR}_{\mathrm{max}}$ is set to the value of 3 W/kg corresponding to the SAR threshold for significant risk in the human head according to the Food and Drug Administration (FDA) (13), and ΔT is the time duration of the given RF pulse. $T_{R,\mathrm{min}}$ therefore represents the minimum repetition time for a pulse sequence in which the optimized excitation is the only RF component (such as in a GRE imaging experiment or a pulse-and-acquire spectroscopy experiment). Values are unique to both the magnitude of the static field and the specific volume head coil used in this study but may serve as useful guidelines when using similar coil configurations at 7 T.

3.2.8 Simulation of the Bloch equation

Magnetization response to a composite of k sub-pulses with constant phase and amplitude was modeled as a series of rotations (R_j, where $j = 1, \ldots, k$), each representing the operation due to a relaxation-independent form of the Bloch equation (3). With each rotation corresponding to one of the k individual sub-pulses, the collective operation of all components of a composite pulse is described by

$$\mathbf{M}^f = R_k R_{k-1} R_{k-2} \dots R_1 \mathbf{M}^0 \,, \tag{3.2.6}$$

where $\mathbf{M}^0$ is the magnetization vector preceding the pulse and $\mathbf{M}^f$ is the magnetization vector following the pulse. For all cases in this study, the initial magnetization was taken to be in the z-direction such that the components of $\mathbf{M}^0$ were given by $(M_x^0, M_y^0, M_z^0) = (0, 0, 1)$. A more detailed description of strategies for simulating the Bloch equation is presented in Appendix B.

3.2.9 Phantom experiments

A spoiled, 3D, echo-planar, GRE sequence ($T_R = 500\,\mathrm{ms}$, $T_E = 5\,\mathrm{ms}$, 3 mm isotropic voxels, EPI factor 3) was used to image the entire volume of the 17 cm FBIRN phantom with the same hardware configuration described in Section 3.2.1. This experiment was carried out with the 4.096 ms excitation pulses shown in the first row of Figure 16: a 30° maximum-bandwidth block pulse, a 30° BIR-4 pulse, and a 30° optimized composite pulse. For each excitation pulse, data were acquired both for the case of second-order static field volume shimming and the case in which all static field shimming gradients were turned off. Respectively, these ΔB_0 shimming scenarios allowed for the evaluation of excitation pulse performance when (1) in-slice static field variations were similar to those found in the well-shimmed human brain at 7 T (e.g., compare the *in vivo* ΔB_0 map of Figure 11a with the unshimmed phantom

ΔB_0 map of Figure 22) and when (2) in-slice static field variations were minimal.

Data for calculation of the parameter β (Equation 3.2.1) in a 2D axial slice corresponding to the central slice of the 3D volume were obtained according to the protocol described in Section 3.2.1. Since the steady-state signal (S_{ss}) can be expressed as a product of B_1^-- and B_1^+-dependent factors β and F such that

$$S_{ss} = \beta F \,, \tag{3.2.7a}$$

with F being explicitly given by

$$F(\lambda, T_1, T_2^*; \alpha_0, T_R, T_E) = \frac{|\sin(\lambda\,\alpha_0)|\left(1 - e^{-T_R/T_1}\right)e^{-T_E/T_2^*}}{1 - |\cos(\lambda\,\alpha_0)|\,e^{-T_R/T_1}} \,, \tag{3.2.7b}$$

and

$$\lambda = B_1^+ / B_{1,\text{nom}}^+ \,, \tag{3.2.7c}$$

central-slice images from the 3D acquisitions were divided by the calculated map of β. This procedure resulted in six maps of F (three excitation pulses with two static field shimming schemes) which were then compared in terms of uniformity. To avoid signal scale discrepancies arising from the fact that S_{ss} values were acquired with a 3D sequence while β values were calculated from 2D sequence data, S_{ss} and β were normalized prior to the calculation of F such that $S_{ss} = \beta = 1$ for voxels with $\lambda = 1$.

3.3 Results

3.3.1 Optimized pulses

The 4 flip angles (30°, 60°, 90°, 180°), 8 N_s values (16, 32, 48, 64, 80, 96, 112, 128), and 8 Δt_s values (6.4, 12.8, 19.2, 32.0, 64.0, 128.0, 192.0, 320.0 μs) for which composite pulses were optimized resulted in a total of 256 composite pulses produced for this study. Actual cost function values are presented in Appendix D as a function of the parameters N_s and Δt_s, but the dependence of δ_α on total pulse duration in emphasized in the present chapter. In Figure 13, δ_α values (Equation 3.2.2) for each of these pulses are plotted as a function of total pulse duration (ΔT) for all values of N_s. In Figure 14, the same information is presented but organized according to pulses with a given Δt_s. While these data collectively indicate the sensitivity of pulse performance to the design parameters N_s and Δt_s, they firstly illustrate the radical improvement in flip-angle uniformity that is possible with optimized composite pulses as compared to maximum-bandwidth block pulses (the performance of which is indicated by a '×' symbol in each sub-plot of Figures 13 and 14). In general, composite pulse performance clearly increases (i.e., δ_α decreases) with increasing ΔT. One obvious exception to this trend occurs for 30° pulses with $\Delta T \gtrsim 5\,\text{ms}$. For most values of N_s in Figure 13, δ_α clearly reaches a minimum value when ΔT is between 2 and 10 ms. Smaller N_s values lead to δ_α minima at the lower end of this range while larger N_s values lead to δ_α minima at the upper end of this range. Similar behavior in the ΔT-dependence of δ_α can be seen to a lesser degree as α_0 increases.

Examination of δ_α vs. ΔT in light of Δt_s (Figure 14) reveals that shorter Δt_s pulses rather consistently provide increased performance when ΔT is long ($\gtrsim 5\,\mathrm{ms}$). For shorter ΔT, Δt_s appears to make little difference in pulse performance.

Absolute minimum values of δ_α are found at the following combinations of N_s and Δt_s, respectively: 128 and $64\,\mu$s for 30°, 60°, and 90° pulses; 128 and $128\,\mu$s for 180° pulses. By this measure alone, performance of pulses appears limited simply by N_s, while the ideal value of Δt_s depends on both the optimal bandwidth of the component sub-pulses and the available RF power for the entire composite pulse. From this, it can be inferred, given the objective of the optimization, that the ideal composite pulse would have the maximum value of N_s within the limits of the optimization algorithm and the shortest value of Δt_s as long as ΔT is sufficiently long. While these findings are consistent with the optimal control studies of Skinner et al. (75), further interpretation of the N_s, Δt_s, and ΔT dependencies of δ_α are saved for the discussion section.

Based on a 2D linear interpolation of the data in Figures 13 and 14, Figure 15 provides a visual representation of pulse performance in the near-continuous parameter space of N_s vs. Δt_s. Using a linearly weighted average of the four nearest data points, both δ_α and $T_{R,\min}$ data for each of the four flip angles were interpolated from an 8×8 ($N_s \times \Delta t_s$) grid to a 128×3136 grid resulting in respective interpolated parameter step sizes of 1 sub-pulse and $0.1\,\mu$s. The value of composite pulses is again obvious given that all colors other than the darkest red in Figure 15 signify an improvement in flip-angle uniformity as compared to maximum-bandwidth block pulses.

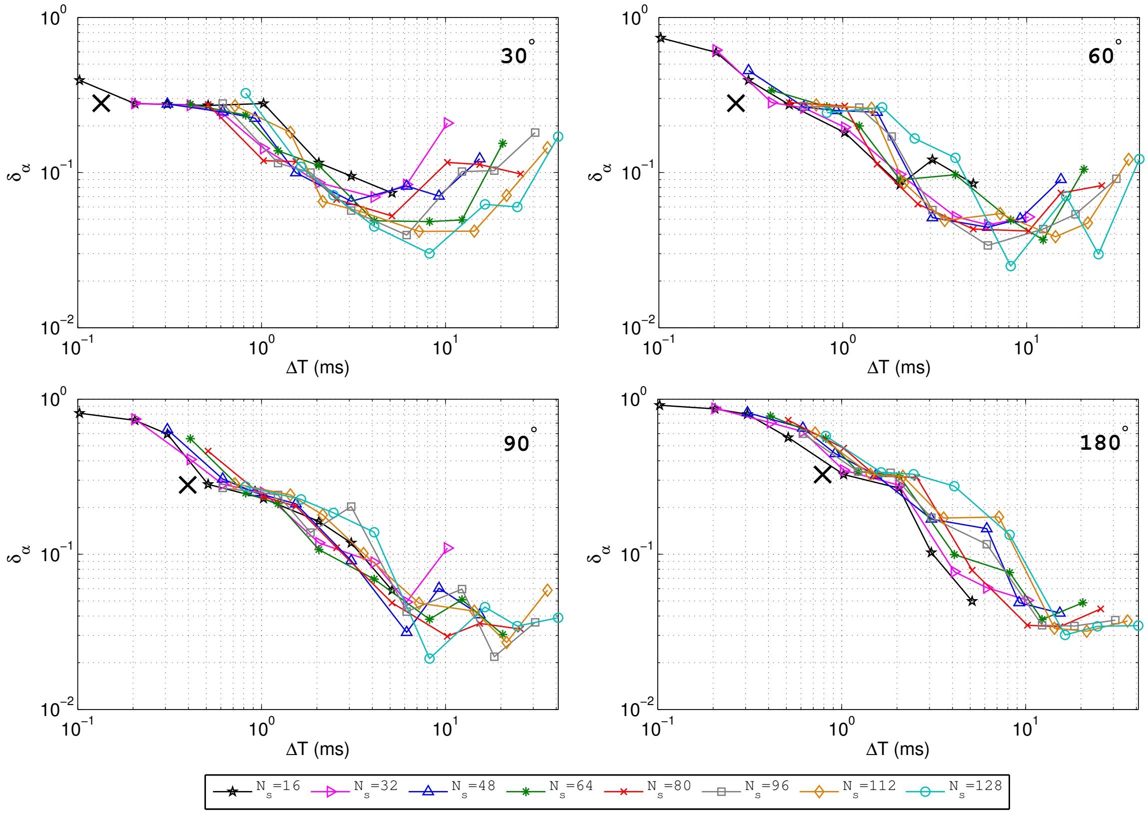

Figure 13: Cost function value (δ_α, Equation 3.2.2) as a function of overall pulse duration (ΔT), with each sub-plot corresponding to a different target flip angle as indicated in the upper right corner. Line colors indicate optimized pulses with different numbers of sub-pulses (N_s). The '×' symbol indicates performance of maximum-bandwidth block pulses for each flip angle. For short pulse durations, optimization tends to result in similar pulse performance for the various values of N_s due to the limited available RF power. Longer pulses tend to result in better pulse performance but with δ_α depending more noticeably on the value of N_s.

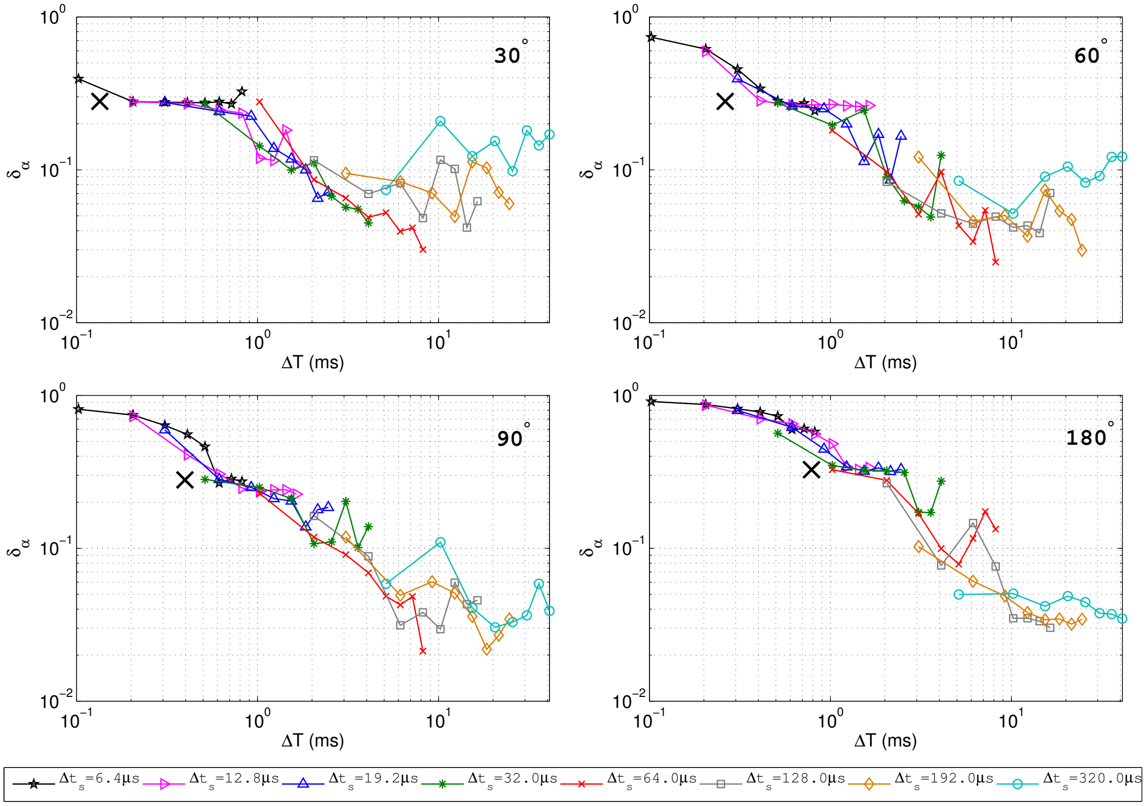

Figure 14: Cost function value dependence on ΔT as in Figure 13 but with line colors corresponding to optimized pulses with different sub-pulse durations (Δt_s). As in Figure 13, the performance of shorter pulses is similar for the various values of Δt_s due to the limited available RF power. Longer pulses tend to result in better pulse performance with δ_α often being lower for smaller values of Δt_s. This likely reflects the reduced bandwidth associated with longer Δt_s values.

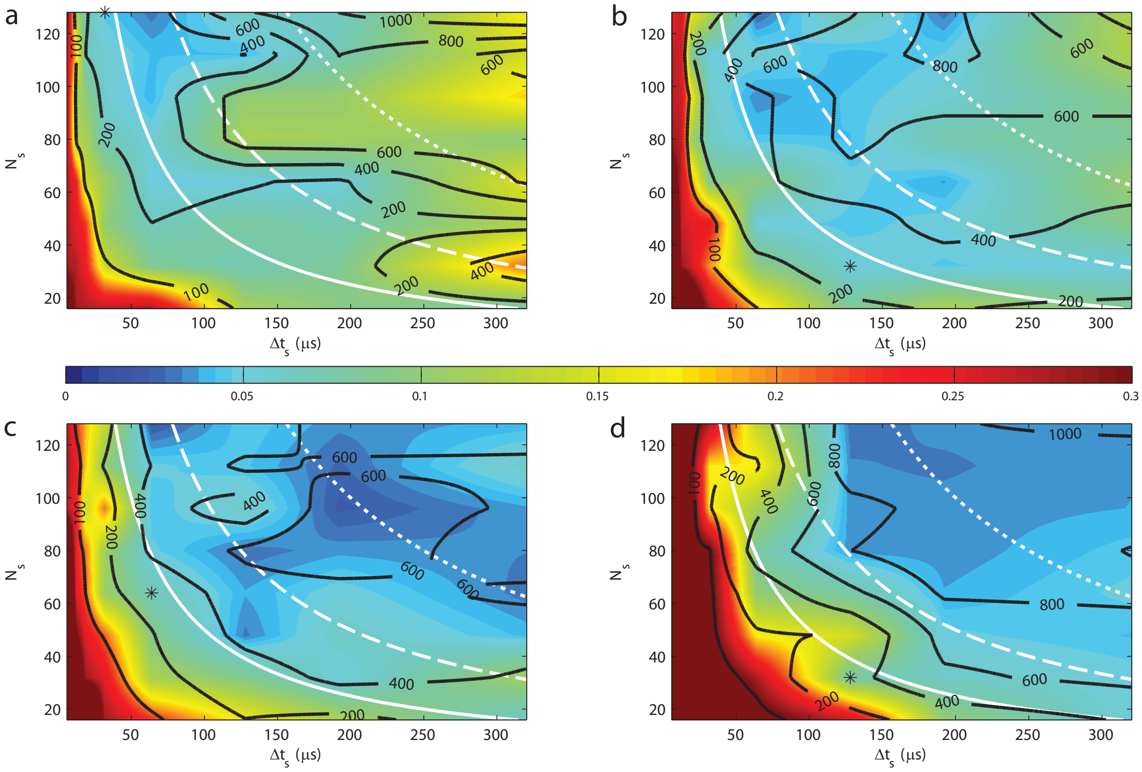

Figure 15: Results of composite pulse optimizations interpolated across the 2D parameter space of sub-pulse duration (Δt_s) and the number of sub-pulses (N_s) with sub-figures (a), (b), (c), and (d) corresponding respectively to α_0 values of 30°, 60°, 90°, and 180°. Color scale indicates the minimized function value (δ_α); black contours give corresponding minimum repetition times ($T_{R,\min}$) in milliseconds; solid, dashed, and dotted white lines are isocontours of total pulse duration (ΔT) at 5, 10, and 20 ms, respectively. Black asterisks indicate the values of N_s and Δt_s for the optimized pulses specifically compared to block and BIR-4 pulses in Figures 16, 17, and 18 and Table 3.3.1. Data indicate that the lowest values of δ_α migrate toward the top right corner of the parameter space with increasing α_0—thus reflecting increased power requirements. At lower α_0, δ_α minima tend to be found in the upper left, suggesting that the maximum number of short-duration sub-pulses yields the best performance given that a certain power threshold is satisfied.

In the context of Figure 15, the strong correlation between values of δ_α (colors), $T_{R,\mathrm{min}}$ (black contours), and ΔT (white lines) also becomes apparent. These relationships emphasize that little improvement in flip-angle uniformity can be achieved when the available RF power is too limited. Such a power threshold is, however, noticeably reduced for smaller α_0. For example, 30° composite pulses can drastically improve flip-angle uniformity for T_R values less than 200 ms while 180° pulses offer significantly reduced benefits under the same restriction. Conversely, the regions in which pulses perform the best don't necessarily correlate well with regions of high $\overline{P}$ (i.e., highest $T_{R,\mathrm{min}}$ values). This effect is most easily observable for the lower α_0 pulses (i.e., 30° and 60°). For example, the lowest δ_α values for 30° pulses occur in the $T_{R,\mathrm{min}}$ range of $200 - 400\,\mathrm{ms}$. Similarly, there is no significant advantage to be gained in selecting 60° pulses with $T_{R,\mathrm{min}} > 400\,\mathrm{ms}$, and, in fact, many such pulses perform significantly worse than their lower $\overline{P}$ counterparts.

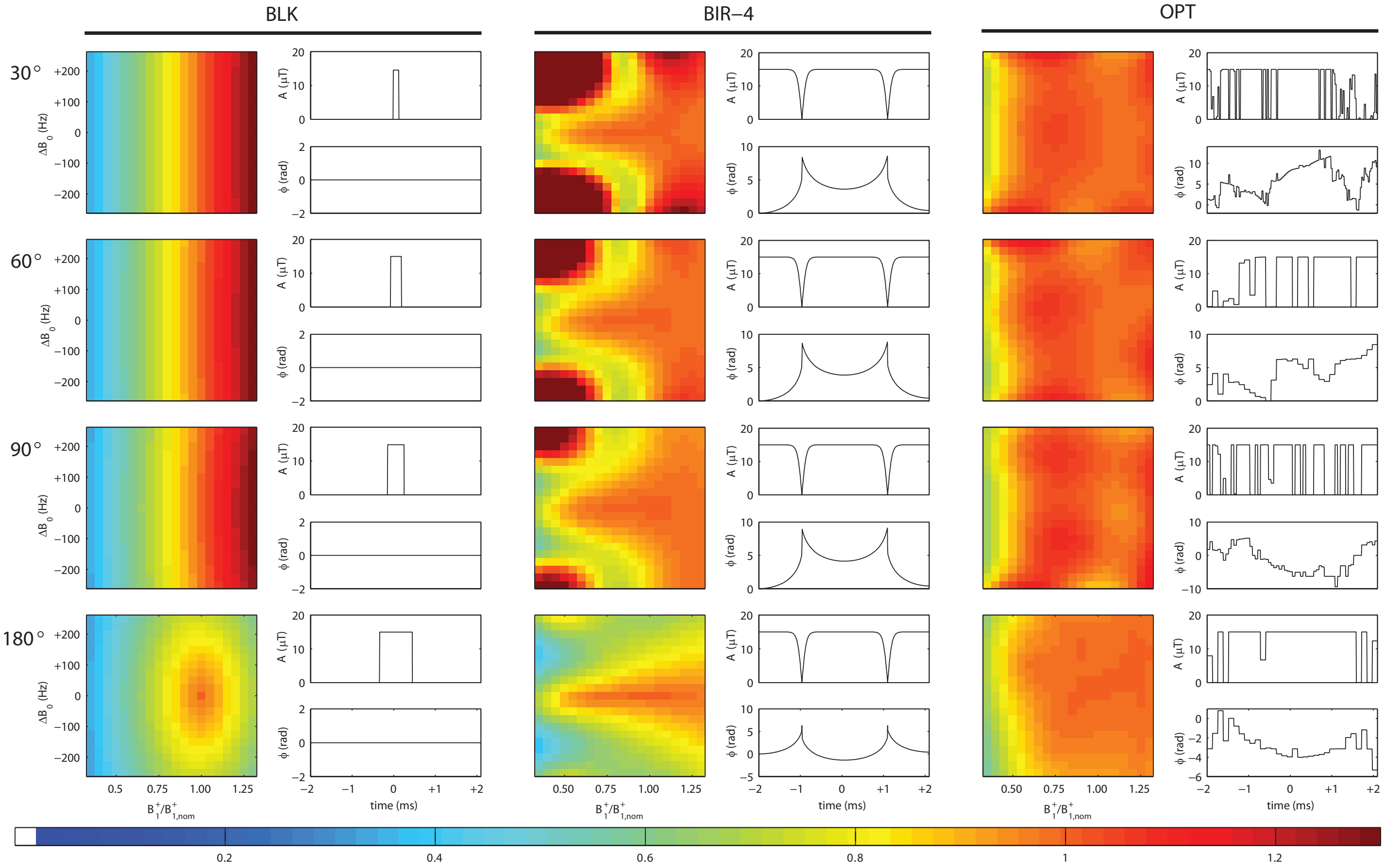

Figure 16: The ratio of actual to nominal flip angle (α/α_0) as simulated on the 20×21 B_1^+-ΔB_0 optimization grid (color) along with RF amplitude and phase modulation waveforms (columns 2, 4, and 6). Columns 1 and 2 are maximum-bandwidth block pulses; columns 3 and 4 are BIR-4 pulses ($\Delta T = 4.096\,\mathrm{ms}$); columns 5 and 6 are select optimized composite pulses ($\Delta T = 4.096\,\mathrm{ms}$); rows correspond to different nominal flip angles (indicated at left). Maps reflect the on-resonance B_1^+-insensitivity of BIR-4 and optimized pulses while optimized pulses result in significantly improved off-resonance behavior.

3.3.2 General performance comparison of select optimized pulses to maximum-bandwidth block pulse and BIR-4 counterparts

In order to facilitate comparison of optimized composite pulses to block and BIR-4 pulses of the same α_0, a subset of four optimized pulses was identified according to the practical criterion of $\Delta T = 4.096\,\text{ms}$. Given this total duration, the composite pulse with the lowest δ_α value was selected for each α_0. The respective N_s and Δt_s values for these pulses are 128 and $32\,\mu$s for 30°, 64 and $64\,\mu$s for 90°, and 32 and $128\,\mu$s for both 60° and 180° and are indicated by asterisks in Figure 15. Simulated flip angles on the B_1^+-ΔB_0 optimization grid are shown in Figure 16 for these four selected composite pulses along with the optimized amplitude and phase modulation waveforms. Also given in this figure are the corresponding simulated results for maximum-bandwidth block pulses and 4.096 ms BIR-4 pulses. Upon visual inspection of Figure 16, optimized composite pulses appear to outperform the other pulse types in terms of flip-angle uniformity but also quantitatively demonstrate their increased performance when normalized mean ($\overline{\alpha}/\alpha_0$), mean-normalized standard deviation ($\sigma_\alpha/\overline{\alpha}$), and coefficient of variations ($c_v = \sigma_\alpha/\overline{\alpha}$) are compared (Table 3.3.1). Depending on the nominal flip angle, composite pulses show a $\sim$ 4-fold reduction in δ_α values as compared to block pulses. Block pulses exhibit the expected linear relationship between actual flip angles and B_1^+ field strength (Equation 3.2.3) while BIR-4 pulses demonstrate strong B_1^+-insensitivity for static field strengths very close to resonance. It is in areas of off-resonance, especially at low B_1^+ field strengths, that composite pulses designed in the manner of this study offer a distinct advantage over their adiabatic counterparts. Although the colors in Figure 16 are thresholded at $\delta_\alpha = 1.3$, BIR-4 pulses actually result in δ_α values as high as 5.0 (i.e., α is 500% of α_0) for $\alpha_0 = 30°$. This fact is reflected in the large standard deviation for this BIR-4 pulse as simulated on the B_1^+-ΔB_0 grid (Table 3.3.1).

Optimized pulse phase modulations in Figure 16 have been unwrapped from the $\pm\pi\,\text{rad}$ constraints of the optimization according to the MATLAB function `unwrap` in order to emphasize the tendency of optimized modulation functions to be characterized by a frequency sweep coupled with a near-constant amplitude. A frequency sweep can be described in general terms of phase modulation as a smoothly varying and cyclic function. Such behavior in the amplitude and phase modulation is evidence of the quasi-adiabatic nature of the optimized composite pulses. In other words, pulses appear to be largely functioning by way of a gradual change in the direction of the effective field ($\vec{B}_{\text{eff}} = \vec{B}_1^+ + \Delta\vec{B}_0$) and a simultaneous spin-lock achieved through a high RF amplitude, although the adiabatic condition is, in general, not satisfied throughout the pulse. Similar phase modulation in the context of composite pulses has been previously reported (38) while the strongly modulated pulses of Boulant et al. (9; 10) appear to implicitly incorporate similar behavior into their design.

Table 3.3.1: Quantitative comparison of pulses featured in Figures 16 and 17. Nominal flip angle (α_0) and pulse type are indicated in columns 1 and 2. Columns 3–5 show the mean flip angle (normalized to α_0), standard deviation (normalized to the mean), and coefficient of variation for three contexts in which pulse performance was evaluated: the B_1^+-ΔB_0 optimization grid, the central axial slice through a spherical phantom, and the central axial slice of the human brain. Column 6 gives the minimum repetition time ($T_{R,\min}$), while columns 7 and 8 respectively show the average power ($\overline{P}$) and the ratio of $\overline{P}$ to the average power of the corresponding block pulse ($\overline{P}_{\text{BLK}}$) with the same α_0.

α_0	pulse	grid	phantom	brain	$T_{R,\min}$ (ms)	$\overline{P}$ (μT^2)	$\overline{P}/\overline{P}_{\text{BLK}}$
30°	BLK	$0.82 \pm 0.28(\pm 35\%)$	$0.67 \pm 0.17(\pm 26\%)$	$0.62 \pm 0.11(\pm 18\%)$	13	7	1.0
	BIR-4	$1.31 \pm 0.86(\pm 66\%)$	$0.94 \pm 0.03(\pm 4\%)$	$0.93 \pm 0.08(\pm 8\%)$	382	198	29.4
	OPT	$0.98 \pm 0.07(\pm 8\%)$	$1.00 \pm 0.03(\pm 3\%)$	$0.99 \pm 0.05(\pm 5\%)$	274	142	21.1
60°	BLK	$0.82 \pm 0.28(\pm 35\%)$	$0.67 \pm 0.17(\pm 26\%)$	$0.62 \pm 0.11(\pm 18\%)$	27	14	1.0
	BIR-4	$1.01 \pm 0.31(\pm 30\%)$	$0.95 \pm 0.03(\pm 3\%)$	$0.92 \pm 0.07(\pm 7\%)$	382	198	14.1
	OPT	$0.98 \pm 0.08(\pm 8\%)$	$1.00 \pm 0.03(\pm 3\%)$	$1.01 \pm 0.05(\pm 5\%)$	261	136	9.7
90°	BLK	$0.82 \pm 0.28(\pm 35\%)$	$0.67 \pm 0.17(\pm 26\%)$	$0.62 \pm 0.11(\pm 18\%)$	40	21	1.0
	BIR-4	$0.92 \pm 0.16(\pm 17\%)$	$0.95 \pm 0.03(\pm 3\%)$	$0.92 \pm 0.07(\pm 8\%)$	382	198	9.6
	OPT	$0.97 \pm 0.10(\pm 10\%)$	$1.01 \pm 0.07(\pm 7\%)$	$0.96 \pm 0.09(\pm 10\%)$	256	132	6.4
180°	BLK	$0.82 \pm 0.28(\pm 35\%)$	$0.67 \pm 0.17(\pm 26\%)$	$0.62 \pm 0.11(\pm 18\%)$	80	42	1.0
	BIR-4	$0.75 \pm 0.13(\pm 18\%)$	$0.92 \pm 0.03(\pm 4\%)$	$0.86 \pm 0.10(\pm 12\%)$	382	198	4.8
	OPT	$0.92 \pm 0.10(\pm 11\%)$	$0.93 \pm 0.05(\pm 5\%)$	$0.93 \pm 0.06(\pm 6\%)$	344	179	4.3

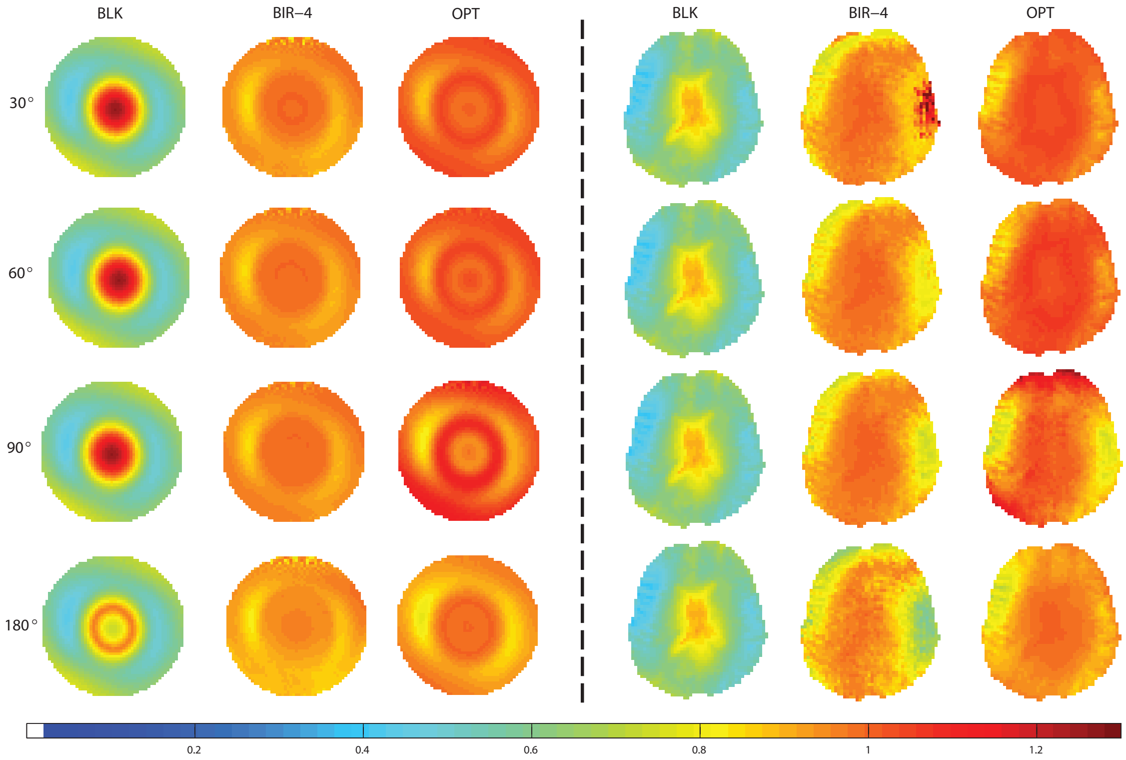

Figure 17: Flip-angle maps (expressed as a ratio of actual to nominal values) simulated in the central axial slice of a 17 cm phantom (left side) and the human brain (right side) for block (BLK), BIR-4, and optimized composite (OPT) pulses. Simulations are based on multi flip-angle B_1^+ and 3D ΔB_0 maps acquired at 7 T. Colors denote flip angles normalized to the nominal values indicated at the beginning of each row. Optimized and BIR-4 pulses show superior flip-angle uniformity to that of block pulses while *in vivo* simulations highlight the increased susceptibility of BIR-4 pulses to off-resonances. Optimized pulses appear to combine desirable features of the other pulse types—the high effective bandwidth of the block pulses and the B_1^+-insensitivity of BIR-4 pulses.

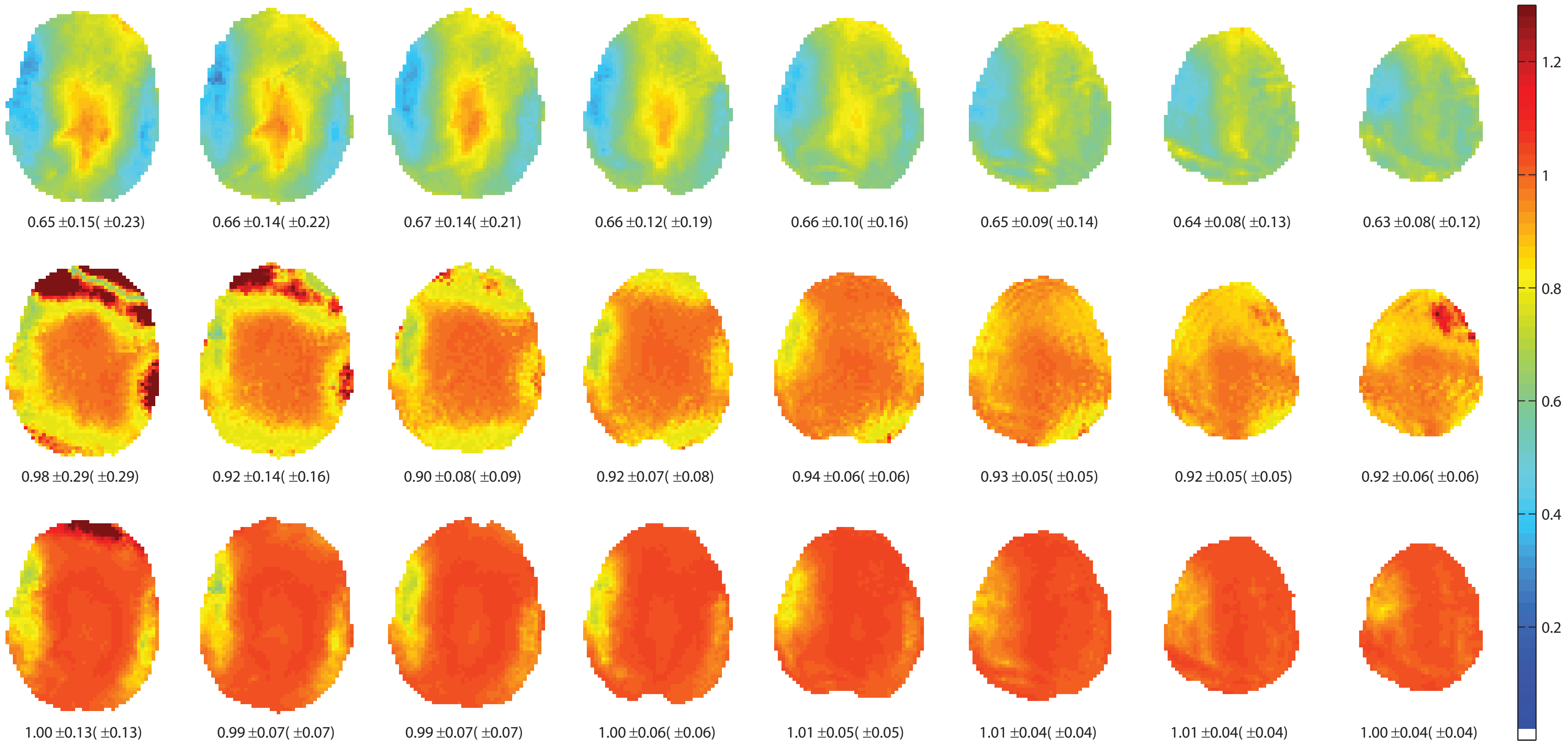

Figure 18: Flip-angle maps simulated in eight axial slices of the brain for the 30° block, BIR-4, and optimized composite pulses shown in Figure 16. Simulations are based on 3D ΔB_0 and AFI maps acquired at 7 T. Results indicate improved on-resonance flip-angle uniformity but lower effective bandwidth of BIR-4 and optimized pulses as compared to block pulses. Relative to optimized pulses, increased sensitivity of BIR-4 pulses to variations in the static field is apparent in all slices. Below each sub-figure are the nomalized mean, the mean-normalized standard deviation, and the coefficient of variation for the simulated flip-angle distributions in the given slice.

3.3.3 Phantom and *in vivo* simulations of maximum-bandwidth block, BIR-4, and optimized composite pulses

Simulated flip-angle maps (normalized to α_0) are shown in Figure 17 for the single axial slices of both the spherical phantom and the *in vivo* human brain. These simulations are based on the 7 T multi flip-angle B_1^+ maps and the corresponding slices of the 3D ΔB_0 maps described in Section 3.2.1. Flip-angle maps for maximum-bandwidth block pulses are characterized by a central hot spot due to the combination of attenuation and constructive interference of the B_1^+ field and the flip angle's linear dependence on the time-integrated magnitude of this field (83). This effect is somewhat reduced *in vivo* due to geometrical asymmetry and the resulting incoherences in the transmitted field. BIR-4 pulses do not rely on a linear relationship between flip angle and $\int B_1^+ dt$ but instead on the process of adiabatic spin-locking. The resulting improvement in flip-angle uniformity is dramatic when compared to that of the block pulse. In the phantom, static field shimming appears sufficient such that the undesirable off-resonance behavior of BIR-4 pulses seen on the B_1^+-ΔB_0 grid (Figure 16) does not effect flip angles in the central axial slice. In this context, performance of BIR-4 and optimized composite pulses is remarkably similar, with BIR-4 pulses even outperforming optimized pulses in terms of flip-angle c_v values at 90° and 180° (Table 3.3.1). *In vivo* simulation, however, begins to emphasize the significant advantage of the optimized pulses. In the *in vivo* case, with B_0 shimming being more challenging, BIR-4 pulses result in much reduced flip-angle uniformity as compared to the phantom. In particular, it is the low-B_1^+ off-resonance areas (roughly corresponding to the right side and upper left of the axial brain slice) in which flip-angles deviate the most (compare column 5 of Figure 17 to column 2 of Figure 11). Although optimized pulse performance also suffers somewhat in the lowest B_1^+ regions, these pulses are not as susceptible to variations in the static field. The *in vivo* results of Table 3.3.1 indicate significant improvements in flip-angle mean and c_v for optimized pulses, with the lone exception being c_v for the 90° pulse. It is noteworthy that such increases in performance as compared to BIR-4 pulses can be attained while simultaneously reducing $\overline{P}$ (or equivalently, $T_{R,\min}$) values by an average of 23% (Table 3.3.1).

Although B_1^+ field maps may be less accurate than the multi flip-angle data set used in Figure 17, 3D AFI data were used to simulate flip-angle response to 30° block, BIR-4, and optimized composite pulses in eight adjacent axial slices in the brain (Figure 18). These results are convincing in their illustration of the improvements possible with optimized pulses. Inferior slices in this stack are proximal to many air-tissue interfaces (such as the frontal sinus) with magnetic susceptibility changes giving rise to sharp variations in B_0. As expected due to its large effective bandwidth, the block pulse appears least affected by these off-resonances but nonetheless suffers from dramatic B_1^+-induced flip-angle variations. The BIR-4 pulse drastically improves flip-angle uniformity in the superior slices and the central regions of inferior slices; however, undesirable off-resonance effects are obvious in most slices and especially so in the inferior-most regions. In fact, the outline of the shim volume (a cuboid) is visibly recognizable in the central slices (Figure 18, row 2, columns 1–5), again emphasizing that the BIR-4 pulse performs well only under an ideal B_0 shimming scenario. The optimized composite pulse is considerably more resilient to static field variations than the BIR-4 pulse, with undesirable flip angles appearing in much more confined regions of the inferior-most slices. In fact, the optimized pulse decidedly outperforms the block and BIR-4 pulses in terms of flip-angle uniformity across all ten slices presented in Figure 18 (compare statistical measures beneath each sub-plot).

3.3.4 Time-evolution and off-resonance simulations of BIR-4 and optimized pulses

In addition to simulated flip-angle maps following the execution of the pulse, the performances of 30° BIR-4 and optimized pulses were investigated by simulating the time evolution of the magnetization throughout the pulse duration as well as the off-resonance behavior out to $\pm 5\,\text{kHz}$. Plots of α vs. time are shown for BIR-4 and optimized pulses in Figure 19 for different combinations of B_1^+ and ΔB_0. Although the amplitude of fluctuations in $\alpha(t)$ are considerably larger for the BIR-4 pulse, the oscillatory behavior of $\alpha(t)$ shows some resemblances between the two pulse types. For example, local minima are apparent in the neighborhood of $t = -1, 0,$ and $+1\,\text{ms}$. Such similarities may be indicative of the quasi-adiabatic nature of the optimized pulse. The analytical design of BIR-4 pulses, relying on adiabatic manipulation of the magnetization, results in smooth and predictable changes in the magnetization with time. The optimized composite pulses were designed to produce uniform flip angles at the conclusion of the pulses with no regard for what happens along the way. For this reason, optimized pulses are free to take advantage of adiabatic spin-locking but only to the extent that best satisfies the minimization condition (Equation 3.2.2).

The $\alpha(t)$ curves of Figure 19 are suggestive of such quasi-adiabatic behavior. This figure also clearly demonstrates the way in which magnetization vectors for BIR-4 and optimized pulses converge to the target flip angle at the end of the pulse, regardless of the B_1^+ and B_0 offsets. The one exception to this behavior is for the BIR-4 pulse when off-resonance at low B_1^+. This serves as a good example of the loss of adiabatic behavior responsible for the undesirable off-resonance effects illustrated in Figures 16, 17, and 18.

Terminal flip-angle values for the same BIR-4 and composite pulses of Figure 16 are shown in Figure 20 for ±5 kHz and nominal B_1^+. These data indicate qualitative similarities in the magnetization response to both BIR-4 and optimized pulses, again suggesting the quasi-adiabatic nature of the latter. Off-resonance data also emphasize that both pulse types (in their current form) are truly limited to volume excitations since large flip angles are produced very far from the target bandwidth.

3.3.5 Phantom experiments

Results from phantom experiments using 30° excitation pulses in a 3D gradient echo sequence are shown in Figure 21 with line profiles given in Figure 22 and relevant statistical measures presented in Table 3.3.2. In the case of second-order static field shimming (first row of Figure 21), the calculated maps of the B_1^+-dependent factor F (Equation 3.2.7b) are consistent with the phantom flip-angle map simulations presented in Figure 17, thus lending further credibility to the other simulated results presented in this work. In experiment, both BIR-4 and optimized composite

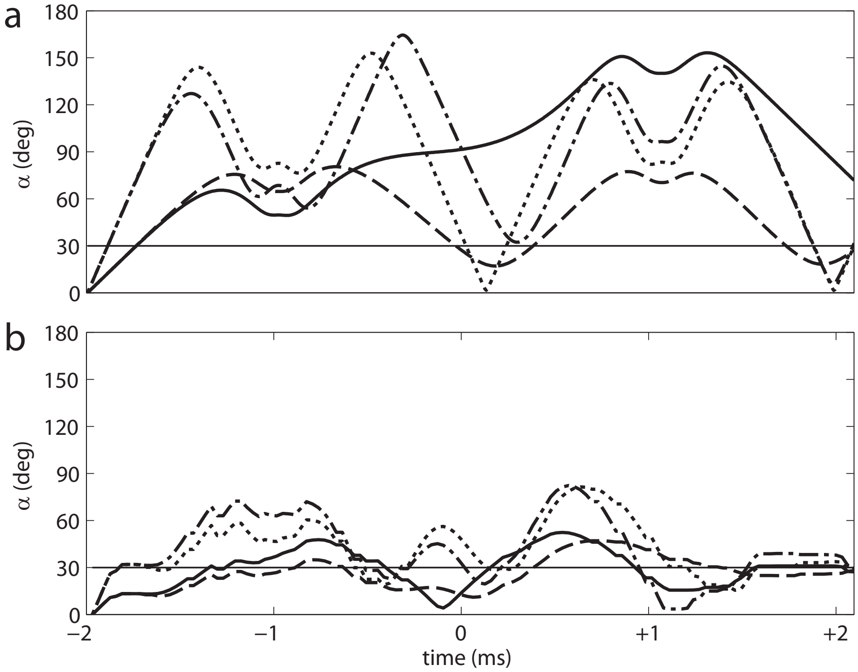

Figure 19: Flip angle as a function of time simulated for the 30° BIR-4 (a) and optimized composite (b) pulses of Figure 16. Solid, dashed, dotted, and dash-dotted lines indicate flip-angle behavior at the $(B_1^+/B_{1,\mathrm{nom}}^+, \Delta B_0)$ coordinates respectively given by $(0.5, +150\,\mathrm{Hz})$, $(0.5, 0\,\mathrm{Hz})$, $(1.2, 0\,\mathrm{Hz})$, and $(1.2, +150\,\mathrm{Hz})$. At the end time of the pulse, the four trajectories would ideally converge at the target flip-angle value of 30°. The objective of the optimization in this study is to design a composite pulse that simultaneously forces such behavior for all 420 points on the B_1^+-ΔB_0 grid. The lower effective bandwidth of BIR-4 pulses relative to optimized pulses is evident in the solid line of (a) which terminates at a flip angle more than twice the target value.

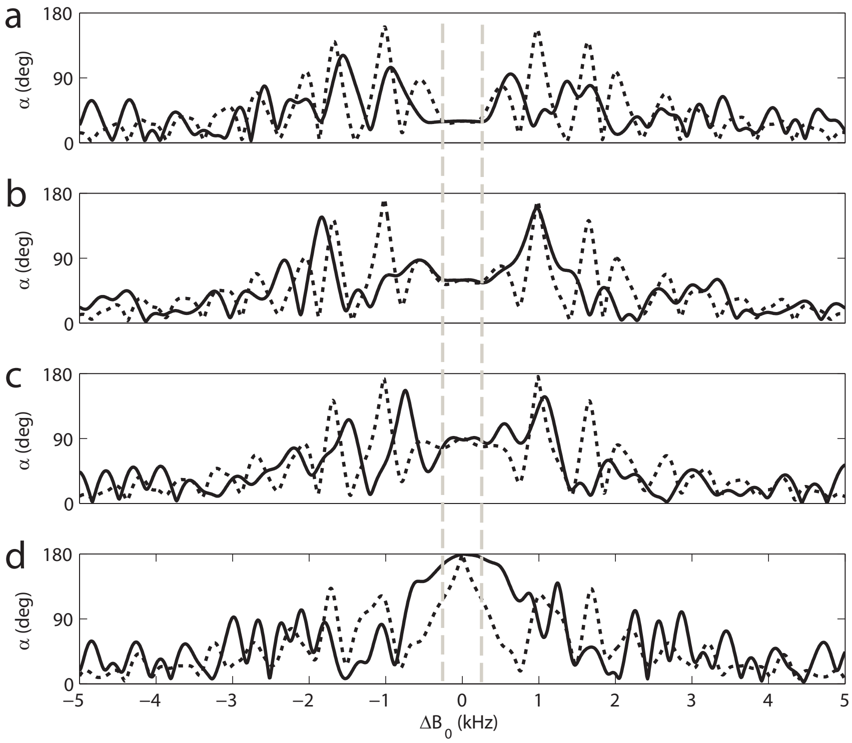

Figure 20: Nominal B_1^+, off-resonance behavior out to ±5 kHz for the (a) 30°, (b) 60°, (c) 90°, and (d) 180° BIR-4 (dashed lines) and optimized composite (solid lines) pulses of Figure 16. Vertical dashed lines denote the ±250 Hz optimization region. At nominal B_1^+, both pulses show remarkably similar off-resonance behavior and are obviously unsuitable for slice-selection.

pulses perform very well in terms of the uniformity of F when static field shimming is applied. In contrast, the maximum-bandwidth block pulse results in highly B_1^+-dependent values of F, as anticipated. In the case that the static field shimming gradients are turned off, the F maps in Figure 21 indicate the sensitivity of the BIR-4 pulse to off-resonance effects and the insensitivity of both the maximum-bandwidth block pulse and the optimized pulse to the same changes in B_0. Thus, the optimized composite pulse combines the desirable qualities of the maximum-bandwidth block pulse and the BIR-4 pulse in that the resulting excitation is highly insensitive to variations in the both the static field and the transmitted RF field. Vertical line profiles for the images and F maps of Figure 21 are given in Figure 22 and provide a different perspective on the same results. The intensity profiles in Figure 22a reflect the fact that B_1^+-insensitive pulses still result in images with considerable intensity variations due to the inhomogeneous B_1^- field associated with the receiving coil while Figure 22b shows the component of the signal dependent on B_1^+ (i.e., F). A comparison of solid and dotted lines allows for an evaluation of off-resonance sensitivity for a given pulse type. In Table 3.3.2, the distributions of F values for each combinations of pulse type and B_0-shimming scheme are described quantitatively. When comparing c_v values, the optimized pulse can be seen to perform roughly twice as well as the BIR-4 pulse when B_0 shimming is applied and about four times better in the case of no B_0 shimming. The latter case more closely reflects anticipated performance in the human brain at 7 T.

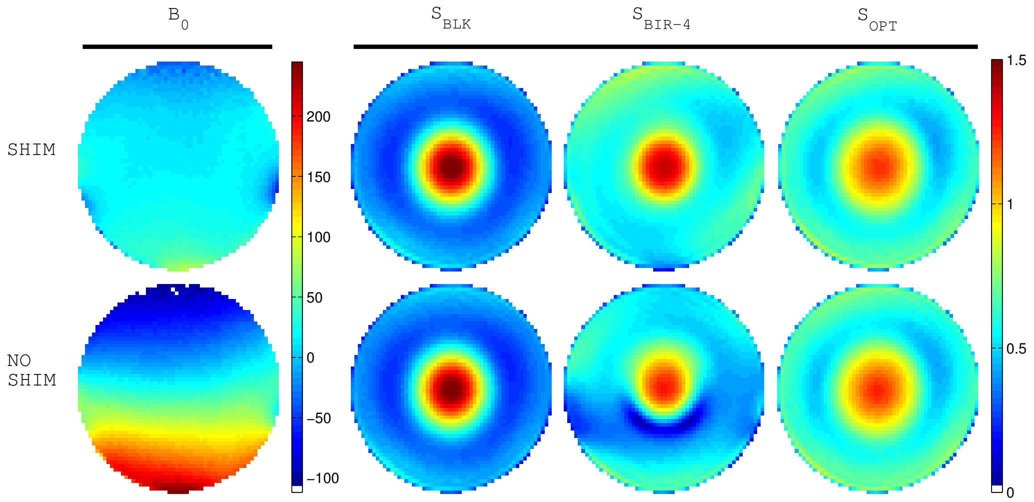

(a) Signal intensities.

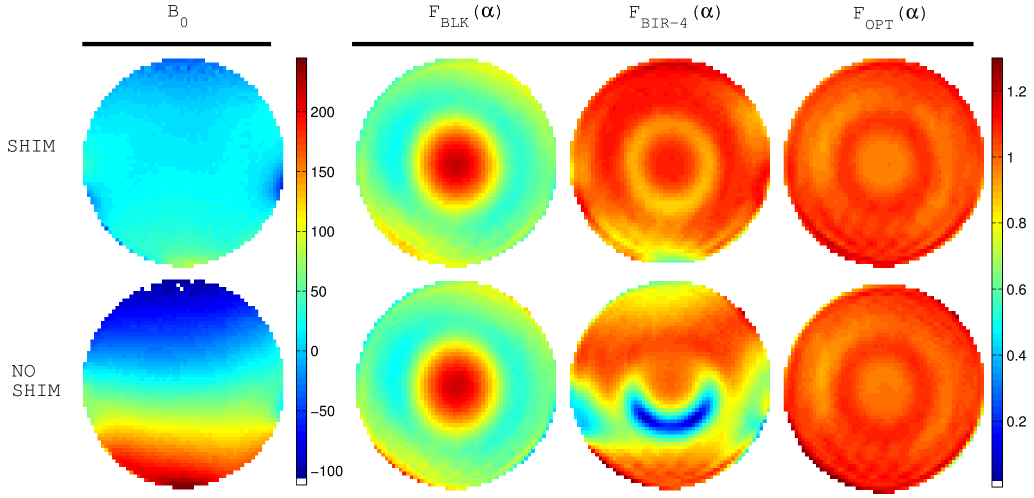

(b) Calculated maps of the flip-angle dependent function.

Figure 21: Phantom signal intensity (S) from experiment and calculated steady-state B_1^+-dependent factor (F in Equation 3.2.7b) values for the cases of second-order static field shimming (first row) and no static field shimming (second row). Static field maps are shown in column 1, and S and F maps for the three pulse types are indicated at the top of the other columns. When static field shimming is active, the BIR-4 and optimized composite pulses result in significant improvement in flip-angle uniformity as compared to the block pulse. When no static field shimming is present (and B_0 variations are similar in range to that of the human brain at 7 T), the BIR-4 pulse results in much reduced flip-angle uniformity while optimized pulse performance is similar to the case when static field shimming is applied.

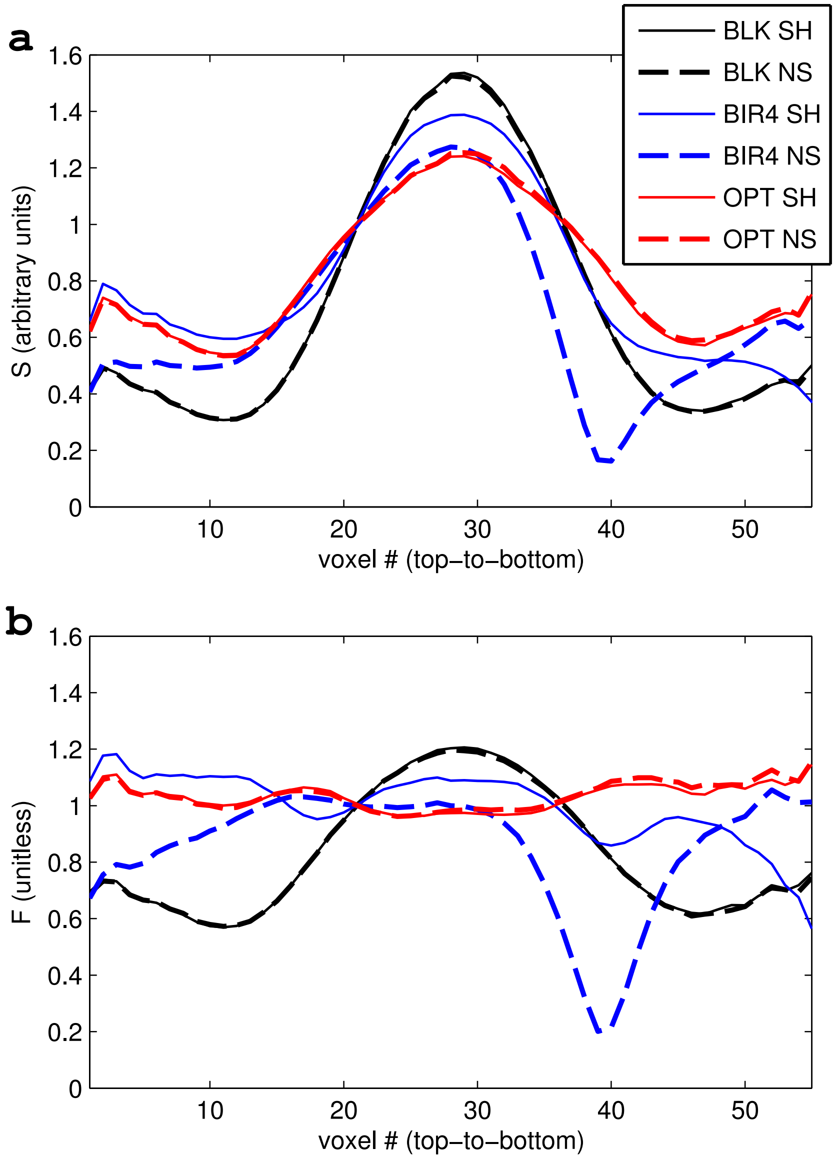

Figure 22: Central, vertical line profiles through the images (a) and F maps (b) found in Figure 21. Voxels are numbered from top to bottom, corresponding to the direction in which the static field predominantly increases (see field maps in Figure 11). The case of static field shimming (SH) is indicated by solid lines while the case of no static field shimming (NS) is indicated by dashed lines. Comparison of solid and dashed lines of a given color reveals the superior off-resonance stability of maximum-bandwidth block (black) and optimized composite (red) pulses as compared to the BIR-4 pulse (blue). Of the three pulses, the optimized composite pulse is closest to producing the ideal combination of B_0- and B_1^+-insensitivity, which would be characterized in (b) by both solid and dashed lines having the constant value $F(\alpha) = 1$.

Table 3.3.2: Distribution statistics for the experimental phantom maps of the B_1^+-dependent factor F found on the right side of Figure 21. The mean of F, standard deviation of F, and the sc_v value are given for 30°, 4.096 ms maximum-bandwidth block (BLK), BIR-4, and optimized composite (OPT) pulses. In terms of the width of the distribution of F, the optimized pulse performs slightly better that BIR-4 pulse when ΔB_0 variations are minimal. When no B_0 shimming is applied, the optimized pulse demonstrates superior flip-angle uniformity.

ΔB_0	BLK	BIR-4	OPT
SHIM	$0.69 \pm 0.16 (\pm 23\%)$	$1.00 \pm 0.09 (\pm 9\%)$	$1.03 \pm 0.05 (\pm 5\%)$
NO SHIM	$0.69 \pm 0.16 (\pm 23\%)$	$0.83 \pm 0.20 (\pm 24\%)$	$1.04 \pm 0.06 (\pm 6\%)$

3.4 Discussion

The results of this feasibility study into the applicability of numerically optimized composite pulses for 7 T demonstrate the possibility of marked gains in flip-angle uniformity as compared to block and BIR-4 pulses. Simulations and phantom experiments straightforwardly signify improved off-resonance behavior of the optimized pulses relative to BIR-4 pulses and dramatically improved excitation homogeneity relative to block pulses. The optimized waveforms in their current form are implementable for volume excitation on commercial human MR systems and, although designed specifically for a volume head coil at 7 T, can directly be used at other field strengths and for other coil/field configurations for which the B_1^+ field is highly inhomogeneous (e.g., surface coils or 3 T torso imaging).

The optimized pulses of this study are specifically designed for arbitrary flip-angle volume excitation within the practical limits dictated by a commercial 7 T MR imager. Comparisons of flip-angle uniformity between RF pulse classes (e.g., block, adiabatic, and optimized composite pulses) are complicated by the array of intended applications. For example, although emphasis in this analysis has been placed on comparison with BIR-4 pulses, it should be noted that the optimized composite pulses presented here do not in general result in plane rotations as achieved by BIR-4 pulses and, therefore, cannot be used for refocusing. For this application, composite pulses would have to be specifically designed by changing the minimization condition of Equation 3.2.2 to include the reversal of one or both orthogonal transverse magnetization components. For the purposes of excitation and inversion, it would be useful for future studies to compare the flip-angle uniformity of optimized composite pulses to that of other B_1^+-insensitive waveforms such as hyperbolic secant (72) and chirp (7) pulses within the context of 7 T human imaging. Of particular interest would be a direct comparison with the offset-independent adiabaticity (OIA) representation of such pulses (78; 45). While some such pulses offer the advantages of high bandwidth and sharp frequency profiles thus making them potentially more suitable for spectroscopy and slice-selective imaging, composite pulses could be optimized via the methods of this study with slice-selection or high bandwidth being the primary objective. The performance of such pulse designs is presently unknown.

While the phase of the transverse magnetization is unconstrained in the optimization in order to increase the resulting flip-angle uniformity, phase should in general be monitored such that variations with respect to B_1^+ and ΔB_0 do not result in signal loss from intravoxel dephasing. While the experiments in this study (with 3 mm isotropic voxels) did not appear affected by magnetization phase variations, use of optimized composite pulses could potentially result in signal intensity fluctuations in regions where the static field changes rapidly with respect to voxel dimensions. Examples of scenarios that might lead to such conditions are the use of larger voxels, the presence of extreme magnetic susceptibility fluctuations, or the use of strong gradients for suppression of signal arising from beyond the imaging volume. In such scenarios, variations in the phase of transverse magnetization produced by optimized composite pulses may warrant further scrutiny.

In addition to demonstrating notable excitation uniformity in the context of 7 T human brain imaging, data from the present study illuminate several ways in which the design process for composite pulses could be altered to produce further improvements for *in vivo* applications. The remainder of this discussion addresses the potential of data-driven alterations to composite pulse anatomy, the optimization grid, incorporation of SAR limits into the optimization algorithm, utilization of competing minimization strategies, and hardware modifications.

The performance of the optimized composite pulses relies on the combination of pulse parameters ΔT, N_s, and Δt_s in ways that are not always obvious. Perhaps the most straightforward dependence is the general trend of improved performance with increasing ΔT. Since optimized pulses tend to be characterized by high amplitudes sustained for large fractions of the pulse length, the dependence of performance on ΔT can be interpreted as a need for high average power of the total RF waveform. This idea is consistent with the adiabatic interpretation of magnetization behavior since adiabatic pulses utilize high RF amplitudes to maintain spin-locking conditions so that the direction of the effective magnetic field may be slowly varied by way of a phase or frequency sweep. As ΔT values increase, pulse performance also generally becomes more dependent on the parameters N_s and Δt_s, suggesting that a power threshold necessary for adiabatic behavior is satisfied. This effect does appear to be somewhat dependent on the target flip angle given that the minimum δ_α values in Figures 13 and 14 favor higher ΔT values as the target flip angle is increased. When the influence of N_s is visible in the data, it is usually the case that higher N_s lead to increased pulse performance for a given ΔT, although individual exceptions can certainly be found. The value of Δt_s appears to have a more subtle influence on pulse performance, but shorter Δt_s does appear somewhat favorable when comparing pulses of a given length. The effects of Δt_s are likely related to the bandwidth of the individual sub-pulses and may influence results only slightly since all Δt_s investigated in this study correspond to bandwidths much larger than the target range of ΔB_0 values (e.g., the bandwidth of a $320\,\mu$s sub-pulse is $\sim 3.1\,$kHz). Lastly, the bandwidth associated with the total pulse length ΔT may be an additional factor affecting pulse performance. For example, the eventual reduction in performance at large ΔT seen in lower flip-angle data of Figure 13 could be fostered by the fact that the bandwidth associated with the overall pulse length is actually narrower than the target ΔB_0 range of $\pm 250\,$Hz (e.g., the effective bandwidth of a 10 ms block pulse is $\pm 100\,$Hz). Such an effect would certainly seem relevant in the case that the amplitude modulation waveform approximates a that of a block pulse with the same duration.

Although the distribution of *in vivo* B_1^+-ΔB_0 values of Figure 12b are representative of only a single subject, the data are suggestive that there are large regions of the chosen optimization grid that are not relevant to 7 T volume excitation of the human brain. Furthermore, areas in which *in vivo* pulse performance is worst (e.g., Figure 18, near the frontal sinus) have resonance offsets of as much as ±700 Hz, again suggesting that the optimization region for composite pulses could be defined more suitably for uniform volume excitation of the brain. Instead of simply choosing limits for the B_1^+-ΔB_0 grid based on the maxima and minima of both phantom and brain data, only the relevant combinations of *in vivo* B_1^+ and ΔB_0 values could be identified. Ideally, such an analysis would be based on data from multiple subjects with differing head sizes and geometries. Such a customized optimization grid could result in better pulse performance at low B_1^+ values or at large resonant offsets.

Consistency of simulated flip-angle maps across the contexts of optimization grids (Figure 16) and phantom/brain data (Figure 17) indicates that discretization of the grids is sufficient to represent true variations in the underlying fields. Thus, the behavior of the magnetization for a given combination of B_1^+ and ΔB_0 is sufficiently represented by the corresponding values of neighboring points on the grid. Consequently, there appears to be no need for further discretization while reduced discretization may be possible for the sole purpose of saving computational time.

Since specific applications were not targeted in this study, $\overline{P}$ constraints were not incorporated into the optimization algorithm. The disadvantage of this approach is that a given pulse with a certain $T_{R,\min}$ is not necessarily the best pulse for a specific target application—that is, there may be a different combination of N_s and Δt_s that results in the same $\overline{P}$ but with a lower value of δ_α. A specific $\overline{P}$ limit could easily be incorporated in the optimization scheme by calculating $\overline{P}$ at every iteration and comparing that value to the prescribed constraint.

Solutions to optimization problems like the one investigated in this study are only as good as the underlying minimization technique. Given that subsequent optimizations for a pulse with particular N_s and Δt_s result in different waveforms due to the differing random initial conditions, it can be concluded that the minimization algorithm utilized here (Section 3.2.4) is not in general successful at finding a global minimum—thus, resulting pulses may not be the best possible ones given the design criteria. It is unknown if optimal control theory as implemented by Skinner et al. (74) is better suited for finding a global minimum. The condition of a uniquely defined phase for the final magnetization vector in that work would need to be relaxed to facilitate a comparison of optimization methods given that the lone condition of flip-angle uniformity in the present study does not constrain the phase of the magnetization; however, the relaxation of this phase condition does not appear straightforward. In a future study, the two algorithms (optimal control and `fmincon`) could be directly compared in the context of RF pulse design given that the final phase of the magnetization is specified. This would at least allow for a general performance comparison and an analysis of the sensitivity to initial conditions inherent in both methods. Preliminary results of a similar analysis are presented in Appendix E. In the context of the same minimization problem, optimal control theory has the advantage of efficiently handling very large numbers of free parameters, thus allowing for the design of composite pulses with arbitrarily short Δt_s. Indeed, the present study (Section 3.3.1) and others (75) have shown that pulses with short Δt_s are more likely to produce superior results. In light of these comments on the efficacy of minimization algorithms, it is worth stating that the primary objective of this work is to design a pulse that provides a practical solution to the given optimization problem, and, although algorithms with improved efficiency and performance are always preferable, determination of a global minimum is not a priority.

As alluded to in Section 3.3.3, potential for numerically optimized composite pulses should be re-evaluated in light of any relevant hardware advancements. Since sensitivity to off-resonance is apparently a relevant design issue for optimized composite and BIR-4 pulses alike, it is a noteworthy conclusion of this work that both pulse types would potentially benefit greatly from improved B_0 shimming schemes such as dynamic shimming (5) due to the corresponding reduction in the minimum required RF bandwidth (i.e., the range of ΔB_0 represented on the optimization grid). Not only would better B_0 shimming result in enhanced performance of both existing BIR-4 and optimized composite pulses but would also likely reduce the power requirements for the latter class—thus, increasing optimized pulse performance for short-T_R applications. This observation serves to emphasize the interconnected relevance of inhomogeneities in the static and RF fields. As for transmission coil technology, composite pulses should be re-designed to ensure the best possible performance if maximum RF amplifier outputs above $15\,\mu$T are available. Indications from this study are that limited RF amplitude is a significant inhibitory factor in pulse performance given that many optimized amplitude modulation functions utilize the maximum available amplitude for a large fraction of the pulse duration (see Figure 16).

3.5 Conclusion

An optimization algorithm for producing composite excitation pulses with B_1^+-insensitivity has been investigated in the context of human brain imaging at 7 T. In addition to demonstrating significant improvements of optimized pulses over block and BIR-4 pulses, this study has documented the performance of these existing methods of volume excitation. When compared to block-shaped pulses, optimized composite pulses are capable of dramatic enhancement of flip-angle uniformity at the costs of increased power, duration, and susceptibility to static field variations. Given the measured distribution of ΔB_0 values and estimated SAR values at 7 T, these drawbacks seem manageable, especially if applications are identified for which pulse sequence repetition times are sufficiently long ($\gtrsim 100\,\mathrm{ms}$). When compared to BIR-4 pulses of the same duration, optimized composite pulses also show compelling gains in flip-angle uniformity, primarily with respect to off-resonance sensitivity, and do so with reduced power requirements. Further customization to the optimization grid and direct incorporation of power constraints into the optimization algorithm may result in pulses with better *in vivo* performance and suitability to short-T_R applications. Despite such possible improvements, the pulses generated for this study already demonstrate the convincing way in which B_1^+ inhomogeneity problems at high field can be addressed through the numerical optimization of composite RF waveforms for a single channel transmitter.

CHAPTER IV

SLICE-SELECTIVE EXCITATION WITH B_1^+-INSENSITIVE COMPOSITE PULSES

4.1 Introduction

The problem of spatially-dependent signal fluctuations arising from variations in the strength of the transmitted radio frequency field (B_1^+) (83) has received much attention over the last decade due to the proliferation of high-field ($\geq$3 T) magnets for human MR imaging and spectroscopy. The challenge of mitigating such signal variations in order to more fully realize the potential of high-field imaging systems has sparked a renewed interest in the design of RF pulses that invoke a magnetization response insensitive to the B_1^+ field strength (76; 23; 60; 78; 45; 9; 1; 10; 56). Due to rough frequency profiles and non-linear transverse magnetization phase in the through-slice direction, many such pulses are limited in application to whole-volume acquisitions. Related pulse designs that could provide the B_1^+-insensitivity needed for high-field applications while additionally permitting slice-selective imaging by way of a gradient-recalled echo (GRE) are therefore of interest. Design criteria for such a class of pulses are extensive and include: (1) durations short enough to avoid significant T_2^* signal loss at 7 T; (2) bandwidths low enough to allow for imaging of thin ($\lesssim$ 5 mm) slices but high enough to avoid slice profile distortions due to in-plane B_0 variations; (3) linear (or quasi-linear) through-slice magnetization phase profiles that allow for proper rephasing (i.e., GRE); (4) slice profiles comparable to those attained with Gaussian or apodized sinc pulses; (5) peak amplitudes consistent with the performance limits of typical RF amplifiers used by clinical scanner manufacturers; and (6) average RF power levels that permit safe scanning of human subjects given the currently accepted limits on specific absorption rates (SAR $\lesssim$ 3W/kg in the brain (13)).

Although the above requirements for B_1^+-insensitive slice-selection are certainly daunting, progress has been made recently in the development of such pulses. In 1998, a gradient modulation technique was demonstrated as a means for maintaining spatial selectivity for composite excitation pulses (27). The technique relied upon a series of gradient lobes of alternating polarity—each of which was responsible for allowing the spatial selectivity of a given sub-pulse in the composite waveform while simultaneously rephasing the magnetization produced by the prior sub-pulse. Today, this approach is widely adopted in the design of *sparse spokes* pulses used for flip-angle inhomogeneity corrections (68; 89) but has proven adaptable to other pulse types. In 2008, Balchandani et al. (1) utilized such oscillating selection gradients to transform a non-selective BIR-4 excitation pulse with a 90° flip angle into a spatially selective pulse with similar B_1^+-insensitive properties. In this technique, BIR-4 phase and amplitude modulation patterns served as envelopes defining the phases and amplitudes of a train of spectrally selective sub-pulses formed from the central lobes of `sinc` functions (hereafter referred to as a SINC modulation). In the context of a GRE sequence with a 90° excitation, the study showed improvements in flip-angle uniformity for 10 mm slice thicknesses in a phantom and the *in vivo* human brain at 3 T and represents a significant step in advancing the limits of practical single-channel pulse designs.

The work presented here uses the same spatial selectivity strategy as that discussed above but in conjunction with composite pulses numerically optimized to produce uniform flip angles over specified ranges of B_0 and B_1^+ field variations (56). The optimization procedure results in a non-selective pulse that is then endowed with spectral selectivity via the replacement of block-shaped sub-pulses with Gaussian (hereafter referred to as GAU) or SINC sub-pulses. Due to a cost function involving only the flip angle, the resulting class of excitation pulses does not rely explicitly on adiabatic spin-locking to achieve immunity to B_1^+ variations. This characteristic is potentially advantageous given that the pulse durations and high RF power needed for adiabaticity are not always attainable in the human brain at 7 T due to the combination of large B_1^+ variations, RF amplifiers with limited peak amplitudes, SAR restrictions, and relatively short T_2^* values. Furthermore, the design protocol incorporates prescribed B_0 variations into the optimization problem, thus resulting in slice profiles that are generally stable within the specified range of static field offsets. In addition to the described optimization procedures, we expand on the work of Balchandani et al. to investigate (1) the use of higher gradient strengths for achieving imaging slice thicknesses of $\sim 2\,\text{mm}$, (2) the slice profile variations resulting from different sub-pulse amplitude modulations (i.e., GAU and SINC), (3) the use of a wide range of total pulse durations ($\sim 2-20\,\text{ms}$) so as to explore the potential trade-off between pulse performance (i.e., insensitivity to B_1^+ and B_0 variations) and relaxation effects (i.e., T_2^* and $T_{2,\rho}$ (52; 51)), and (4) the exploration of pulse performance at arbitrary flip angles (results for nominal flip angles of both 45° and 90° are presented).

Given the above objectives, it is the underlying motive of the present study to further test the limitations of single-channel, slice-selective pulse designs for practical use at 7 T. While multi-transmit technologies promise to meet many of the same needs, single-channel pulse designs are very much of interest given that all scanners are not yet equipped with multi-transmit hardware and that the SAR demands of multi-transmit systems have not been fully established. Furthermore, exploring the limits of single-channel designs helps to determine the true advantages of multi-transmit techniques and to establish the contexts in which such techniques are most suitable. Such pulses as the ones of this study may also find a role in clinical scanning at lower field strengths since the field variations observed in those contexts may not always warrant the expense of additional transmission channels. Regardless of field strength, the pulses of this study have an inherent advantage over current multi-transmit methods in that subject-specific field maps and subsequent pulse calibrations do not have to be made—pulses are designed with the goal of delivering the required performance despite subject-specific differences in B_0 and B_1^+ field geometries. While this feature is certainly attractive in terms of practicality, the true pros and cons of this class of pulses (as well as its proper place in the context of MRI) will only be better understood in time.

4.2 Methods

The description of methods is presented in three main parts: pulse designs, simulations, and experiments.

4.2.1 Pulse designs

This section begins with a review of the previously described protocol (56) for the optimization of non-selective exitation pulses, including adjustments that have been made for the current slice-selective application (Section 4.2.1). The procedure used to translate these non-selective pulses into their slice-selective counterparts is then described. Lastly, a preliminary analysis of various gradient and amplitude modulation shapes for achieving slice-selective excitation (including the effects of these choices on resulting slice profiles) is presented. These simulations justify the gradient and amplitude modulations selected for implementation in this study.

Structure and optimization of non-selective composite pulses

To generate non-selective composite pulses with inherent insensitivity to variations in the B_0 and B_1^+ fields, a discrete grid comprised of pairs of ΔB_0 and B_1^+ values was established. The included ranges of ΔB_0 and B_1^+ values correspond to the ranges of field variations over which the resulting pulse is required to perform and were determined from our previous study that reported such variations within the human brain at 7 T (56). An appropriate ΔB_0 range for a central axial slice was determined to be ±150 Hz, while the corresponding B_1^+ range was found to be $[0.25, 1.00]$ in units of the nominal B_1^+ field strength ($B_{1,\mathrm{nom}}^+$). These ranges were discretized into 31 steps in the ΔB_0 direction (resulting in steps of 10 Hz) and 16 steps in the B_1^+ direction (resulting in steps equivalent to 5% increments of $B_{1,\mathrm{nom}}^+$). This B_1^+-ΔB_0 grid provided a visualization tool when magnetization response to a given RF pulse was simulated and also served as a context in which a numerical optimization problem was formulated.

While still series of block-shaped sub-pulses (i.e., each sub-pulse had constant phase and amplitude values), composite pulses for the present study differed from those designed previously (56) in that (1) sub-pulse duration was significantly lengthened to accommodate the substitution of GAU and SINC modulations needed for slice selection and (2) peak RF amplitudes were further limited such that necessary amplitude adjustments for the slice-selective sub-pulses could be made without exceeding the amplifier limit of 15 μT. These constraints resulted in sub-pulse durations of 665.6 μs and 1062.4 μs (integer multiples of the digital RF amplifier's dwell time of 6.4 μs) and maximum amplitudes of 8.8 μT and 5.0 μT for the SINC and GAU formats, respectively. Motivation for these particular duration and amplitude values is further described later on in this section.

With these sub-pulse durations and maximum amplitude values established, the k phases ($\boldsymbol{\phi} = \{\phi_1, \phi_2, \ldots, \phi_k\}$) and k actual amplitudes ($\mathbf{A} = \{A_1, A_2, \ldots, A_k\}$) of a given sequence of block-shaped sub-pulses were determined through minimization of the cost function

$$\delta_\alpha(\mathbf{A}, \boldsymbol{\phi}) = \frac{1}{mn} \sum_{i,j=1}^{m,n} \left| \frac{\alpha_{i,j}^S(\mathbf{A}, \boldsymbol{\phi}) - \alpha_{i,j}^T}{\alpha_{i,j}^T} \right| , \tag{4.2.1}$$

where i is the B_1^+ index on the B_1^+-ΔB_0 grid, j is the ΔB_0 index on the B_1^+-ΔB_0 grid, and α is the flip angle given by $\cos^{-1}(M_z/M_0)$ with S and T denoting simulated and target values. In this study, $\alpha_{i,j}^T$ values were set to either 45° or 90° over the entire optimization grid, thus prescribing uniform flip angles over the specified ranges of field variations. The value of function δ_α represents the average deviation of simulated flip angles from the target flip angle over the entire B_1^+-ΔB_0 grid and is expressed as a fraction of the target flip angle. Solutions to the minimization problem were found using the `fmincon` function in Matlab (The MathWorks, Natick, MA, USA) with the `interior-point` algorithm. In summary, this constrained minimization technique involves numerical approximations to the Hessian of the LaGrangian of δ_α in combination with a series of linear and conjugate-gradient steps. Initial conditions for all performed optimizations were defined by randomly assigned phase and amplitude values for each sub-pulse (within the constraints of $-\pi \leq \phi_k \leq +\pi$ and $0 \leq A_k \leq 15\,\mu\mathrm{T}$) while the intial magnetization vector was given by $\mathbf{M}_0 = (M_x, M_y, M_z) = (0, 0, 1)$. The numerical optimization was carried out for four categories of pulses corresponding to the two target flip angles (45° and 90°) and the two amplitude/duration formats (GAU and SINC) described above. Within each pulse category, composite pulses were generated with $k = 1, 2, \ldots, 19$ sub-pulses, thus reflecting the desired range of total pulse durations to be investigated, i.e., $\Delta T \sim$ 1-20 ms.

Despite the relatively low number of free parameters in the optimization problem (the maximum number is 40 in the case of 20 sub-pulses), the minimization algorithm was found to be rather sensitive to initial conditions. To ensure avoidance of outlying

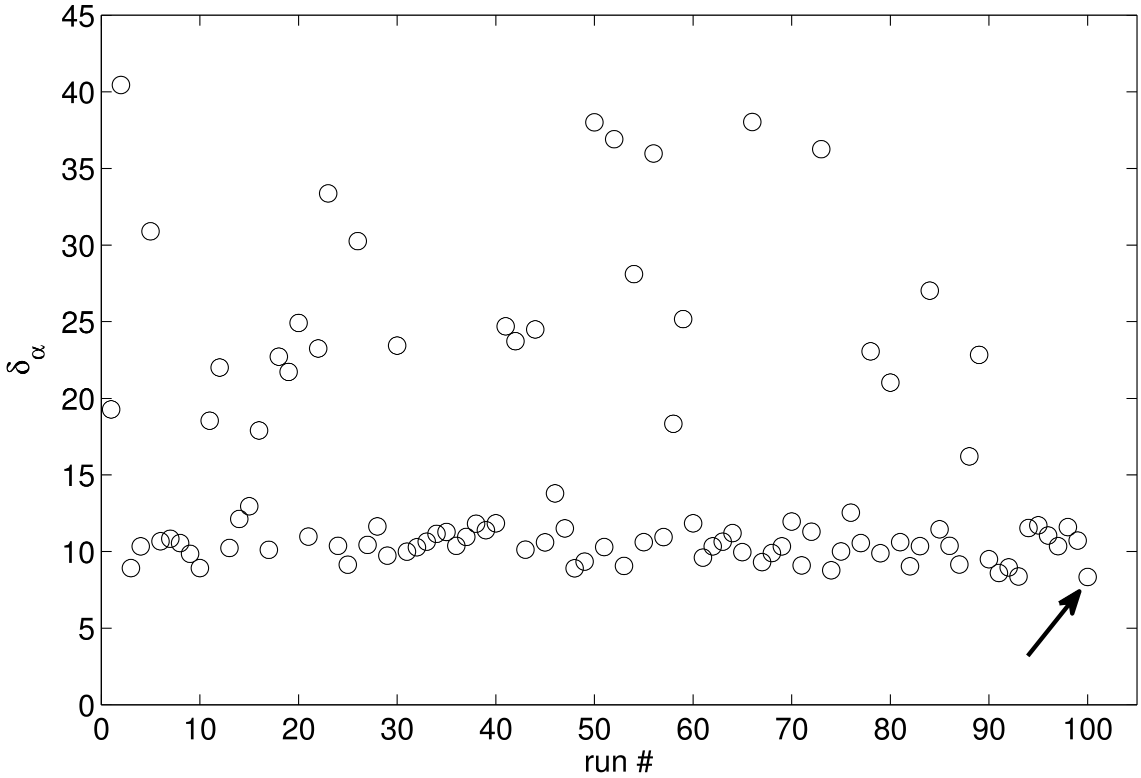

Figure 23: Optimization performance (δ_α, Equation 4.2.1) as a function of run number for a 13-element composite pulse with a target flip angle of 45° and a maximum amplitude of 8.8 μT, as is the case for SINC pulse format. Runs represent identical optimizations with different random initial conditions (i.e., random initial sub-pulse phases and amplitudes). The arrow indicates the run with lowest δ_α which was selected to represent pulses of the given composition. Although the majority of runs converge to $\delta_\alpha \sim 10$, this minimization problem with 26 free-parameters clearly demonstrates a sensitivity to initial conditions that warrants repeating the optimization to check for the possibility of a more favorable starting point.

local minima, the optimization was repeated 100 times for each pulse as defined by a unique combination of target flip angle (α^T), total duration (ΔT), sub-pulse duration, and maximum sub-pulse amplitude values. Only phase and amplitude sets resulting in the lowest value of δ_α for a given pulse structure were considered in the subsequent analysis of pulse performance. An example of the observed sensitivity to initial conditions for one pulse structure is shown in Figure 23 and helps to justify the repetition of optimizations.

Construction of slice-selective pulses

Once all optimizations had been performed, the resulting non-selective composite pulses were translated into slice-selective pulses via a two-step process. Firstly, the block-shaped amplitude modulations were replaced by either GAU or SINC waveforms of the same duration. The peak amplitude of each GAU/SINC sub-pulse was adjusted such that the integrated amplitude (or, equivalently, flip angle as given by $\int \gamma A_k dt$) was left unchanged relative to that of the corresponding block-shaped sub-pulse. Sub-pulse phases were not adjusted in the translation from non-selective to slice-selective pulses. Secondly, the phase and amplitude modulations of the composite pulse were synchronized with an oscillating gradient in the slice-selection direction. Because of limited gradient slew rates (166 T/m/s in this case), an appropriate inter-sub-pulse delay was chosen to avoid ill effects on the resulting slice profile. This was not a straightforward choice given the subjectivity of characterizing an acceptable slice profile. Thus, the remainder of this subsection is devoted to a preliminary analysis of the slice profiles resulting from the chosen GAU and SINC modulations in conjunction with selection gradients of varying length. This analysis leads to the choice of selection gradient durations adopted for subsequent simulations and experiments.

Preliminary analysis of slice profiles

The target slice thickness for this study was established at 2 mm. Given this desired slice thickness and a maximum gradient strength of 33 mT/m, the relationship

$$\Delta z = \mathrm{BW}/\left(\gamma \cdot G\right) , \tag{4.2.2}$$

where Δz is slice thickness, BW is the bandwidth of the RF pulse, G is the gradient strength, and $\gamma = 42.57\,\mathrm{MHz/T}$ is the gyromagnetic ratio for ^{1}H, necessitates RF bandwidths of ~ 2800 Hz. According to slice profile criteria described previously (4), the standard deviation of the GAU sub-pulses in this study was fixed to 13.5% of the total sub-pulse duration. The SINC sub-pulses were determined using the `firls` function in Matlab according to Balchandani et al. (1). The target bandwidth in conjunction with these particular amplitude modulations led to the choice of the 665.6 μs and 1062.4 μs durations for the SINC and GAU sub-pulses, respectively, as mentioned in Section 4.2.1.

The Bloch equation was simulated according to the methods of Section 4.2.2 to determine slice profiles for individual GAU and SINC sub-pulses when executed in the presence of different slice selection gradient waveforms. In the first gradient scheme, gradient amplitude was constant for the duration of the sub-pulse. This case affords optimal slice-profiles but leads to additional time (beyond the duration of the RF sub-pulse) to accommodate the slew of the gradient up to and down from its maximum strength—a transition time that takes $\sim 200\,\mu$s. In the second gradient scheme, the RF sub-pulse and the entire trapezoidal gradient waveform had identical durations such that RF amplitude is non-zero during the slew of the gradient. The advantage with this scheme over the first is that additional time is not required to accommodate the slew periods.

Figure 24 shows the resulting slice profile simulations along with the relevant amplitude and gradient waveforms. These results demonstrate that the SINC pulses result in slice profiles with prominent side lobes when the RF waveform overlaps with the gradient slew period. With the ultimate goal in this study being high-resolution imaging of thin slices, such profiles were deemed unacceptable; therefore, all SINC pulses in this study were executed such that gradients are slewed only when the RF amplitude is zero. Conversely, GAU pulses result in smooth and almost identical slice profiles for both gradient schemes; therefore, the gradient was allowed to slew during the execution of GAU pulses so as to reduced the total pulse duration. The fact that GAU pulses are relatively immune to variations in gradient shape near the beginning and end of the RF waveform is not surprising given that a GAU pulse deposits a larger fraction of its power in the middle of the pulse duration as compared to a SINC pulse.

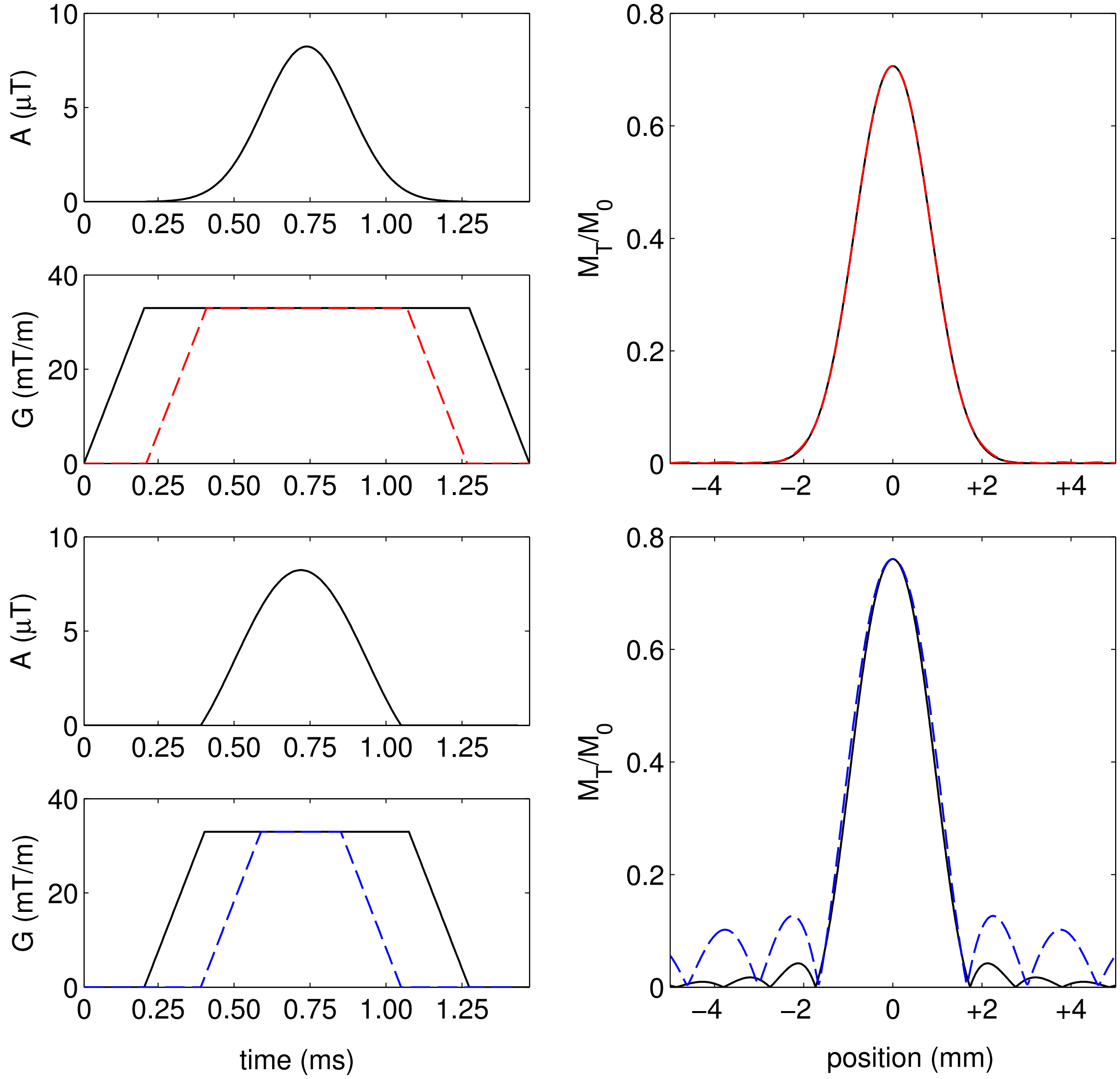

Figure 24: A comparison of simulated slice profiles for Gaussian (top) and central-`sinc` lobe (bottom) amplitude modulation waveforms of the same bandwidth executed in the presence of various slice-selection gradients. Dashed/solid profiles in the right column result from the given amplitude modulation in the presence of the corresponding dashed/solid gradient in the left column. Gradients indicated with the dashed lines are equal in total duration to the corresponding RF waveforms. Gradients designated by solid lines allow the entire RF waveform to be executed during the gradient plateau. While these two gradient schemes result in very similar slice profiles for the Gaussian pulse, the shorter gradient results in much amplified side-lobes in the case of the `sinc` pulse.

4.2.2 Simulations

Magnetization response to the non-selective composites of k sub-pulses with constant phase and amplitude were modeled as a series of rotations (R_j, where $j = 1, \ldots, k$), each representing the operation due to a relaxation-independent form of the Bloch equation (3). Such strategies for simulation the Bloch equation are the subject of Appendix B. With each rotation corresponding to one of the k individual sub-pulses, the collective operation of all components of a composite pulse is described by

$$\mathbf{M} = R_k R_{k-1} R_{k-2} \ldots R_1 \mathbf{M}_0 \,, \tag{4.2.3}$$

where $\mathbf{M}_0$ is the magnetization vector preceding the pulse and $\mathbf{M}$ is the magnetization vector following the pulse. For all cases in this study, the initial magnetization was taken to be in the z-direction such that the components of $\mathbf{M}_0$ were given by $(M_x^0, M_y^0, M_z^0) = (0, 0, 1)$. For optimization of non-selective pulses, magnetization response was simulated over the B_1^+-ΔB_0 grids of the dimensions described in Section 4.2.1; however, simulation data presented in this manuscript was calculated over grids with much higher resolution (i.e., 1% and 1 Hz increments in the $B_1^+/B_{1,\text{nom}}^+$ and ΔB_0 directions, respectively).

Simulations of the Bloch equation for slice-selective composite pulses were according to the same methods as for non-selective pulses except that each of the k sub-pulses was further discretized into l parts (with l being the number of $6.4\,\mu$s intervals within the sub-pulse) over which RF amplitude, RF phase, and gradient strength were considered constant. Thus, an entire composite pulse required $k \times l$ rotation operators, such that each R_k in Equation 4.2.3 is expressible as

$$R_k = R_{k,l} R_{k,l-1} R_{k,l-2} \ldots R_{k,1} \,. \tag{4.2.4}$$

Such simulations resulted in magnetization responses that were illustrated on high-resolution B_1^+-z grids, with z denoting position along the slice-selection direction. Magnetization was calculated in this way over a range of $\pm 5\,\mathrm{mm}$, thus well beyond the target slice thickness. The large number of rotation operaters was not prohibitive in this case since all optimizations were performed using non-selective pulses.

To evaluate the dependence of magnetization on the decay constant T_2^* during application of a given RF pulse, the Bloch equation was simulated such that relaxation effects were considered (see Appendix B), as was not the case with the rotation operations previously employed. For this purpose, a finite difference method was adopted for which the iterative cycle is 100 times shorter than the $6.4\,\mu$s intervals used for relaxation-free simulations. Such short increments were necessary to ensure realistic behavior of the simulated magnetization response when the Bloch equation is modeled in this way.

To help establish practical limitations, a set of values reflecting SAR and echo time constraints were calculated for each pulse. These values include the integral of the square of the amplitude (a quantity directly proportional to SAR), the minimum allowed repetition time given the SAR constraint of 3 W/kg ($T_{R,\mathrm{min}}$), and the minimum possible echo time ($T_{E,\min}$). The first of these is a straightforward calculation involving the amplitude modulation of the slice-selective version of each pulse. The second value, $T_{R,\min}$, is determined from inverting the relationship

$$\mathrm{SAR} = \frac{C}{T_R} \int_0^{\Delta T} |A(t)|^2 \, dt \,, \tag{4.2.5}$$

in which $A(t)$ is the amplitude modulation function and C is a coil specific constant describing the rate of energy dissipation of 298 MHz radiation in human brain tissue, in order to determine the T_R that corresponds to a SAR value of 3 W/kg. The value $T_{E,\min}$ is determined by taking half of the total pulse duration and adding the time needed for a rephasing gradient of the same duration as a single sub-pulse. This reflects the way minimum echo times are typically calculated by commercial MR scanner software.

4.2.3 Experiments

All experiments were conducted on a 7 T Philips Achieva whole body scanner (Philips Healthcare, Best, the Netherlands) based on a Magnex (Varian Medical Systems, Palo Alto, CA) 90 cm magnet. RF transmission and reception was carried out with a single-channel, quadrature volume head coil from Nova Medical (Wilmington, MA). All phantom experiments were based on a 17 cm spherical dielectric phantom from FBIRN (Function Biomedical Information Research Network) with relaxation constants of $T_1/T_2^* = 1150/42$ ms as measured at 7 T. For *in vivo* experiments, one healthy volunteer was recruited from the community, and written informed consent was obtained according to the guidelines of the local Institutional Review Board.

Static field maps were obtained in the phantom and human subject using a 2D GRE sequence with a double-echo acquisition ($\Delta T_E = 1\,\mathrm{ms}$), a repetition time ($T_R$) of 5 ms, and a flip angle of 10°. Slice orientation was axial, and scan resolution was 3×3 mm within a 240×192 field of field in the anterior-posterior, right-left directions, respectively. Slice thickness was 2 mm, corresponding to the target slice thickness of the pulses in this study. $B_1^+/B_{1,\mathrm{nom}}^+$ maps were calculated via a voxel-by-voxel fitting of signal intensities from a multi-flip-angle, multi-slice, multi-shot (3 lines of **k**-space per shot) GRE-EPI scan with a T_R of 5 s (89; 30). The in-plane resolution, slice thickness, and field of view matched those of the B_0 scan. Projection-based, second-order volume B_0 shim currents were used during collection of all data. Shim currents and the RF drive scale remained unchanged for the series of experiments in the same imaging volume. B_0 maps were used to perform EPI distortion corrections of the B_1^+-mapping data (35) which were minimal in this case due to the low EPI factor. Given that the signal resulting from a long-T_R, short-T_E GRE sequence is expressible as

$$S = \beta F = \beta \left|\sin \lambda \alpha_0\right| \,, \tag{4.2.6}$$

where β represents the product of the equilibrium magnetization (M_0) and the relative intensity of the RF field associated with the receiver coil (B_1^-), λ represents the relative strength of the transmitted RF field ($B_1^+/B_{1,\mathrm{nom}}^+$) and α_0 is the nominal flip angle, the fitting procedure of the B_1^+ measurement technique results in estimates of both β and λ. While λ gives a measure of actual variations in B_1^+, the parameter β can be used for evaluating the uniformity of excitations produced by various RF pulses as described below.

Imaging experiments for evaluating pulse performance employed the same 2D GRE sequence as used for B_1^+ mapping. In order to reflect the practical limitations associated with pulses of different duration, echo time (T_E) was set to the shortest possible value for a given excitation pulse. This resulted in signal acquisitions that began $\sim 1\,\mathrm{ms}$ after the end of any given RF excitation, thus allowing time for the rephasing gradient which was in all cases the same duration but half the strength as the individual gradient lobes used during application of the RF pulse. Imaging experiments were performed for only a small sample of the 80 pulses derived in this work. In addition to a single Gaussian pulse, only the pulses circled in Figure 25—namely, the GAU and SINC pulses with 5 and 8 components (hereafter referred to using the abbreviations 5-GAU, 8-GAU, 5-SINC, and 8-SINC)—were implemented on the scanner. While all of these pulses were tested on the phantom, only the single Gaussian and 5-SINC pulses were tested in the brain. In all cases, both 45° and 90° versions of pulses were used. As a measure of the flip-angle uniformity produced by each pulse, both phantom and *in vivo* images (comprising S in Equation 4.2.6) were divided on a voxel-by-voxel basis by the corresponding map of β derived from B_1^+-mapping procedures—thus producing maps of the flip-angle dependent function F in Equation 4.2.6. Prior to division, both images and β maps were normalized to their respective values at locations for which $B_1^+/B_{1,\text{nom}}^+ = 1$. This normalization step compensates for the fact that the slice profiles attained with a given RF pulse are slightly different from those produced during the B_1^+-mapping sequence upon which the determination of β is based. Considering these slice-profile variations, division of the unnormalized intensities could result in unfeasible values of F, i.e., values that imply the `sin` function in Equation 4.2.6 has a value > 1. An alternative approach would be to adjust signal intensities based on the slice-profile measurements described below; however, this procedure was avoided since it would rely upon additional measurements that incorporate additional sources of error.

To verify target slice thickness, slice profiles were measured in the same phantom for all pulses used in the previously described imaging experiments. For this purpose, the phase-encoding of the read-out was oriented along the slice-selection direction in a 2D GRE sequence. All other scan parameters were the same as those of the 2D GRE sequence adopted for imaging experiments, with the only exception being a 1 mm acquisition resolution in the phase-encoding direction.

4.3 Results

Similarly to the Methods section, results are presented in three parts. Firstly, the results of all non-selective pulse optimizations are given in Section 4.3.1. Secondly, simulations of pulse performances for both non-selective and slice-selective pulses are presented in Section 4.3.2. Lastly, in Section 4.3.3, the results of phantom and *in vivo* brain experiments are described, including measurements of slice profiles.

4.3.1 Optimizations

The results of non-selective pulse optimizations are presented in Figure 25. The final cost function values (Equation 4.2.1) for all pulses (not including optimization repetitions for the same pulse structure) are given as a function of total pulse duration. This data contains several noteworthy features. Firstly, regardless of the type of pulse (i.e., 45° or 90°, GAU or SINC), cost function values decrease dramatically as a function of total pulse duration out to $\sim 10\,\text{ms}$. Beyond this point, improvements in the cost function become increasingly small. Secondly, the SINC pulses result in better performance at any given duration beyond 3 ms. Thirdly, the 90° pulses largely perform better than their 45° counterparts.

Entries encircled by dashed lines in Figure 25 indicate the pulses selected for in-depth analysis. All other results presented in this manuscript pertain to one or more of these eight pulses or to one of the single-Gaussian pulses referred to in Section 4.2.3. It should be noted that, although these selected pulses represent practical options in terms of duration and performance, they do not reflect the maximum B_1^+-insensitivity (as measured by the cost function) of pulses produced in this study. Reductions in δ_α of $\sim 50\%$ are possible when considering longer pulses (e.g., compare the 90° SINC pulses of 8.5 ms and 20.2 ms durations in Figure 25).

4.3.2 Simulations

Simulated magnetization responses to both non-selective and slice-selective versions of the designated sub-set of pulses are shown in Figure 26 for $\alpha^T = 45°$ and in

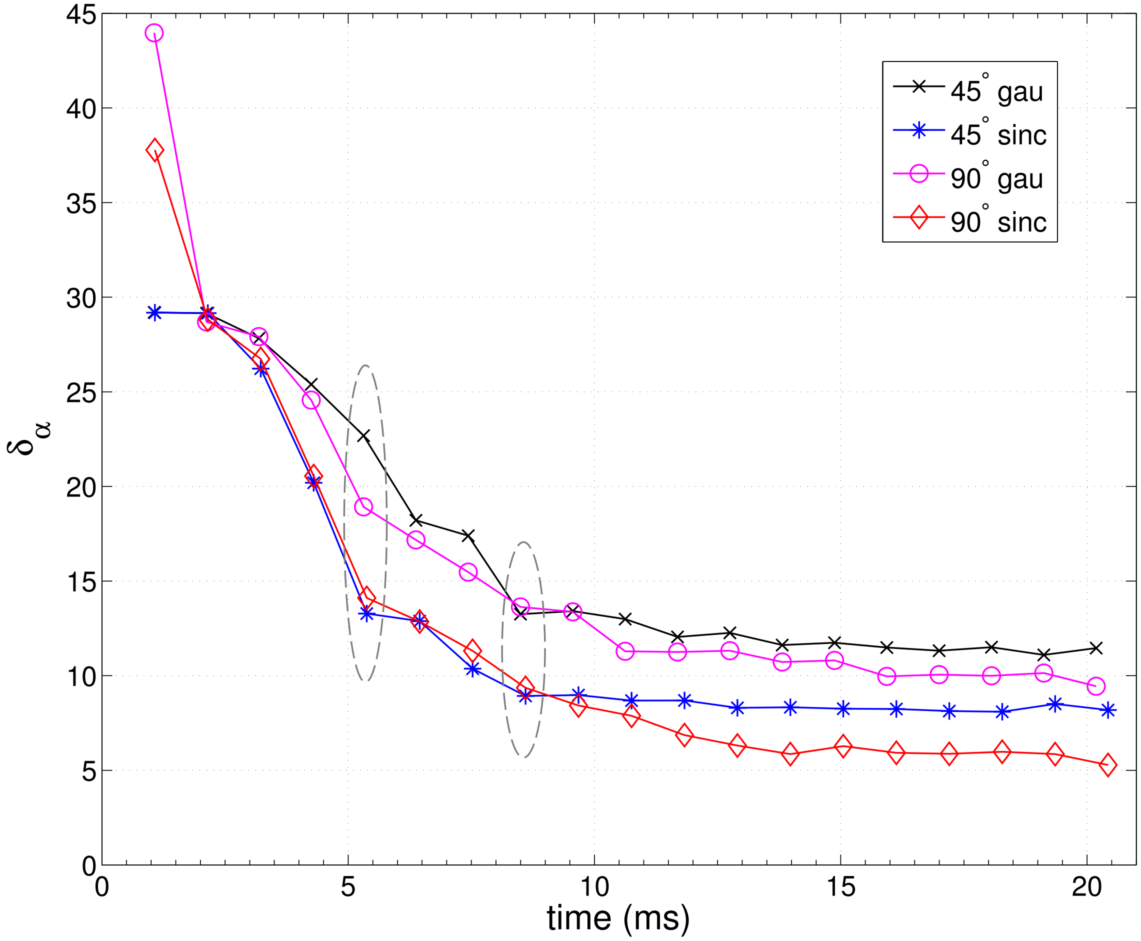

Figure 25: Cost function values (δ_α, Equation 4.2.1) for non-selective composite pulses as a function of total pulse duration. Each data point represents a unique composite pulse with the different combinations of sub-pulse shape (GAU or SINC) and target flip angle (45° or 90°) indicated by different colors. Dashed ellipses indicate the pulses chosen for in-depth analysis via simulation and experiment. In all cases, the largest degree of cost function improvement is achievable with pulse durations $< 10\,\text{ms}$, with longer durations only leading to modest performance gains. SINC composites systematically outperform GAU pulses of the same structure while higher flip angles (i.e., 90°) lead to improved cost function values especially for pulse durations $> 10\,\text{ms}$.

Figure 27 for $\alpha^T = 90°$. In addition to the magnitude of the transverse magnetization ($|M_T|$), these figures display the non-selective and slice-selective RF waveforms, the slice-selective gradients and, in the case of slice-selection, the phase of the transverse magnetization (ϕ_{MT}). Magnetization uniformity within the optimization regions on the B_1^+-ΔB_0 grids is greatly improved (with respect to the single-Gaussian pulses) through the use of optimized composite pulses, and, indeed, the degree of uniformity appears to correlate with the cost function values reported in Figure 25. Moreover, the simulations of slice-selective pulses exhibit similar B_1^+-insensitivity to their non-selective counterparts—thus validating, in part, the methods adopted by this study for the generation of B_1^+-insensitive, slice-selective pulses.

While the composite pulses largely reflect the desired degree of B_1^+-insensitivity, there are some complications with such pulses that become apparent through the simulated magnetization responses. Perhaps most significant is the introduction of non-linear through-slice phase. This effect is most prominent in the waveforms with the highest integrated amplitudes and at the highest $B_1^+/B_{1,\text{nom}}^+$ values (see the 90° 8-SINC pulse in Figure 27 for an obvious example). The detriment of non-linear phase is the potential signal loss resulting from residual incoherencies in ϕ_{MT} following application of a linear rephasing gradient. Due to this phenomenon, pulses with the lowest cost function values may not always result in the largest signal gains. Given the relative importance of linear phase for maximizing signal produced by excitation pulses, details of the simulated through-slice phase following the application of a rephasing gradient are presented in Figure 28. In this representation, phase is shown for only a few $B_1^+/B_{1,\text{nom}}^+$ values and for only the central 2 mm of the slice. The range of data in the slice-selection direction is limited to reflect the region from which the majority of signal arises. These simulations indicate that total phase dispersion is $\leq \pi/3$ radians in all cases except that of the 90° 8-SINC pulse for which the dispersion is approximately twice as large. The maximum phase dispersion for a particular pulse always occurs at the highest value of B_1^+, while dispersion at lower B_1^+ values is significantly less. Also noteworthy is the observation that the single-Gaussian pulses do not result in perfectly linear through slice phase either, although the level of dispersion is significantly less. For all pulses, the non-linear phase is more prominent at higher flip angle.

Figures 26 and 27 also illuminate differences in slice profiles resulting from the various pulses. While SINC pulses generally exhibit the greatest B_1^+ insensitivity and a more sharply defined central excitation region, the anticipated side lobes associated with the use of sinc-center pulses (Figure 24) are apparent in the composite pulse simulations. Additionally, some subtle asymmetries in slice profiles can be seen for the 45° pulses. These features are most prominent for the 5-GAU and 8-GAU pulses and appear to correlate with the degree of asymmetry along the ΔB_0 direction in the magnetization plots for the corresponding non-selective pulses.

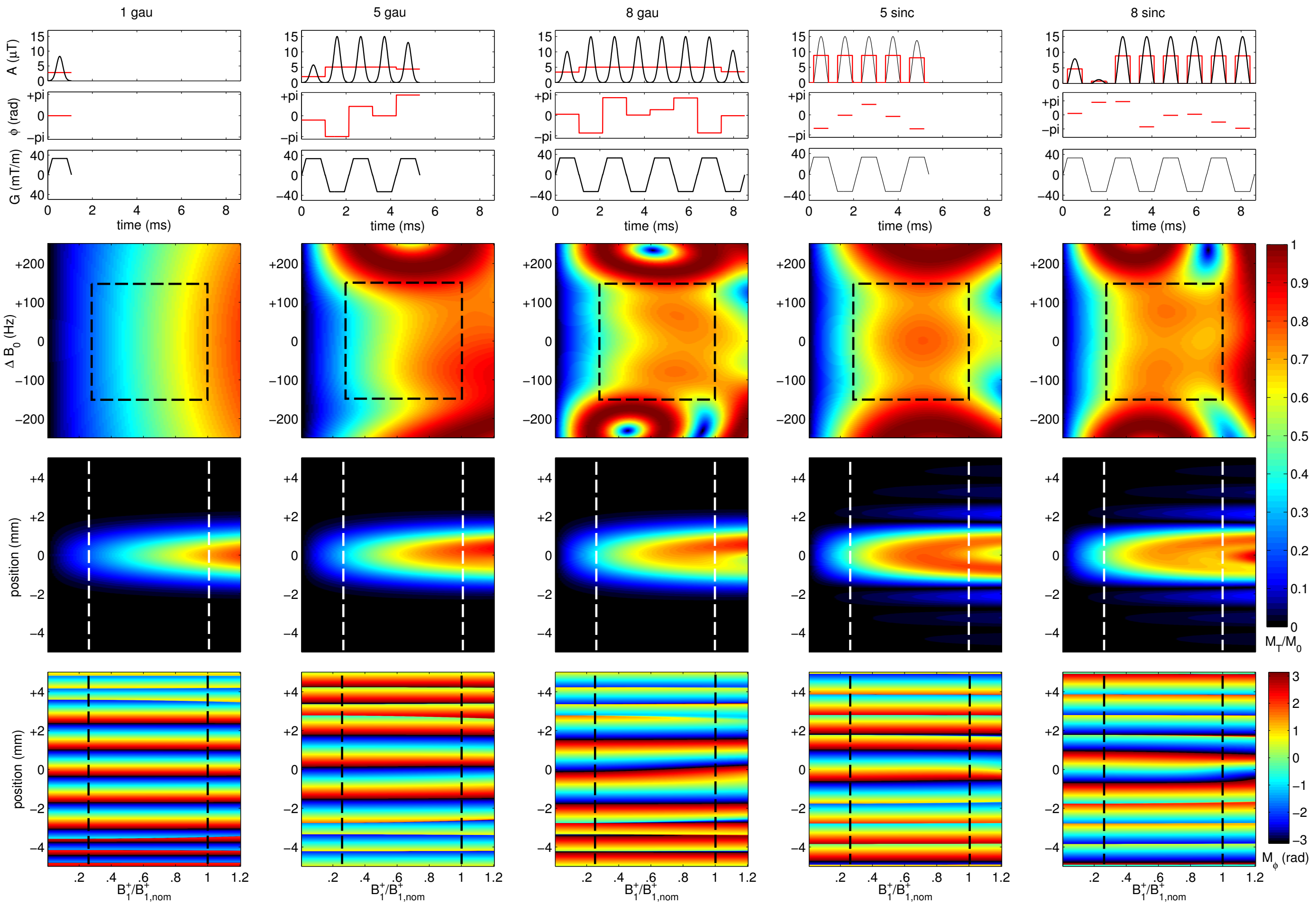

Figure 26: Amplitude, phase, and gradient modulation waveforms (top row, non-selective in red, slice-selective in black) for 45° pulses circled in Figure 25 and a single-Gaussian pulse (far left). Simulated magnetization responses for non-selective and slice-selective pulse configurations are shown in the second and third rows, respectively. The last row indicates transverse magnetization phase in the slice-selective case. Dashed lines indicate optimization limits for the non-selective pulses.

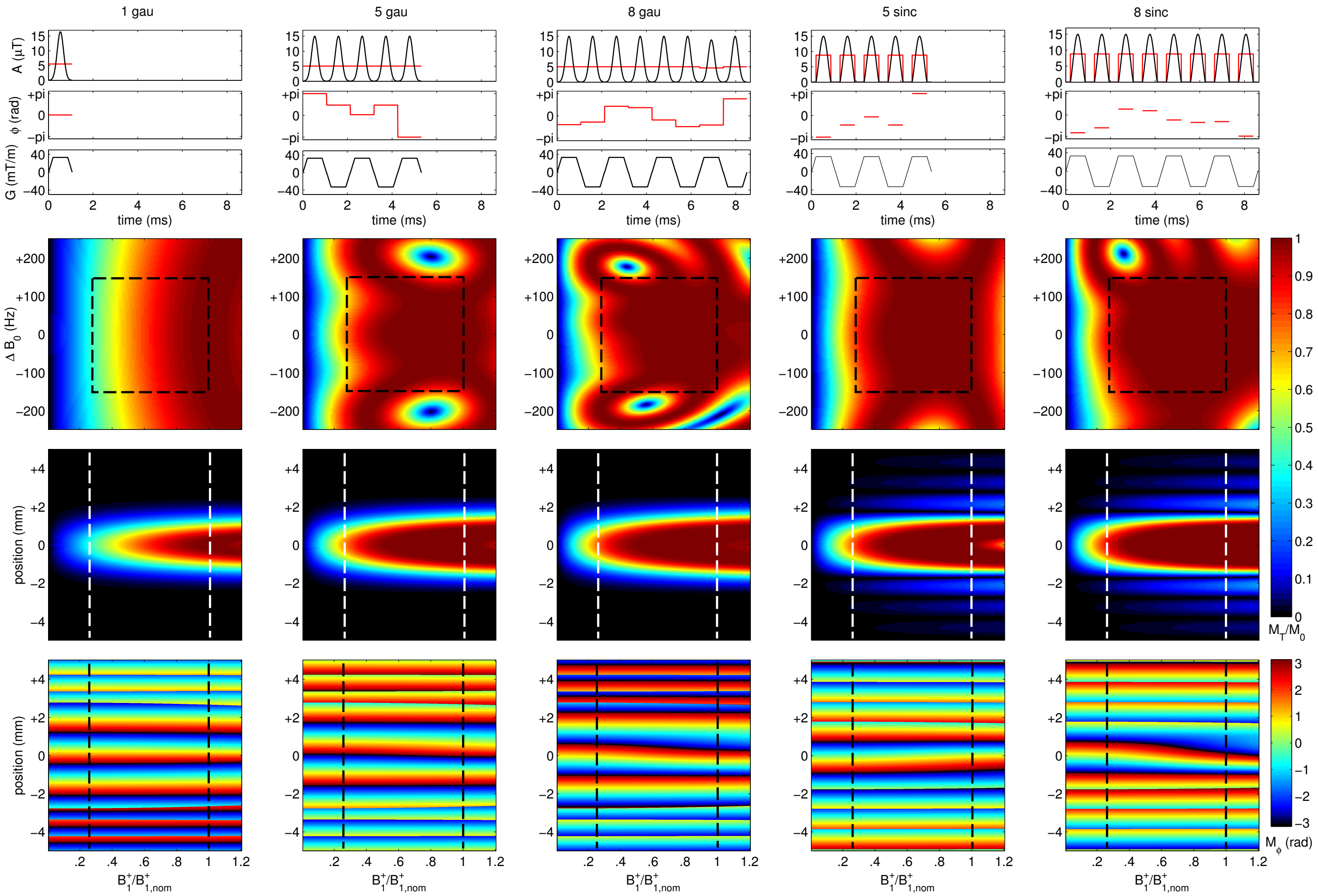

Figure 27: RF and gradient waveforms and magnetization plots as shown in Figure 26 but for selected 90° pulses. As for the corresponding 45° pulses, the SINC composites exhibit better immunity to field variations than do the GAU composites but at the expense of prominent lobes in the sidebands of the slice profiles. 90° pulses tend to result in more pronounced non-linear phase variations in the through-slice direction when compared to the corresponding 45° pulses of Figure 26.

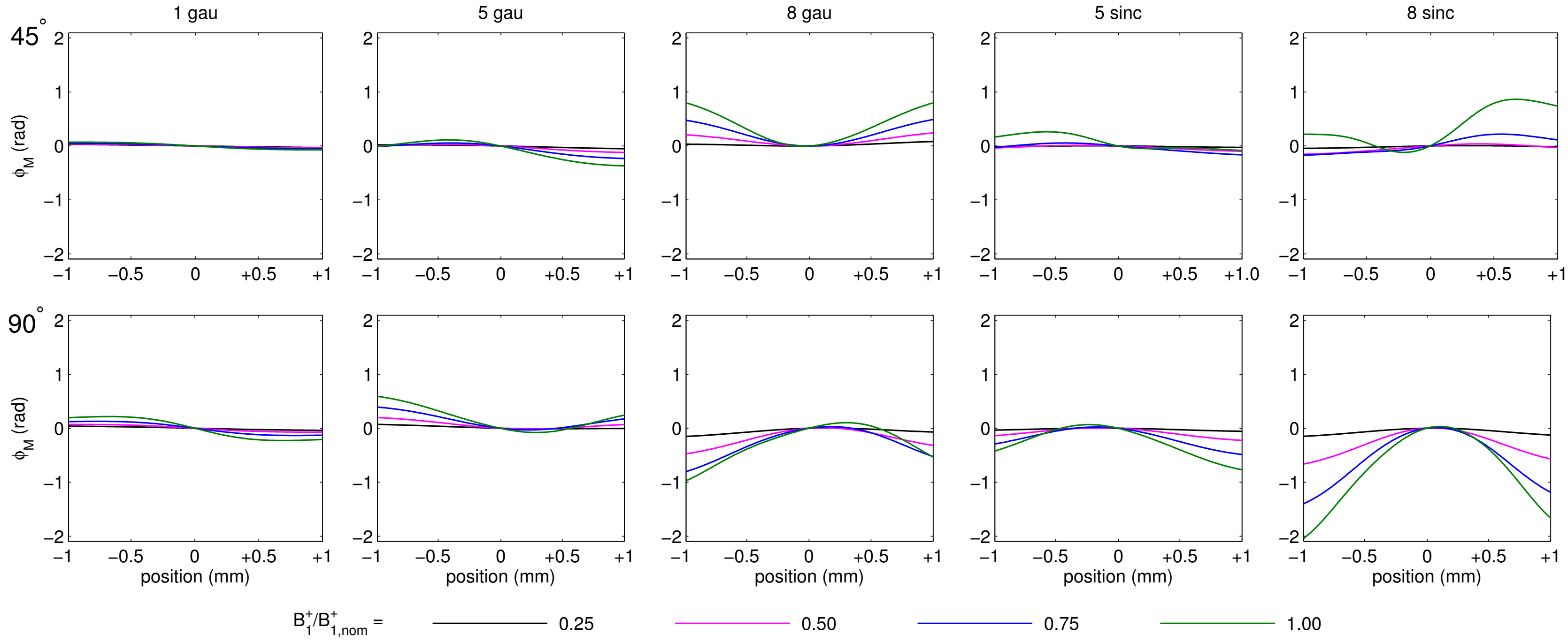

Figure 28: Non-linearities in through-slice phase of the transverse magnetization after application of rephasing gradients for both the 45° pulses highlighted in Figure 26 (top) and the 90° pulses highlighted in Figure 27 (bottom). Single-Gaussian pulses (far left) result in a low level of phase non-linearity which generally increases with the presence of additional sub-pulses. For a given pulse, the degree of phase non-linearity is strongly dependent on the relative magnitude of the B_1^+ field strength as indicated by different line colors, with most linear phase distributions always occurring at low B_1^+. Out of these examples, only the non-linearities exhibited by the 90° 8-SINC pulse are likely to become a serious performance issue in terms of signal loss, and, even in this case, the troublesome phase dispersions are confined to $B_1^+/B_{1,\text{nom}}^+ \geq 0.5$.

Results of simulations for a ±200 Hz range of off-resonance values are presented in Figures 29 and 30, which show $|M_T|$ and ϕ_{MT}, respectively. For the sake of brevity, results are only given for the 90° 5-GAU pulse. In Figure 29, $|M_T|$ appears largely stable out to the prescribed limits of ±150 Hz. At and beyond this range, the slice profile deteriorates significantly, mirroring non-uniformities in $|M_T|$ beyond the optimization region for the corresponding non-selective pulse as presented in Figure 27. This observation further validates the proposed methods for slice-selective, B_1^+-insensitive pulse design in that the ΔB_0 range targeted in the optimization of non-selective pulses translates to a slice-profile stability for the corresponding slice-selective pulses. The simulations of Figure 30 indicate that through-slice phase within the ±150 Hz optimization region remains highly linear at lower values of B_1^+. At higher B_1^+ values there exist some noticeable deviations from linearity such as at -50 Hz and -100 Hz; however, the largest deviations from linearity are confined to off-resonance values beyond the optimization range, suggesting that the optimization in some way promotes the desired behavior.

Another simulation result involves the effects of T_2^* decay on $|M_T|$ during execution of a given excitation pulse and are presented in Figure 31. Values of $|M_T|$ are calculated for a T_2^* value of 30 ms—which reflects an approximate whole-brain mean value at 7 T (59)—and are reported as ratios to the same quantities as calculated for $T_2^* = \infty$. For the single-Gaussian pulses, this ratio is $\sim 98\%$ due to the short duration (~ 1 ms) and is found to be independent of B_1^+ intensity. For the 5-GAU and 8-GAU pulses the ratio decreases to $\sim 90-95\%$ and $\sim 80-90\%$, respectively, with $|M_T|$ loss

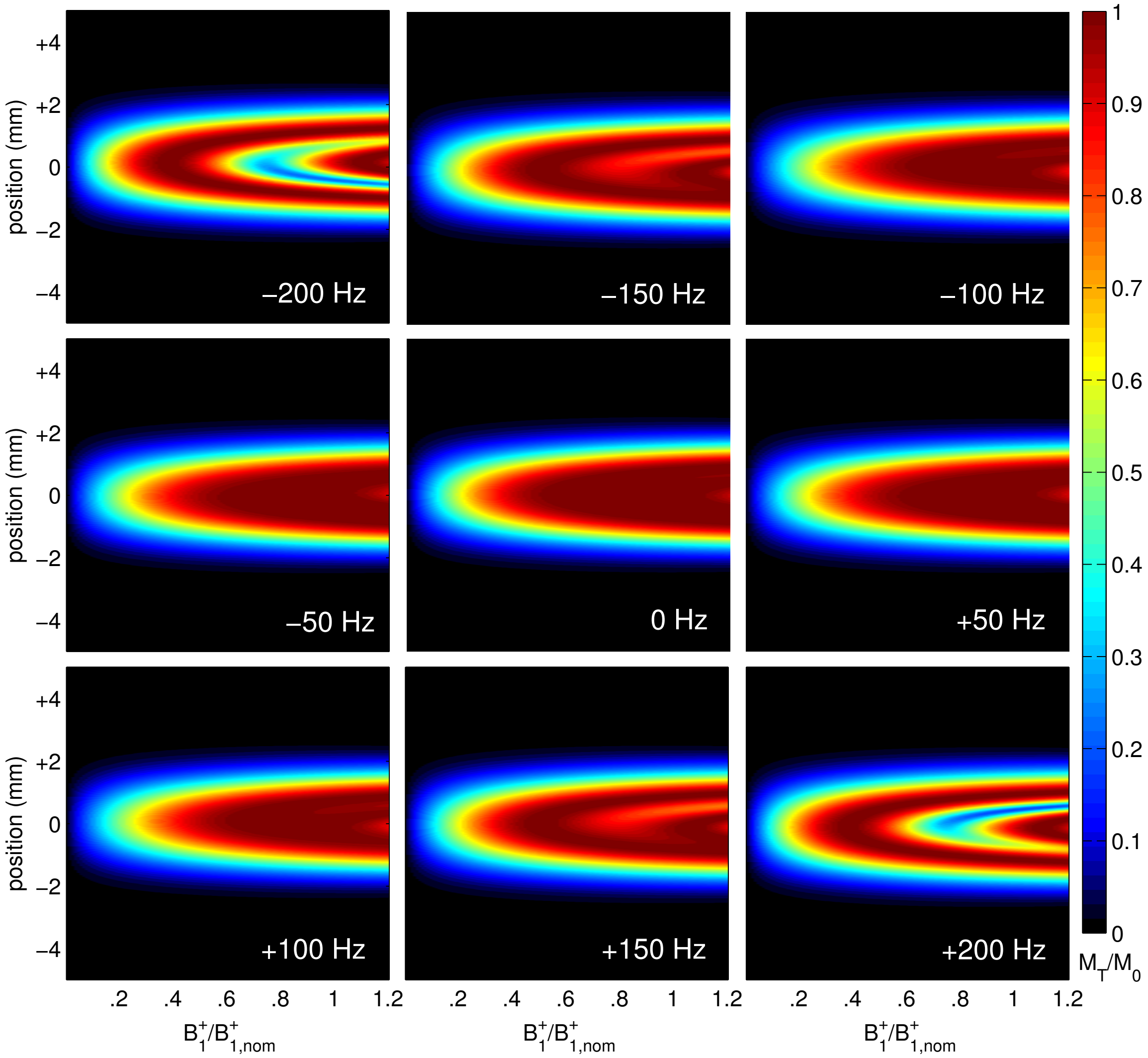

Figure 29: The slice profile of the 90° 5-GAU pulse as simulated for a ±200 Hz range of frequency offsets. The profile is largely unchanged within the optimization region of ±150 Hz at and beyond which significant deterioration is noticeable. This behavior echoes the magnetization response for the corresponding non-selective pulse as shown in Figure 27.

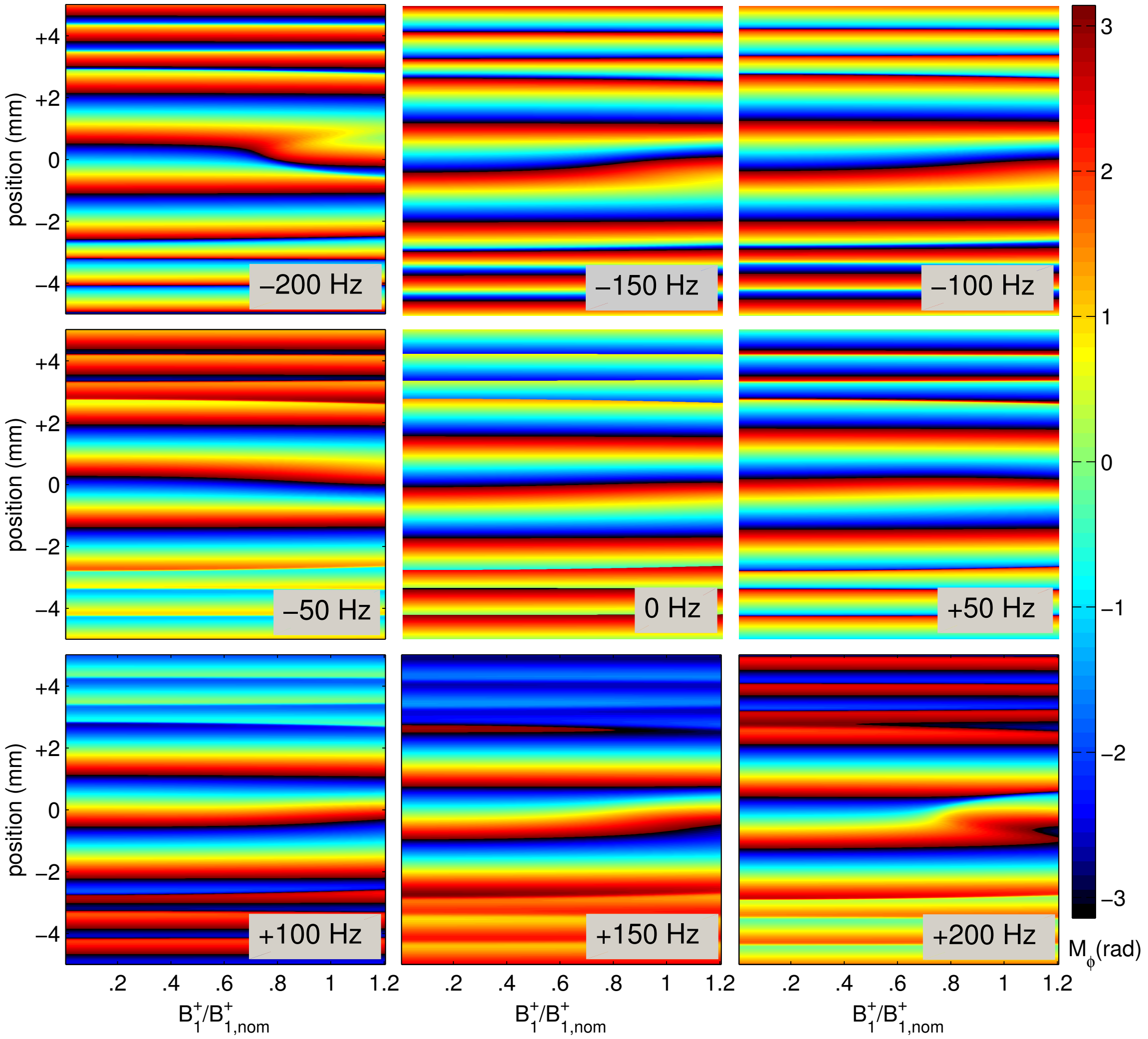

Figure 30: The transverse magnetization phase of the 90° 5-GAU pulse as simulated for a ±200 Hz range of frequency offsets. On-resonance, the phase is highly linear at all B_1^+ values. At and beyond the optimization limits of ±150 Hz, phase non-linearities become prominent, particularly at high B_1^+.

being noticeably greater for the 90° pulses. While additional loss of $|M_T|$ is expected for the 8-GAU pulses relative to the 5-GAU pulses due to the extended duration, the same effect is not necessarily expected to depend on α^T. Furthermore, SINC pulses appear to be less susceptible to T_2^* decay as compared to their GAU counterparts with $|M_T|$ being reduced to $\sim 93\%$ for the 5-SINC pulses and to the the range of $\sim 90-98\%$ for the 8-SINC pulses. Again, the 45° pulses appear to suffer from less $|M_T|$ losses as compared to the 90° pulses, although the difference is quite subtle in the case of 5-SINC pulses. For all composite pulses, $|M_T|$ loss depends to some degree on B_1^+, with the greatest losses generally occurring at high values of B_1^+. Possible explanations and implications of the above T_2^*-related phenomena are left for the discussion.

The final results not originating from experiment take the form of Table 4.3.1 in which values related to practical implementation of the pulses highlighted in Figures 26 and 27 are reported. Given here are the quantities described at the end of Section 4.2.2, namely, $\int |A|^2 \, dt$, $T_{R,\min}$, and $T_{E,\min}$. These numbers imply that composite pulses result in significantly (anywhere from $\sim$ 5 to 25 times) higher SAR values for a given T_R and minimal possible echo times that are approximately doubled as compared to the single-Gaussian pulses of the nominal same flip angle.

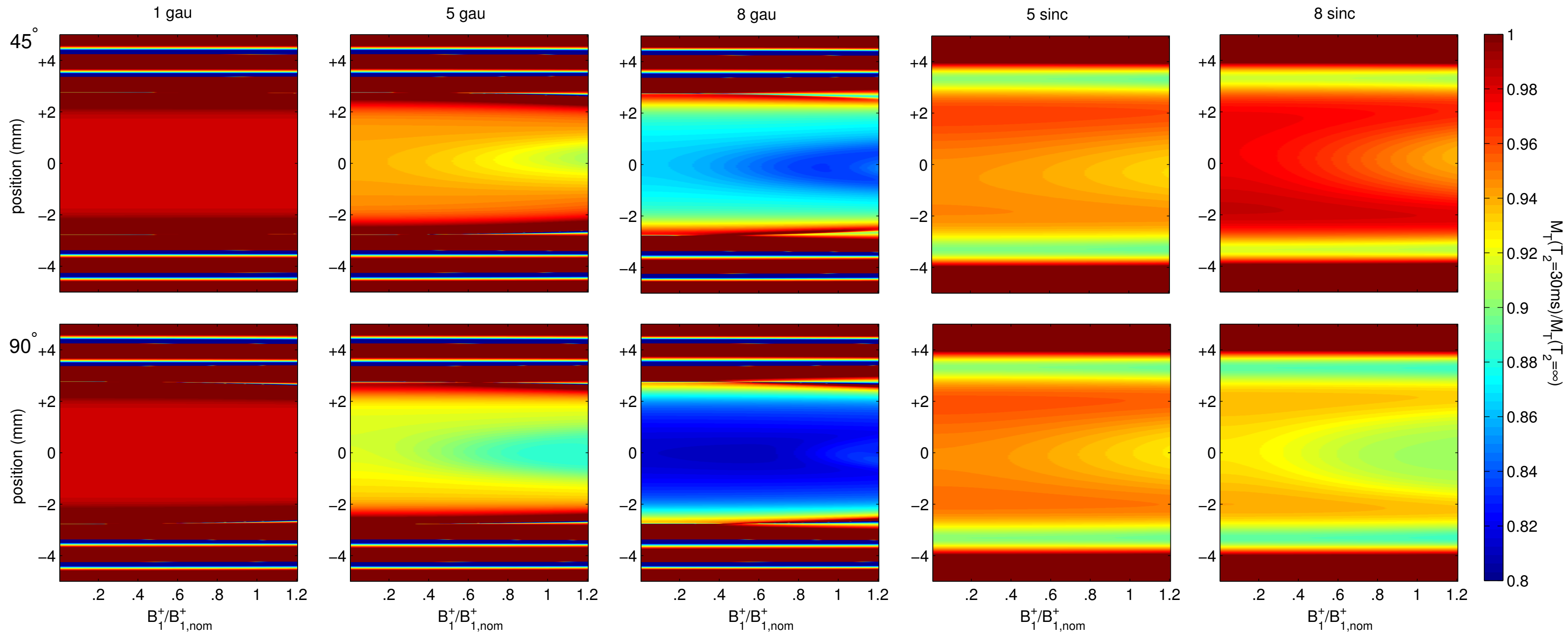

Figure 31: Simulations of T_2^*-related transverse magnetization losses for the same 45° (top row) and 90° (bottom row) pulses highlighted in Figures 26 and 27, respectively. The ratio of transverse magnetization as calculated for a T_2^* value of 30 ms to that calculated for infinite T_2^* is shown for each pulse. Simulations are performed for the slice-selective versions of each pulse and reflect transverse magnetization loss as a function of both position in the slice-selection direction and relative B_1^+ magnitude. Results indicate that loss of transverse magnetization due to T_2^* decay is not a simple function of total pulse duration, particularly in the case of SINC waveforms. Moreover, T_2^* effects are dependent on the target flip angle and suggest that the ordering of sub-pulses with different amplitudes strongly affects the susceptibility of composite pulses to transverse magnetization decay.

Table 4.3.1: Various quantities pertaining to the practical limitations of selected pulses. Included are the integral of the square of the amplitude modulation (a value directly proportional to SAR, Equation 4.2.5), the minimum possible T_R value given a SAR constraint of 3 W/kg, and the minimum possible T_E value as described in Section 4.2.2. SAR levels of composite pulses are as much as 25 times greater than single-Gaussian excitations of the same flip angle, a characteristic that is one of the greatest drawbacks to the proposed pulse designs.

α^T	pulse	$\int \lvert A\rvert^2\,dt$ ($\mu\mathrm{T}^2 \cdot \mathrm{s}$)	$T_{R,\min}$ (ms)	$T_{E,\min}$ (ms)
45°	1-GAU	0.017	10	1.6
	5-GAU	0.221	135	2.7
	8-GAU	0.392	239	3.7
	5-SINC	0.324	197	2.7
	8-SINC	0.421	257	3.7
90°	1-GAU	0.068	42	1.6
	5-GAU	0.283	173	2.7
	8-GAU	0.445	271	3.7
	5-SINC	0.335	204	2.7
	8-SINC	0.536	327	3.7

4.3.3 Experiments

Maps of ΔB_0, B_1^+, and B_1^- are given in Figure 32 for the same axial slices through the phantom and the brain for which all other experimental results were obtained.

Phantom results for the same 10 pulses highlighted in Figures 26 and 27 are presented in Figure 33. Included are both normalized signal intensities and calculated values of the flip-angle dependent function F as described in Section 4.2.3. While signal intensity variations are visibly reduced through the use of B_1^+-insensitive composite pulses (relative to those of the single-Gaussian pulses), it should be noted that even the most uniform excitation would still result in large signal variations due to inhomogeneities in the B_1^- field. Signal intensity remains useful for judging the ulti-

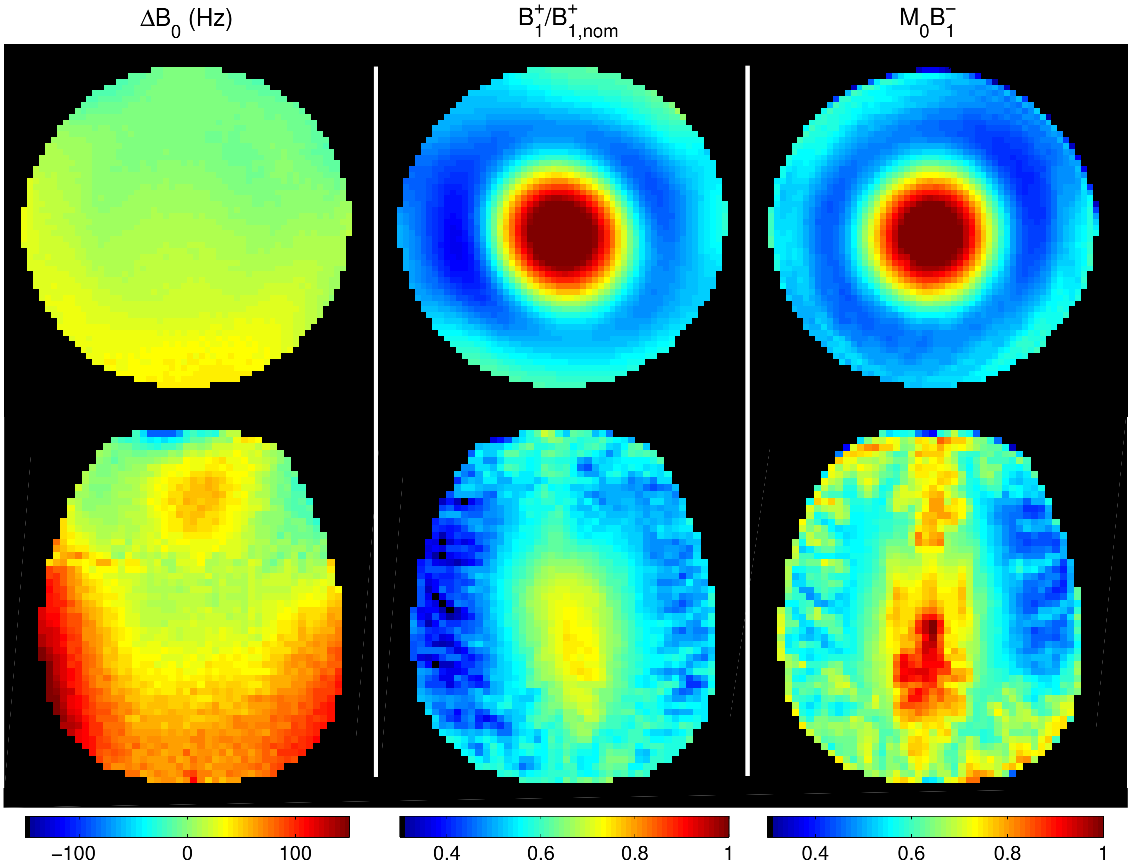

Figure 32: Measured maps of the static field (left, in units of Hz), the transmitted RF field (middle, in units of the nominal field strength), and the received RF field (right, including any M_0 contributions and given in arbitrary units) are shown for central axial slices through a spherical phantom (top) and the human brain (bottom). The static and transmitted RF field measurements were used to determine the relevant ranges of field inhomogeneities to be targeted by composite pulse optimizations while the received RF field measurements were used in calculations to determine flip-angle uniformity.

mate effects of excitation pulses, but calculated maps of F are a more direct indication of pulse performance. By this latter measure, all tested composite pulses result in improved excitation uniformity with respect to single-Gaussian pulses; however, in accordance with simulations, results do vary significantly depending on pulse composition and target flip angle. For example, F maps for 90° pulses generally display less variation than those for 45° pulses. This observation is partially explainable by the fact that the `sin` function upon which F depends has a small first derivative with respect to its argument in the vicinity of 90°—thus, a given range of actual flip angles translates to a smaller range of F values around 90° than it does at lower angles. This property of the `sin` function is responsible for the fact that the 90° single-Gaussian pulse exhibits less variation in F than does its 45° counterpart and demands that the most meaningful comparisons of F maps can be made only for pulses of a given target flip angle.

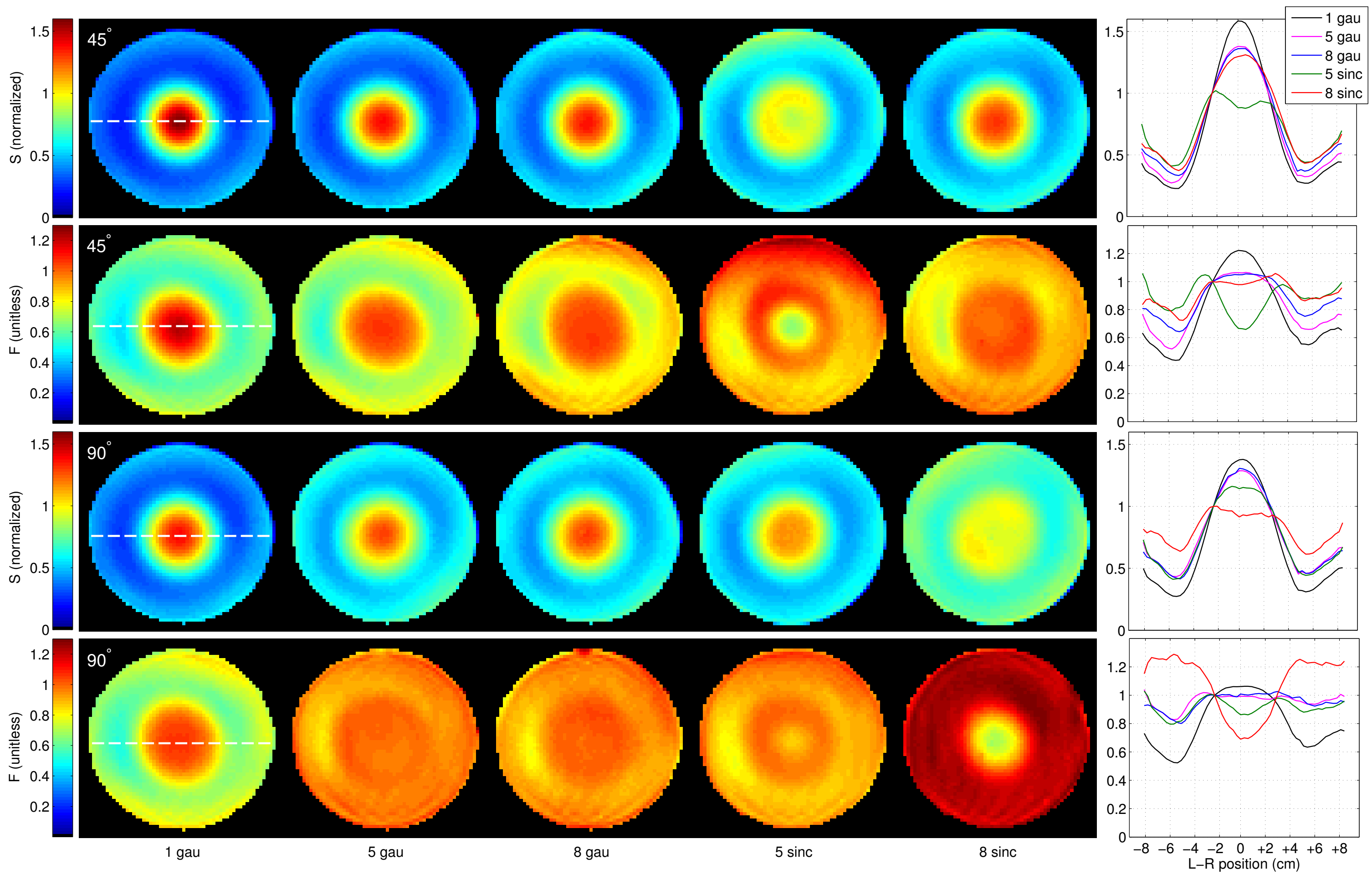

Figure 33: Experimental results in the phantom at 7 T for the same 45° (top two rows) and 90° (bottom two rows) pulses highlighted in Figures 26 and 27, respectively. Normalized signal intensity is shown in the first and third rows and the flip-angle dependent function F (Equation 4.2.6) in the second and fourth rows. Pulse compositions are indicated at the bottom of each column. Line profiles reflect values along the position indicated by dashed lines in the far left column.

When comparing pulse performance for a given flip angle, the SINC pulses are found to produce more uniform excitations at 45° than do the GAU pulses—a result predicted by simulations. While all composite excitations are fairly uniform in the 90° case, the degree of performance variations anticipated from cost function values for the corresponding pulses are not observed. This effect could be caused by a combination of increased levels of non-linear through-slice phase for the SINC pulses and the fact that cost function values reflect performance at a wider range of ΔB_0 values than actually occurs in the phantom. In at least two cases—namely the 45° 5-SINC and 90° 8-SINC pulses—prominent "holes" can be seen in the center of the F maps. These features are likely due to non-linear phase at high B_1^+ in the latter case and a combination of non-linear phase and slice profile deterioration in the former case. While such magnetization responses are certainly undesirable in the context of slice-selective excitation, it should be noted that the B_1^+ values reached in the center of the phantom (Figure 32) are beyond the corresponding optimization limits.

Slice profiles as measured in the phantom are presented in Figure 34 for the same 10 pulses detailed previously. Results are consistent with the simulated slice profiles shown in Figures 26 and 27. As expected, the composite GAU pulses produce slice profiles comparable to those of the single-Gaussian pulses. Broadening at the base of the SINC profiles likely results from the presence of the side-lobes indicated in the simulations—a feature becoming more prominent at the higher flip angle. In general, results indicate that the targeted slice thickness of 2 mm is achieved in all cases and that highly selective excitation is possible with the proposed composite pulse designs.

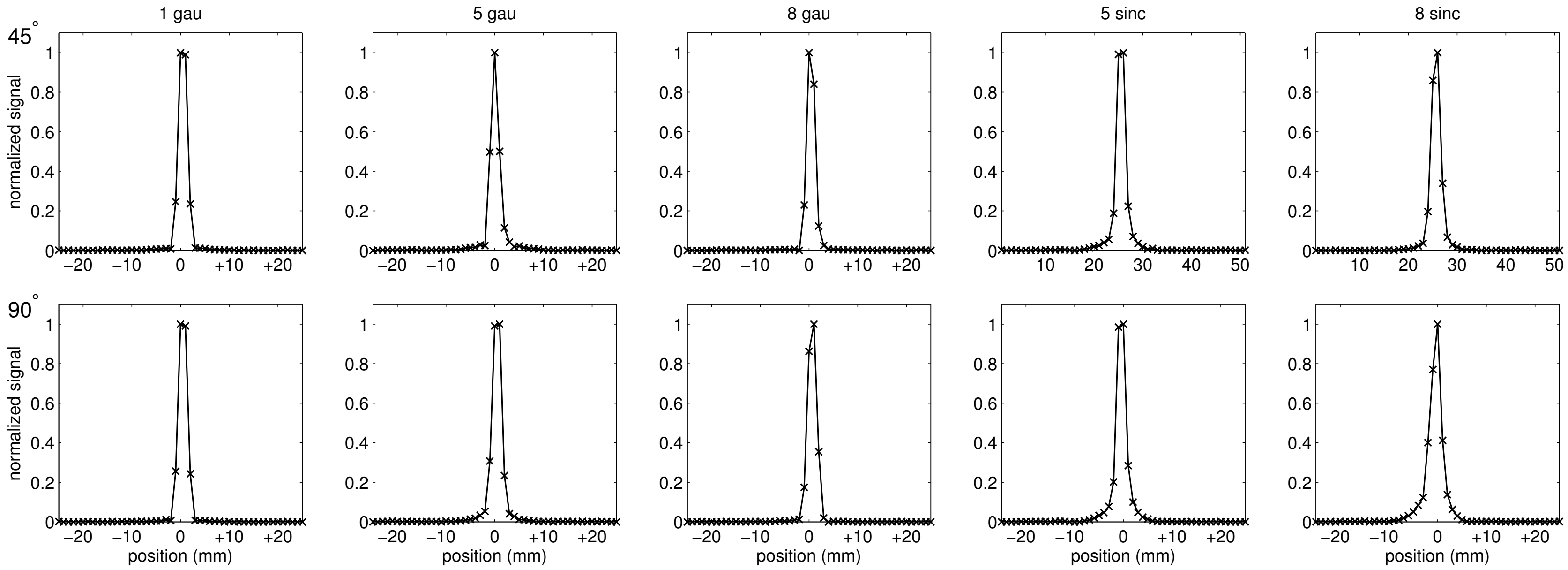

Figure 34: Slice profiles measured in the phantom for the same 45° (top row) and 90° (bottom row) pulses highlighted in Figures 26 and 27, respectively. Pulse names are given at the top of each column. In all cases, slice thicknesses of $\sim 2\,\mathrm{mm}$ are attained. In agreement with the simulations of Figures 26 and 27, gau composites produce cleaner slice profiles than sinc composites, with the latter resulting in a widening of the slice profile base which is likely due to the presence of the side lobes evident in Figures 26 and 27 for the corresponding pulses.

In vivo results for the 45° and 90° 5-SINC pulse including normalized signal intensities and calculated F maps are shown in Figure 35. Both composite pulses result in improved signal and flip-angle uniformity. To some degree, these improvement in excitation uniformity, while significant, do not appear as dramatic as they do in the phantom results. This is at least partially due to the range of B_1^+ variations in the featured slice of the brain being smaller than that in the central slice of the phantom (see Figure 32). Indeed, imaging volumes with reduced B_1^+ inhomogeneities are less susceptible to the benefits of B_1^+-insensitive pulse designs. Nevertheless, the composite pulses appear to be functioning as designed to improve flip-angle uniformity in the low-B_1^+ regions of the brain. Moreover, the resulting excitations appear to be stable with respect to the range of B_0 variations existing in the brain—an observation that helps establish the validity of enforcing ΔB_0-stability through the proposed pulse design protocol.

4.4 Discussion

Simulations and experiments have both validated the proposed pulse design methods as means for the construction of slice-selective composite pulses with inherent insensitivity to the field variations observed in the human brain at 7 T within the relevant hardware limitations. While the pulses selected for in-depth analysis in this study are suitable for immediate practical application, the results of the study are illuminating as to the potential of future designs with a similar objective. To be discussed in this section are considerations for the shape of individual sub-pulses followed by interpretations and implications of the observed non-linear phase, T_2^* susceptibility,

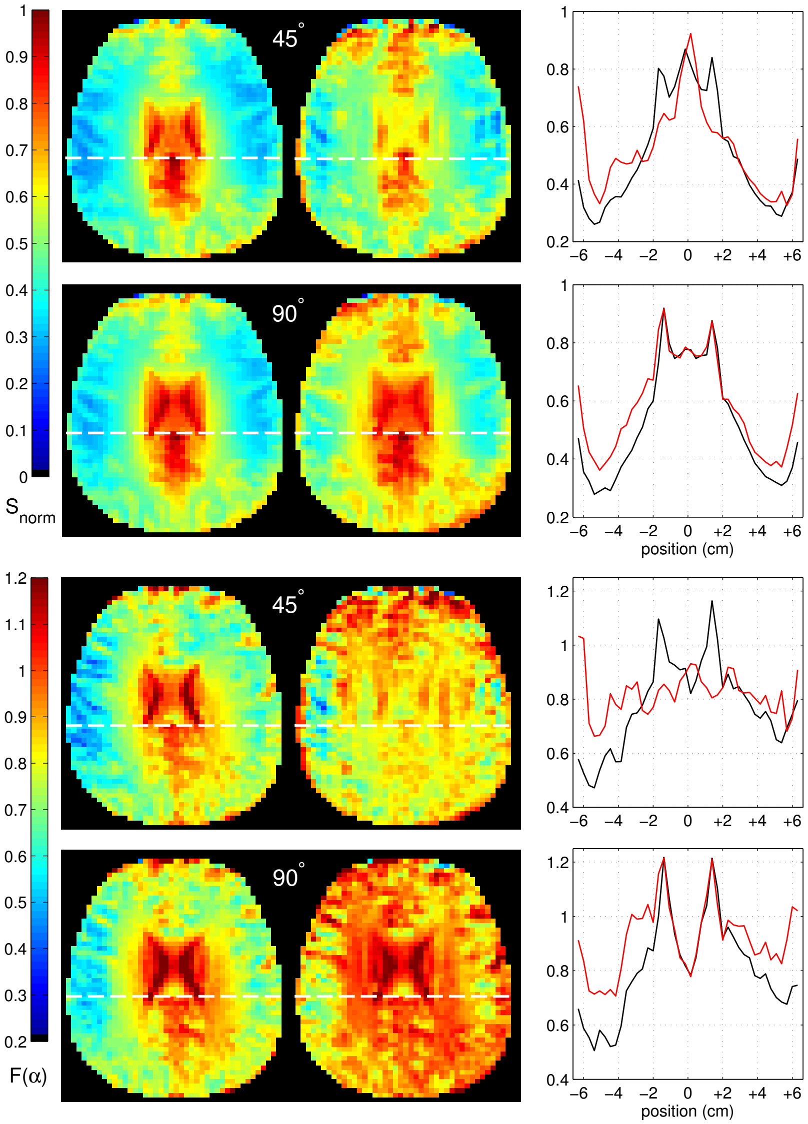

Figure 35: Normalized signal (top set) and the flip-angle dependent values F (bottom set) for a central axial slice of the brain at 7 T. Results are shown for the single-Gaussian pulses (left) and the 5-SINC composite pulses (right) with nominal flip angles of 45° and 90°, as indicated. Line profiles (black for single-Gaussian and red for 5-SINC pulses) reflect values along the dashed lines found in the same row. As with the corresponding phantom results (Figure 33), signal intensities for composite pulses remain considerably inhomogeneous due largely to variations in the B_1^- field; however, F values indicate a significantly more uniform excitation in the case of the optimized pulses. The more modest improvements in flip-angle uniformity as compared to that observed in the phantom for the same composite pulses are likely a result of the relatively smaller range of B_1^+ values occurring in the given slice (see Figure 32).

and SAR limitations. Finally, a discussion of the context of this work and relevance to other studies with similar objectives is presented.

Results indicate that composite pulses constructed from SINC sub-pulses outperform their GAU counterparts in terms of insensitivity to field variations. This inherent advantage of the SINC sub-pulses designed for this study arises from a $\sim 10\%$ larger integrated amplitude that such waveforms have when compared to GAU sub-pulses with the same peak amplitude and bandwidth. The larger integrated amplitude translates to higher allowed amplitudes in the constrained optimization of non-selective pulses and, thus, improved performance in terms of the cost function of the optimization. Drawbacks associated with the use of SINC pulses include the existence of side lobes in the slice profiles and the required dead time during gradient slew period. Such characteristics of SINC sub-pulses raise the question of how to re-design sub-pulses such that the integrated amplitude is maintained while the slice profile is sharpened without considerable increase in duration. Many strategies such as the Shinnar-Le Roux (SLR) algorithm (58) and frequency modulation could potentially be employed to customize the frequency profiles of sub-pulse waveforms. Furthermore, time-dependent gradient modulation techniques (14) could allow for incorporation of the gradient slew period in the design of RF sub-pulse modulations. Interesting future work might involve an analysis of the advantages of such alternative RF strategies in the context of designing sub-pulses for use in composite waveforms. Findings would certainly be relevant to single- and multi-channel sparse spokes pulses, as are the results of the present study.

Regardless of the intended shape of sub-pulses, the target flip angle has been shown to affect the optimization performance for the pulses presented in this study for total pulse durations $\gtrsim 10\,\mathrm{ms}$, with lower flip angles proving more challenging (Figure 25). The fact that this trend is most prominent at longer durations points to the initial conditions of the optimization as a possible culprit. If random amplitudes are assigned to each sub-pulse prior to the optimization, pulses that require higher integrated amplitude for best performance might be intrinsically favored. Thus, restricting the peak amplitude of the random initial conditions for pulses with long durations and low α^T values could potentially result in better optimization performance. While this is a possible explanation for the observed optimization results, it is also noteworthy that $|M_T|$ values as plotted in Figures 26 and 27 will always appear biased to α^T values near 90°. This effect is due to both the symmetry and slope of the `sin` function (and thus the transverse magnetization given the relationship $|M_T| = |\sin\alpha|$) around 90° and is independent of the actual cost function values given that cost is defined in terms of flip angle and not transverse magnetization. This observation suggests that the cost function would possibly be more suitably defined in terms of $|M_T|$ rather than α.

Other results of this study also suggest that alterations to the optimization protocol could result in improved insensitivity to variations in B_1^+ and ΔB_0. For example, the fact that optimized sub-pulse amplitudes are usually near the maximum allowed values suggests that fixing amplitudes and only using sub-pulse phases in the minimization problem might ease the demands on the optimization algorithm and result in better performance, or at least performance that is less sensitive to initial conditions. The use of peak amplitudes higher than $15\,\mu$T, as is currently supported by the coil/amplifier combinations of some human scanner manufacturers, would certainly result in improved optimization performance, although it appears from the results of this study that non-linear phase might become more of an issue in that scenario. Higher gradient slew rates ($> 166\,$T/m/s) are also currently available on human scanners and will only serve to shorten the duration of the SINC version of proposed composite pulses, thereby making pulses less susceptible to T_2^* effects. The possible detriments of higher slew rates are generation of image artifacts caused by gradient-induced eddy currents and an increased likelihood of peripheral nerve stimulation (24).

Yet another change to the optimization protocol that might prove advantageous is a customization of the B_1^+-ΔB_0 optimization grid to include only combinations of those values that are actually observed in the brain at 7 T. The optimization grid could be guided by either subject-specific field maps or by field map data collected for multiple subjects. In the latter case, the resulting optimized pulses would retain the desirable quality of being applicable to any subject without the need for subject-specific field mapping. In either case, the performance of composite pulses would likely be improved due to the reduced number of unique B_1^+-ΔB_0 combinations being considered in the optimization (56).

The levels of non-linear phase reported in Figure 28 are not prohibitive in terms of signal loss; however, the fact that non-linear phase increases with the number of sub-pulses suggests that the effect may become a more serious limitation for pulses of longer duration (e.g., $> 10\,\mathrm{ms}$). Since the largest phase dispersions for a given pulse are always observed at the highest B_1^+ values, the objective of this study to increase signal in low-B_1^+ regions is inherently less susceptible to this undesirable effect, albeit the gain of signal in low-B_1^+ regions does come with a price of signal loss in the highest-B_1^+ regions in some cases. While some phantom results appear to exhibit signal losses due to non-linear phase in the highest-B_1^+ regions (Figure 33), the same is not evident for *in vivo* results (Figure 35). This discrepancy is due to the higher peak B_1^+ values observed in the phantom (Figure 32) and suggests that signal loss from non-linear phase is not a major concern for practical human brain imaging—at least for the $< 10\,\mathrm{ms}$ pulses subjected to detailed analysis in this study. Nevertheless, the level of non-linear phase in this class of composite pulses might be controllable through alteration of the cost function and may be relevant to future studies. For example, it is possible, yet untested, that enforcing zero phase dispersion in the cost function (as is done in the optimizations of Skinner et al., e.g., (74; 75)) could favorably affect the degree of non-linear phase in the resulting slice-selective pulses or at least improve the ΔB_0 stability of phase linearity (Figure 30). Another potential approach would be to address non-linear phase at the level of sub-pulse modulation designs, e.g., through the use of the SLR algorithm. Non-linear phase is clearly present in the Gaussian sub-pulses employed in this study (Figure 28), so it is no surprise that composites of such waveforms result in amplified phase dispersion. Improving phase response of sub-pulse modulations would certainly improve the phase response the composite waveforms. Furthermore, with regard to a slightly different imaging application, it is noteworthy that, if the pulse designs of this study were implemented in a 3D imaging sequence for which slab selection was accomplished through a reduction in selection gradient strength, the practical requirements on the degree of phase linearity would be greatly reduced since intra-voxel dephasing, rather than intra-slice dephasing, would be the limiting factor. To make such an application practical, however, SAR limitations would have to be incorporated into the cost function, a scenario for which performance is yet to be verified.

The signal losses due to T_2^* decay reported in Figure 31 offer insights into the advantages of certain pulse constructions. Clearly, SINC pulses result in reduced $|M_T|$ losses with respect to comparable GAU pulses. This observation also holds true with respect to GAU pulses of shorter total duration (e.g., compare the 8-SINC pulses to 5-GAU pulses in Figure 31). Thus, while SINC composites may incur the penalties of additional non-linear phase and higher SAR, the use of this sub-pulse modulation has the considerable advantage of reduced susceptibility to T_2^* effects. The reduced T_2^* loss of SINC pulses is likely accomplished through the higher average amplitude (with respect to GAU pulses) during application of the pulse. Thus, the composite pulse is better capable of exploiting the spin-locking behavior permitted by the Bloch equation such that transverse phase dispersion is reduced. Such effects have been previously documented in the context of adiabatic pulses, with the resulting decay of $|M_T|$ being characterized by the time constant $T_{2,\rho}$ (52; 51).

The observation that 45° composite pulses are less susceptible to collective T_2

effects than are comparable 90° pulses (Figure 31), suggests that the amplitudes of sub-pulses at the beginning of the composite pulse are critical in determining the amount of T_2^* decay that is possible. As evidenced by the 8-SINC pulses in Figures 26 and 27, the reduced amplitude of the first two sub-pulses of the 45° pulse (with respect to the 90° pulse) appears to translate to the reduced $|M_T|$ loss exhibited by the corresponding pulses in Figure 31. This explanation is plausible given that small amplitude sub-pulses produce less transverse magnetization thus limiting the amount of decay that is possible through T_2 mechanisms. In future composite pulse designs, attention could be given to this process so as to limit the susceptibility of the resulting pulses to T_2 effects, with relevant constraints even being incorporated into the optimization. Such design considerations are relevant not only to other B_1^+-insensitive composite pulses (e.g., (10; 56; 61; 54)) but also to sparse spokes pulses designed for either single or multiple transmission channels (89).

For long-T_R GRE imaging applications at 7 T, the SAR levels associated with the composite pulses of the present study will not likely be prohibitive, with the most likely compromise being a reduction of the number of slices in a multi-slice acquisition. Even in the case of the 45° pulses, which would likely be utilized in a steady-state sequence with shorter T_R, an Ernst angle of 45° and a T_1 of 1.5 s (as is typical for the brain at 7 T (66)) imply an ideal T_R of $\sim$ 500 ms, a value greater than the highest $T_{R,\min}$ values reported in Table 4.3.1. Thus, all of the 45° pulses presented in Table 4.3.1 are immediately implementable in such a single-slice GRE imaging sequence without the need for SAR-related adjustments. Sequences used at 7 T with shorter

T_R values would demand lower α^T values, and, at some point, SAR constraints would need to be enforced in the optimization to ensure the practicality of composite pulses for such applications. Of course, SAR constraints are likely to adversely affect pulse performance; however, the severity of this trade-off and the degree to which it affects the usefulness of the resulting composite pulses has not yet been investigated.

While discussion up to this point has focused on an explanation of results and the future design considerations motivated by these results, the remainder of the discussion is devoted to establishing the relevance of this work in the context of other studies. The presented pulse design scheme does provide a significant advantage over some existing field-insensitive designs in that selective excitation of thin slices is achieved in tandem with prescribed degrees of B_1^+- and ΔB_0-insensitivity. Furthermore, pulses can be designed and implemented for use on any subject or slice orientation without the need for subject-specific field mapping, as is the case for multi-transmit RF shimming and sparse spokes designs. Additionally, the pulse design protocol allows for designation of arbitrary flip angles and, in most cases, results in only small deviations from a linear through-slice phase of the transverse magnetization. There exist pulse designs for addressing these needs individually, but the strength and usefulness of the proposed design is the incorporation of all such requirements into a single protocol. For example, the SLR algorithm can be used for generating slice-selective waveforms but has not been incorporated into a design scheme addressing the need for both B_1^+- and ΔB_0-insensitivity. Adiabatic pulses have been used for achieving immunity to B_1^+ variations for more than 20 years but either lack the capacity for linear phase and arbitrary flip angles (e.g., hyperbolic secant pulses (72; 73)) or are not suitable for slice selection (e.g., BIR-4 pulses (76)). Also, adiabatic pulses are designed in a very different way—ensuring B_1^+-insensitivity for RF amplitudes above a certain value that fulfills the adiabatic condition—whereas the pulses of this study were designed for B_1^+-insensitivity within a particular RF amplitude range, without concern for the adiabatic condition (i.e., the cost function involves only the net flip angle produced by the pulse). Thus, improvements in flip-angle uniformity may be realized even when design constraints make the adiabatic condition impossible to satisfy.

As mentioned in Section 4.1, Balchandani et al. (1) recently provided a means for transforming non-selective adiabatic pulses such as BIR-4 into spatially selective pulses with similar B_1^+-insensitivity. While this design can presumably be extended to arbitrary flip-angle excitation, there may exist significant differences in the performance limitations of such pulses as compared to those produced in the present study. For example, Balchandani et al. have not yet reported on the success of arbitrary flip-angle excitation or on complications due to any non-linear phase resulting from their design. Furthermore, the design was demonstrated at 3 T rather than 7 T and for a slice thickness of 10 mm as opposed to the slice thickness of 2 mm achieved in the present study, thus its suitability for thin slice excitation at higher field strengths has not yet been demonstrated. In theory, thinner slices can be produced by simply increasing the gradient strength; however, this increases the total pulse duration in order to accommodate the extended gradient slew periods and may increase the effects of T_2^* decay. While the present study has demonstrated that similar results in terms of B_1^+-insensitivity (at least for 90° pulses) can be accomplished in less than half the time, for a greater ΔB_0 range, and for thinner slices, the similar motivations of the two pulse designs calls for a future study in which both can be compared in the same context. Only in this way can the true advantages of the two designs be fairly illuminated.

While the adiabatic pulses of Balchandani et al. were perhaps the most similar design to that of that present study at the onset of this investigation, a more recent publication by Boulant et al. (8) describes what appears to be a more closely related class of spatially selective, B_1^+-insensitive pulses. Although derived from different principles and in the context of different hardware limitations, the two classes of pulse designs share the common goal of producing field-insensitive, slice-selective excitations for practical high-field imaging sequences. Moreover, the two methods employ numerically optimized composite pulses rather than adiabatic pulses. Such similarities in design demand direct future comparisons such that the pros and cons of the varying strategies can be better understood. Also, during preparation of the present manuscript, Balchandani et al. published their findings on designs involving adiabatic pulses produced in conjunction with the Shinnar-Le Roux algorithm (2). This scheme allows for control over non-linear phase and slice profiles while enforcing B_1^+-insensitivity through the adiabatic condition. While this appears to be another promising design for producing slice-selective, B_1^+-insensitive pulses, further comparisons of the pulse designs of Balchandani et al., Boulant et al., and the present study are left as the subject of future research. The quantity of recent work toward the same goal, however, does indicate a rising interest in such pulse designs and justifies the continued investigation of these varied approaches to producing B_1^+-insensitive excitation pulses for use with a single transmission channel.

4.5 Conclusion

The results of this study indicate that construction of composite slice-selective pulses via the described techniques can be used to significantly improve flip-angle uniformity in the human brain at 7 T. The desired levels of B_1^+- and ΔB_0-insensitivity are specified in the design process, thus making the resulting pulses suitable for use without the need for subject-specific field mapping and RF calibrations. Composite pulses with the desired characteristics can be used to achieve slice thicknesses of $\sim 2\,\mathrm{mm}$ in as little as $\sim 5\,\mathrm{ms}$ when operating within the hardware limitations of a commercial 7 T human scanner. While performance in terms of insensitivity to field variations tends to increase with pulse duration, non-linearities in the through-slice magnetization phase were also found to become larger with duration and may limit the usefulness of longer composite pulses. The study also demonstrated how pulse performance depends on the structure of the component sub-pulses, with central `sinc`-lobe waveforms offering stronger immunity to field variations and T_2^* effects but rougher slice profiles as compared to Gaussian modulations. The proposed pulse designs may prove useful in many contexts in which insensitivity to field variations is desired in conjunction with selective excitation.

CHAPTER V

DESIGN AND EVALUATION OF NON-SELECTIVE REFOCUSING PULSES

5.1 Introduction

Imaging protocols reliant upon the non-selective refocusing of transverse magnetization (e.g., 3D versions of spin-echo (SE), turbo spin-echo (TSE), and gradient spin-echo (GraSE) (21) sequences) usually employ either block- or sinc-shaped refocusing pulses resulting in flip angles that scale with the integral of the transmitted RF (B_1^+) field intensity. Adiabatic pulses such as BIR-4 (76) and hyperbolic secant composites (31) provide refocusing options that are somewhat insensitive to B_1^+ variations but are largely avoided in ultra-high field ($\geq 7\,\mathrm{T}$) human imaging due to off-resonance performance issues and high specific absorption rates (SAR). Although comparisons of refocusing pulses have been presented previously (e.g., by Poon and Henkelman (61)), the performance and SAR limitations of a wide range of applicable refocusing pulses remain untested in the context of 7 T human brain imaging. In response to the need for practical, B_1^+-insensitive refocusing pulses for use in ultra-high field human imaging, the present study was undertaken with the goals of (1) identifying pulse designs that could potentially improve refocusing performance at 7 T within practical limits of SAR, (2) modifying or redesigning such pulses to achieve performance that is specifically focused on 7 T brain imaging, (3) simulating the refocusing characteristics of chosen pulses given actual measurements of static (B_0) and B_1^+ field distributions at 7 T, and (4) measuring the signal gains obtainable with the selected pulses. The results of this work will assist in the selection of suitable refocusing pulses for given applications as well as form a basis for establishing the performance limits of practical refocusing pulses executed on a single transmission channel.

To ensure a degree of practicality, we limited our studies to refocusing pulses with relatively short durations and low SAR levels. Considered pulse designs include: a 180° block pulse; a block pulse with nominal flip-angle tuned for 7 T; a three-part composite of block pulses (44) and its 7 T-tuned counterpart; BIR-4 pulses (76) of various duration ($\Delta T \lesssim 5\,\mathrm{ms}$); numerically optimized BIR-4 pulses (53) of the same durations; composites of block pulses numerically optimized for both generalized and subject-specific field inhomogeneities (54); and a rendition of the version-S pulse (60). With the exception of the single block design, all pulses included in the study incorporate some level of B_1^+-insensitivity and are thus particularly relevant to high-field applications. Theoretical pulse performances were evaluated by simulating magnetization response over generic grids of B_0 and B_1^+ variations as well as throughout the given imaging volumes by using field maps obtained experimentally. The actual measured signal gains resulting from each pulse are reported relative to the signal obtained using a 180° block pulse in the context of a 3D SE sequence with a single-shot, echo-planar imaging (EPI) readout in a 17 cm spherical phantom at 7 T. Selected pulses were also evaluated by the same means in the human brain at 7 T. In all cases, the excitation pulse was the same—a Gaussian-modulated sinc pulse with a 90° nominal flip angle. For analysis, pulses were grouped into *short*, *moderate*, and *long* duration categories so as to facilitate both the comparison between pulses with similar SAR values and the selection of pulses best suited for particular applications. In addition to in-depth performance comparisons, this study used measured field maps to establish the theoretical maximum signal gains (again, relative to a 180° block pulse) achievable in a phantom and the brain for a SE sequence at 7 T. Furthermore, this study served to investigate the numerical optimization of refocusing pulses through a cost function defined in terms of the principal components of magnetization and applied this strategy to both BIR-4 and block-composite waveforms.

At the lowest SAR levels, adjusting the nominal flip angle of a single block refocusing pulse was found to result in significant signal gains as averaged over the whole imaging volume and represents a simple yet effective way to improve refocusing performance at 7 T. While numerical optimization of BIR-4 waveforms provides the most notable improvements over status quo BIR-4 implementations when pulse duration is shortest, it was at intermediate duration ($\Delta T \sim 2.5\,\text{ms}$) that BIR-4 pulses outperformed all others. Numerically optimized block-composite pulses, although competitive regardless of duration, provided the greatest performance boost when duration was long and SAR levels the highest. The cost function investigated in this study appears to perform similarly to the one used previously by Poon and Henkelman (60; 61). Furthermore, the practice of restricting optimization to subject-specific field values provided minimal benefit over the use of more generic ranges of the anticipated field inhomogeneities. While the novel pulse designs exhibited in this work do not provide the best refocusing solutions in all contexts, it should be emphasized that the driving force behind this study was not to provide new designs promising improved performance but to illuminate and catalog the actual performance variations among the many relevant and competing pulse designs currently available.

5.2 Theory

Following an excitation pulse of arbitrary phase, an RF pulse with a 180° flip angle and arbitrary phase will result in complete refocusing of transverse magnetization lost to T_2' decay. Underlying this statement are the assumptions that the refocusing pulse is executed at a time $T_E/2$ halfway between the excitation and signal acquisition and that B_1^+ field inhomogeneity does not alter the effective flip angle of the pulse. When variations in the B_1^+ field are present, a refocusing pulse with a nominal flip angle (β_0) of 180° will result in in an actual rotation angle given by $\beta_0 \cdot B_1^+/B_{1,\text{nom}}^+$, where $B_{1,\text{nom}}^+$ is the nominal, unaffected RF field strength. In these terms, on-resonance signal intensity for a SE sequence with repetition time T_R can be expressed as

$$S_{\text{SE}} = M_0 B_1^- \left|\sin\left(\frac{\alpha_0 B_1^+}{B_{1,\text{nom}}^+}\right)\right| \sin^2\left(\frac{\beta_0 B_1^+}{2B_{1,\text{nom}}^+}\right)\left(1 - e^{-T_R/T_1}\right) e^{-T_E/T_2}\,, \tag{5.2.1}$$

where M_0 is the equilibrium magnetization, B_1^- is the relative intensity of the RF field associated with reception, α_0 is the nominal flip angle of the RF pulse used for excitation, T_1 is the time constant of longitudinal relaxation, and T_2 is the time constant of transverse relaxation due to non-reversible mechanisms. This relationship implies that, for a given value of $B_1^+/B_{1,\text{nom}}^+$ and a fixed value of α_0, the maximum achievable signal occurs in the event that $\beta_0 \cdot B_1^+/B_{1,\text{nom}}^+ = \pi$ radians (i.e., the actual flip angle of the refocusing pulse is 180°).

When comparing signal intensities resulting from sequences with the same excitation pulse, the same T_E, and the same T_R but different refocusing pulses (as is the case in the present study), all factors in Equation 5.2.1 are common with the exception of the β-dependent argument of the $\sin^2$ function. Thus, the ratio of two such signals $S_{\mathrm{SE},1}$ and $S_{\mathrm{SE},2}$ is expressible as

$$\frac{S_{\mathrm{SE},1}}{S_{\mathrm{SE},2}} = \frac{\sin^2\left(\beta_{0,1} B_1^+/(2B_{1,\mathrm{nom}}^+)\right)}{\sin^2\left(\beta_{0,2} B_1^+/(2B_{1,\mathrm{nom}}^+)\right)} . \tag{5.2.2}$$

The ratio of the signal from an ideal refocusing pulse (for which $\beta_0 \cdot B_1^+/B_{1,\mathrm{nom}}^+ = \pi$) to that of any other refocusing pulse is then given by

$$\frac{S_{\mathrm{SE,ideal}}}{S_{\mathrm{SE,BLK}}} = \frac{1}{\sin^2\left(\beta_0 B_1^+/(2B_{1,\mathrm{nom}}^+)\right)} . \tag{5.2.3}$$

In the present study, we use Equation 5.2.3 along with measurements of $B_1^+/B_{1,\mathrm{nom}}^+$ to calculate 3D maps of the largest possible signal gains achievable in reference to a block-shaped pulse with a 180° nominal flip angle. Signal ratios (again in reference to the block-shaped pulse with $\beta_0 = 180°$) for all pulses evaluated in this study are determined through experiment but reflect the value expressed in Equation 5.2.1 with $S_{\mathrm{SE},2}$ representing the signal of the $\beta_0 = 180°$ pulse.

For the purposes of performance simulation and numerical optimization, we adopt a three-dimensional magnetization space (M_x, M_y, M_z) in which reversal of the transverse magnetization phase implies a change in direction of one of the transverse magnetization components, e.g., (M_x, M_y, M_z) is changed to either $(M_x, -M_y, \pm M_z)$ or $(-M_x, M_y, \pm M_z)$. Such phase reversal can be achieved either by reflection or rotation operators. The $(M_x, -M_y, M_z)$ and $(-M_x, M_y, M_z)$ phase reversals are achieved by reflection across the $(M_x\, M_z)$ and $(M_y\, M_z)$ planes, correspondingly. Phase reversals $(M_x, -M_y, -M_z)$ and $(-M_x, M_y, -M_z)$ can be accomplished through the action of rotation operators—specifically by 180° rotations about the x and y axes, respectively. Due to the proclivity of the Bloch equation for rotation rather than reflection operations, we chose to express refocusing in this study in terms of the $(M_x, -M_y, -M_z)$ phase reversal, as the other rotation is equivalent. In addition to the completeness of this rotation operation, we evaluated simulated pulse performance in terms of the phase of the transverse magnetization as given by

$$\phi_M = \arctan\left(M_y^{\text{final}}/M_x^{\text{final}}\right) , \tag{5.2.4}$$

with the subscript M denoting a magnetization phase rather than an RF phase (ϕ_{RF}) and *final* indicating magnetization resulting from the action of a refocusing pulse on given initial magnetization components. Thus, for the ideal refocusing pulse, $\phi_M = -\pi/4$ when the initial transverse magnetization components are given by $(M_x^{\text{init}}, M_y^{\text{init}}) = (\frac{1}{\sqrt{2}}, \frac{1}{\sqrt{2}})$. Although a reversal of ϕ_M is equivalent to a 180° rotation about the x axis, the two measures for evaluating refocusing performance illuminate different imperfections of a given RF pulse and therefore serve as complementary analytic tools.

5.3 Methods

5.3.1 Pulse designs

The refocusing pulses chosen for evaluation in this study can be divided into three major classes that we refer to as (1) designs that have been previously established in the MR literature, (2) modified designs, and (3) numerically optimized designs.

Established designs

These widely implemented pulses have been established in the MR literature for achieving non-selective refocusing.

BLK This is the shortest duration 180° block-shaped pulse given a peak RF amplitude of $15\,\mu$T, thus resulting in a duration of 0.7 ms. The choice of peak amplitude (minimum duration) maximizes the pulse bandwidth, thus making performance less susceptible to B_0 variations.

COMP3 This is the three-part composite rotation ($90^\circ_x - 180^\circ_y - 90^\circ_x$, with subscripts indicating the axis of rotation) described in (44). The amplitude of each block-shaped component is again set to the maximum RF amplitude of $15\,\mu$T for maximum bandwidth and a total pulse duration of 1.4 ms.

BIR-4 These pulses are 4-part, B_1-insensitive rotations with 180° nominal flip angles ($\Delta\phi_{\mathrm{RF}} = \frac{3}{2}\pi$) defined according to the RF modulation function in reference (76). We chose to implement these pulses at three different durations: 1.5 ms, 2.5 ms, and 5.1 ms. In all cases, the maximum RF amplitude was set to $15\,\mu$T.

Modified designs

These pulses were modified from existing designs simply by increasing the flip-angle of the individual RF components.

$\mathbf{BLK_b}$ This pulse is identical to BLK but with a flip angle of 270°. The 50% increase in duration allows for a 180° rotation for the $B_1^+/B_{1,\mathrm{nom}}^+$ value (0.67) corresponding to the approximate mean of the $B_1^+/B_{1,\mathrm{nom}}^+$ distribution in the human brain at 7 T.

$\mathbf{COMP3_b}$ This pulse is similar to the $\mathrm{BLK_b}$ pulse in that nominal flip angles of the components were increased by 50% relative to the COMP3 pulse, resulting in a $135^\circ_x - 270^\circ_y - 135^\circ_x$ rotation.

$\mathbf{VS_b}$ This pulse is the 16-component 5.4π composite pulse (version-S) by Poon and Henkelman (60) following modification by means of increasing the flip angle of each component by 50%. The duration of each component ($806.4\,\mu$s) was determined by setting the RF amplitude of the highest flip-angle sub-pulse to $15\,\mu$T resulting in a total duration of 12.9 ms.

Numerically optimized designs

The third class of pulses considered in this study consists of waveforms derived from in-house numerical optimization procedures. We applied these techniques to (1) composites of block-shaped pulses (similarly to (60) but with a different cost function) and (2) the BIR-4 waveforms described above. In the first case, it is the individual phases and amplitudes of the sub-pulses that are the subject of the optimization while, in the second case, parameters determining the overall amplitude, phase, and frequency modulation patterns are optimized. Optimization routines were written in Matlab (The MathWorks, Natick, MA) and employ the `fmincon` minimization function and the `interior-point` algorithm (a gradient-descent method) to handle minimization of the expression:

$$\frac{1}{n\,m}\sum_{i,j=1}^{n,m} W_{ij}\cdot\left(\left|M_{x,ij}^{\text{init}}-M_{x,ij}^{\text{final}}\right|+\left|M_{y,ij}^{\text{init}}+M_{y,ij}^{\text{final}}\right|\right)\ , \tag{5.3.1}$$

where i and j are indices on the B_1^+-ΔB_0 ($n\times m$ dimensional) optimization grid on which the magnetization responses were simulated, and M_x^{init} and M_y^{init} correspond to the initial values of the initial transverse components of magnetization to be refocused. Optimizations were performed on the orthogonal basis of transverse magnetization vectors: $\mathbf{M}^{\text{init}}=(M_x^{\text{init}},M_y^{\text{init}},M_z^{\text{init}})=(1,0,0)$ and $\mathbf{M}^{\text{init}}=(0,1,0)$. Pulses optimized using this set of initial magnetizations will perform on any (allowed) linear combination of basis vectors, i.e., any initial magnetization vector. The components of $\mathbf{M}^{\text{final}}=(M_x^{\text{final}},M_y^{\text{final}},M_z^{\text{final}})$ were found through simulation of the Bloch equation for the refocusing pulse under consideration.

We considered two choices of the weighting matrix W. In the first case, which we refer to as the *low-*B_1^+ scheme, $(W)_{ij}=\left(B_1^+/B_{1\,\text{nom}}^+\right)_{ij}^{-1}$ such that pulse performance at low B_1^+ values was favored over that at high values. In the second case, which we refer to as the *subject-specific* scheme, W corresponds to a binary mask determined from a relative-density threshold of 0.015 applied to the actual 2D B_1^+-ΔB_0 histograms shown in Figure 36. Measurements of these field variations (further described below

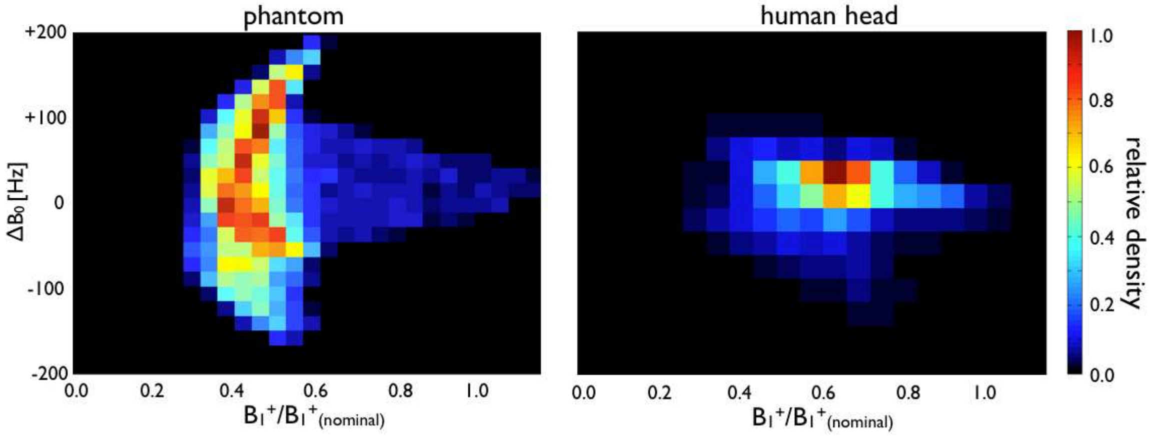

Figure 36: 2D histograms of relative voxel density over a grid of B_1^+ and ΔB_0 values as measured in an FBIRN phantom (left, static-field shimming *off*) and the human brain (right, static-field shimming *on*). These histograms are based on the field map data presented in Figure 37 but, collectively, for all slices in the imaging volumes. For both phantom and human, the field variations can be described roughly by ranges of [0.3-1.0] and $\pm150\,$Hz in the B_1^+ and ΔB_0 directions, respectively.

in Section 5.3.3) were performed in the same scan session during which all refocusing pulses were evaluated. For phantom scans, all static field shim currents were set to zero, such that B_0 variations across the phantom more resembled those anticipated in the human brain. For in-vivo human scans, second-order, projection-based static field shimming was used.

OPT$_{100}$ These 16-part composites of constant-amplitude/constant-phase sub-pulses resulted from the optimization problem described in Equation 5.3.1 (16 phases + 16 amplitudes = 32 free parameters) with the low-B_1^+ weighting scheme. The B_1^+-ΔB_0 optimization grid covered the field ranges of [0.2 1.0] and $\pm100\,$Hz (thus the subscript of 100) in the respective $B_1^+/B_{1,\text{nom}}^+$ and ΔB_0 directions as justified by field values measured in human brain at 7 T (Figure 36). Sub-pulse durations were fixed to either 96, 160, or 320 μs resulting in total pulse durations of 1.54, 2.56, 5.12 ms, respectively. Sub-pulse amplitudes were allowed to range from 0 to 15μT while phase was free to vary over the entire range of $\pm\pi$ radians.

OPT$_{\mathbf{cust}}$ These composite pulses were designed in an identical fashion as the OPT$_{100}$ pulses but using the subject-specific, **cust**omized weighting scheme.

OPT$_{\mathbf{BIR\text{-}4}}$ Numerical optimization of the 6 parameters determining the amplitude, phase, and frequency modulation of the BIR-4 waveforms (76) was performed on the same B_1^+-ΔB_0 grid as used for the OPT$_{100}$ pulses with the low-B_1^+ weighting scheme. Three BIR-4 pulses of varying length (1.54, 2.56, and 5.12 ms) and maximum amplitude of 15 μT were designed in this way.

5.3.2 Simulation methods

All simulations of magnetization response to RF pulses in this study were based on a rotation matrix formulation of a relaxation-independent form of the Bloch equation (3). Details are provided in Appendix B. Pulses constructed from constant-phase/constant-amplitude sub-pulses (such are the majority of pulses in this study) naturally lend themselves to such calculations. Pulses with continuously varying modulations (i.e., the BIR-4 and OPT$_{\text{BIR-4}}$ pulses) were divided into discrete, 6.4 μs steps over which the phase and amplitude were considered to be constant. This step length is the electronics dwell time of our digital RF amplifier, and the discretization accurately reflects the way in which continuous waveforms are executed on such hardware. For all pulses, magnetization response to the appropriate composite of k sub-pulses, each with constant phase and amplitude, was modeled as a series of rotations (R_j, where $j = 1, \ldots, k$). With each rotation corresponding to one of the k individual sub-pulses, the collective operation of all such components of a pulse is described by

$$\mathbf{M}^{\text{final}} = R_k R_{k-1} R_{k-2} \ldots R_1 \mathbf{M}^{\text{init}}\,. \tag{5.3.2}$$

The final magnetization resulting from each of the refocusing pulses was calculated on a grid of B_1^+-ΔB_0 values with ranges of ± 250Hz and $[0.2, 1.2]$ in the ΔB_0 and $B_1^+/B_{1\,\text{nom}}^+$ directions, respectively. This was done for two different initial conditions corresponding to the orthogonal components of transverse magnetization: $\mathbf{M}^{\text{init}} = (1, 0, 0)$ and $\mathbf{M}^{\text{init}} = (0, 1, 0)$.

5.3.3 Imaging protocols

All experiments were conducted on a 7 T Philips Achieva whole body scanner (Philips Healthcare, Best, the Netherlands) based on a Magnex (Varian Medical Systems, Palo Alto, CA) 90cm magnet. RF transmission and reception was carried out with a single-channel, quadrature volume head coil from Nova Medical (Wilmington, MA). All phantom experiments used a 17 cm dielectric phantom from FBIRN (Function Biomedical Information Research Network) with relaxation constants of $T_1/T_2^* = 1150/42\,\text{ms}$ as measured at 7 T. For *in vivo* experiments, one person (male, 33 y.o.) was recruited from the community, and written informed consent was obtained according to the guidelines of the local Institutional Review Board.

Static field maps were obtained in the phantom and human subject using a 3D GRE sequence with a double-echo acquisition ($\Delta T_E = 1\,\mathrm{ms}$). Scan resolution was $3 \times 3 \times 5\,\mathrm{mm}$ within a $240 \times 192 \times 135$ field of field in the anterior-posterior, right-left, and foot-head directions, respectively. $B_1^+/B_{1,\mathrm{nom}}^+$ maps were calculated via a voxel-by-voxel fitting of signal intensities from a multi-flip-angle, multi-slice, single-shot GRE-EPI scan ($T_R = 5000\,\mathrm{ms}$) (30; 89). Slices were oriented in the transverse plane with a 5 mm thickness and a 5 mm gap between slices. The in-plane axial resolution and field of view matched those of the B_0 scan. The same projection-based, second-order volume B_0 shim currents were used during collection of all *in vivo* data. For phantom experiments, B_0 shim currents were set to zero so that susceptibility of the various refocusing pulses to off-resonance effects could be more clearly determined. Shim currents and the RF drive scale remained unchanged for the series of experiments in the same imaging volume. B_0 maps were used to perform EPI distortion corrections of the B_1^+-mapping data (35).

Imaging experiments for evaluating refocusing pulse performance employed a SE-EPI sequence composed of an excitation pulse, a refocusing pulse, and a slice-by-slice, single-shot EPI acquisition. The excitation waveform—a Gaussian-modulated sinc pulse with a nominal flip angle of 90°—was executed in the presence of a weak selection gradient so as to reduce signal from outside the designated imaging volume. Refocusing pulses were executed such that the center of the waveform corresponded to the sequence time $T_E/2 = 25\,\mathrm{ms}$. Echo and repetition times were fixed to $T_E/T_R = 50/5000\,\mathrm{ms}$ with only the RF waveform of the refocusing pulse being modified between subsequent experiments. As a simple indication of SAR, the minimum T_R allowed by the scanner was recorded when using each refocusing pulse. These values are listed in Table 5.4.1.

5.4 Results and Discussion

Results with integrated discussion are presented in three parts: 1) a short description of the phantom and human brain static and RF field maps with a discussion of the ways these measurements facilitate interpretation of experimental results; 2) presentation of the simulation data for all considered refocusing pulses with a discussion of the utility and practical limitation of such simulations; 3) presentation of phantom and in vivo experimental results exhibiting the varying degree of improvement in signal intensity observed for the refocusing pulses under consideration.

5.4.1 B_1^+ and B_0 field measurements

The distributions of B_1^+ and ΔB_0 field measurements throughout the fBIRN phantom and the human brain are shown in Figure 36, and actual field maps are shown in Figure 37. Major differences between phantom and human B_1^+ and ΔB_0 field distributions can be summarized as follows: for the phantom, $B_1^+/B_{1\text{nom}}^+$ values are concentrated slightly lower (mean ~ 0.4) than for the human head (mean ~ 0.6) with much wider distribution in this direction, i.e., [0.2,1.2] for the phantom and [0.3,1.0] for the human head; the distribution of ΔB_0 values for the phantom is wider, i.e., [-200 Hz,+200 Hz] vs. [-100 Hz,+100 Hz], respectively. These two facts tend to suggest that the performance limits are pushed further in the case of the phantom experiments.

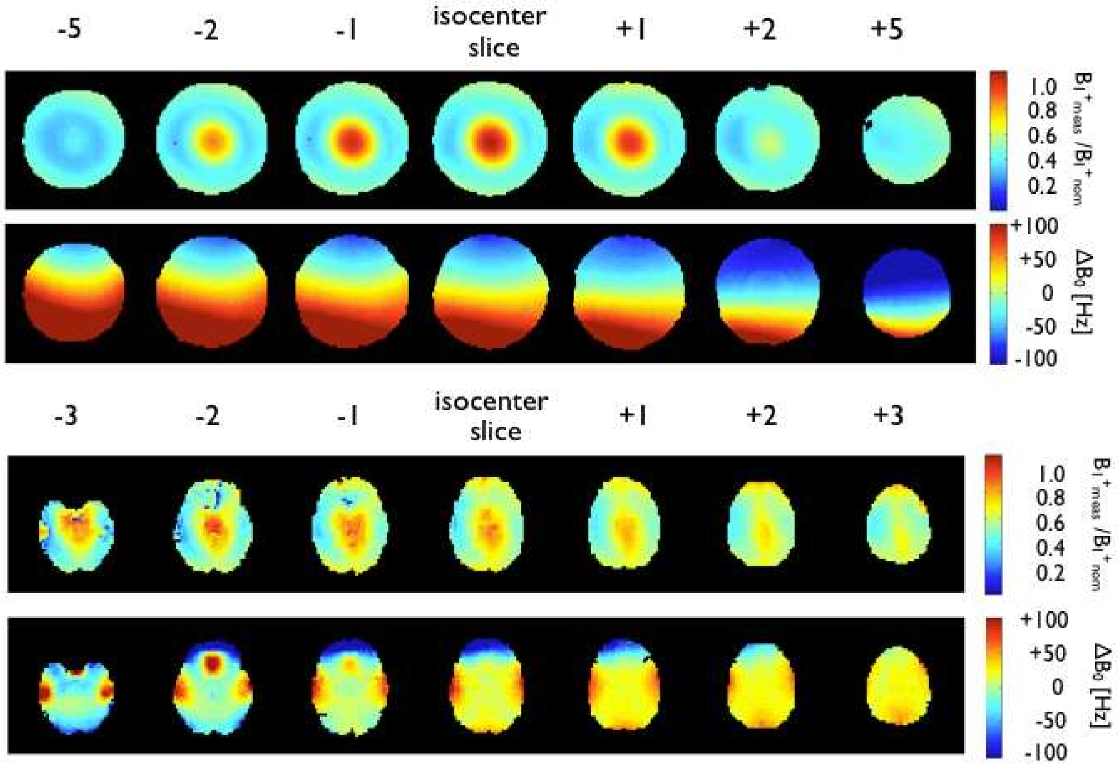

Figure 37: Maps of the B_1^+ and ΔB_0 fields as measured in the phantom (top) and the human brain (bottom). Phantom measurements are obtained with static-field shim currents set to *zero* such that the overall range of B_0 variations is more similar to that encountered when imaging the human brain. Shown here are field maps for a sample of axial slices in each imaging volume with offset from the central slice indicated at the top of each column in terms of slice number. Slices are 5 mm thick such that an offset of +2 slices is equivalent to +10 mm along the z-direction in the magnet.

Specifically, refocusing performance at values of $B_1^+/B_{1\,\mathrm{nom}}^+ > 1$ in the phantom may not be relevant to the human subjects while the same is true for $|\Delta B_0| \gtrsim 100\,\mathrm{Hz}$.

According to Equation 5.2.3, maps of the B_1^+ field were used to calculate the maximum possible signal gains in reference to the case in which a BLK pulse is used for refocusing. These results are shown for multiple slices of the phantom and the brain in Figure 38 and indicate that average signal gains of $\sim 150\%$ ($\sim 100\%$) are

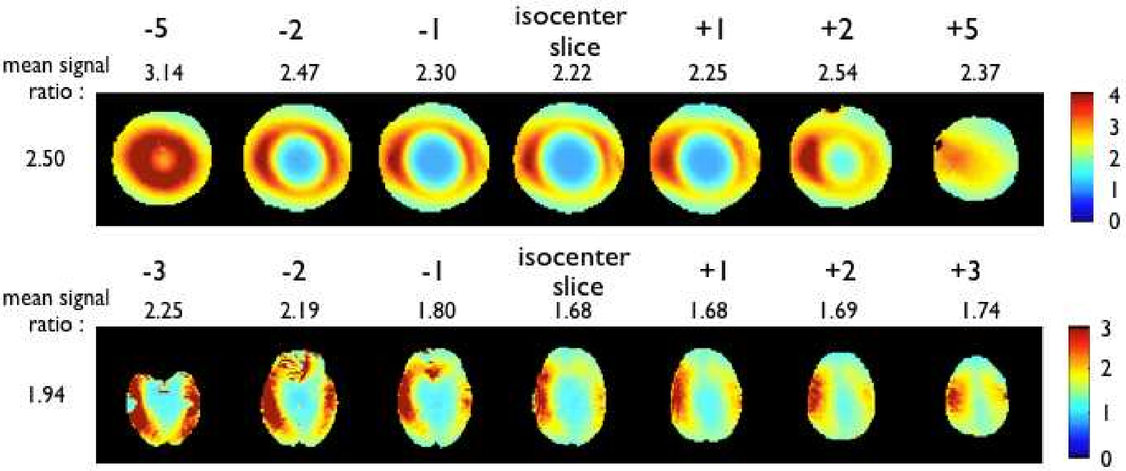

Figure 38: Theoretical maximum-signal ratios as calculated from Equation 5.2.3 given the B_1^+ maps appearing in Figure 37. These results indicate that adjustment of refocusing pulses in a spin-echo sequences at 7 T can result in localized signal gains (with respect to the signal obtained via a 180° block or sinc pulse) of no more than $\sim 200\%$ (brain) or $\sim 300\%$ (phantom). Slice-wise averages are given above each ratio map with the whole-volume averages given at left. Slice numbering is the same as in Figure 37. Maximum-signal ratios serve as a basis for evaluating refocusing pulse performance by allowing for the comparison of measured signal gains to an ideal. Values are relevant to refocusing pulses transmitted on single or multiple channels.

possible in the phantom (brain). Potential local signal gains in regions of the lowest measured B_1^+ values are roughly twice as large.

5.4.2 Simulations

Waveforms of all of the discussed pulses are shown in Figures 39-42 together with maps of the transverse components of refocused magnetization on the B_1^+-ΔB_0 grid. The binary mask obtained from the relative-density map in the phantom (Figure 36) was overlaid on each of the magnetization maps to show the most relevant regions on the B_1^+-ΔB_0 grid. Moreover, we have included histogram distributions of the components of refocused magnetization (M_x^{final} and M_y^{final}) within the mask. The histogram data were weighted by the contributions of B_1^+-ΔB_0 points extracted from the relative density distribution of 3D B_1^+-ΔB_0 data for the fBIRN phantom (Figure 36) with static field shim currents set to zero. Finally, maps and histogram distributions of phase of the refocused magnetization are shown for all of the pulses. While the ideal refocusing pulse will reverse the direction of My and leave Mx undisturbed, the relationship between these transverse componets (i.e., ϕ) is also relevant in evaluating pulse performance. Specifically, the ideal refocusing pulse will result in $\phi = -\pi/4$ given the initial simulation conditions of M_x^{init}=$M_y^{\text{init}} = 1$. In order to visualize performance in terms of the transverse phase, the value is shown on the grid in Figures 39-42 along with corresponding histograms. Furthermore, the percent deviation of ϕ from the ideal value of $-\pi/4$ is reported in Table 5.4.1.

In general, comparison of simulated M_x^{final}, M_y^{final}, and ϕ distributions for all pulses indicates that modified and optimized pulse designs result in improved refocusing performance relative to the established designs. This confirms that the modification and optimization procedures we have chosen to implement are successful in producing improved refocusing pulses. However, from this simulated data alone, it is difficult to predict refocusing performance beyond stating that pulses perform increasingly well with pulse duration. While simulations are certainly useful in the design and preliminary evaluation of performance, the resulting increase in signal remains the most practical indicator of improvement.

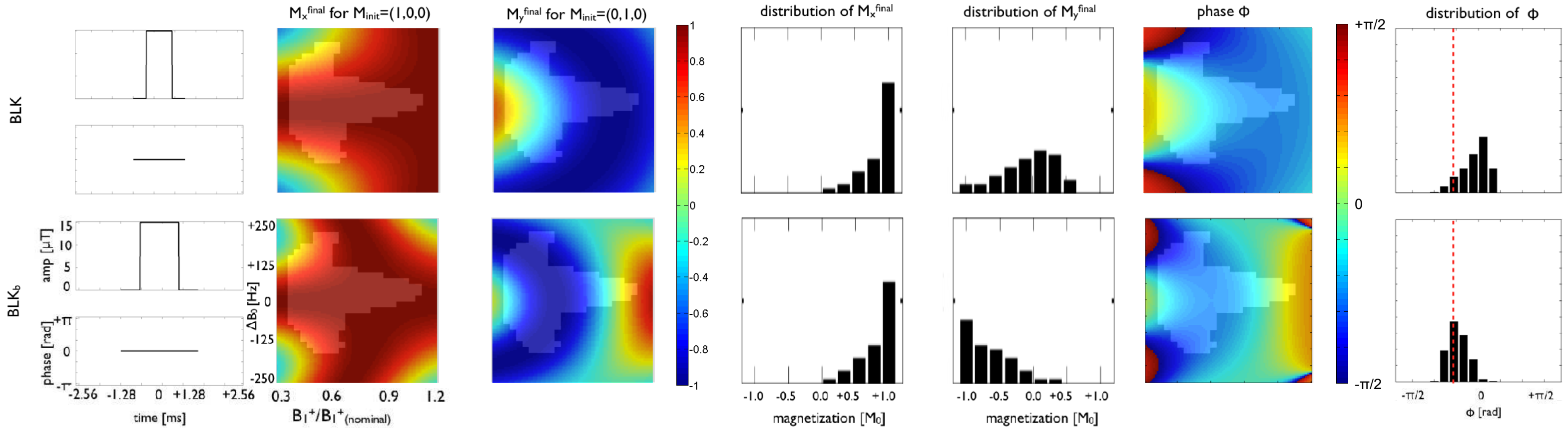

Figure 39: Amplitude and phase modulation waveforms (alternating in the first column) for the BLK and BLK_{b} pulses of the *short* family (names indicated at far left) together with corresponding components of the refocused transverse magnetization for initial conditions $(M_x, M_y, M_z) = (1, 0, 0)$ (second and fourth columns) and $(M_x, M_y, M_z) = (0, 1, 0)$ (third and fifth columns). The maps in the second and third columns display magnetization as simulated over a grid of B_1^+ and ΔB_0 values with the extent of the field variations measured in the phantom indicated by a lighter shading (see Figure 36). Magnetization values from within these shaded region are shown in the form of histograms in the fourth and fifth columns. The ideal refocusing pulse would result in $M_x^{\mathrm{final}} = 1$ and $M_y^{\mathrm{final}} = -1$. Maps of the transverse magnetization phase (ϕ in Equation 5.2.4) over the same B_1^+-ΔB_0 grid are displayed in the sixth column with corresponding histograms for the shaded phantom region appearing in the last column. Transverse phase, although not used in our optimizations, serves as another indication of proper refocusing, with the optimal final phase of $-\pi/4$ radians for the given initial conditions.

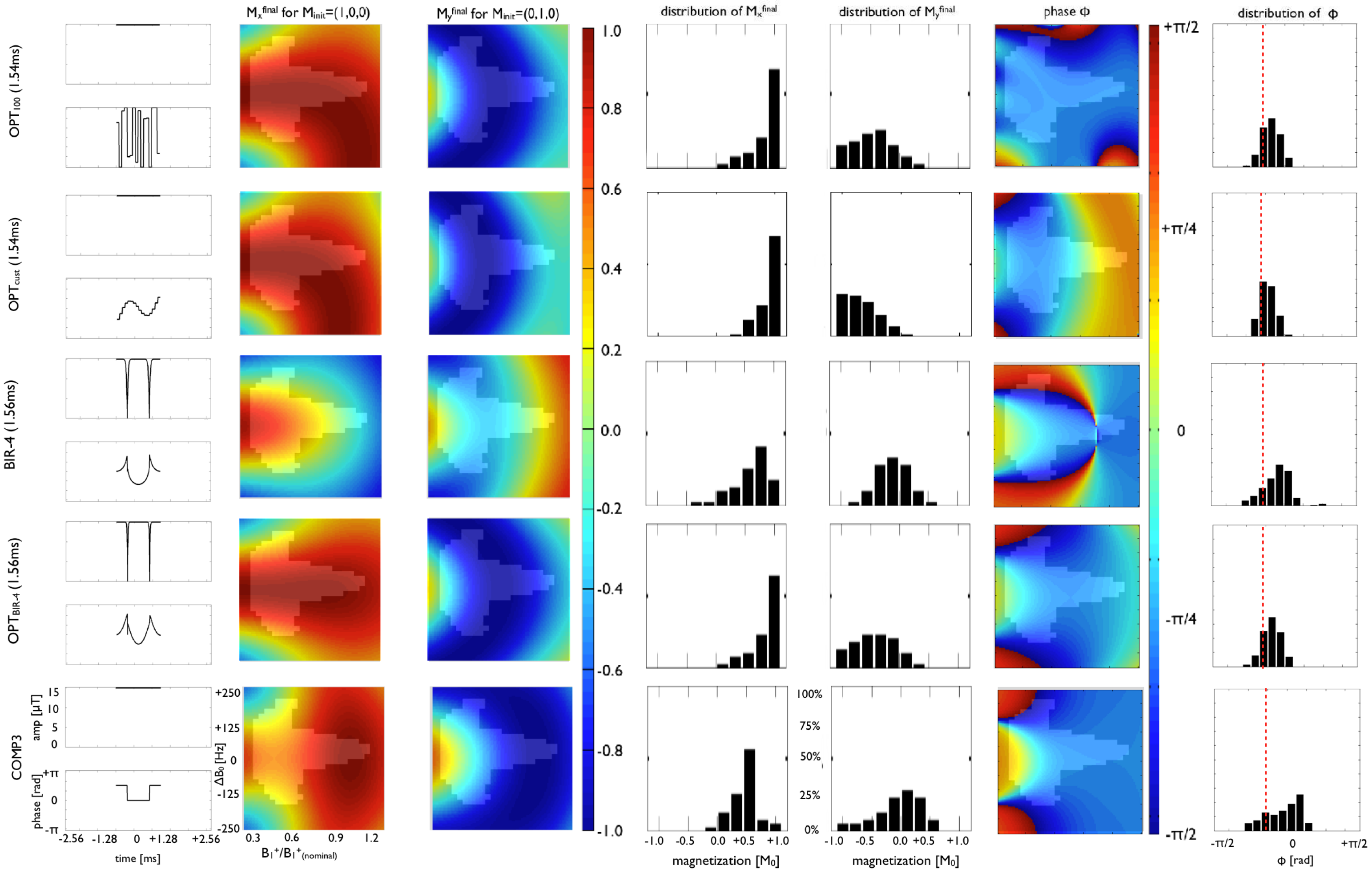

Figure 40: Amplitude and phase modulation waveforms with simulated magnetization responses for the COMP3$_b$, OPT$_{100}$, OPT$_{cust}$, BIR-4, and OPT$_{BIR\text{-}4}$ pulses of the *short* family (names indicated at far left). See Figure 39 caption for details.

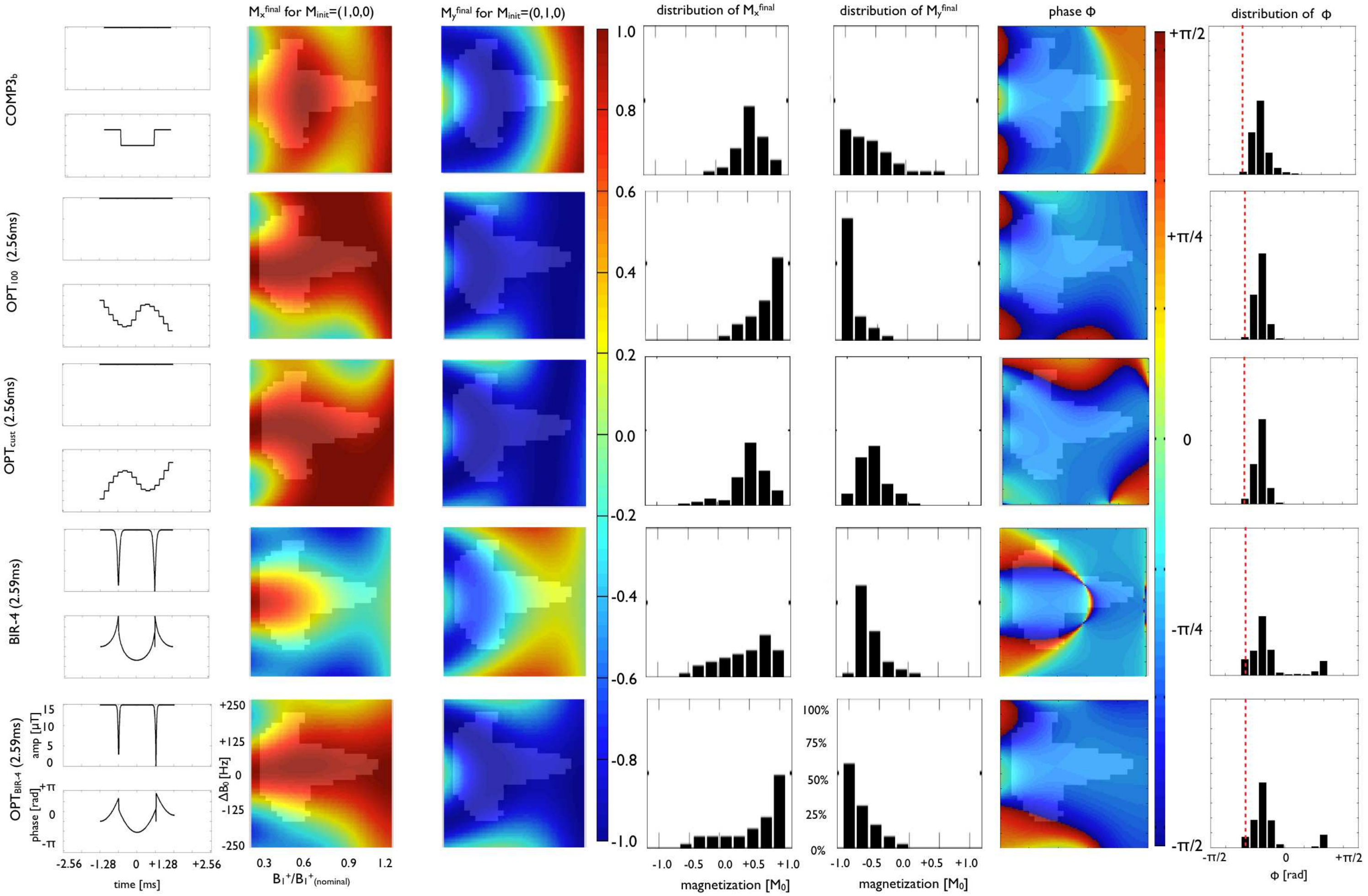

Figure 41: Amplitude and phase modulation waveforms with simulated magnetization responses for the *moderate* family of pulses (names indicated at far left). See Figure 39 caption for details.

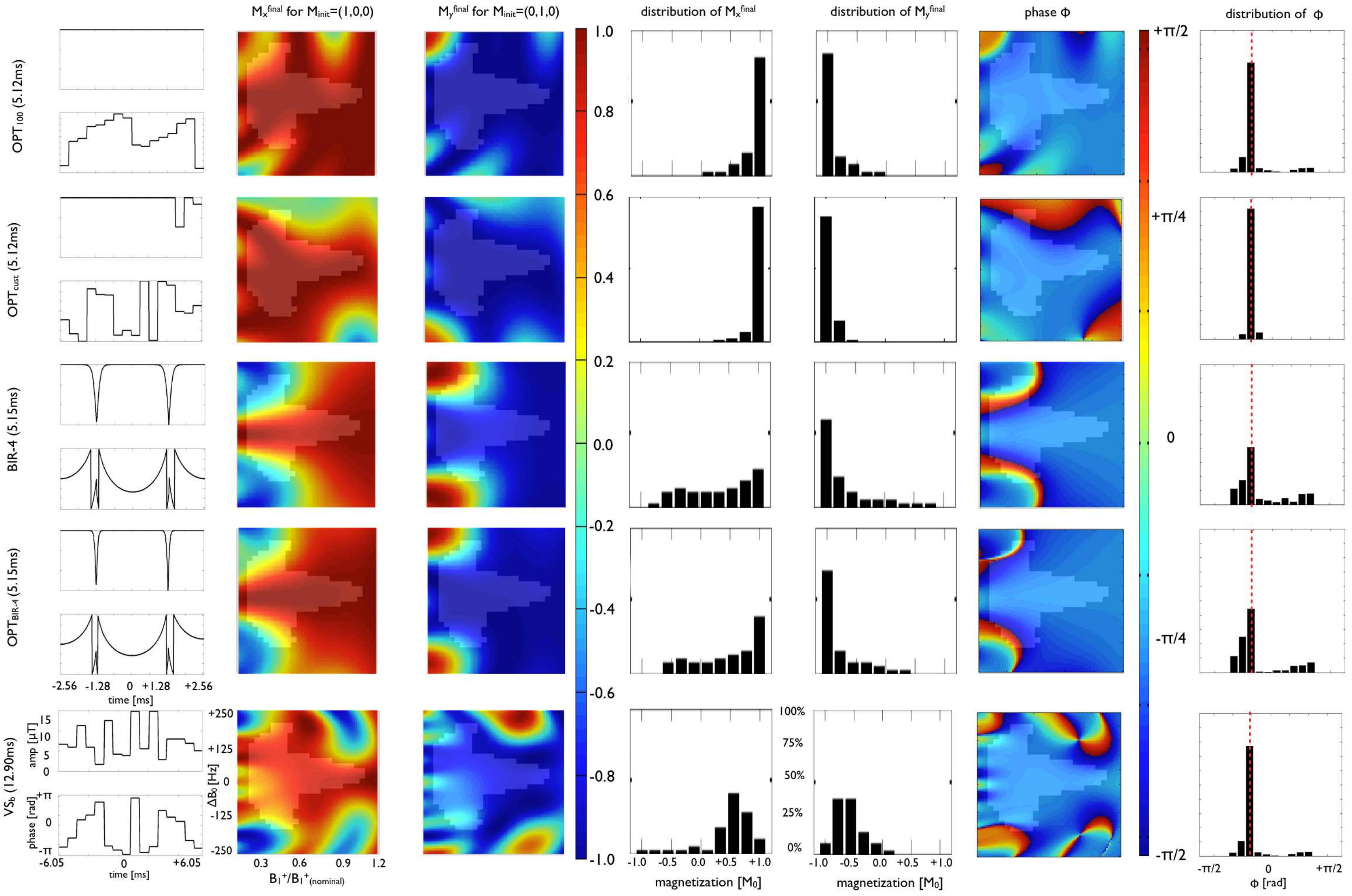

Figure 42: Amplitude and phase modulation waveforms with simulated magnetization responses for the *long* family of pulses (names indicated at far left). See Figure 39 caption for details.

5.4.3 Experiments

In addition to B_1^+ and ΔB_0 maps for 7 axial slices of the phantom, Figures 43, 45, 47 show 3D SE-EPI signal intensities (relative to those of the BLK pulse) for all 16 refocusing pulses. Similar ratios and field maps for the human data are shown in Figures 44, 46, and 48. Mean values of the signal intensity ratios (averaged over the entire 3D volume and for specific slices) were calculated for all pulses for both phantom and human data and are given in the relevant figures. Pulse performance observed in the brain correlates closely with that observed in the phantom. This fact is expected given that the ranges of B_1^+ and ΔB_0 values in the phantom encompass those observed *in vivo* (see Section 5.4.1) and, furthermore, validates the use of phantom signal as a means of comparing pulse performance. Table 5.4.1 summarizes the results of simulations (mean transverse components of the refocused magnetization (M_x^{final} and M_y^{final}) and deviation of refocused magnetization phase (ϕ)) and lists values of mean signal ratios for both phantom and in-vivo experiments. Additionally, this table provides the total duration, equivalent flip angle, and minimum possible repetition time for the 3D SE sequence (as determined by maximum SAR limits) for all pulses. Finally, as examples of how the use of improved refocusing pulses effects image quality, raw signal intensities of axial slices in the phantom and human brain obtained using BLK, BLK_b, and VS_b pulses are shown in Figure 49. For further comparison of pulse performance and detailed discussion, we have divided pulses into three families based on total pulse duration: *short* ($\Delta T < 2\,\text{ms}$); *moderate* ($2\,\text{ms} < \Delta T < 3\,\text{ms}$); and *long* ($\Delta T > 5\,\text{ms}$).

Short family

Perhaps the most striking improvement among the *short* family of pulses comes from the BLK_b pulse which results in overall signal gains of $\sim 50\%$ in both the phantom and *in vivo* with signal gains of more than $\sim 100\%$ in localized areas. Such large improvement in local regions was expected in this case because, by design, the pulse was adjusted to perform best at low B_1^+. The main drawback to this design is that the resulting increase in signal in areas of low B_1^+ comes at the price of signal loss in areas of high B_1^+. This effect is obvious in both the phantom and brain signal ratio data where a decrease of $\sim 100\%$ and $\sim 40\%$, respectively, is observed at the center of the imaging volumes. However, as the mean signal ratios for both volumes imply, this decrease in signal is more than compensated by the increase in signal elsewhere. This fact is simply a reflection of the distribution of B_1^+ values found in the phantom and in the brain. In comparison to the BLK_b pulse, the COMP3 pulse is desirable due to avoidance of signal loss in high B_1^+ regions; however, this pulse results in relatively low signal increase in other regions. The 1.56 ms BIR-4 pulse results in dramatically less signal as compared to the COMP3 pulse. We interpret this fact as an indication that the pulse is too short (and, therefore, frequency sweeps are too fast) for the adiabatic condition to be satisfied. As a result of the numerical optimization, the $\text{OPT}_\text{BIR-4}$ pulse has a reduced frequency sweep range (and a reduced bandwidth) such that the adiabatic condition is satisfied to a higher degree. This explains why the $\text{OPT}_\text{BIR-4}$ pulse performs significantly better than its non-optimized counterpart. However, there appears to be no advantage in using this optimized pulse over the COMP3 pulse. The OPT_{100} pulse performs similarly to the COMP3 pulse with slightly less signal in high B_1^+ regions and slightly more signal in low B_1^+ regions. The $\mathrm{OPT}_{\mathrm{cust}}$ pulse produces such similar results to the $\mathrm{BLK}_{\mathrm{b}}$ pulse that the former, in light of the necessary but time-consuming field mapping and optimization, provides no tangible advantage over the latter. To summarize the performance of this *short* family of pulses, the $\mathrm{BLK}_{\mathrm{b}}$ pulse represents the simplest way to achieve dramatic signal gains from refocusing. If the resulting signal loss at high B_1^+ is undesirable in practice, the COMP3 pulse represents an attractive compromise. While this conclusion may seem obvious, the fact that adiabatic and numerically optimized pulses do not provide significant advantages given a $\sim 1.5\,\mathrm{ms}$ pulse length has not been previously established in the context of 7 T human imaging.

Moderate family

Within the *moderate* family of pulses, the $\mathrm{COMP3}_{\mathrm{b}}$ pulse results in the greatest overall mean signal increase but suffers from similar high-B_1^+ signal loss as the $\mathrm{BLK}_{\mathrm{b}}$ pulse. However, relative to the $\mathrm{BLK}_{\mathrm{b}}$ pulse, the $\mathrm{COMP3}_{\mathrm{b}}$ pulse has the advantage of significantly larger signal gains ($\gtrsim 150\%$) in low-B_1^+ regions. Thus, the $\mathrm{COMP3}_{\mathrm{b}}$ pulse represents a more attractive refocusing option as compared to the $\mathrm{BLK}_{\mathrm{b}}$ pulse given that the two-fold increase in both pulse duration and SAR can be accommodated in practice. Unlike in the *short* family of pulses, the other members of the *moderate* family (2.54 ms BIR-4, 2.54 ms $\mathrm{OPT}_{\text{BIR-4}}$, 2.56 ms OPT_{100}, and 2.56 ms $\mathrm{OPT}_{\mathrm{cust}}$) provide refocusing solutions that maintain the low-B_1^+ signal gains of the $\mathrm{COMP3}_{\mathrm{b}}$

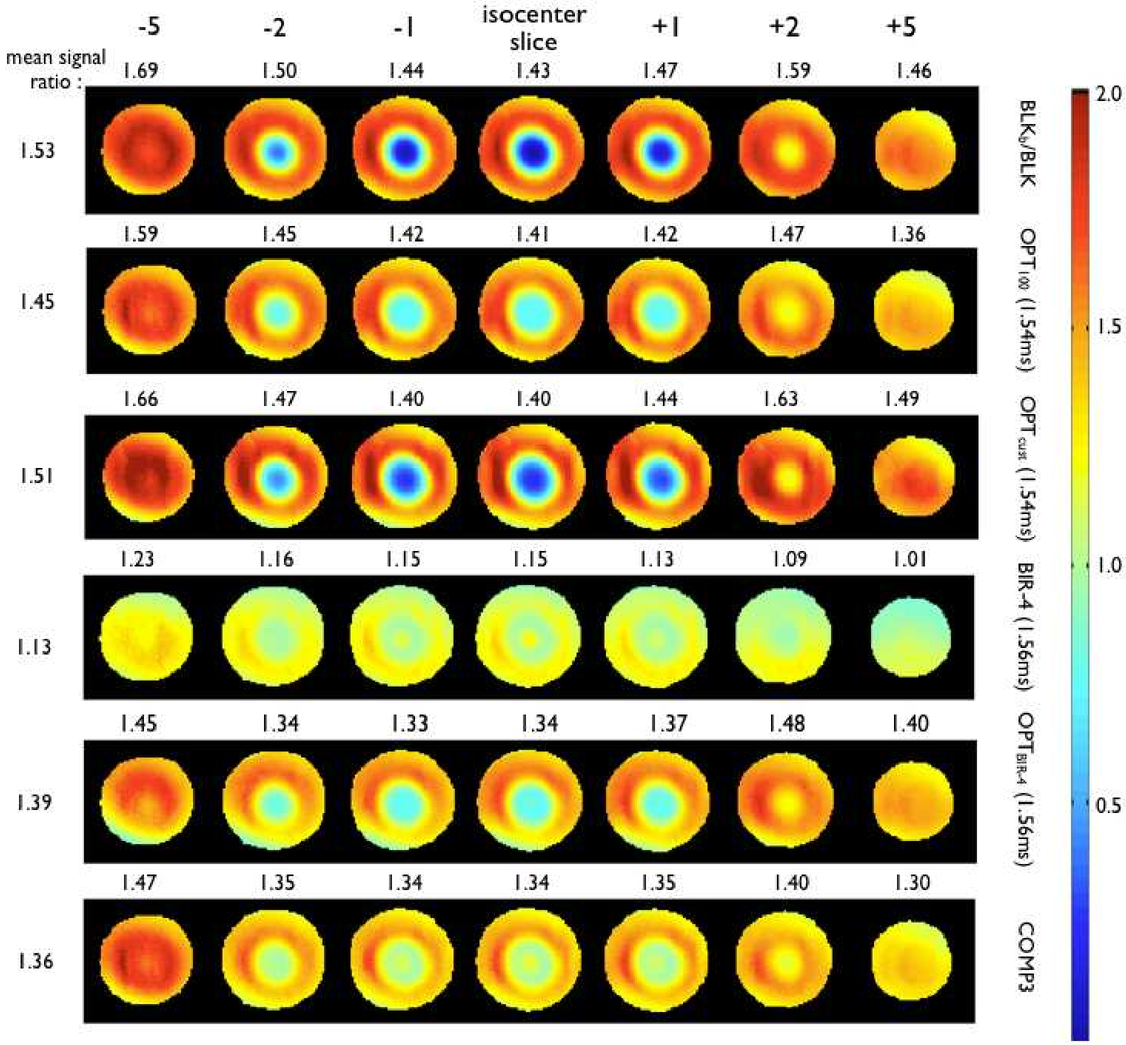

Figure 43: Ratio of signal from a 3D SE-EPI experiment with the *short* family of refocusing pulses (names given at right) to the signal from the same experiment with the BLK refocusing pulse. Mean signal ratios averaged slice-wise and over the entire volume are shown above each slice and at the far left of each row, respectively. The $\mathrm{BLK_b}$ and $\mathrm{OPT_{cust}}$ pulses are most effective in producing high signal gains in the lowest-B_1^+ regions while the $\mathrm{COMP_3}$ and $\mathrm{OPT_{100}}$ pulses avoids signal loss in high-B_1^+ regions. Although the $\mathrm{OPT_{BIR\text{-}4}}$ pulse results in much higher signal than its unoptimized counterpart (BIR-4), it appears more susceptible to B_0 offsets.

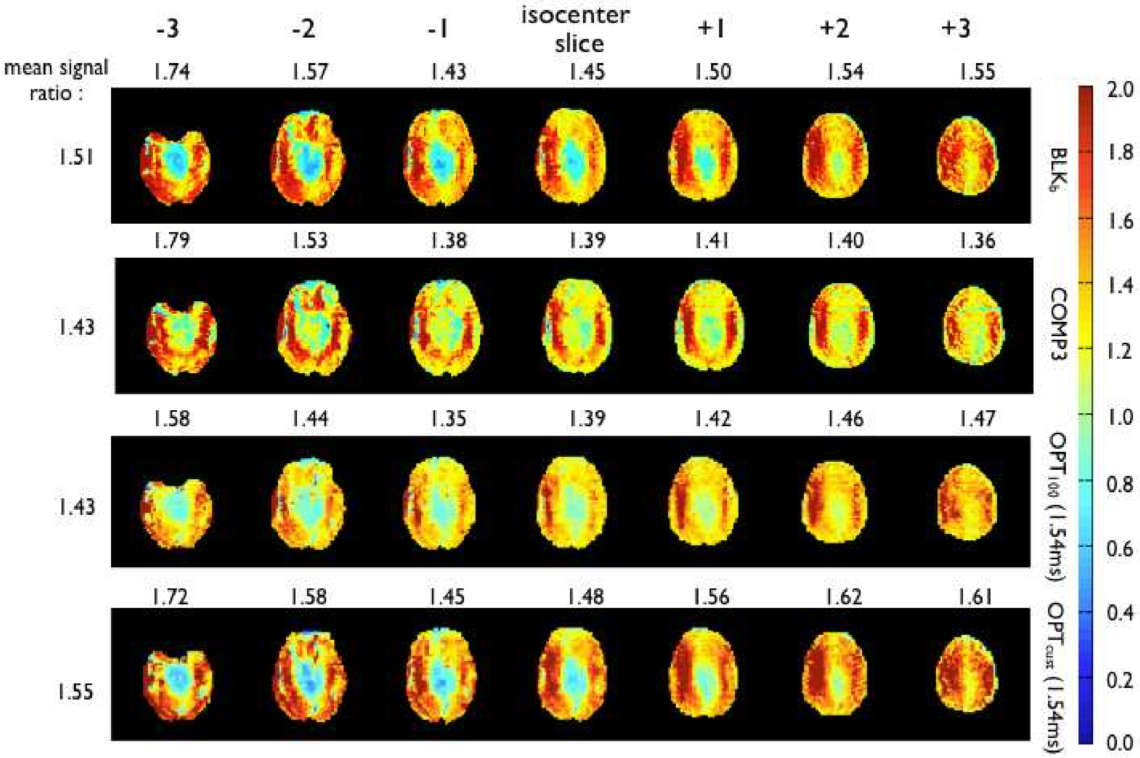

Figure 44: Ratios of SE-EPI signal for a subset of the *short* family of pulses to that for the BLK pulse as measured in the *in vivo* human brain. Results correlate well with the corresponding phantom measurements presented in Figure 43 and thus validate the use of phantom measurements in establishing the performance of refocusing pulses for brain imaging.

pulse while avoiding high-B_1^+ signal loss. With the exception of the 2.54 ms BIR-4 pulse (which was not tested *in vivo*), these other pulses do introduce some undesirable ΔB_0-related problems. This effect is most noticeable in the off-center slices in the phantom and near the frontal sinuses in the brain. While this observations suggests that the BIR-4 pulse may be the best choice from this family, the ΔB_0 problems for the three optimized pulses might be easily remedied through slight adjustments to the optimization regions on the B_1^+-ΔB_0 grid.

Long family

If longer pulse durations and higher SAR values are acceptable given a particular application, the *long* family of pulses provides many viable options for improved refocusing performance. Results for this family of pulses are given in Figure 47 (phantom) and Figure 48 (brain). Phantom experiments reveal the 5.15 ms BIR-4 and $\mathrm{OPT}_{\text{BIR-4}}$ pulses to suffer from more ΔB_0-related signal loss than the other members of the family. This appears to be the primary reason that mean whole-volume signal ratios are relatively low for these two pulses. On the other hand, it is fair to say that the performance of the other members of this family (the 5.12 ms OPT_{100}, 5.12 ms $\mathrm{OPT}_{\mathrm{cust}}$, and 12.90 ms VS_{b} pulses) exceeds that of all other pulses considered in this study. In the phantom, these three pulses result in signal increases $\lesssim 150\%$ in low-B_1^+ regions and $\sim 10\%$ in high-B_1^+ regions while exhibiting minimal ΔB_0-related signal loss. In the brain, however, the VS_{b} pulse results in slightly larger low-B_1^+ signal gain as compared to the OPT_{100} and $\mathrm{OPT}_{\mathrm{cust}}$ pulses while introducing a slight signal loss

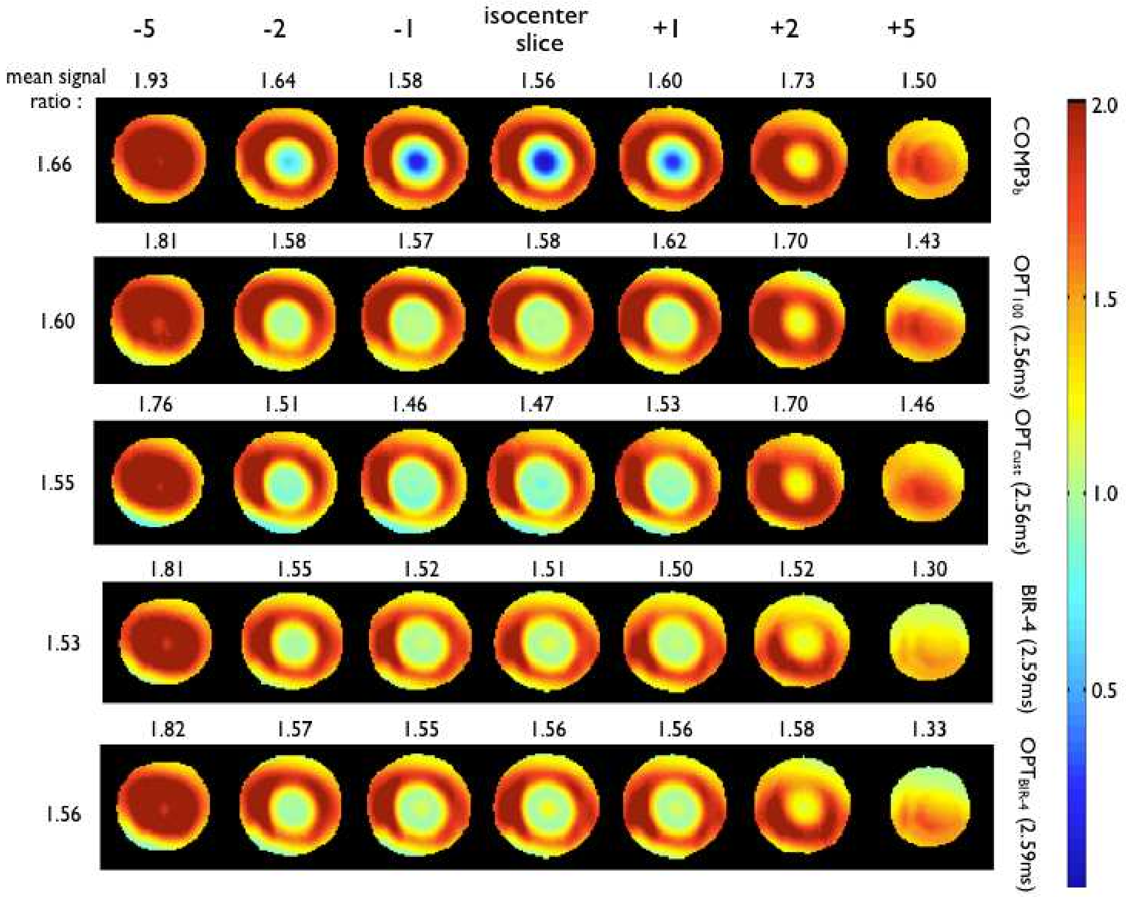

Figure 45: Ratio of signal from a 3D SE-EPI experiment with the *moderate* family of refocusing pulses (names given at right) to the signal from the same experiment with the BLK refocusing pulse. Mean signal ratios averaged slice-wise and over the entire volume are shown above each slice and at the far left of each row, respectively. All pulses result in relatively similar performance, with the most notable exception being for the COMP$_\mathrm{b}$ pulse in high-B_1^+ regions. Contrary to findings for the *short* family of pulses, OPT$_{100}$ and OPT$_\mathrm{cust}$ pulses in the moderate family appear more susceptible to B_0 variations than do the BIR-4 and OPT$_\text{BIR-4}$ pulses. The color scale is truncated at a value of 2.0 so as to better illuminate signal differences across the entire volume.

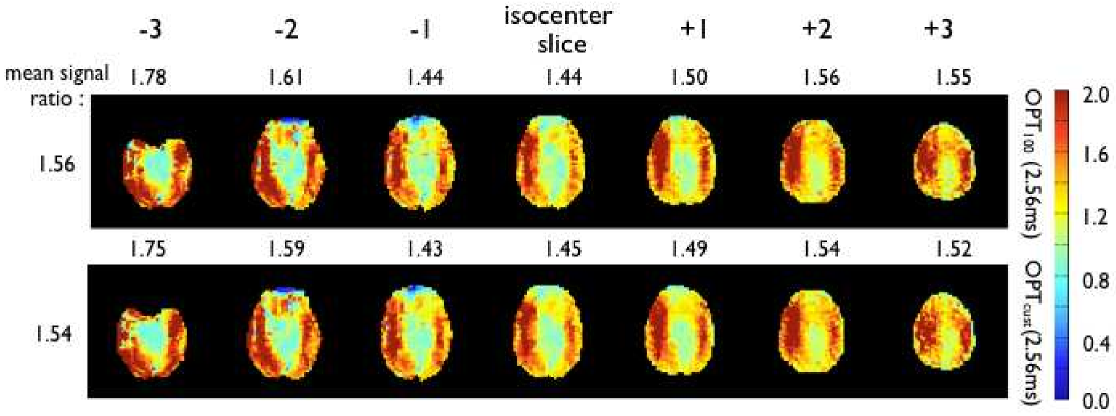

Figure 46: Ratios of SE-EPI signal for a subset of the *moderate* family of pulses to that for the BLK pulse as measured in the *in vivo* human brain. Values correlate well with those measured in the phantom (Figure 45). While the two OPT pulses highlighted here produce significant signal gains at low-B_1^+, they do not outperform the 1.56 ms $\mathrm{OPT}_{\mathrm{cust}}$ of the *short* family. The sensitivity to B_0 that is apparent near the frontal sinuses can likely be remedied by adjustment of the range of ΔB_0

in high-ΔB_0 areas (e.g., near the frontal sinuses) that is not observed for the $\mathrm{OPT}_{\mathrm{cust}}$ pulse. Despite the slight ΔB_0-related signal loss observed in the phantom for the $\mathrm{OPT}_{\mathrm{cust}}$ pulse, the $\mathrm{OPT}_{\mathrm{cust}}$ pulse designed for the brain performs well with respect to the relevant B_0 offsets. This likely reflects dependence of the numerical optimization on the target ΔB_0 range in conjunction with the fact that this range is significantly larger in the phantom than in the brain. Moreover, ΔB_0 signal loss in the phantom (specifically at high ΔB_0 and low-B_1^+ values) is a performance feature common to all $\mathrm{OPT}_{\mathrm{cust}}$ pulses. This observation suggests that ΔB_0-performance of the $\mathrm{OPT}_{\mathrm{cust}}$ pulse may be improved (at least for the phantom) by reducing the density threshold used to create the binary mask designating the optimization region on the B_1^+-ΔB_0 grid (see Section 5.3.1 and Figure 36).

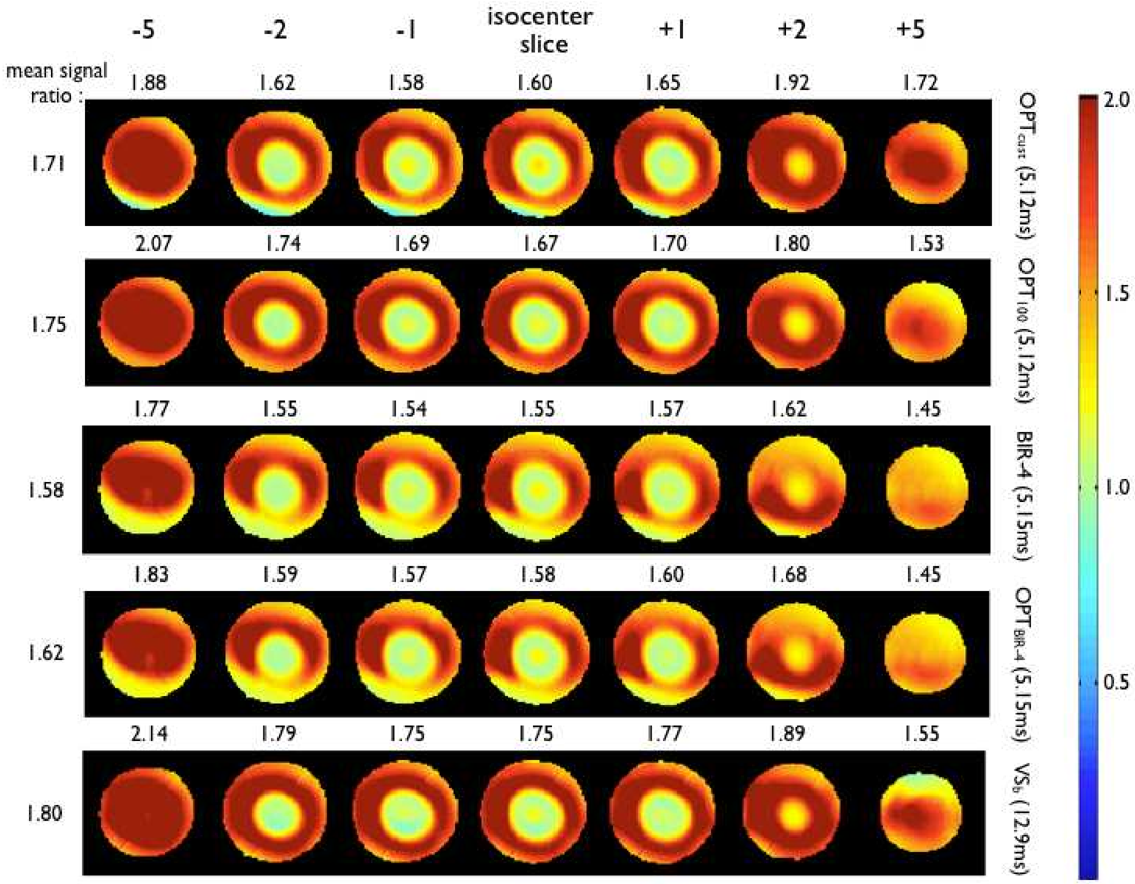

Figure 47: Ratio of signal from a 3D SE-EPI experiment with the *long* family of refocusing pulses (names given at right) to the signal from the same experiment with the BLK refocusing pulse. Mean signal ratios averaged slice-wise and over the entire volume are shown above each slice and at the far left of each row, respectively. Within this family of pulses, the OPT$_{100}$ and VS$_b$ pulses outperform the others in terms of both B_1^+ insensitivity and B_0 susceptibility.

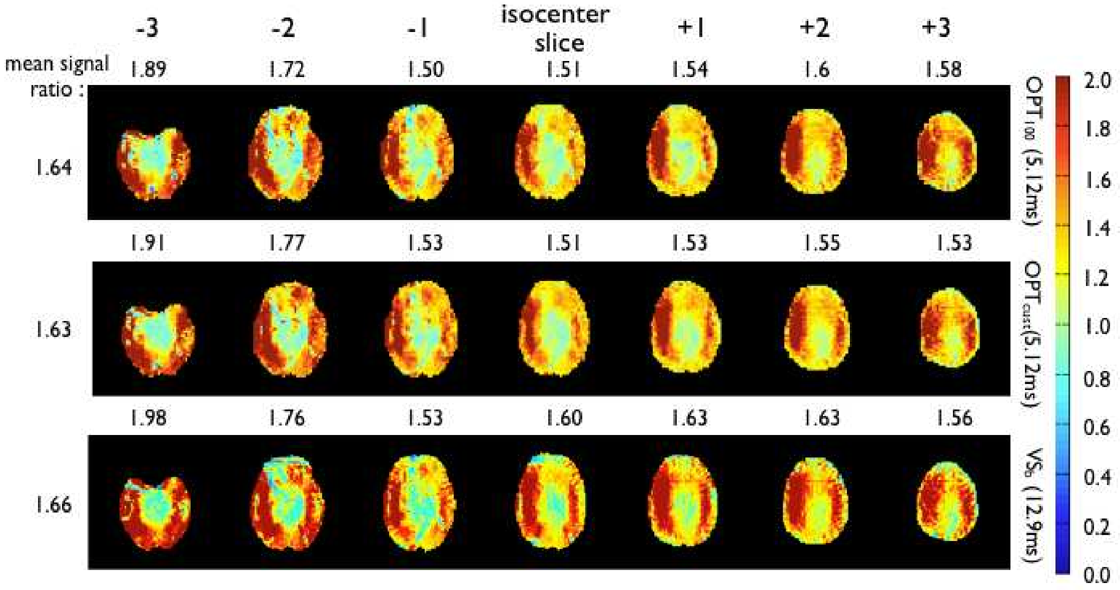

Figure 48: Ratios of SE-EPI signal for a subset of the *long* family of pulses to that for the BLK pulse as measured in the human brain. Performance among these three pulses is nearly indistinguishable, although the $\mathrm{VS_b}$ pulse does appear more sensitive to the large ($\gtrsim 100\,\mathrm{Hz}$) B_0 offsets encountered near the frontal sinuses. Noteworthy is the observation that all three of these pulses achieve whole-brain average signal gains that are approximately two thirds of the theoretical maximum values presented in Figure 38.

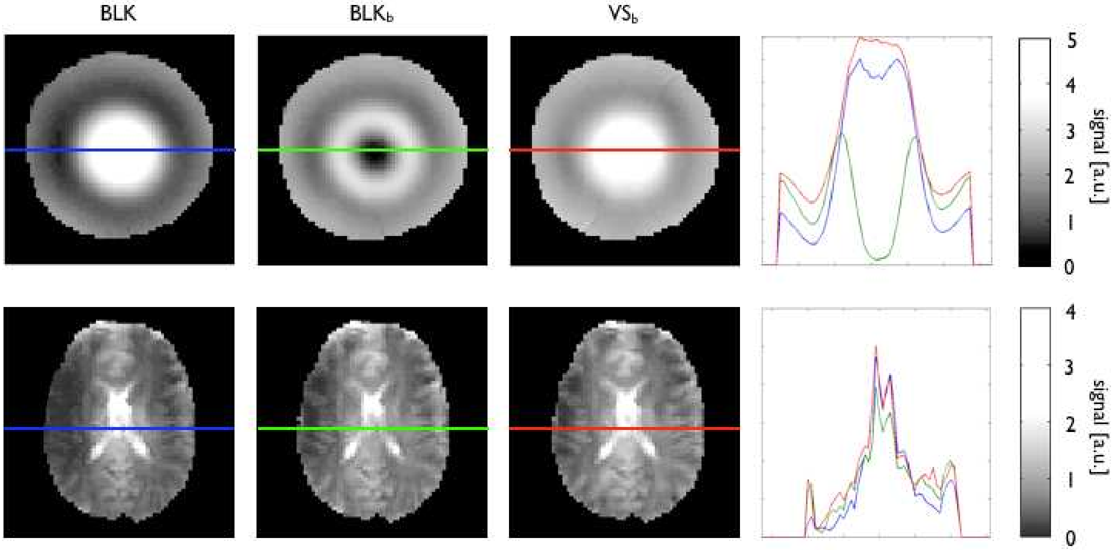

Figure 49: Signal intensities in the phantom (top row) and brain (bottom row) acquired with the 3D SE-EPI sequence used in this study for evaluating refocusing performance. Results are shown for the BLK (first column), BLK$_\mathrm{b}$ (second column), and VS$_\mathrm{b}$ (third column) refocusing pulses. Differences in image brightness may appear subtle in the case of *in vivo* images, but line profiles in the last column reveal the actual signal gains at some locations to be $\gtrsim$ 100% when comparing the VS$_\mathrm{b}$ or BLK$_\mathrm{b}$ pulses to the BLK pulse. Regardless of the efficacy of a given refocusing pulse, signal intensities vary greatly within images due to the B_1^+-sensitivity of the 90° sinc excitation as well as the imhomogeneity of the recieve field (B_1^-). To illuminate the signal contributions arising from the refocusing pulse alone, most results in this study are presented in terms of signal ratios.

Considerations of pulse duration and SAR

Although the $\mathrm{VS_b}$ pulse performs exceptionally well under the given phantom and *in vivo* testing conditions, its lengthy duration poses a potential drawback since refocusing pulse duration directly restricts the minimum possible echo time (T_E) in a SE pulse sequence. Added duration may be costly in imaging scenarios involving chemical species with short T_2 values since this component of T_2^* is not recoverable via RF refocusing or other means. The 5.12 ms $\mathrm{OPT_{100}}$ and $\mathrm{OPT_{cust}}$ pulses, with similar performance to the $\mathrm{VS_b}$ pulse, are almost 8 ms shorter and therefore represent more attractive refocusing options for short-T_2 applications. Of course, depending on the T_2 values under consideration, such an argument can be extended as being reason to consider pulses from the *moderate* and *short* families.

In addition to pulse duration, relative SAR sets a practical limit on the applicability of a given pulse. As an indirect measure of SAR, the minimum repetition time T_R^{min} for the given 3D SE sequence was extracted from the scanner prior to each scan (Table 5.4.1). In general, longer pulse durations imply longer T_R^{min} values, hence longer scan times will be necessary in order to maintain the condition that $\mathrm{SAR} < 3\,\mathrm{W/kg}$. As can be seen in Table 5.4.1, the *short*, *moderate*, and *long* families of pulses result in total scan times that are, respectively, $\lesssim 2$, $\lesssim 3$, and $\lesssim 5$ times longer than when using the BLK pulse. These factors include SAR contribution from the 90° excitation pulse that is necessary for the given 3D SE sequence. Thus, the factors serve as a guide in selecting suitable pulses for a given time constraint.

Table 5.4.1: Selected attributes and performance metrics for all pulses in this study. Included are: total pulse duration (ΔT); minimum repetition time (T_R^{min}) given the 3D SE-EPI protocol used for experimental performance evaluation; equivalent flip angle (α) as calculated from $\int \gamma A\, dt$; the mean of x and y components ($\overline{M_x}$ and $\overline{M_y}$) of simulated magnetization responses reported in the fourth and fifth columns of Figures 39, 40, 41, and 42; the percent deviation of the simulated transverse magnetization phase (reported in the last column of the same figures) from the ideal value of $-\pi/4$; mean experimental signal ratios ($\overline{SI/SI_{\text{BLK}}}$) with respect to signal obtained with the BLK pulse for the entire phantom and human brain—thus reflecting the results presented in Figures 43, 45, 47, 44, 46, 48. Pulses are listed in order of increasing ΔT while grouping reflects the *short*, *moderate*, and *long* families described in the text.

pulse name	ΔT [ms]	T_R^{min} [ms]	α [rad/π]	$\overline{M_x}$	$\overline{M_y}$	$\overline{\phi}$ dev [%]	$\overline{SI/SI_{\text{BLK}}}$ phantom	$\overline{SI/SI_{\text{BLK}}}$ brain
BLK	0.7	136	1.00	0.89	-0.53	39	1	1
BLK_b	1.20	186	1.50	0.89	-0.55	33	1.53	1.51
OPT_{100}	1.54	234	1.96	0.89	-0.68	20	1.45	1.43
OPT_cust	1.54	234	1.96	0.88	-0.65	22	1.51	1.55
BIR-4	1.56	227	1.86	0.30	-0.13	26	1.13	
$\text{OPT}_\text{BIR-4}$	1.56	233	1.92	0.87	-0.69	18	1.39	
COMP3	1.60	235	2.00	0.66	-0.52	35	1.36	1.43
COMP3_b	2.40	335	3.00	0.64	-0.54	28	1.66	
OPT_{100}	2.56	366	3.27	0.82	-0.90	-7	1.60	1.56
OPT_cust	2.56	366	3.27	0.85	-0.91	-1	1.55	1.54
BIR-4	2.59	352	3.07	0.18	-0.26	20	1.53	
$\text{OPT}_\text{BIR-4}$	2.59	361	3.19	0.73	-0.86	13	1.56	
OPT_{100}	5.12	695	5.66	0.91	-0.94	-2	1.75	1.64
OPT_cust	5.12	653	6.30	0.94	-0.94	0	1.71	1.63
BIR-4	5.15	664	6.12	0.59	-0.74	20	1.58	
$\text{OPT}_\text{BIR-4}$	5.15	681	6.34	0.70	-0.86	10	1.62	
VS_b	12.90	553	8.14	0.65	-0.71	8	1.80	1.66

5.5 Conclusion

5.5.1 Summary

Using a 3D SE-EPI sequence, this work has investigated the performance of an array of non-selective refocusing pulses in the context of 7 T human brain imaging. As a means of comparison, pulses were divided into *short*, *moderate*, and *long* families based on total pulse duration—a grouping that correlates with increasing SAR levels. Identification of the pulses in each family with the best performance depends not only on the given application but also on the compromises deemed acceptable by researchers and clinicians. In light of such performance characteristics that are not necessarily quantifiable in terms of a cost function, we have attempted to outline the major pros and cons of the various pulses included in this study so as to facilitate this decision making process. This analysis has resulted in our identification of a few outstanding pulses in each of the duration families.

Within the *short* family ($\Delta T < 2\,\mathrm{ms}$), the $\mathrm{BLK_b}$ pulse, with a 270° nominal flip angle, provides a simple way to dramatically increase signal in low-B_1^+ regions with the sacrifice of signal in high-B_1^+ regions; however, with the choice of a 270° flip angle, signal loss is limited to a small region at the center of the brain, thus making the pulse an attractive option given the ease of implementation. Moreover, the flip angle can be adjusted to achieve a desired compromise between the areas of signal loss and signal gain. The COMP3 pulse avoids high-B_1^+ signal loss but with reduced gain at low-B_1^+ and represents an appealing compromise between these elements of performance.

Within the *moderate* family ($2\,\mathrm{ms} < \Delta T < 3\,\mathrm{ms}$), the COMP3$_\mathrm{b}$ pulse performs outstandingly with regard to low-B_1^+ signal gain and reduces the extent of the signal loss region when compared to the BLK$_\mathrm{b}$ pulse. The 2.59 ms BIR-4 pulse, however, eliminates high-B_1^+ signal loss at the cost of a slight reduction in low-B_1^+ gain and, therefore, should be of high consideration. Optimization strategies for *moderate* family pulses tend not to produce pulses that outperform BIR-4.

Within the *long* family ($\Delta T > 5\,\mathrm{ms}$), the OPT$_{100}$, OPT$_\mathrm{cust}$, and VS$_\mathrm{b}$ pulses result in similar signal gains with slightly different sensitivities to ΔB_0. Although these three pulses outperform all other pulses evaluated in this study, utilization of these designs requires the largest increase in scan time due to higher average power ($\int A^2 dt/\Delta T$). While VS$_\mathrm{b}$ has the lowest average power of the three pulses, its lengthier duration poses a restriction of the minimum possible T_E value that is often selected in practice in order to minimize T_2 signal loss.

In addition to ranking a large sample of refocusing pulses according to performance, this study provides a framework for evaluating pulse performance that relies on comparison of signal ratios for set values of T_R and T_E. Furthermore, the study has established the approximate maximum signal gains achievable with any refocusing pulse design in the human brain at 7 T and thus constitutes a metric for comparing future pulse designs whether for single or multiple transmission channels.

5.5.2 Future Work

The pulses considered in this study are exclusively non-selective, limiting use to 3D sequences in most cases. This fact immediately begs that a similar comparison be performed for slice-selective refocusing pulses. The composite pulses in this study may prove translatable to slice-selective forms by changing component pulse shapes from blocks to sincs or Gaussians while incorporating an oscillating slice-selection gradient in a manner similar to spokes pulses (89). In the event that such slice-selective pulse variants are designed, conclusions in terms of relative pulse performances and SAR limitations would likely remain unchanged. Furthermore, the strategy of increasing nominal flip angles in accordance with the mean of the measured B_1^+ distribution will be directly applicable to slice-selective pulses. For example, the results of this study imply that adjustment of the nominal flip angle of a sinc refocusing pulse from 180° to 270° will result in significant signal gains at most regions in the brain.

In the context of further exploration of non-selective refocusing pulses, the success of the $\mathrm{VS_b}$ pulse in this study suggests that incorporation of a SAR constraint in the optimization algorithm (rather than indirectly limiting SAR through restrictions on pulse duration) may result in an improved balance of SAR and performance given that longer T_E values can be accommodated. The potential in such designs relies on the fact that pulses with longer duration have lower average power for a given equivalent flip angle.

In conclusion, this study lays a firm basis for comparison of other techniques for achieving uniform refocusing in the presence the field inhomogeneities observed in the human brain at 7 T. The work provides a much-needed guide to selecting refocusing pulses given various SAR and time constraints and provides pulse designers with a reference for the advantages and limitations of existing refocusing pulses. Furthermore, the work more properly establishes the performance limits of single-channel refocusing pulses such that the advantages of future multi-channel refocusing designs can be better understood.

CHAPTER VI

RELATED PULSE DESIGNS AND APPLICATIONS

In this chapter, an array of other possible uses for numerically optimized pulses are presented along with preliminary results. In most cases, composite pulses remain the tool of choice, the context is 7 T, and B_1^+-insensitivity is still an objective; however, for some applications these design criteria differ. For example, in Section 6.1 optimizations of continuously varying (non-composite) modulation functions are explored. Additionally, low-field polarization transfer applications are described in Section 6.5. Section 6.2 extends upon the investigations of Chapter III with an investigation of the impact of SAR-limited optimizations on non-selective composite pulses. Additionally, the potential of employing composite pulse designs for frequency selective excitation is evaluated, with applications to slice-selective imaging (Sections 6.3) and MR spectroscopic imaging (Section 6.4). The motivation for inclusion of this chapter in the thesis is to demonstrate the applicability of the pulse design methods proposed thus far to other current NMR research. Moreover, this chapter allows for exhibition of some capabilities of these pulse design strategies that were not demonstrated in the preceding chapters. In this case, potential applications are only, at this point, hypothesized.

6.1 Numerical Optimization of Adiabatic Pulses

Adiabatic pulses achieve a spin lock of the available longitudinal magnetization by satisfying the adiabatic condition, a loosely defined criterium fulfilled if the rate of nuclear precession is much greater than the rate with which the effective magnetic field changes in time. As long as this condition is satisfied, adiabatic pulses can achieve uniform flip angles regardless of inhomogeneities in the transmitted RF field.

In order to satisfy the adiabatic condition, an adiabatic pulse requires sufficient RF amplitude and duration. Due to RF hardware-restricted amplitudes ($15\,\mu$T for the Philips 7 T) and the large-scale B_1^+ inhomogeneities produced at high field, adiabatic pulses designed for low field strengths will not in general satisfy the adiabatic condition at all spatial locations in a sample imaged at high field, thereby corrupting resulting image with spatial varying signal intensity. Furthermore, MR literature apparently does not present systematic methods for choosing optimal values of the various adiabatic pulse parameters as a function of field strength. The investigation described here employs numerical optimization methods to select pulse parameters for 180° hyperbolic secant (SECH) pulses (72; 73) and 90°, 4-part B_1^+-insensitive rotations (BIR-4) (76) over a range of bandwidths (0.2–2.0 kHz) and a range of B_1^+ variations representative of those observed within the human brain at 7 T.

For both SECH and BIR-4 pulses, parameter optimization is determined according to the following methods. Desired flip angles are specified for a grid of appropriate B_1^+ and ΔB_0 values. For the examples presented here, a $B_1^+/B_{1,\mathrm{nom}}^+$ range of 0.35-1.30 was selected to represent typical variations throughout the human head at 7 T, and a uniform flip angle of 180° (SECH) or 90° (BIR-4) was targeted over the entire B_1^+-ΔB_0 optimization grid. For a given optimization, the range of ΔB_0 values represented on the parameter grid corresponds to the targeted bandwidth of the given pulse. Using custom algorithms written in C++ / Matlab (The Mathworks, Natick, MA, USA), RF waveform parameters are optimized via minimization of the functions

$$\overline{\sigma}(A_0, \beta, \mu) = \frac{1}{mn} \sum_{i=1}^{m} \sum_{j=1}^{n} \left| \frac{\alpha_{i,j}^{S}(A_0, \beta, \mu) - \alpha_{i,j}^{T}}{\alpha_{i,j}^{T}} \right| \tag{6.1.1}$$

and

$$\overline{\sigma}(A_0, \beta, \lambda, \Delta\phi_1, \Delta\phi_2) = \frac{1}{mn} \sum_{i=1}^{m} \sum_{j=1}^{n} \left| \frac{\alpha_{i,j}^{S}(A_0, \beta, \lambda, \Delta\phi_1, \Delta\phi_2) - \alpha_{i,j}^{T}}{\alpha_{i,j}^{T}} \right| , \tag{6.1.2}$$

where i and j are the respective B_1^+ and ΔB_0 indices on the corresponding parameter space grid, α^S is the flip angle according to Bloch equation simulation, and α^T is the designated target flip angle. The amplitude and phase (or frequency) modulations for the SECH pulse are described by the parameters A_0, β ,and μ, and the BIR-4 modulations are described by the parameters A_0, β, λ, $\Delta\phi_1$, and $\Delta\phi_2$. The role of each parameter in determining the modulation patterns can be inferred from the modulation functions and associated discussion provided in Appendix C.

Parameter values resulting from each optimization are presented in Figures 50 and 51 for the SECH and BIR-4 pulses, respectively. These figures can be used as look-up tables for the appropriate parameter values given a desired pulse bandwidth. As anticipated, amplitudes of both adiabatic pulse types should be maximized. As functions of optimization bandwidth, optimized SECH parameters change smoothly and predictably. For a given bandwidth, optimized SECH pulses show marked improvements over traditionally designed SECH pulses, especially in low-B_1^+ regions; the most significant penalty may be the smoothness of the slice profile. Optimized BIR-4 phase changes ($\Delta\phi_1$ and $\Delta\phi_2$) deviate very little from the respective theoretical values of $\pi + \alpha/2$ and 0 (where α is the nominal flip angle). Optimized BIR-4 parameters β and λ apparently do not change in a systematic way. This result may highlight an area in which the numerical optimizations are particularly useful since the corresponding ideal waveform adjustments may not be analytically derivable. For both SECH and BIR-4 pulses, large gains in flip-angle uniformity may be realized simply by choosing the lowest acceptable bandwidth for a given application.

In addition to the actual optimized parameter values, pre- and post-optimization waveforms are compared by example in three contexts: amplitude and phase modulation waveforms, simulated slice profiles, and flip-angle values as simulated on ΔB_0-B_1^+ grids relevant to 7 T human brain imaging. These results are presented in Figures 52 and 53.

Plots of σ vs. bandwidth emphasize that flip-angle uniformity is a linear function of the desired bandwidth for both SECH and BIR-4 pulses. As previously mentioned, this implies that pulse bandwidth should be chosen as low as possible for a given application in order to ensure an adequate level of B_1^+-insensitivity. Figure 54 demonstrates the power of such an appropriate bandwidth selection in the context of SECH pulses used for T_1 weighting at 7 T. Reported in the figure are simulated

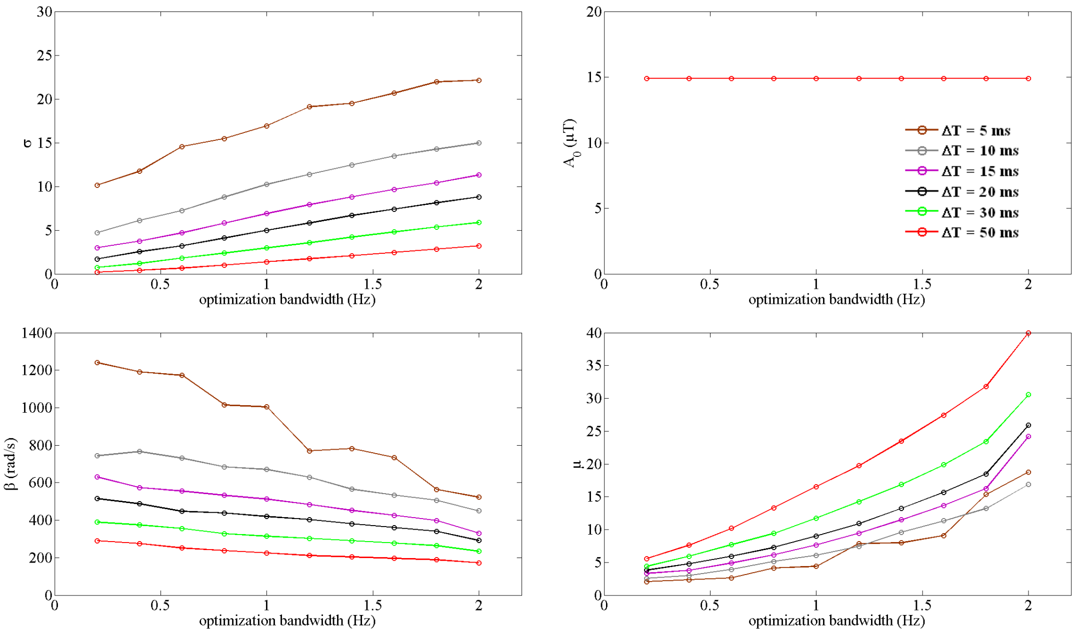

Figure 50: Parameter values resulting from numerical optimization of hyperbolic secant pulses for magnetization inversion in the human brain at 7 T. These parameter values are plotted as a function of the pulse bandwidth targeted in the optimization. The value of the cost function (Equation 6.3.1) is indicated by σ (upper left) and was found to depend linearly on the optimization bandwidth. All parameter values change with bandwidth in somewhat predictable ways with amplitude always at the maximum allowed value (upper right), β decreasing linearly with bandwidth, and μ increasing with bandwidth in a somewhat exponential fashion. Colors indicate the various pulse durations investigated (from 5–50 ms in this case).

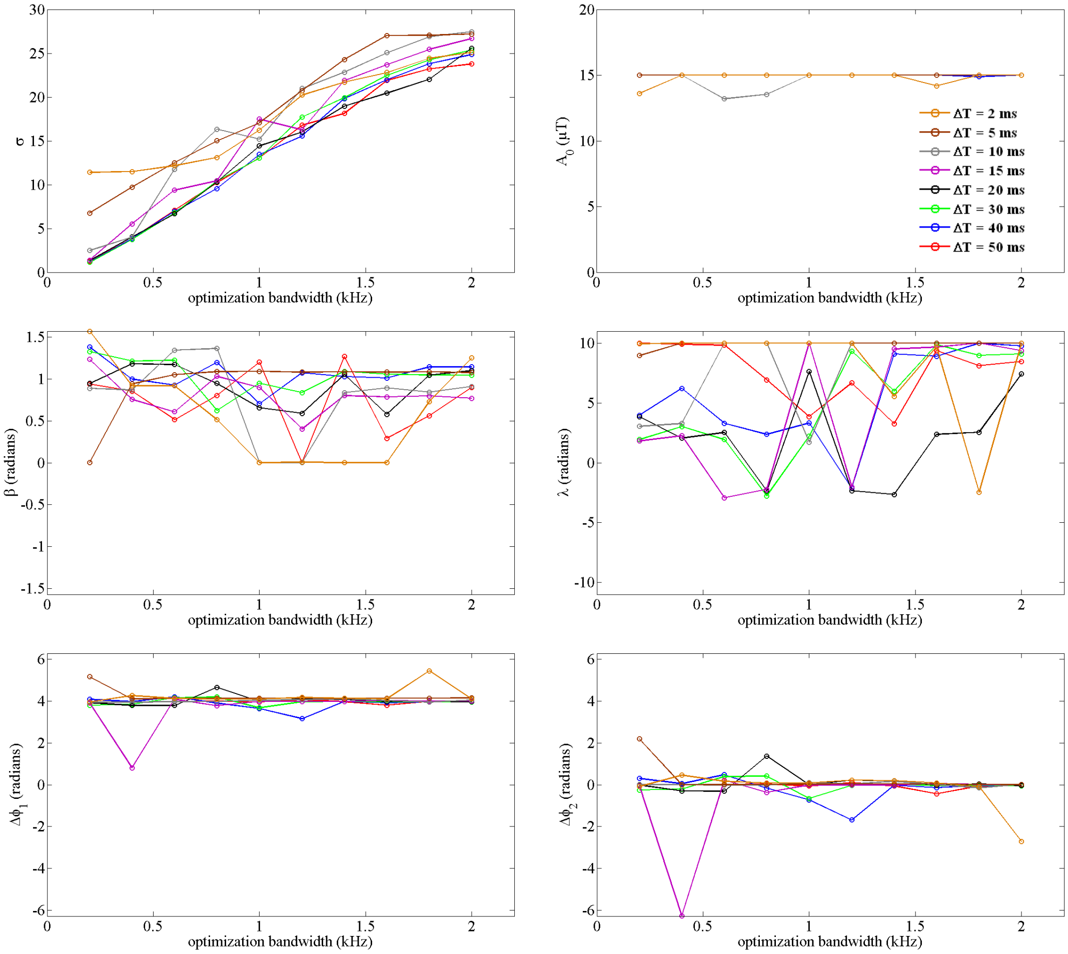

Figure 51: Parameter values resulting from numerical optimization of BIR-4 pulses to achieve 90° excitation over a ranges of field variations observed in human brain at 7 T. These parameter values are plotted as a function of the pulse bandwidth targeted in the optimization. The value of the cost function (Equation 6.3.3) is indicated by σ (upper left) and was found to depend linearly on the optimization bandwidth, just as in the case of hyperbolic secant pulses (Figure 50). While amplitude (top right) and phase-shift parameters (bottom row) were found to be largely constant as a function of bandwidth, values of the parameters β and λ vary with bandwidth in unpredictable ways. Colors indicate the various pulse durations investigated (from 2–50 ms in this case).

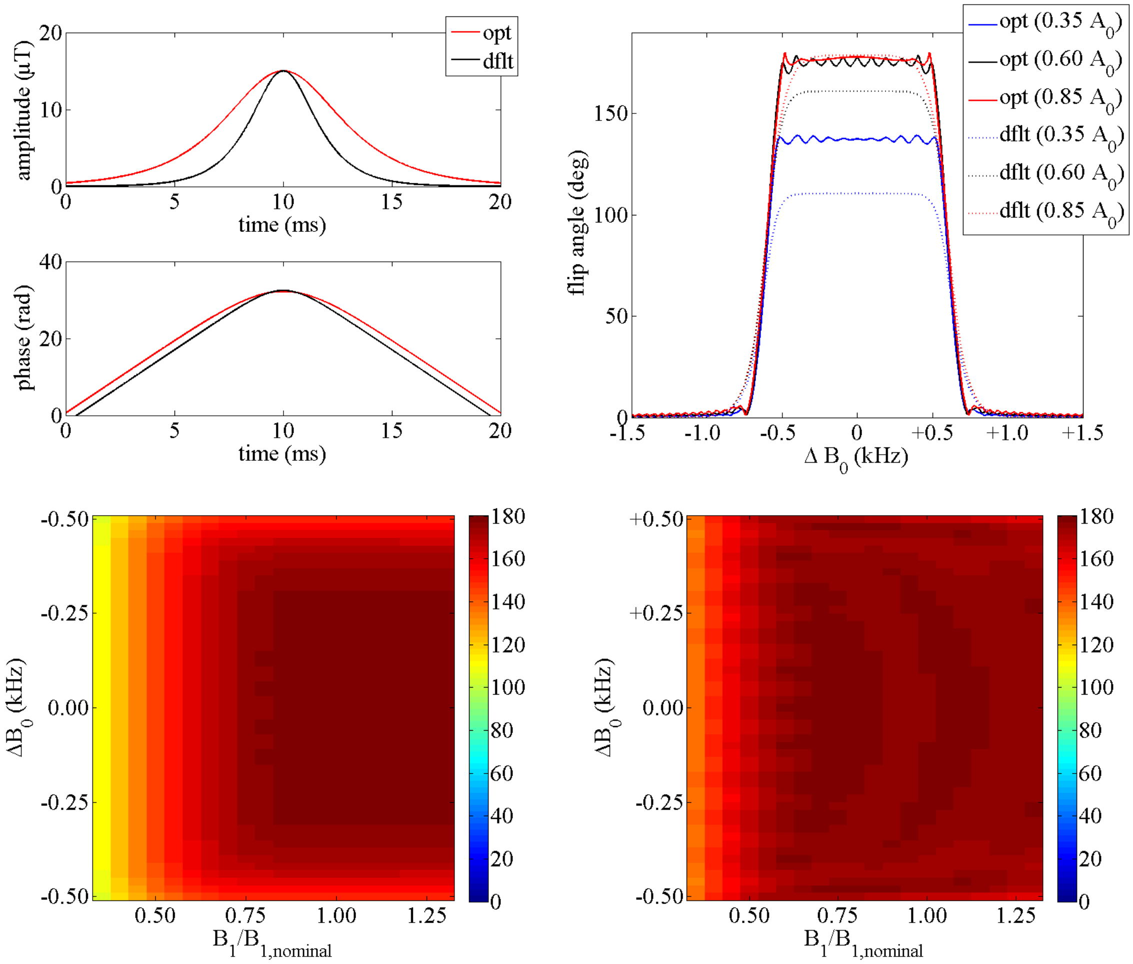

Figure 52: Comparison of two 20 ms hyperbolic secant inversion pulses, one with modulation functions suggest by MR literature (72; 73) (denoted by `dflt`) and the other with numerically optimized modulation functions (indicated by `opt`). Included in the comparison are amplitude and phase modulation patterns (upper left), simulated slice profiles for a range of relative B_1^+ magnitudes, and flip angles as simulated on grids of ΔB_0 and B_1^+ values relevant to field variations observed in the human brain at 7 T. The bottom right grid corresponds to the `dflt` pulse and the bottom right to the `opt` pulse. Significant differences can be seen in the magnetization response to the pulses, with the optimized pulse most notably extending B_1^+-insensitivity to lower B_1^+ values.

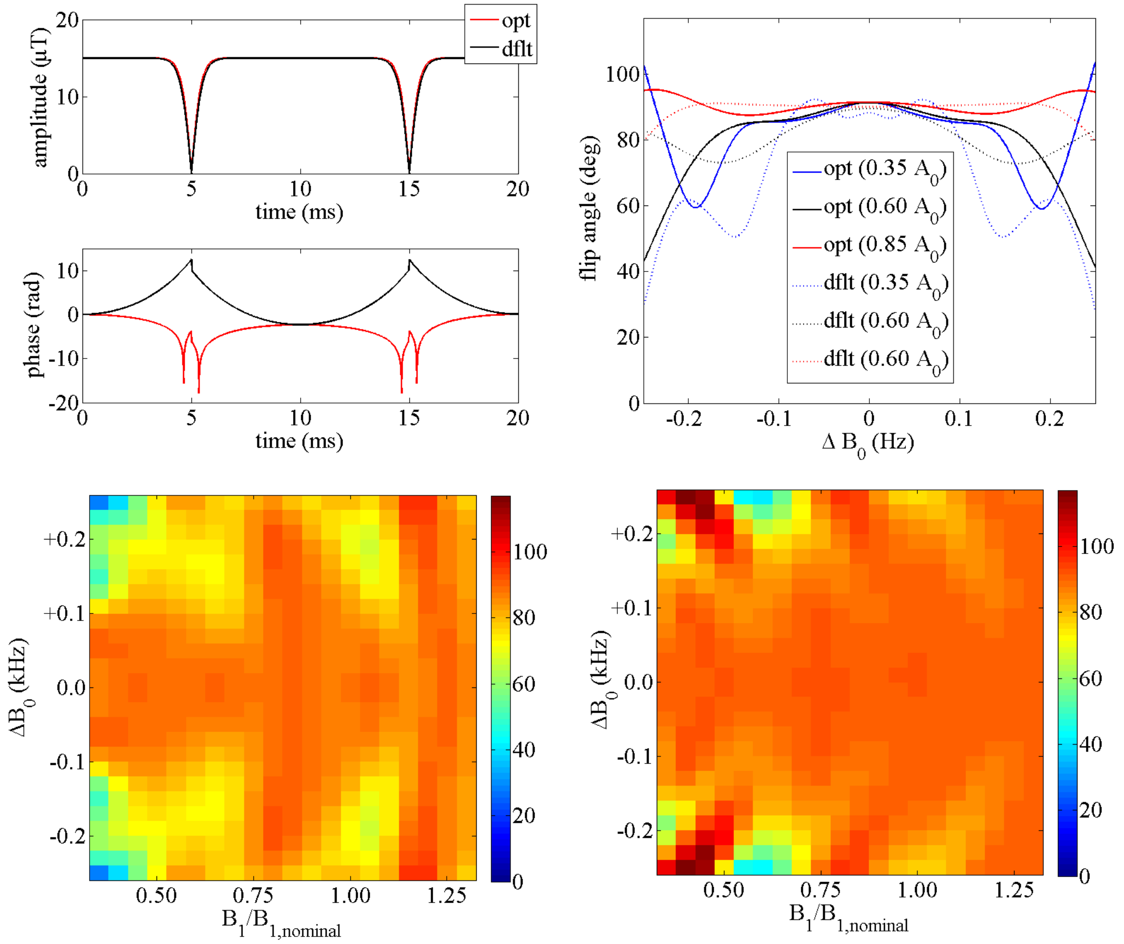

Figure 53: Comparison of two 20 ms, 90° BIR-4 excitation pulses, one with modulation functions suggest by MR literature (76) (denoted by `dflt`) and the other with numerically optimized modulation functions (indicated by `opt`). Included in the comparison are amplitude and phase modulation patterns (upper left), simulated slice profiles for a range of relative B_1^+ magnitudes, and flip angles as simulated on grids of ΔB_0 and B_1^+ values relevant to field variations observed in the human brain at 7 T. The bottom right grid corresponds to the `dflt` pulse and the bottom right to the `opt` pulse. Significant differences can be seen in the magnetization response to the pulses, with the optimized pulse most notably extending B_1^+-insensitivity over a wider bandwidth.

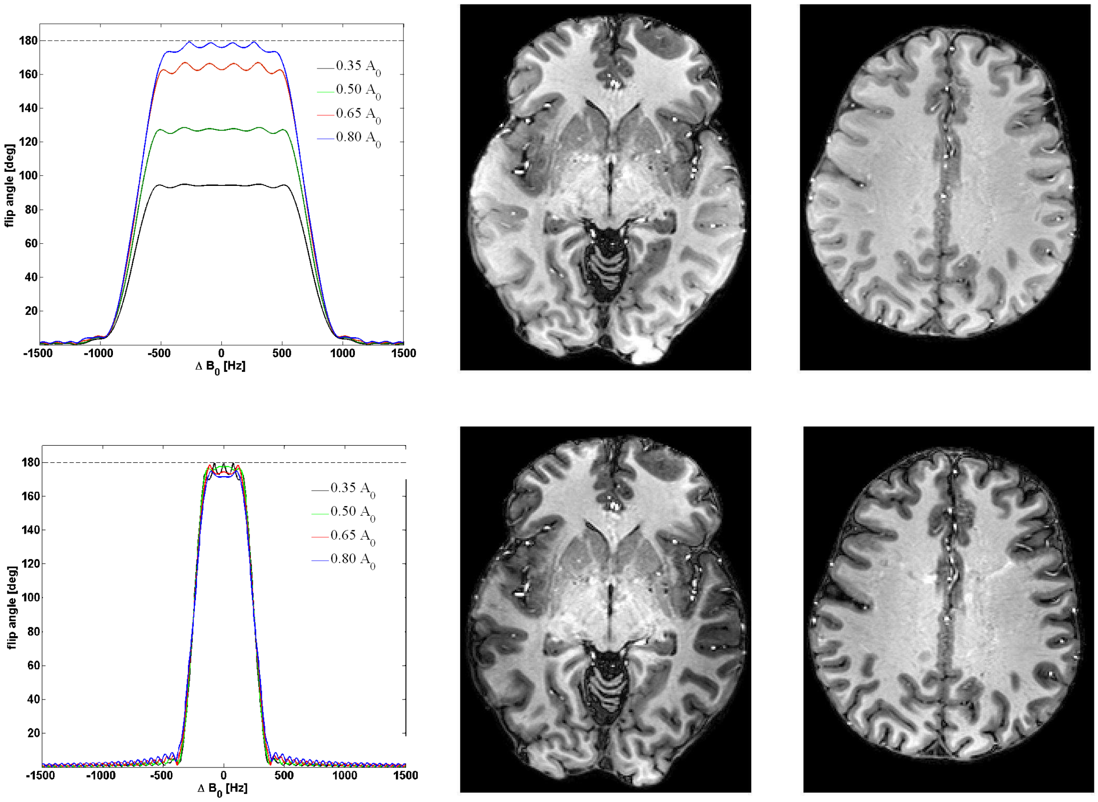

Figure 54: Slice profile simulations and T_1 weighted images acquired at 7 T for a manufacturer-implemented SECH inversion pulse (top row) and a numerically optimized SECH pulse (bottom row). When using the optimized pulse, whole-brain averaged grey/white matter contrast-to-noise measurements were found to increase by $\sim 30\%$ due to improved inversion efficiency in the face of severe B_1^+ inhomogeneities. In this case, improved inversion efficiency is largely due to the appropriate choice of a narrower pulse bandwidth in order to maximize B_1^+ insensitivity.

slice profiles and T_1-weighted images for which different SECH inversion pre-pulses were used. Use of the optimized pulse results in significantly more T_1 contrast, the production of which is the goal of the given inversion recovery sequence.

6.2 SAR-limited optimization of composite pulses for short-T_R applications

The volume excitation pulses presented in Chapter III would perhaps most commonly be utilized in conjunction with a 3-D, steady-state signal acquisition. Such an imaging sequence relies upon short repetition times so as to make the acquisition time across a large 3-D volume practical. At high field, scan times for these sequences are likely limited by SAR restrictions. Thus, due to their high power, many of the pulsed resulting from the study of Chapter III, may not prove practical for use with such sequences. A potential strategy of improving the practicality of these pulses is to incorporate power constraints directly into the optimization procedure. The purpose of this investigation was to test the efficacy of such an approach and evaluate the effects of this additional optimization constraint on pulse performance.

In practice, SAR constraints were included in optimizations in the form of minimum repetition times ($T_{R,\text{min}}$) as described by Equations 3.2.5a and 3.2.5b. For a given optimization, a maximum acceptable T_R value ($T_{R,\text{max}}$) was designated and the minimization of the cost function performed subject to the constraint $T_{R,\text{min}} \leq T_{R,\text{max}}$. In addition to the use of this T_R constraint, the pulses considered in this investigation differ from those presented in Chapter III in that the target flip angle (α^T) for a given optimization was determined by considering the designated $T_{R,\text{max}}$ and an approximate mean T_1 value for the brain at 7 T. The latter was taken to be 1650 ms as suggested by the MR literature (66). Together, $T_{R,\text{max}}$ and T_1 define a flip angle, known as the Ernst angle, for which the transverse component of the steady-state magnetization is maximized. The Ernst angle (α_E) is given in these terms by the expression

$$\alpha_E = \arccos\left(e^{-T_{R,\mathrm{max}}/T_1}\right) . \tag{6.2.1}$$

Given these optimization constraints, five non-selective, B_1^+-insensitive composite pulses were generated with $T_{R,\mathrm{max}}$ values of 50, 100, 200, 300, and 400 ms. The optimization grids spanned respective $B_1^+/B_{1,\mathrm{nom}}^+$ and ΔB_0 ranges of 0.3–1.0 and ±250 Hz. In accordance with the results of Chapter III, the largest number of sub-pulses that could be confidently employed without detrimentally affecting the efficacy of the optimization were used. In this case, 200 sub-pulses were chosen. Sub-pulse durations were varied such that the 200 sub-pulses resulted in total pulse durations of approximately 1–10 ms in 1 ms increments for a total of 10 pulses for each $T_{R,\mathrm{max}}$ value (50 optimized pulses total). The pulses in each $T_{R,\mathrm{max}}$ class with the best performance as measured by the minimization cost function are presented in Figures 55–57 along with a block pulse of the same nominal flip angle as the $T_{R,\mathrm{max}} = 50$ ms pulse.

The simulation results in Figures 55–57 indicate that the optimization is fairly robust even for T_R values as low as 100 ms. At and below this point, the performance of resulting pulses suffers, particularly at the lowest B_1^+ values. However, even at T_R of 50 ms a high degree of B_1^+-insensitivity is still present. Thus, there is promise that the use of power constrained optimizations can result in composite pulses that exhibit B_1^+-insensitivity while conforming to the practical demands of 3-D steady state imaging sequences.

The five optimized pulses presented in Figures 55–57 and a `sinc` pulse with simi-

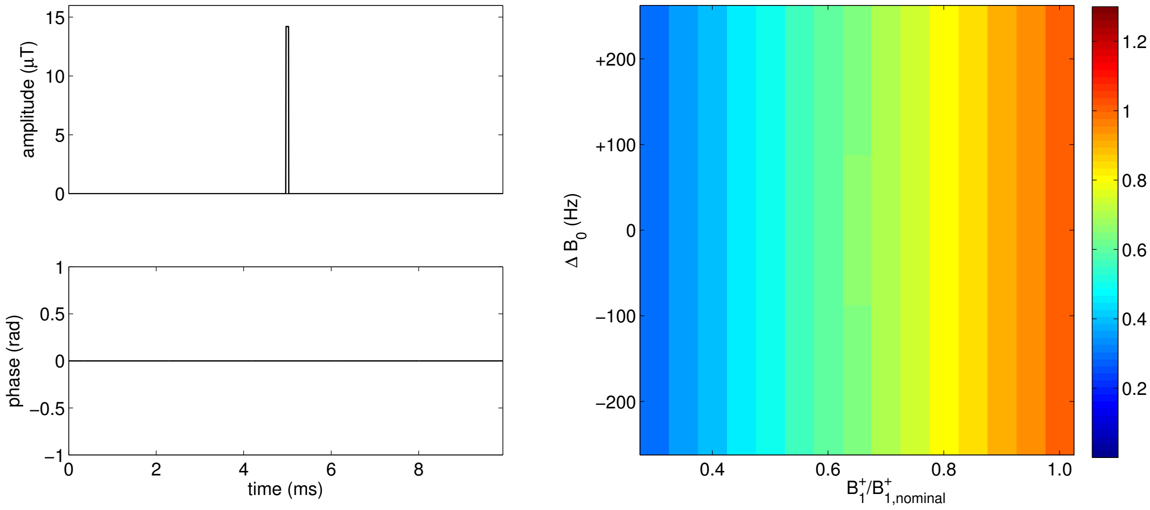

(a) $T_{R,\mathrm{min}} = 8\,\mathrm{ms}$

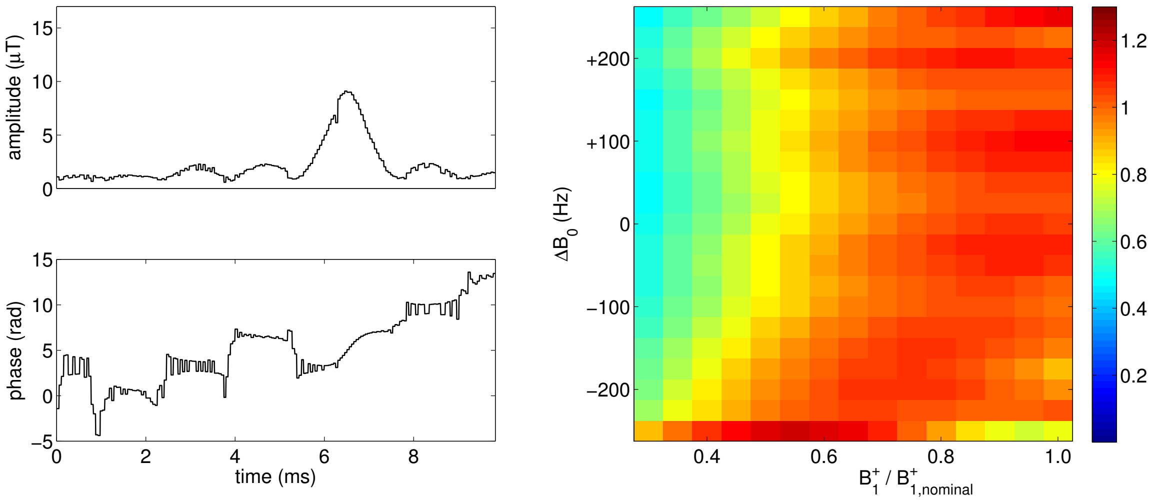

(b) $T_{R,\mathrm{max}} = 50\,\mathrm{ms}$

Figure 55: A power-limited volume excitation pulse with $T_{R,\mathrm{max}} = 50\,\mathrm{ms}$ (b) and a block pulse with the same nominal flip angle (a). For each pulse, amplitude and phase modulation waveforms are show at left and simulated flip angles over a grid of ΔB_0 and B_1^+ values are shown at right. Flip-angle values have been normalized to the target flip angle (which is a function of $T_{R,\mathrm{max}}$) of each pulse. The block pulse is not optimized and thus is assigned a value of $T_{R,\mathrm{min}}$ rather than a value of $T_{R,\mathrm{max}}$. Results indicate that a significant degree of B_1^+-insensitivity is attainable even at $T_{R,\mathrm{max}}$ values as low as 50 ms

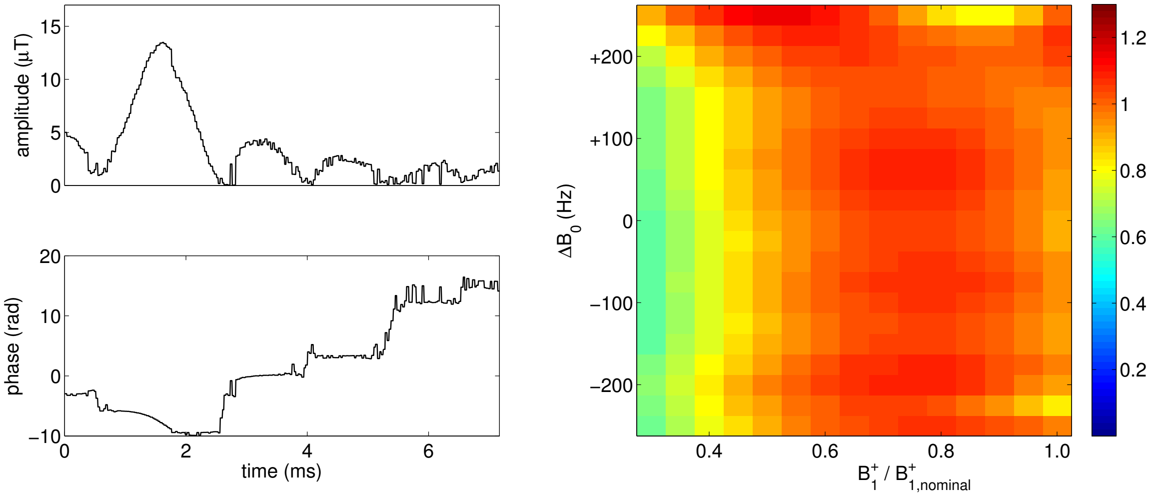

(a) $T_{R,\max} = 100\,\mathrm{ms}$

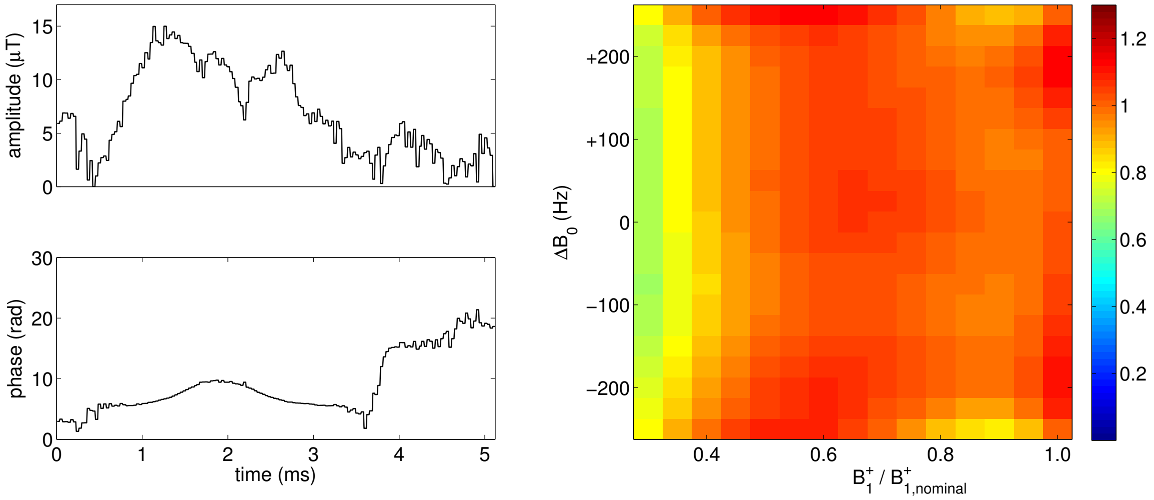

(b) $T_{R,\max} = 200\,\mathrm{ms}$

Figure 56: Power-limited volume excitation pulses for the given values of $T_{R,\max}$. For each pulse, amplitude and phase modulation waveforms are show at left and simulated flip angles over a grid of ΔB_0 and B_1^+ values are shown at right. Flip-angle values have been normalized to the target flip angle (which is a function of $T_{R,\max}$) of each pulse.

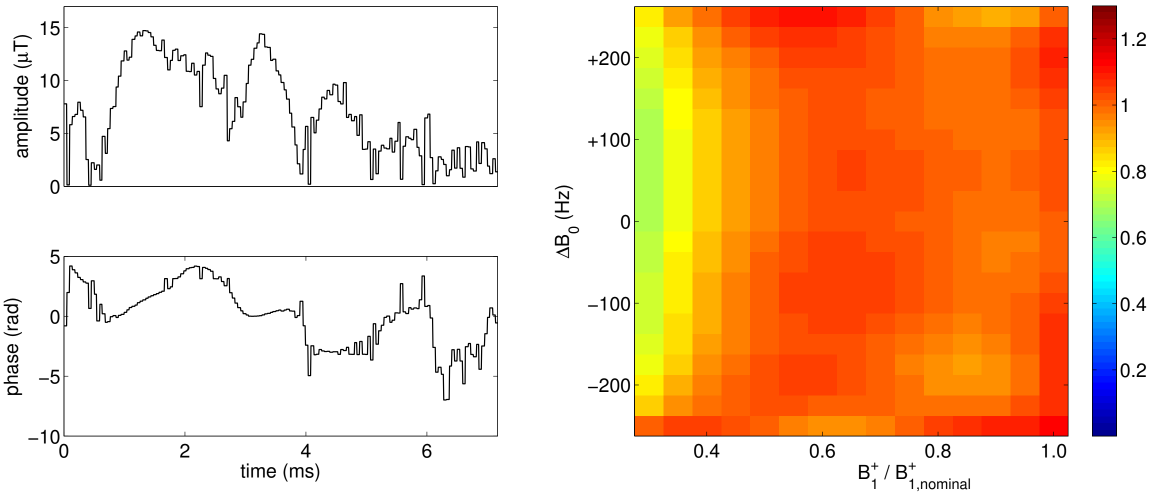

(a) $T_{R,\max} = 300\,\mathrm{ms}$

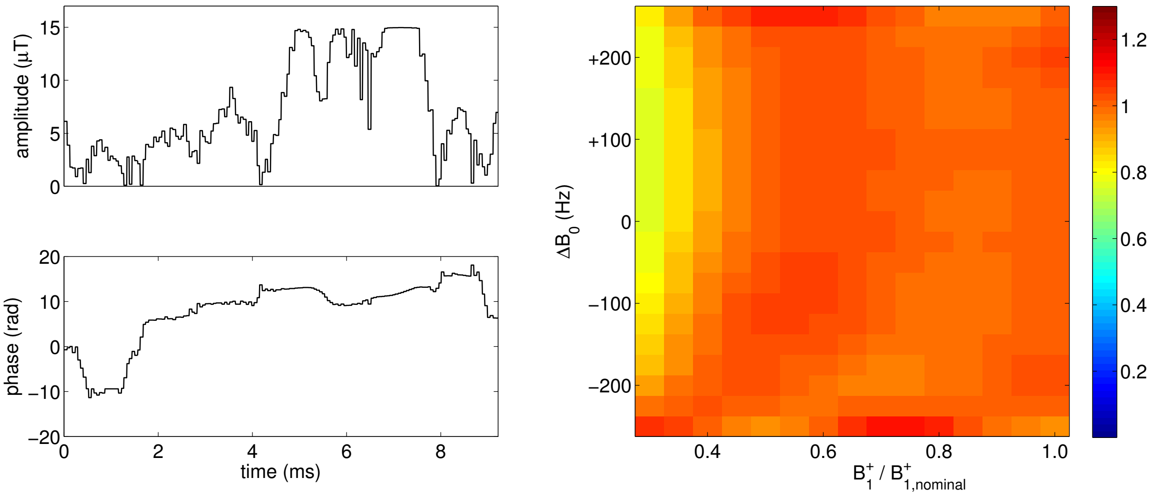

(b) $T_{R,\max} = 400\,\mathrm{ms}$

Figure 57: Power-limited volume excitation pulses for the given values of $T_{R,\max}$. For each pulse, amplitude and phase modulation waveforms are show at left and simulated flip angles over a grid of ΔB_0 and B_1^+ values are shown at right. Flip-angle values have been normalized to the target flip angle (which is a function of $T_{R,\max}$) of each pulse.

lar field-sensitive properties to those of the block pulse shown in Figure 55 were also implemented for human scanning at 7 T. In order to accommodate whole-brain scanning with the longer T_R values necessitated by some of the pulses, voxel dimensions were somewhat coarse at $3 \times 3 \times 5$ mm. Axial images through the 3-D volume are shown in Figure 58 for each of the pulses highlighted in Figures 55–57 as well as for a `sinc` pulse. In the latter case, a T_R value of 50 ms was chosen and the nominal flip angle was set to the same value as that of the corresponding optimized pulse. *In vivo* results indicate that power-limited composite pulse optimizations are successful in producing pulses with B_1^+-insensitivity as can be inferred from the increased MR signal uniformity. These desired effects are most noticeable in the cerebellum, a location at which the the B_1^+ field is especially weak; however, the center brightening (or, equivalently, signal reduction on the periphery) observed for the `sinc` pulse is also notably reduced in the central slices of all scans performed with optimized pulses. In some case, optimized pulses do result in potentially undesirable effects. For example, there exists some banding artifacts in the uppermost slices, particularly for the longer T_R pulses. This may be indicative of signal aliasing from outside the imaging field of view and thus reflects on the non-selective nature of the composite excitations. The `sinc` pulse on the other hand results in no such artifacts, presumably because of the sharp frequency profile that allows for excitation only within the limited field of view. Additionally, optimized pulses, in some cases, result in pronounced T_2^* weighting. These effects appear to correlate somewhat with the amplitude and duration of the pulses such that T_2^* weighting is strongest when durations are long but amplitudes (really, integrated amplitudes) are low. The $T_R = 100\,\mathrm{ms}$ pulse is a good example of this.

Future explorations of power-limited pulses could include several different objectives. One goal would be to attempt to better understand the origin of the observed T_2^* weighting and determine pulse design strategies that could be used to control such tissue weighting. Additionally, improved B_0 shimming approaches could be utilized to reduce the necessary ΔB_0 range targeted in pulse optimizations, thereby potentially improving B_1^+-insensitivity for low $T_{R,\max}$ values.

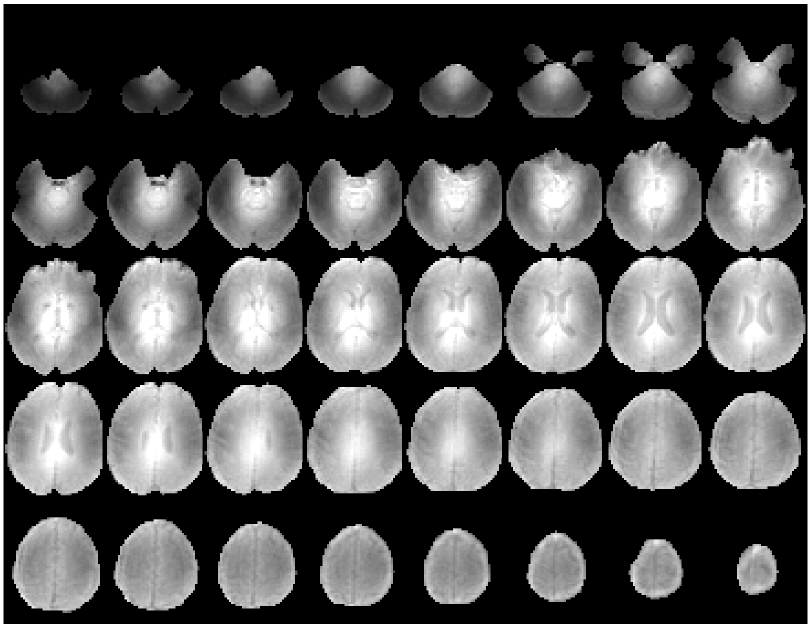

(a) `sinc`

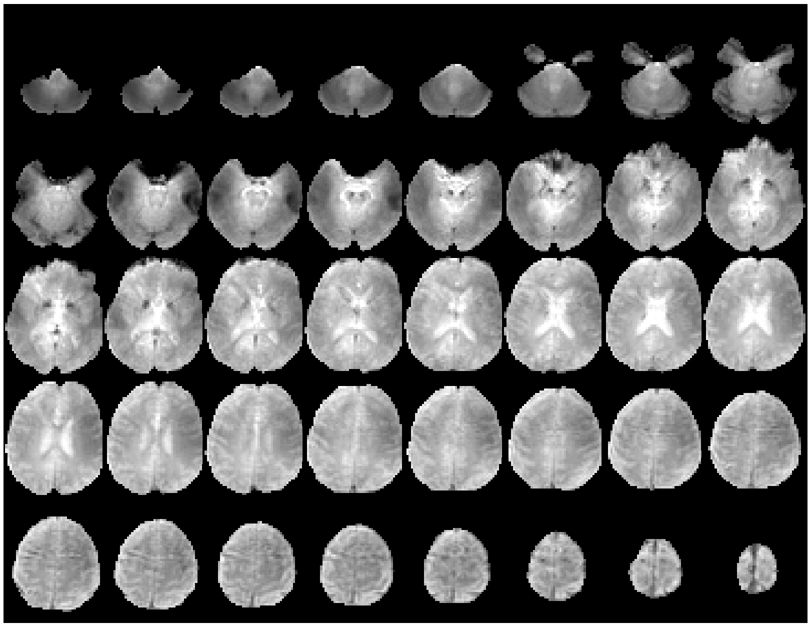

(b) $T_{R,\max} = 50\,\mathrm{ms}$

Figure 58: *In vivo* results for a `sinc` pulse (a) and the power-limited, volume excitation pulse with $T_{R,\max} = 50\,\mathrm{ms}$ (b). The optimized pulse result in improved excitation uniformity with respect to the `sinc` pulse as evidenced by reduced center brightening and signal gains in low-B_1^+ regions such as the cerebellum. The optimized pulse exhibits T_2^* weighting as well as banding artifacts that may be indicative of excitation beyond the imaging field of view.

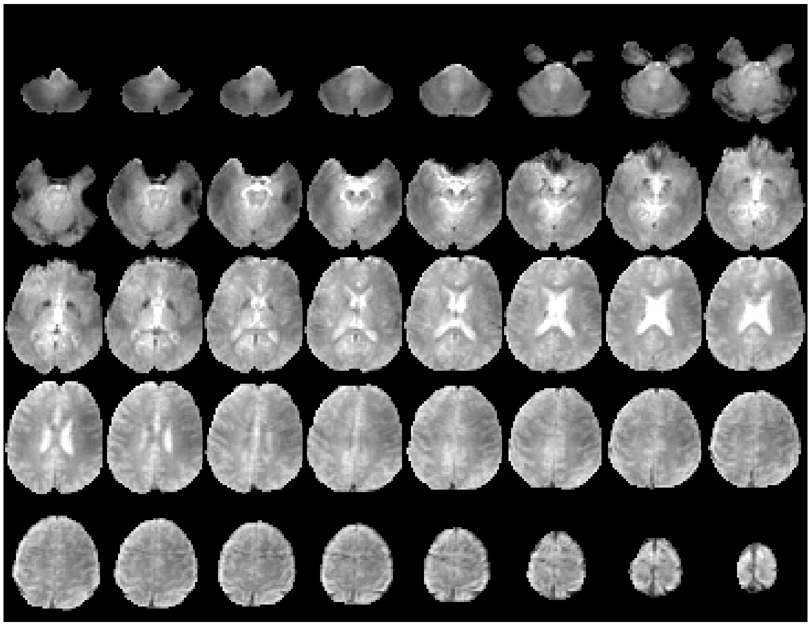

(a) $T_{R,\max} = 100\,\mathrm{ms}$

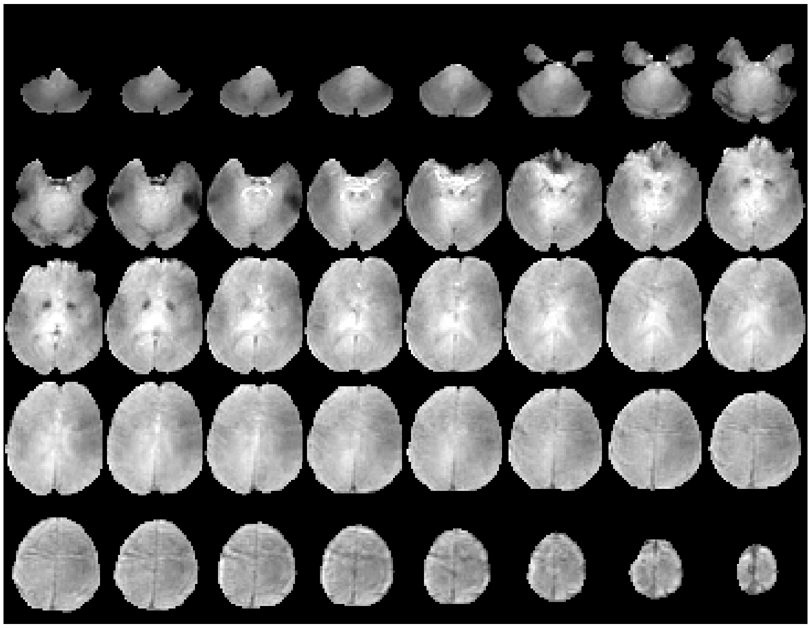

(b) $T_{R,\max} = 200\,\mathrm{ms}$

Figure 59: *In vivo* results for power-limited, volume excitation pulses with the indicated $T_{R,\max}$ values. Both optimized pulses result in improved excitation uniformity with respect to the `sinc` pulse as evidenced by reduced center brightening and signal gains in low-B_1^+ regions such as the cerebellum. Optimized pulses exhibit varying degrees of T_2^* weighting as well as banding artifacts that may be indicative of excitation beyond the imaging field of view.

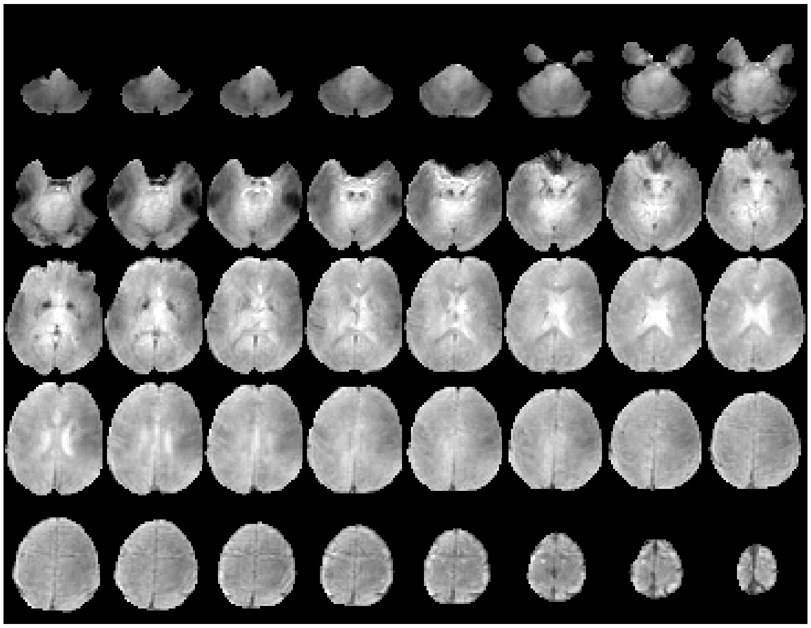

(a) $T_{R,\max} = 300\,\mathrm{ms}$

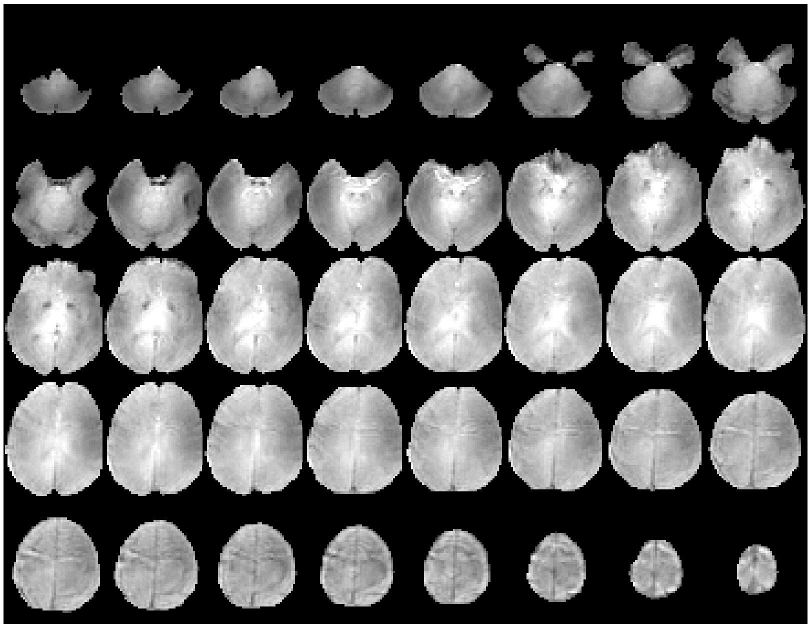

(b) $T_{R,\max} = 400\,\mathrm{ms}$

Figure 60: *In vivo* results for power-limited, volume excitation pulses with the indicated $T_{R,\max}$ values. Both optimized pulses result in improved excitation uniformity with respect to the `sinc` pulse as evidenced by reduced center brightening and signal gains in low-B_1^+ regions such as the cerebellum. Optimized pulses exhibit varying degrees of T_2^* weighting as well as banding artifacts that may be indicative of excitation beyond the imaging field of view.

6.3 Composite RF Pulses for Frequency-selective, B_1^+-insensitive Excitation

The goal of this investigation was to determine the feasibility of producing frequency-selective excitation from composites of block-shaped sub-pulses. All pulse designs share the aims of generating B_1^+-insensitive, frequency-selective, 90° excitations suitable for use in the human brain at 7 T. If successful, these pulses could be used in conjunction with a linear field gradient to provide an alternative to the pulse designs presented in Chapter IV or be used as slab-selective variants of those presented in Chapter III. Additionally, there would likely be applications in high-field NMR spectroscopy for such B_1^+-insensitive pulses with sharp frequency profiles.

Amplitudes and phases for 128 block-shaped sub-pulses, each with 64 μs duration (total pulse duration = 8.2 ms), were numerically optimized with two conditions being simultaneously imposed on the magnetization response:

1. the transverse magnetization should be maximized within a specified frequency bandwidth (chosen for these preliminary studies to be ±0.5 kHz) and for a range of relative B_1^+ magnitudes characteristic of the human brain at 7 T.
2. the transverse magnetization in a frequency band outside the target bandwidth (e.g., from 2.5 to 0.5 kHz and from +0.5 to +2.5 kHz) should be minimized for the same range of relative B_1^+ magnitudes.

Optimization of the composite amplitude and phase modulations was performed by minimizing the average value of a cost function across a grid of B_1^+ and $\Delta\omega$ values[†], and cost functions involved a difference between actual magnetization and

---

[†] The symbol ω appears here rather than B_0 only to emphasize that it is the frequency profile of

that of specified target values. Three different conditions on the phase of transverse magnetization were independently explored with the goal of producing pulses for three separate potential applications: slice-selective saturation, slice-selective excitation for imaging with a linear rephasing gradient, and slice-selective excitation with zero through-slice phase. The three corresponding optimization schemes are described as follows:

Optimization Scheme I: target flip angle

In this case, only target flip angles were specified (i.e., no information related to the final magnetization phase is considered in the optimization problem). The cost function is given by

$$\begin{aligned}\delta_\alpha(\mathbf{A},\boldsymbol{\phi}) =& \frac{\lambda}{m\,n}\sum_{\sigma,\rho=1}^{m,n}\left|\frac{\alpha^S_{\sigma,\rho}(\mathbf{A},\boldsymbol{\phi})-\alpha^T_{\sigma,\rho}}{\alpha^T_{\sigma,\rho}}\right| \\ &+\frac{(1-\lambda)}{p\,q}\sum_{\mu,\nu=1}^{p,q}\left|\frac{\alpha^S_{\mu,\nu}(\mathbf{A},\boldsymbol{\phi})-\alpha^T_{\mu,\nu}}{\alpha^T_{\mu,\nu}}\right|,\end{aligned} \tag{6.3.1}$$

where σ and ρ are indices of $B_1^+/B_{1,\mathrm{nom}}^+$ and ΔB_0 in the targeted frequency band of the optimization grid, μ and ν are the corresponding indices for the portion of the optimization grid outside the targeted frequency band, α^T is the target flip angle, α^S is the simulated flip angle, $\mathbf{A}$ and ϕ are the vectors of composite pulse amplitudes and phases, and λ is used to achieve relative weighting of the targeted and untargeted frequency bands. In this study, target flip angles were set to 90° in the target bandwidth and 0° everywhere outside this region,

---

the pulse that is subject to optimization rather that the sensitivity of the pulse to B_0 offsets.

and λ was set to 0.5 to denote equal weighting of the two frequency domains. Since the magnetization phase resulting from minimization of this cost function may vary erratically within the targeted frequency band, this approach may be conducive to slice-selective or slab-selective saturation. In these applications, incoherent transverse phase is advantageous since this state of magnetization (typically produced by dephasing/spoiling field gradients) is required to achieve signal cancellation.

Optimization Scheme II: magnetization dot product with linear phase

In this scheme, a target linear phase along the $\Delta\omega$-direction of the optimization grid was specified. In order to enforce this target phase in the optimization, a cost function was formulated in terms of the dot product between the target and simulated magnetization vectors ($\mathbf{M}^T$ and $\mathbf{M}^S$, respectively). If ϕ^T_{BW} represents the phase of $\mathbf{M}^T$ at the edge of the targeted bandwidth such that the phase of $\mathbf{M}^T$ as a function of $\Delta\omega$ is given by

$$\phi^T_{\mathbf{M}}(\Delta\omega) = \frac{\Delta\omega}{\Delta\omega_{\mathrm{BW}}}\phi^T_{\mathrm{BW}}\,, \tag{6.3.2}$$

where $\Delta\omega_{\mathrm{BW}}$ corresponds to the value of $\Delta\omega$ at the edge of the slice-selection region of the optimization grid, a cost function in which the value ϕ_{BW} is one of the optimization parameters can be written as

$$\begin{aligned}\delta_{\text{dot}}(\mathbf{A},\boldsymbol{\phi},\phi^T_{\mathbf{M}}) =& \frac{\lambda}{m\,n}\sum_{\sigma,\rho=1}^{m,n}\left(1-\mathbf{M}^S_{\sigma,\rho}(\mathbf{A},\boldsymbol{\phi})\cdot\mathbf{M}^T_{\sigma,\rho}(\phi^T_{\mathbf{M}})\right)\\ &+\frac{(1-\lambda)}{p\,q}\sum_{\mu,\nu=1}^{p,q}\left(1-\mathbf{M}^S_{\mu,\nu}(\mathbf{A},\boldsymbol{\phi})\cdot\mathbf{M}^T_{\mu,\nu}(\phi^T_{\mathbf{M}})\right)\ ,\end{aligned}\tag{6.3.3}$$

with all indices being the same as in Equation 6.3.1. Thus, the ideal amount of linear phase through the slice is determined by the optimization, thus eliminating the need to anticipate this quantity prior to minimization. Again, the parameter λ was set at 0.5. This optimization scenario is relevant to slice-selective gradient echo imaging since a linear rephasing gradient could be used to provide a coherent signal.

Optimization Scheme III: magnetization dot product with zero phase

This scheme is identical to Scheme II in all respects except that the target magnetization is specified with $\phi^T_{\mathbf{M}} = 0$ at all points on the optimization grid. For consistency and clarity, the cost function is given again with this subtle modification:

$$\begin{aligned}\delta_{\text{dot}}(\mathbf{A},\boldsymbol{\phi}) =& \frac{\lambda}{m\,n}\sum_{\sigma,\rho=1}^{m,n}\left(1-\mathbf{M}^S_{\sigma,\rho}(\mathbf{A},\boldsymbol{\phi})\cdot\mathbf{M}^T_{\sigma,\rho}\right)\\ &+\frac{(1-\lambda)}{p\,q}\sum_{\mu,\nu=1}^{p,q}\left(1-\mathbf{M}^S_{\mu,\nu}(\mathbf{A},\boldsymbol{\phi})\cdot\mathbf{M}^T_{\mu,\nu}\right)\ .\end{aligned}\tag{6.3.4}$$

Thus, the phase of the target magnetization is not considered in the optimization. Pulses resulting from this optimization scheme could potentially be used for imaging without the need to rephase the transverse magnetization, which is typically accomplished via application of a field gradient after execution of a linear-phase excitation pulse. The advantage of eliminating this rephasing gradient is a potential reduction in T_E which is valuable for maximizing signal when imaging short-T_2^* chemical species.

Results of composite pulse optimizations conducted according to these three optimization schemes indicate varying degrees of success with respect to different desired pulse attributes. Simulation results are presented in Figures 61, 62, and 63. For comparison of these results to those of a B_1^+-sensitive frequency-selective pulse, identical simulations were performed using a 90° Gaussian-modulated `sinc` excitation with a 1 kHz bandwidth (Figure 64). In general, optimized pulses exhibit sharp frequency profiles corresponding to the targeted 1 kHz bandwidth, so thus were successful in selecting a targeted frequency band. While the Scheme III pulse has the most ragged frequency profile of the three, the Scheme I and II pulses have sharper frequency profiles than the `sinc` pulse (i.e., the transition band is narrower, although Scheme II shows increased side lobes). The B_1^+-insensitivity of the Scheme I pulses is generally excellent, with the only undesirable feature of this pulse being the imperfect in-slice frequency profile at low-B_1^+. On the other hand, the B_1^+-insensitivity of the Scheme II pulse is not as impressive and may not differ significantly from the response of the `sinc` pulse with a $\sim 50\%$ increase in amplitude. The Scheme III pulse fulfills the zero-phase and B_1^+-insensitivity conditions rather well but at the expense of a compromised frequency profile. In this case, the correct frequency band is successfully affected but the overall frequency envelope is significantly noisier than for any of the other pulses. Perhaps these characteristics can be improved upon in future studies through modification of the λ parameter. Other possible future adjustments that are relevant to all design schemes include the designation of transition frequency bands to be ignored in the optimization (thus possibly allowing for control of the sharpness of the frequency profile) and the use of Scheme I for the untargeted frequencies in conjunction with Schemes II or III for the in-slice frequencies. The latter adjustment might prove to ease constraint on the optimization so as to enhance in-slice performance, with the assumption that the phase in the untargeted region is inconsequential. Another potential optimization scheme involves maximization/minimization of the signal inside/outside the targeted bandwidth such that the complex sum of magnetization values in these regions is maximized/minimized, for example. Finally, it is worth reiterating the fact that transverse magnetization outside the ± 2.5 kHz optimization region was not constrained in any of the examples presented here, and, in general, magnetization response in this area is significant and nonuniform. Such characteristics of the magnetization response are only an issue in imaging if the frequency domains fall within the imaging volume and the sensitivity area of the coil and are even less problematic in certain spectroscopic applications. In any event, unwanted magnetization response can be suppressed by expansion of the optimization grid in the $\Delta\omega$-direction, albeit at the potential detriment to the optimization performance.

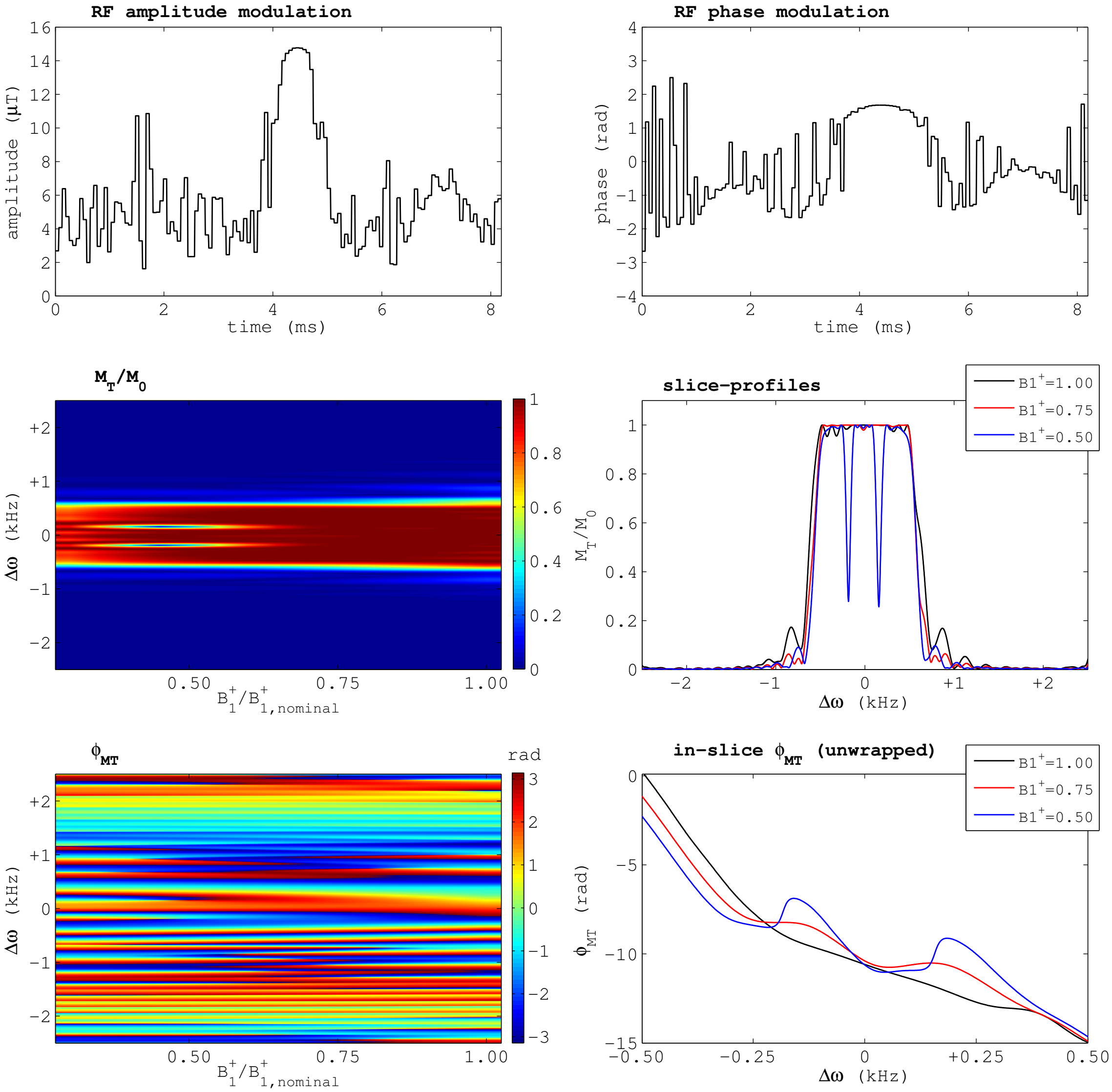

Figure 61: Simulations of an Optimization Scheme I (Equation 6.3.1) composite pulse with $\alpha^T = 90°$ and a target bandwidth of 1 kHz including: amplitude modulation (top left); phase modulation (top right); magnitude of transverse magnetization (middle left) on a grid of $B_1^+/B_{1,\text{nom}}^+$ magnitudes (horizontal axis) and frequency offsets (vertical axis); transverse magnetization as a function of frequency offset for selected $B_1^+/B_{1,\text{nom}}^+$ values (middle right); transverse magnetization phase (bottom left) on the grid of $B_1^+/B_{1,\text{nom}}^+$ and frequency offset values; and within-slice transverse magnetization phase as a function of frequency offset for selected $B_1^+/B_{1,\text{nom}}^+$ values (bottom right). As compared to the `sinc` pulse of Figure 64, this pulse achieves a high level of B_1^+-insensitivity and has somewhat of a sharper frequency profile. The non-linear phase makes the pulse conducive to saturation.

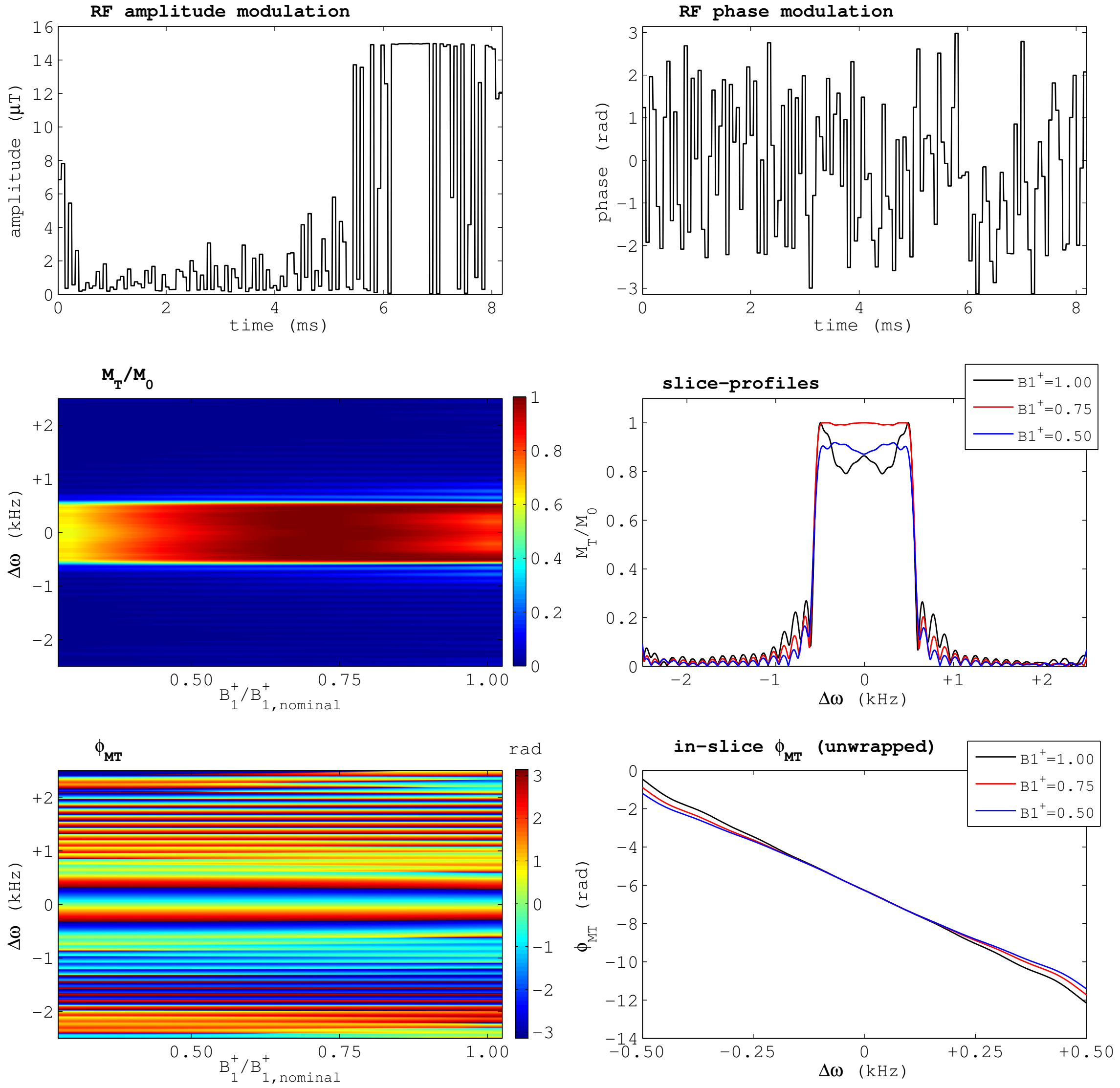

Figure 62: Simulations of an Optimization Scheme II (Equation 6.3.3) composite pulse with $\alpha^T = 90°$ and a target bandwidth of 1 kHz including: amplitude modulation (top left); phase modulation (top right); magnitude of transverse magnetization (middle left) on a grid of $B_1^+/B_{1,\text{nom}}^+$ magnitudes (horizontal axis) and frequency offsets (vertical axis); transverse magnetization as a function of frequency offset for selected $B_1^+/B_{1,\text{nom}}^+$ values (middle right); transverse magnetization phase (bottom left) on the grid of $B_1^+/B_{1,\text{nom}}^+$ and frequency offset values; and within-slice transverse magnetization phase as a function of frequency offset for selected $B_1^+/B_{1,\text{nom}}^+$ values (bottom right). The level of B_1^+-insensitivity achieved by this pulse is rather weak; however, the frequency and phase profiles are conducive of slice-selective imaging.

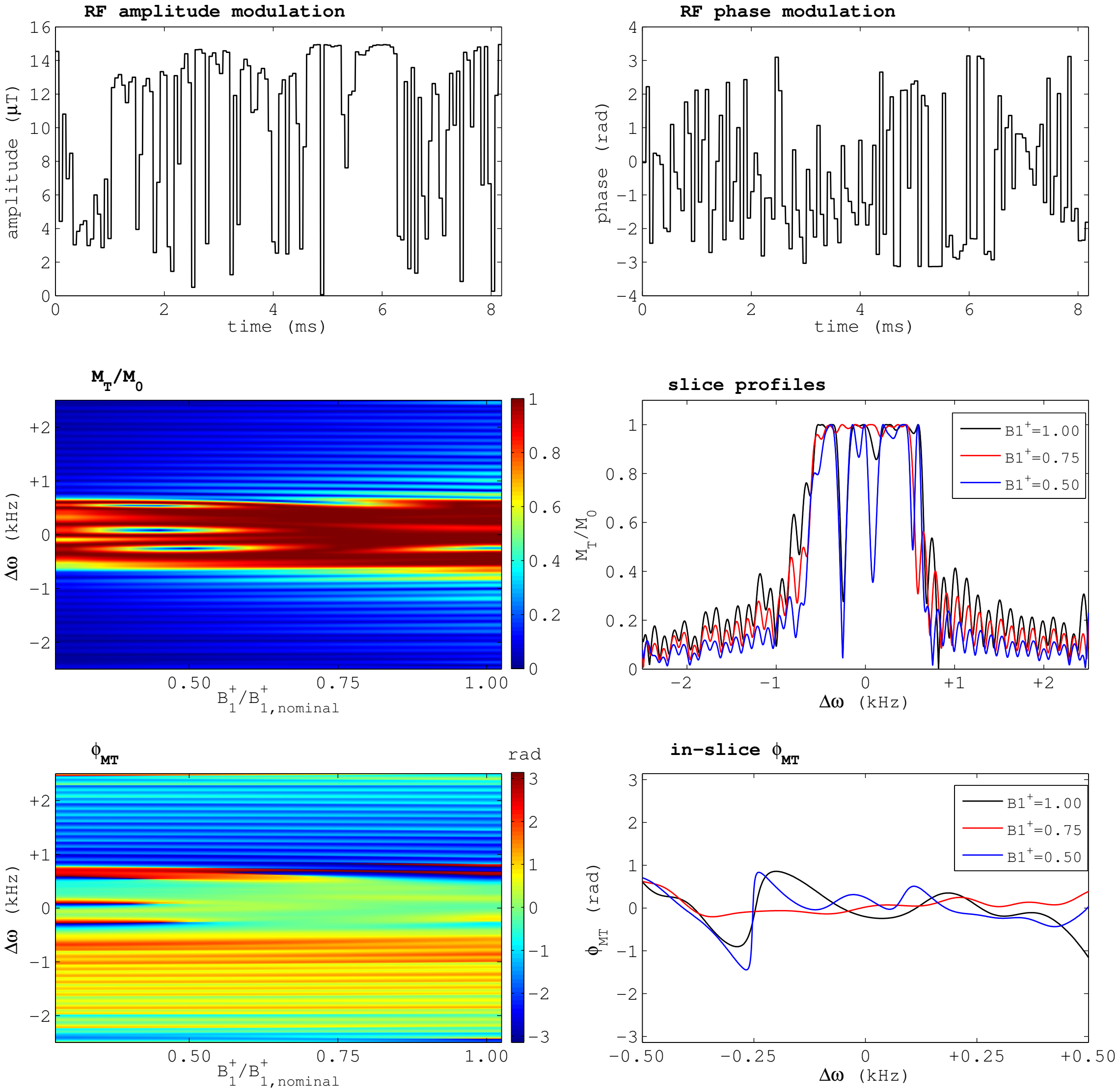

Figure 63: Simulations of an Optimization Scheme III (zero phase) composite pulse with $\alpha^T = 90°$ and a target bandwidth of 1 kHz including: amplitude modulation (top left); phase modulation (top right); magnitude of transverse magnetization (middle left) on a grid of $B_1^+/B_{1,\text{nom}}^+$ magnitudes (horizontal axis) and frequency offsets (vertical axis); transverse magnetization as a function of frequency offset for selected $B_1^+/B_{1,\text{nom}}^+$ values (middle right); transverse magnetization phase (bottom left) on the grid of $B_1^+/B_{1,\text{nom}}^+$ and frequency offset values; and within-slice transverse magnetization phase as a function of frequency offset for selected $B_1^+/B_{1,\text{nom}}^+$ values (bottom right). The B_1^+-insensitivity achieved by this pulse is apparent, and the zero-phase condition is met with some success. The frequency profile, however, is quite rough, certainty limiting the usefulness of the pulse.

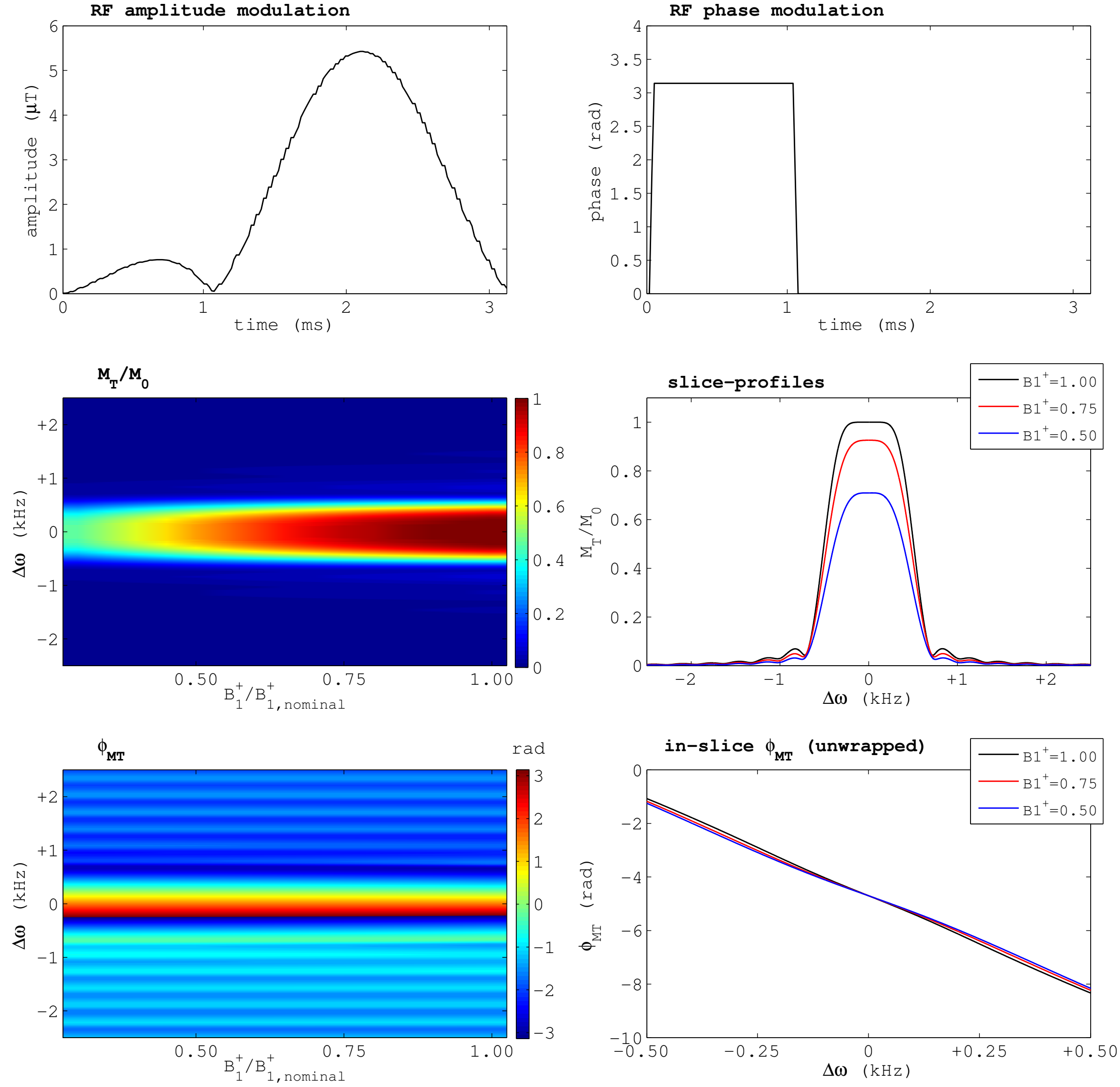

Figure 64: Simulations of an asymmetric Gaussian-modulated `sinc` pulse with $\alpha^T = 90°$ and a bandwidth of 1 kHz including: amplitude modulation (top left); phase modulation (top right); magnitude of transverse magnetization (middle left) on a grid of $B_1^+/B_{1,\mathrm{nom}}^+$ magnitudes (horizontal axis) and frequency offsets (vertical axis); transverse magnetization as a function of frequency offset for selected $B_1^+/B_{1,\mathrm{nom}}^+$ values (middle right); transverse magnetization phase (bottom left) on the grid of $B_1^+/B_{1,\mathrm{nom}}^+$ and frequency offset values; and within-slice transverse magnetization phase as a function of frequency offset for selected $B_1^+/B_{1,\mathrm{nom}}^+$ values (bottom right). Results for this `sinc` pulse are shown as a reference indicating performance typical of frequency selective pulses without B_1^+-insensitivity.

6.4 Frequency-selective Pulse Designs for Water and Lipid Suppression in MR Spectroscopy

Proton MR spectroscopic imaging (MRSI) at 7 T offers potential for gains in the SNR, increased chemical shift, and higher spectral resolution for mapping of a number of brain metabolites (32; 28). However, MRSI at 7 T is also challenged because of the short T_2 relaxation times of metabolites, as well as by B_0 and B_1^+ inhomogeneities, and the need for higher bandwidth pulses (32; 28). Preliminary MRSI results at 7 T show promises of quantifying the distributions of metabolites like NAAG, Glu, Gln, myo-Inositol in addition to the more commonly studied metabolites NAA, Creatine and Choline. However, spectral deterioration near the skull due to infiltration of skull-lipid signals has been consistently observed. In addition to prominent lipid signals in voxels closest to the skull, the use of SENSE-accelerated MRSI acquisitions results in lipid signals folding-over (SENSE-aliasing) into deeper regions of the brain. To address this issue, B_1^+-insensitive composite pulses that target the specific frequency band of lipids have been designed and implemented according to the methods of Section 6.3. The lipid-suppression strategy is to produce lipid saturation using a 90° B_1^+-insensitive excitation at the lipid resonance followed by appropriate dephasing gradients. The appropriate RF attributes for this composite pulse are shown in Figure 65. The pulse was inserted into a SENSE-accelerated 2D STEAM MRSI sequence along with appropriate dephasing gradients. The resulting MRSI spectrum obtained at 7 T (Figure 65) demonstrates promise to overcome the SENSE-aliasing artifact in the regions near the brain midline. Furthermore, the quality of lipid signal suppression was observed to be consistent across the MRSI matrix, including voxels near the scalp.

These lipid suppression results in the context of MRSI are certainly preliminary. The next step for evaluating the efficacy of such pulses is to compare results with those obtained using an excitation pulse that in not B_1^+-insensitive (such as a `sinc` pulse). Furthermore, using a phantom with the relevant metabolites, the frequency offset of the composite excitation could be verified and further calibrated so as to maximize lipid suppression while minimizing the effect of neighboring metabolites such as NAA.

In addition to this lipid-suppression pulse, a dual-band, B_1^+-insensitive composite pulse has been designed using the same methods as described in Section 6.3. The purpose of this particular design is the simultaneous saturation of water and lipid—both of which produce large NMR signals that plague the identification and quantification of MRS metabolite signals in human brain. The pulse design is presented in Figure 67 but is yet to be used experimentally.

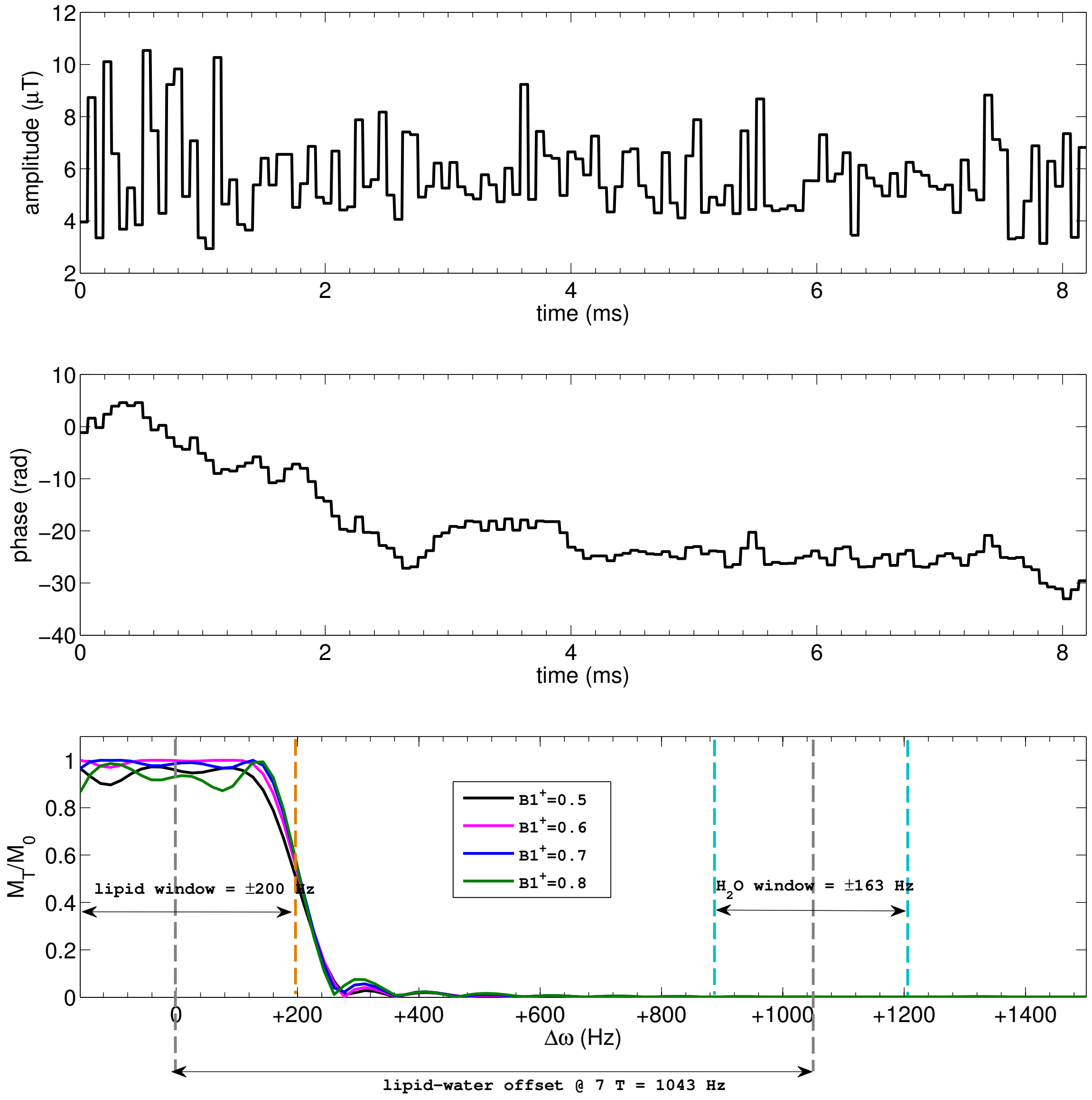

Figure 65: Suppression of the lipid signal with a spectrally-selective composite pulse that targets a ±200 Hz window for a 90° excitation while minimally effecting metabolites of interest and water which have resonances up to +1200 Hz with respect to the central lipid resonance. As reflected in the $\Delta\omega$ labels on the plot of M_T/M_0 (bottom), the pulse is designed to be executed with a carrier frequency corresponding to the center of the lipid resonance. Amplitude and phase modulations are shown at top and middle, respectively.

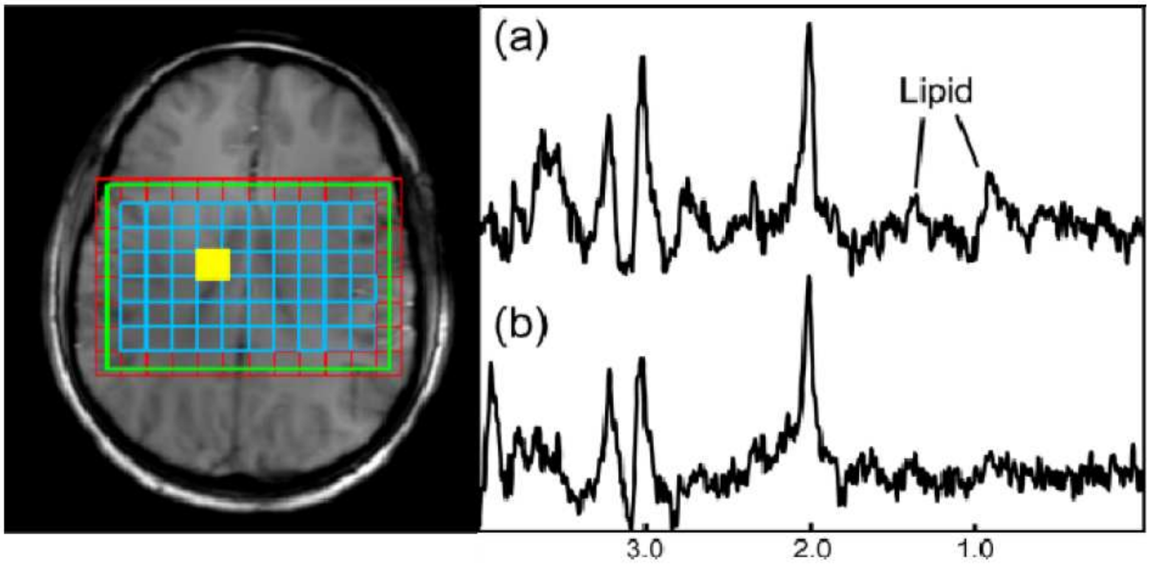

Figure 66: (a) Representative SENSE-accelerated 2-D STEAM MRSI spectrum at 7 T obtained (from the yellow voxel in the scout image) without fat-suppression pulse-trains; and (b) with the lipid-suppressing composite pulse shown in Figure 65. Clearly, the lipid suppression pulse is effective. What remains to be investigated is how much the B_1^+-insensitive characteristics of the pulse contribute to its efficacy.

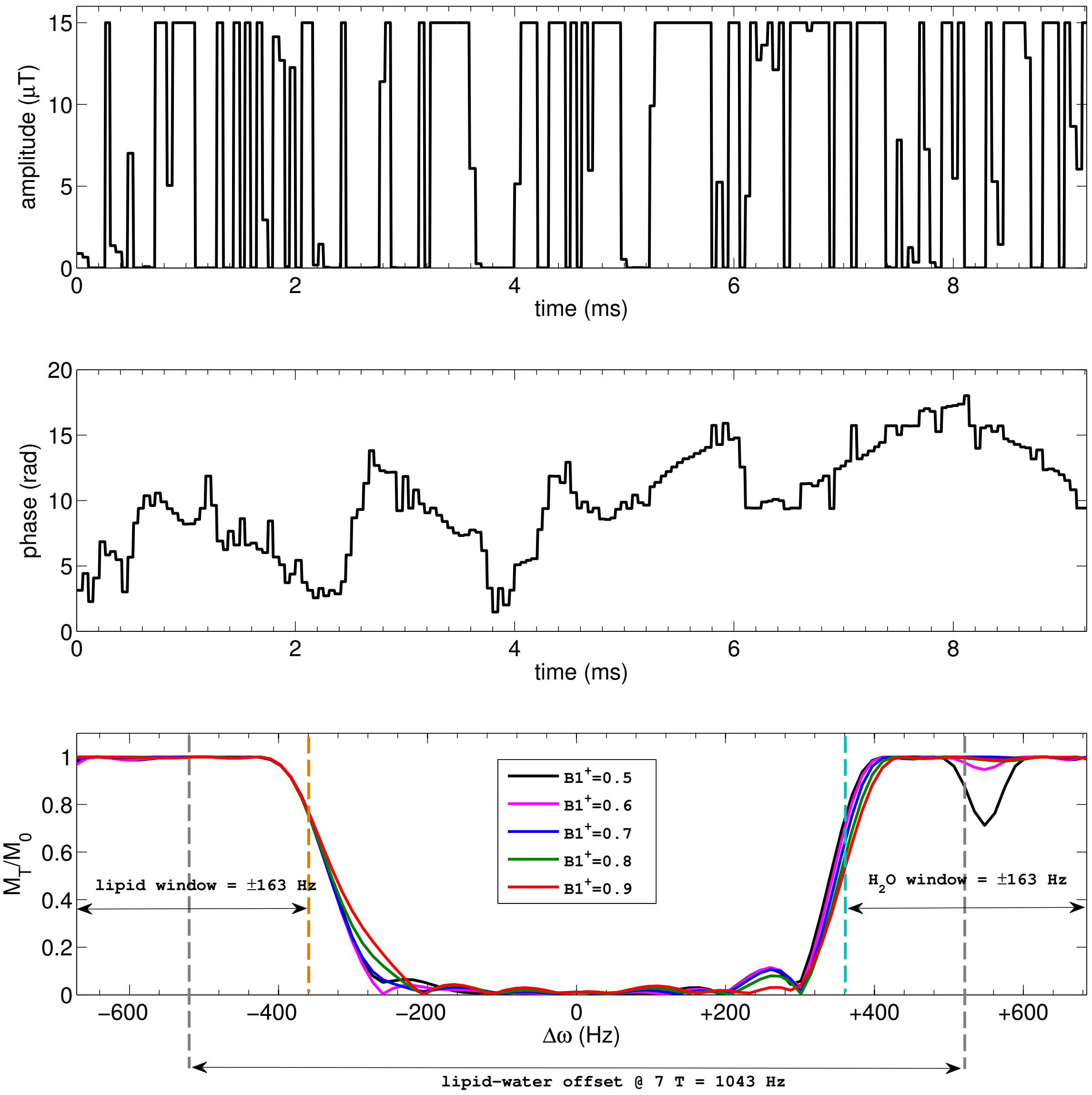

Figure 67: Simultaneous suppression of the lipid and water signals with a spectrally-selective composite pulse that targets ±163 Hz windows for a 90° excitation while minimally effecting metabolites of interest which have resonances between the two suppression bands. As reflected in the $\Delta\omega$ labels on the plot of M_T/M_0 (bottom), the pulse is designed to be executed with a carrier frequency corresponding to the mean of the lipid and water resonances. Amplitude and phase modulations are shown at top and middle, respectively.

6.5 Phase Modulation Waveforms for Harmonic Spectroscopy: Application to Polarization Transfer at a Single Transmission Frequency

The use of in vivo MRS in biomedicine for the detection of abnormal metabolism has increased recently in parallel with improvements in technology for increasing polarization toward the theoretical limit. These methods are often referred to as hyperpolarization and, for application to metabolism, aim to polarize spin-states principally by either of two techniques - utilizing nuclear interaction with electrons (DNP) or parahydrogen (PASADENA and SABRE) (85; 11). To the extent that polarization is achieved on protons where longitudinal relaxation times are on the order of a few seconds in favorable cases, additional techniques are necessary to transfer magnetization to a reservoir with more favorable relaxation properties. While the details for achieving this transfer depend on J-couplings and initial spin-states, an essential ingredient is application of coincident radio frequency pulses applied to the coupled partners.

Clinical MR spectrometers and portable (typically low-field) scanners are usually not equipped with multiple channels but generally are capable of producing amplitude and phase-modulated waveform. Moreover, adding additional phase-coherent transmitters ad hoc would likely be a considerable distraction for most research labs and particularly those equipped with commercial instruments. To circumvent this limitation, we have developed phase and amplitude modulation schemes to manipulate heteronuclear coherences at a single applied frequency.

The creation of these harmonics for spectroscopy (referred to here as HARMONY) is ideally suited to low-field applications and can readily be tailored for simultaneous, phase-specific transformations using numerical optimizations of composite pulses. The RF pulses for HARMONY have been designed using an optimal control algorithm based upon a technique originally developed to produce wide-band RF pulses for mono-nuclear spectroscopy at ultra-high field (19 T) (74; 75). We propose modifications of the cost function and intrinsic hardware limitations of this numerical minimization method so as to produce dual-band pulses capable of multi-nuclear excitation at low field (12 mT), thus enabling polarization transfer experiments with a single-channel transmission coil.

The optimal control algorithm (summarized here and detailed in Appendix E) iteratively determines adjustments to a composite amplitude and phase modulated waveform seeded with random initial amplitudes and zero phases by determining the difference in the physical paths associated with 1) the forward RF-induced propagation of the magnetization $M^F(t)$ from the given initial conditions M_0 and 2) the propagation of the magnetization $M^R(t)$ due to the time-reversed RF waveform starting with the target magnetization state M^{target}. The difference in these two spatial trajectories $\Delta\omega(t)$ is quantified by the vector cross product of the magnetization states at each time point in the composite RF waveform such that

$$\Delta\omega(t) = M^F(t) \times M^R(t)\,. \tag{6.5.1}$$

The composite pulse for the next computational iteration is determined by

$$\Delta\tilde{A}(t) = \lambda \left|\Delta\omega(t)\right| \,, \tag{6.5.2}$$

with $A(t)$ being the complex amplitude such that the physical amplitude is given by $A(t) = \Re(\Delta\tilde{A}(t))$ and the phase by $\Delta\phi(t) = \Im(\Delta\tilde{A}(t))$. In our implementation of this procedure, the parameter λ is determined by a secondary least-squares minimization procedure such that improvement in the cost function is maximized for the given iteration. Calculation of magnetization trajectories $M^F(t)$ and $M^R(t)$ is achieved using an analytic solution of a relaxation-free form of the Bloch equation (3). For the proposed low-field polarization transfer experiments, we propose the modified cost function of the minimization procedure to be given by

$$\delta(\tilde{A}) = \frac{\kappa}{m}\sum_{i=1}^{m}\left(1 - M_i^F(t)\cdot M_i^{\text{target}}\right) + \frac{1-\kappa}{n}\sum_{j=1}^{m}\left(1 - M_j^F(t)\cdot M_j^{\text{target}}\right) \,, \tag{6.5.3}$$

where the indices i and j indicate the step number through the lower and upper frequency bands, respectively. In these targeted frequency bands, the dot product between the final magnetization state for a given set of complex amplitudes (as determined by simulation of the Bloch equations) and the target end magnetization state specified by the user serves as a metric of pulse performance. The parameter κ acts as a Lagrange multiplier in weighting the importance of the two specified frequency bands. As opposed to the formulation in (74), we opt to neglect homogeneities in the transmitted RF field intensity due to the small volumes and large wavelengths under consideration at low field. To generate pulses for HARMONY, the carrier frequency is chosen at the mean nuclear resonant frequency of the chemical species of interest. In practice, this choice is reflected in the effective value of the gyromagnetic ratio γ_{eff} used in simulation of the Bloch equations. For dual excitation of ^{1}H and ^{13}C,

$$\gamma_{\text{eff}} = \frac{1}{2}\left(\gamma_{1\text{H}} + \gamma 13\text{C}\right) = 167.39\,\text{rad/s/T}\,, \tag{6.5.4}$$

implying a carrier frequency $\omega_0 = 319.69\,\text{kHz}$ for a field strength of 12 mT. The 12 mT resonant frequencies of ^{1}H and ^{13}C being 510.91 kHz and 128.46 kHz, respectively, the resonant offsets for the center of the targeted frequency bands are defined to be ±191.22 kHz. In our preliminary pulse designs, the target bandwidth of excitation regions is set to 2 kHz in order to accommodate the expected level of field inhomogeneity in our low-field spectrometer, but preliminary results suggest that larger bandwidths are feasible. In compliance with the hardware limitations of our single-channel RF amplifier, amplitude and phase modulations are optimized at 2.1 μT intervals resulting in 3000 free parameters for a 3.15 ms pulse. RF amplitude is limited to 100 μT and enforced during the optimization according to established methods (75).

Presented here are five pulse designs generated with the given optimal control algorithm for use in excitation of ^{1}H and ^{13}C at 12 mT using a single, centrally-located carrier frequency ($\omega_0 = 319.69\,\text{kHz}$). The goal of the first design (Figure 1) is the simultaneous but out-of-phase excitation of both nuclear species. Simulations of resulting magnetization states (Figure 1) indicate a high degree of convergence of the numerical algorithm. Thus, such an excitation appears attainable with the given single-channel hardware configuration. Note that the excitation bands observable in the vicinity of ±100 kHz (as well as the on-resonance band) are not a condition of the optimization but are rather a side effect of the optimal solution.

The six pulse designs presented here (Figures 68–70) demonstrate the effectiveness of the numerical algorithm in generating off-resonance excitation in a single band and are directly applicable to polarization transfer experiments such as PASEDENA and SABRE (85; 11). Figure 68 exhibits pulses resulting in 90° excitations about either the $+x$- or $+y$-axes for the ^{13}C band. Likewise, Figure 68 shows that such rotations are equally possible in the ^{1}H band. For these four single-band pulses, magnetization in the region of the untargeted nucleus is minimally disturbed without the need to specify such a condition in the pulse optimization. Examples of dual-band pulses for both excitation and refocusing are shown in Figure 70. All figures include amplitude modulation (top row) and phase modulation (2nd row) for 3.15 ms RF pulses designed for execution with a carrier frequency of 319.69 kHz such that the ^{13}C and ^{1}H resonances lie at -191.22 kHz and $+191.22$ kHz, respectively. The simulated magnetization response shown via the components M_x (3rd row), M_y (4th row), and total transverse magnetization M_T (last row) demonstrate the impressive extent to which the conditions of the optimization are fulfilled. In all cases, a 2 kHz bandwidth is targeted at each resonance. For the examples presented here, 3000 free parameters (1500 complex amplitudes) are optimized within constraints dictated by RF amplifier limitations, namely a 2.1 μs dwell with a maximum amplitude of 100 μT.

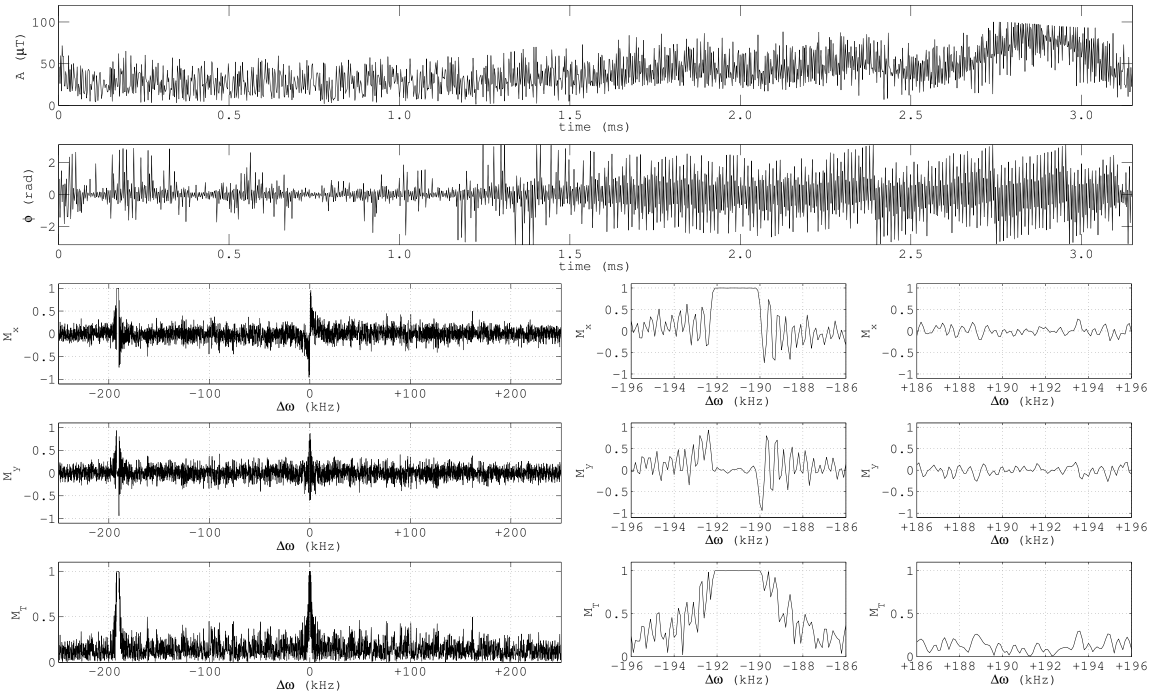

(a) 90° rotation about the y axis.

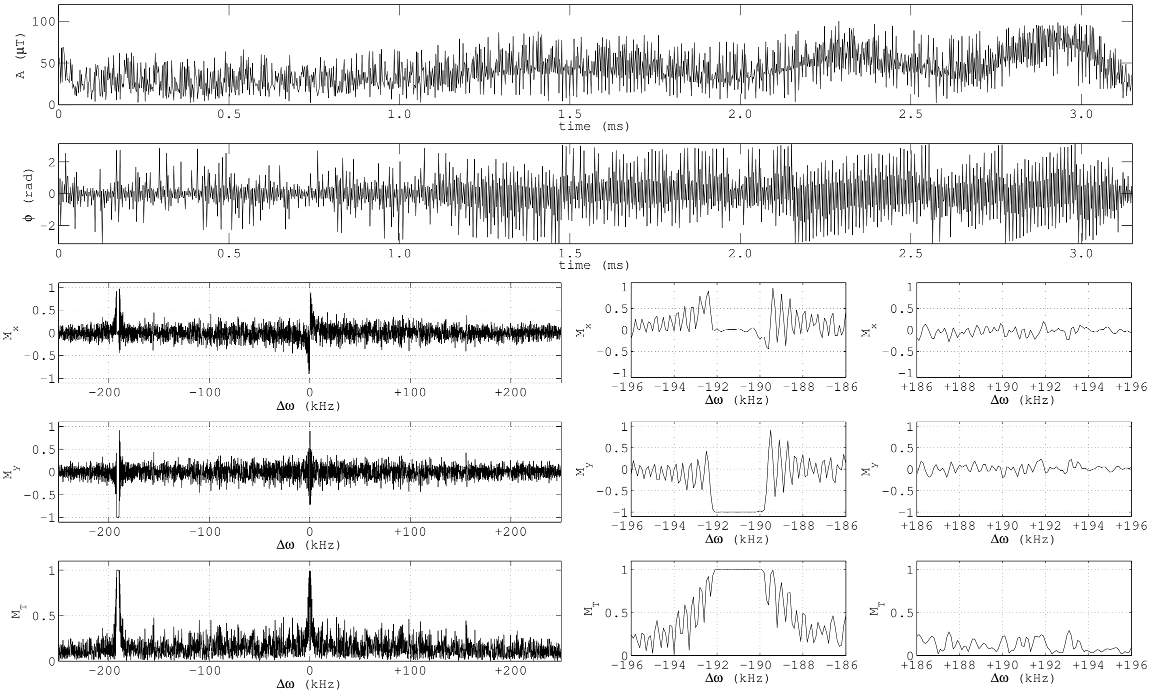

(b) 90° rotation about the x axis.

Figure 68: Excitation of ^{13}C at 128 kHz while transmitting at 319 kHz and suppressing signal from ^{1}H at 510 kHz. The excitation band has a width of 3 kHz and control of the magnetization is demonstrated in (a) vs. (b).

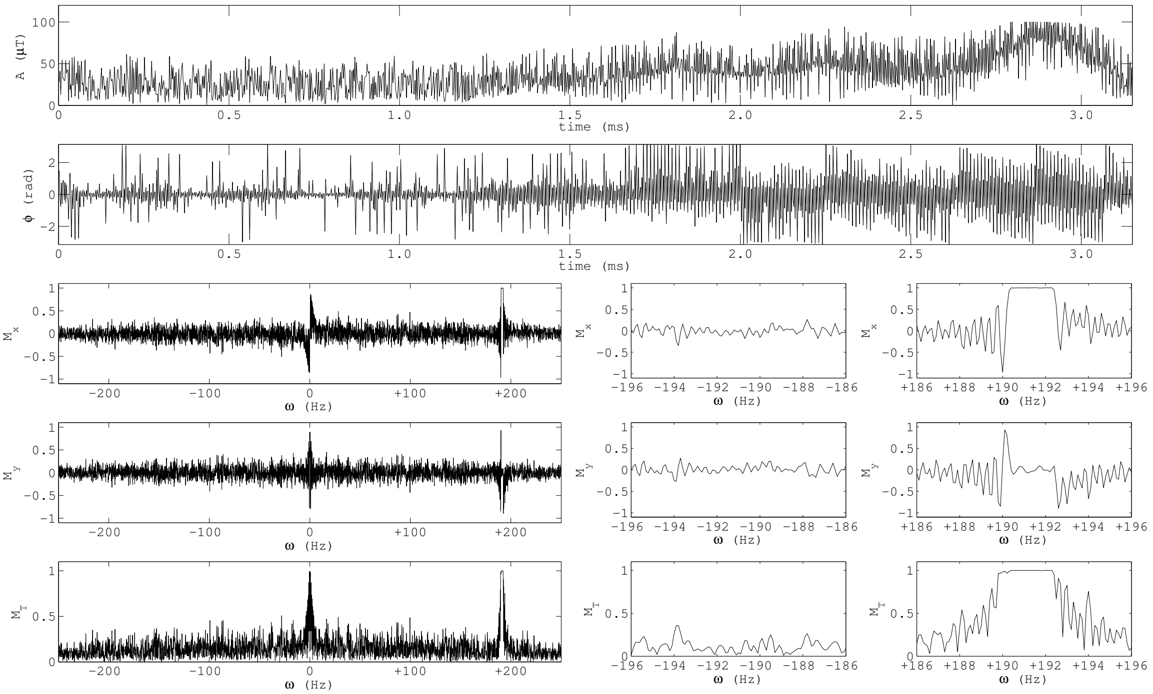

(a) 90° rotation about the y axis.

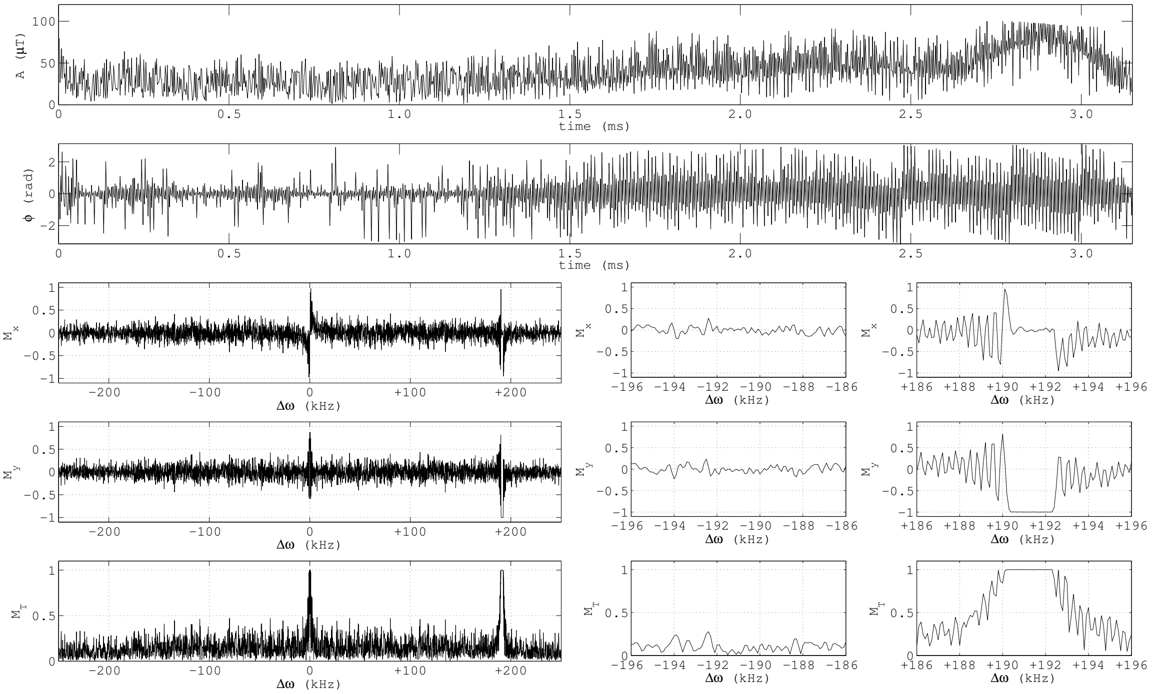

(b) 90° rotation about the x axis.

Figure 69: Excitation of ^{1}H at 510 kHz while transmitting at 319 kHz and suppressing signal from ^{13}C at 128 kHz. The excitation band has a width of 3 kHz and control of the magnetization is demonstrated in (a) vs. (b).

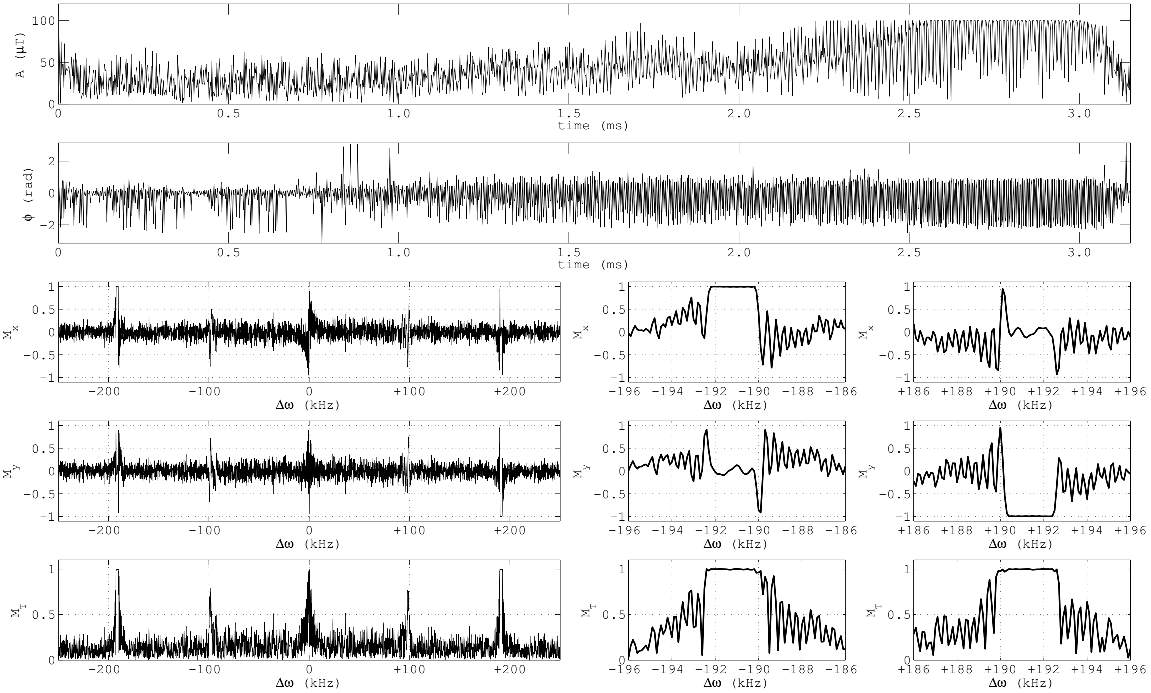

(a) Dual-band excitation.

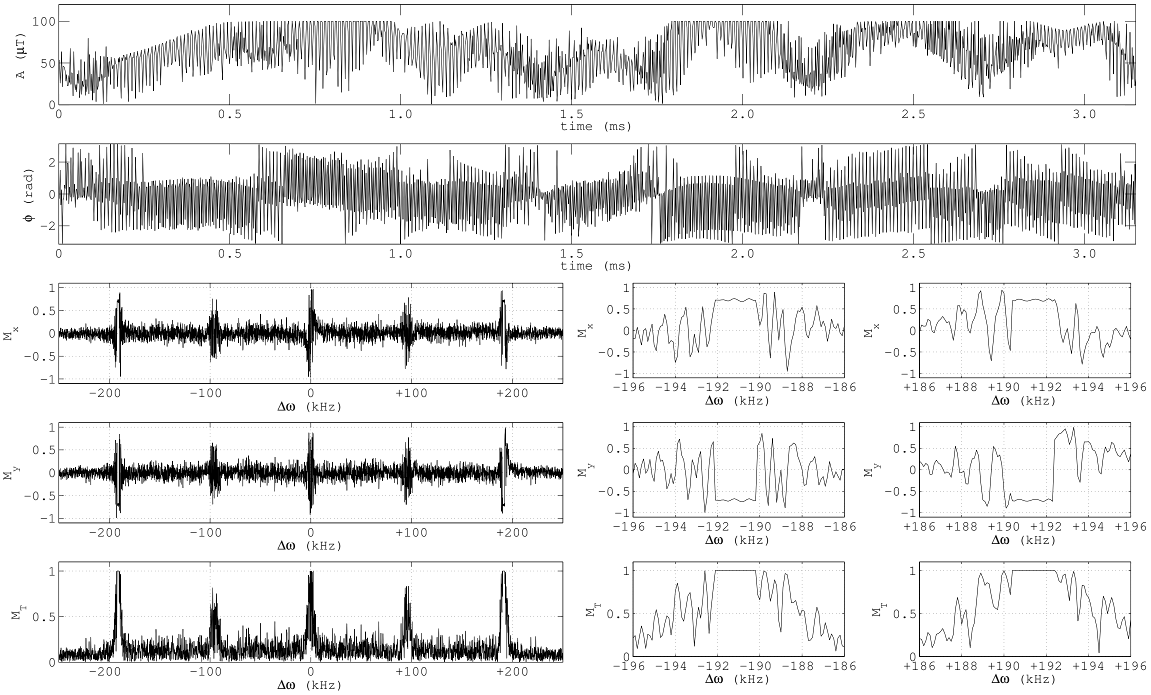

(b) Dual-band refocusing.

Figure 70: Simultaneous excitation (a) and refocusing (b) of ^{1}H at 510 kHz and ^{13}C at 128 kHz while transmitting at 319 kHz. Each excitation band has a width of 3 kHz.

CHAPTER VII

CONCLUSION

Conclusions and potential future studies have, to some degree, been already provided within the preceding chapters; however, those comments are in most cases quite specific to particular studies. Thus, the purpose of this final chapter is to provide a summary of this thesis in its entirety and a more global perspective of the potential for related future investigations.

7.1 Summary

The demands for different RF pulse attributes are almost as many as there are applications of MRI. Thus, the investigations of this thesis are necessarily limited. The work has spanned a range of basic RF objectives, including excitation, inversion, refocusing, and saturation with the idea that, due to the fundamental nature of these pulse designs as the basic building blocks of an MRI pulse sequence, the stated designs may be fine-tuned for use in specific contexts. In some sense, the collection of pulse design strategies presented in this thesis therefore can be viewed as a complete, single-channel solution to challenges related to inhomogeneous transmission of RF pulses at high field. This statement is, of course, made with the assumption that the required increases in pulse duration and power can be accommodated.

Results have demonstrated the extreme flexibility of composite pulses to provide the levels of B_1^+- and ΔB_0-insensitivity demanded by human brain imaging at 7 T.

Thus, the investigated pulse designs work to better realize the SNR gains that provide the primary motivation to pursue MRI at high field. Composite pulses for volume excitation with arbitrary flip angles (Chapter III) have been shown to outperform the existing and competing solution of BIR-4 pulses in terms of insensitivity to field variations and associated SAR levels. Such pulses have been shown to be translatable to slice-selective forms while maintaining the desired field-insensitive characteristics (Chapter IV). The evaluation of refocusing pulses has revealed the significant signal gains that are possible when using composite designs in spin-echo sequences at 7 T. Slice-selective variants of these refocusing designs should prove attainable via the same methods employed to achieve slice-selection for composite excitation pulses, thus significantly broadening the contexts in which they prove useful. Applications demanding non-selective inversion may benefit from either composite excitation pulses with 180° flip angles (Chapter III) or the optimized hyperbolic secant and BIR-4 pulses (Chapter VI), while hyperbolic secant pulses appear to be the best alternative when highly selective, field-insensitive inversions are required. B_1^+-insensitive saturation can potentially be accomplished through the use of either 90° composite excitations in conjunction with appropriate dephasing field gradients or inversion pulses with the appropriate choice of a delay time preceding the ensuing excitation.

With this wide array of B_1^+-insensitive RF tools available, a large number of imaging sequences can be readily modified so as to limit undesirable B_1^+-related effects arising at high field. While resulting improvements may not be in all cases as pronounced as when spectral-spatial designs are implemented for multiple-channel transmission, the B_1^+-insensitive pulse approach thus represents a suitable alternative to multi-transmit technologies when the latter are not available or prove impractical. Furthermore, while multi-transmit technology appears to be here to stay in at least some capacity, the pulse designs presented in this thesis carry the notable advantage of requiring no subject-specific field mapping or RF calibrations and can be implemented on almost any existing coil, in any imaging volume, and over a broad range of field strengths at little or no cost. It is primarily for the reasons of flexibility and cost that these designs may eventually prove useful in clinical practice. For example, in some cases, the additional scan time required for multi-transmit calibrations may prove cumbersome both practically and monetarily, whereas B_1^+-insensitive pulses avoid such issues almost entirely. Moreover, it is likely that such reasons to adopt B_1^+-insensitive pulse strategies will be more compelling at lower field strengths given that both RF field variations and the relative impact of addressing related issues are significantly reduced in this context.

The prevailing limitations of the pulse designs presented in the work involve increased pulse power and duration as compared to typical B_1^+-sensitive pulses. These pulse characteristics translate to lengthened scan times (so as to avoid violation of SAR restrictions) and possible signal losses due to T_2^* relaxation. While multi-transmit technologies certainly provide for relatively short total pulse durations and superior (or at least matching) B_1^+-mitigating capabilities, a comparison of the required alterations to total scan duration as required by multi-transmit and B_1^+-insensitive composite pulse approaches is presently difficult since multi-transmit pulse calibration techniques and SAR evaluations are still under active investigation. It may very well prove true that multi-transmit calibrations can be carried out in a matter of a few minutes with resulting pulse designs suffering little in terms of increased power. In this case, the main advantage of composite pulse designs would be the reduced hardware-related costs. However, very few MR research sites (and even fewer clinical sites) currently have multi-channel transmission capabilities. Thus, there exists a window of time in the immediate future for which B_1^+-insensitive pulses could be used to take better advantage of existing hardware before more attractive alternatives become widely available. Furthermore, composite pulses have been shown capable of avoiding expected levels of T_2^* signal loss due to spin-locking (see Section 4.3.2 and Figure 31), and preliminary studies on limiting pulse power of composite pulse in specific contexts (see Section 6.2) are promising. Clearly, the true potential for adapting composite pulses to specific duration and SAR constraints has not been established, thereby indicating that comparisons of multi-transmit and B_1^+-insensitive pulse design approaches to high field inhomogeneity issues are at this point largely speculative.

In addition to investigations into numerical optimization strategies for B_1^+-insensitive excitation, inversion, saturation, and refocusing, the present work has revealed the applicability of similar methods for producing frequency-selective composite pulses as presented in Chapter VI (Sections 6.4, and 6.5). While applications to alternative methods of slice-selective images (Section 6.3) may be somewhat of a long shot, the general technique proves most useful for translating the non-selective pulses of

Chapter III to more useful slab-selective variants. On the other hand, frequency selective pulses for lipid suppression have already been implemented with promising results. A dual-band version for simultaneous lipid and water suppression has not been put to use but appears functional in simulations. The successful design of composite pulses for low-field polarization transfer has revealed the extreme capabilities of composite pulses for frequency-selective manipulation of magnetization responses in the case that B_1^+ inhomogeneities can be largely ignored. The success at this level opens many doors for future applications of similarly designed composite pulses in NMR and emphasizes how the pulse designs of this thesis may have been motivated by high-field applications but their utility is not confined to that context.

Finally, the work on RF field mapping presented in Chapter II can not be overlooked in its significance. The conclusion that various mapping techniques result in such varied measurements of the B_1^+ field is particularly relevant to multi-transmit spectral-spatial pulse designs. It is for these pulses (and their single-channel spokes counterparts) that accurate RF field measurements are required under stringent time constraints. The observation that the fastest mapping methods (such as PSS) are subject to significant potential errors motivates the need to either develop new techniques or modify more accurate existing techniques so as speed up acquisition. Presently, it appears that use of a moderate EPI factor in conjunction with a multi-slice, multi-flip-angle mapping technique (GEs) may be one route of reaching an acceptable compromise between speed and accuracy.

7.2 Future Work

Presently, the potential for future investigations related to the findings of this thesis appear almost limitless, due largely to the broad array of possible applications. The impacts of using B_1^+-insensitive composite pulses have not been evaluated in any specific context such as arterial spin labeling (ASL), functional MRI (fMRI), diffusion tensor imaging (DTI), fluid-attenuated inversion recovery (FLAIR), or multi-nuclear imaging, just to name a few. Perhaps of most immediate importance to the eventual pursuit of such studies is an investigation into slice-selective variants of the most promising B_1^+-insensitive refocusing pulses of Chapter V. With the performance constraints of these pulses established, non-selective and slice-selective versions of B_1^+-insensitive pulses for excitation, inversion, refocusing, and saturation will be ready for deployment, making replacement of almost all existing B_1^+-sensitive pulses possible in a wide range of pulse sequences. As presented in this thesis, pulses are evaluated individually as should be the case initially; however, the simultaneous use of B_1^+-insensitive pulses for different purposes in the same sequence should only work to exaggerate the kinds of signal gains that have been so far witnessed. The simplest example of this procedure might be in the context of a spin-echo sequence such as the one employed in Chapter V. If the excitation pulse in this sequence is replaced by a composite pulse from Chapter III and the refocusing pulse by one of the many B_1^+-insensitive options, signal gains will likely be significantly larger than when only one pulse is substituted at a time. SNR improvements may continue to become increasingly obvious in more complex scenarios such as a spin-echo inversion recovery sequence as is often employed in FLAIR experiments. After evaluating resulting SNR improvements when using such pulse combinations, initial applications could be identified based on either the simplicity of the sequence (in which case it may be easiest to quantify sources of error and the influence of given pulses to increased SNR) or sequences that might benefit the greatest from B_1^+-insensitivity.

The idea of evaluating the collective effect of multiple B_1^+-insensitive pulses in a pulse sequence together with the observation of large overall signal gains possible through simple RF amplitude adjustments (such as was the case for the $\mathrm{BLK_b}$, $\mathrm{COMP3_b}$, and $\mathrm{VS_b}$ refocusing pulses of Chapter V) suggests that power optimization for all pulses in a given sequence is a topic worthy of future 7 T studies. Typically, commercial MR scanners calibrate the power of RF transmission based on signal maximization within the imaging volume. Presently, these methods result in correct power calibration for the highest B_1^+ regions. RF field maps and associated histograms presented in this thesis (e.g., Figure 10) suggest that a more appropriate power calibration would result in maximizing the *mean* signal through the entire imaging volume. Since the mean of the $B_1^+/B_{1,\mathrm{nom}}^+$ field distribution in any given human brain at 7 T is consistently measured to be ~ 0.7, an *ad hoc* power adjustment of +40% ($1.0/0.7 = 1.4$) could simply be used in conjunction with existing power optimization methods to increase RF pulse efficacy in the majority of regions of the brain. It seems that a proper evaluation of any technique for combating signal variations due to B_1^+ inhomogeneities (whether it be B_1^+-insensitive pulses or multi-transmit techniques) should be performed in reference to the performance of typical

B_1^+-sensitive RF waveforms under the condition of an optimal power calibration.

Another arena of future studies certainly involves the explorations of power-limited optimizations. Power constraints will become increasingly important to the practicality of B_1^+-insensitive pulses when multiple such pulses are utilized in the same pulse sequence. RF power limits have already been successfully integrated into the design of volume excitation pulses as reported in Section 6.2, and SAR limitations were considered heavily in the analysis of refocusing pulses in Chapter V. The next step with regard to this facet of pulse design is to extend power-constrained optimization to the low flip-angle, slice-selective pulses presented in Chapter IV. These pulses could prove useful for slab-selection excitation in the context of a 3-D steady state imaging sequence; however, the utility of such a sequence relies on short T_R values that are not possible if RF pulse power is too high.

The pulse designs of this thesis have largely incorporated insensitivity to the range of B_0 variations observed in the brain at 7 T. These ΔB_0 ranges were determined using similar pencil-beam volume static field shimming approaches. While such shimming strategies are successful in limiting static field variations in the brain to plus or minus a few hundred Hertz, other shimming methods, such a global imaged-based shimming, may prove more efficacious. The value to optimized composite pulses of reducing the range of ΔB_0 values in the imaging volume is that optimization requirements are less stringent, generally resulting in lower attainable cost function values. As for the design of pulses for use at high field, a restricted ΔB_0 range would likely translate to either greater B_1^+-insensitivity or reduced power requirements. Thus, in future studies, the best possible static field shimming scenarios should be investigated and composite pulses optimized accordingly. As developing technologies continue to allow for improved static field shimming, the performance and utility of B_1^+-insensitive pulses will also improve. Such is an example of the ways in which design and control of the RF and static fields are often complementary.

In addition to sharing a common target range of ΔB_0 values, most of the pulse designs of this thesis are designed for use with a volume head coil at 7 T. It is the RF inhomogeneities associated with this combination of coil and anatomy that determine the range of B_1^+ values to be targeted in the pulse design process. The use of different transmission coils is certain to result in changes to pulse design criteria, as is the imaging of different regions of the body. For example, a surface coil used to image the spine at 7 T will likely define a very different set of ΔB_0 and B_1^+ values than for a volume head coil. RF and static field maps will need to be obtained for any such scenario, and composite pulses will need to be redesigned to ensure maximum efficacy. The possible applicability of previously optimized composite pulses will, of course, depend on the new coil/anatomy combinations, but investigation into the design of B_1^+-insensitive pulses for use in such contexts is certainly warranted.

While the RF shimming and spokes pulse strategies described in Section 1.4.2 have proven efficacious in producing uniform excitations on multi-channel systems at high field, the incorporation of composite/arbitrary waveforms in this context has not been thoroughly explored. Investigation of such methods certainly appears worthwhile given the potential advantages, particularly with respect to maximizing the capability of a limited number of transmission channels. As previously noted, the expense of RF amplifiers and the time-consuming RF field mapping necessary for multi-transmit applications motivate the use of as few channels as necessary. Such constraints put more demand on pulse designs to achieve the desired effects with fewer degrees of freedom. The optimization of composite waveforms (such as those of Chapter III) for use on separate transmission channels is a way to introduce additional degrees of freedom in the optimization problem when the number of channels are limited. The methods for doing this in the context of volume (non-selective) excitation are somewhat straightforward and analogous to the design of multi-transmit spokes pulses. After measurement of the RF field associated with each coil element, optimization of composite waveforms would be performed in tandem so as to induce uniform effects on the magnetization throughout the imaging volume. Unlike, the optimizations presented in this thesis, such pulse designs would rely on the spatial distribution of the B_1^+ field, and subject-specific field mapping would be necessary. Perhaps a simpler strategy for marrying the technologies of B_1^+-insensitive composite pulses and multi-channel transmission is analogous to RF shimming. In this case, a single B_1^+-insensitive composite pulse would be selected for use based on loose knowledge of the expected field inhomogeneities associated with each coil element. Subject-specific optimization of constant amplitude and phase offsets to be applied to this composite pulse as executed on each channel would then be performed. Presently, it is unknown whether such an optimization would result in anything but zero amplitude and phase offsets for each channel, but straightforward simulations should be able to shed light on the subject with relative ease. Slice selective versions of composite pulses for multi-transmit are also worthy of investigation; however, as presented in Chapter IV, such composite waveforms already closely parallel spokes pulses in their design. The main difference is the utilization by spokes pulses of transverse field gradients to allow for spectral-spatial excitations. Since these gradients are typically executed in very short times, the advantage in eliminating them may not outweigh the benefits of the alternative method; however, sensitivity of spokes pulses to RF phase instabilities has been reported. It may be that such sensitivities are less pronounced when transverse gradients are not present.

APPENDIX A

OVERVIEW OF MAGNETIC RESONANCE IMAGING PHYSICS

This appendix provides an overview of the physical foundations of magnetic resonance imaging (MRI). An explanation of nuclear magnetic resonance (NMR) is first presented along with classical and quantum mechanical descriptions of the nuclear magnetic moment, its various energy states in a magnetic field, nuclear interactions involving spin transitions, and Larmor precession. Following is a discussion of how nuclear spins can be manipulated via radio frequency (RF) electromagnetic radiation and the processes by which such a disturbed system returns to equilibrium. The basic approaches used in producing images from NMR signals and the hardware necessary to carry out such a task are also described.

1.1 Electromagnetism and the Magnetic Moment

At the heart of any classical interpretation of electromagnetic phenomenon are Maxwell's equations, which describe the origins and interrelations of electric and magnetic fields. These equations explicitly show how electric fields originate from electric current and time-dependent magnetic fields and how magnetic fields originate from electric current and time-dependent electric fields. Maxwell's equations are typically written in the differential and corresponding integral forms found in Table 1.1. Particularly relevant to the following discussion of the magnetic moment are Gauss's Law for electricity and Ampere's Law, while Faraday's law is crucial to magnetic resonance signal detection (Section 1.2). Firstly, using Maxwell's equations as a starting point, let us develop an expression for what is known as the electric dipole moment of a localized charge distribution. Through analogy, the magnetic moment of a current distribution is then more easily understood. Since the curl of the gradient of any scalar field is equal to zero, Faraday's Law permits the definition of a scalar potential, V, such that

$$\mathbf{E} = -\boldsymbol{\nabla} V \,, \tag{A.1}$$

as long as there exists no time-dependent magnetic field ($\partial\mathbf{B}/\partial t = 0$). With this definition made, Gauss's Law for electricity can be written in terms of the scalar potential as

$$\boldsymbol{\nabla}\cdot\mathbf{E} = \boldsymbol{\nabla}\cdot(-\boldsymbol{\nabla} V) = \frac{\rho}{\epsilon_0} \tag{A.2}$$

or

$$\nabla^2 V = -\frac{\rho}{\epsilon_0} \,. \tag{A.3}$$

This relationship between the scalar potential and the charge distribution is known as Poisson's equation. For the case that the charge distribution is localized (i.e. $\rho \to 0$ as $\mathbf{r} \to \inf$), Poisson's equation has the solution

$$V(\mathbf{r}) = \frac{1}{4\pi\epsilon_0}\int \frac{\rho}{|\mathbf{r}-\mathbf{r}'|}\,d\mathbf{r}' \,, \tag{A.4}$$

which is equivalent to the Helmholtz theorem for the special case of $\nabla\times\mathbf{E} = 0$ and $\nabla\cdot\mathbf{E} = \rho/\epsilon_0$. If the observation point is well outside the charge distribution, the electric potential can be binomially expanded such that

$$V(\mathbf{r}) = \frac{1}{4\pi\epsilon_0} \sum_{n=0}^{\infty} \frac{1}{r^{n+1}} \int (r')^n P_n(\cos\theta) \rho \, d\mathbf{r}' \,, \tag{A.5}$$

with $P_n(\cos\theta)$ being the Legendre polynomials. The leading term in this series is the monopole term, the second the dipole term, the third the quadrupole, etc. It is the dipole term ($n = 1$) that is most relevant to a derivation of the magnetic moment. This term has the specific form

$$V_{\text{dipole}}(\mathbf{r}) = \frac{1}{4\pi\epsilon_0 r^2} \int r' \cos(\theta) \rho \, d\mathbf{r}' = \frac{1}{4\pi\epsilon_0 r^2} \, \hat{\mathbf{r}} \cdot \int \mathbf{r}' \rho \, d\mathbf{r}' \,. \tag{A.6}$$

The integral in the last expression is defined as the electric dipole moment, **P**, of the charge distribution such that

$$\mathbf{P} = \int \mathbf{r}' \rho \, d\mathbf{r}' \tag{A.7}$$

and

$$V_{\text{dipole}}(\mathbf{r}) = \frac{\hat{\mathbf{r}} \cdot \mathbf{P}}{4\pi\epsilon_0 r^2} \,. \tag{A.8}$$

Being representative of the size and shape of the charge distribution and simultaneously independent of the point of observation, the electric dipole moment, just as with its counterparts in other terms of the potential's series expansion, is a particularly useful vector to define. It is worth noting as an example that a single point charge has no dipole moment while oppositely charged point particles separated by a

Table A.1: Maxwell's equations of classical electrodynamics in free space describe the interrelations of magnetic fields, electric fields, electric charge, and electric current. In the given representation, $\mathbf{E}$ is the electric field, $\mathbf{B}$ is the magnetic field, ρ is the electric charge density, $\mathbf{J}$ is the electric current density, Q_{enclosed} is the electric charge within a closed surface, $\mathbf{\Phi}_B$ is the magnetic flux, I is the electric current passing through a closed loop, $\mu_0 = 4\pi \times 10^{-7}\,\mathrm{N/A^2}$ is the permeability of free space, and $\epsilon_0 = 8.85 \times 10^{-12}\,\mathrm{C^2/N \cdot m^2}$ is the permittivity of free space.

law	differential form	integral form
Gauss's Law for Electricity	$\boldsymbol{\nabla} \cdot \mathbf{E} = \frac{\rho}{\epsilon_0}$	$\oint_{\text{surf}} \mathbf{E} \cdot d\mathbf{a} = \frac{Q_{\text{enclosed}}}{\epsilon_0}$
Faraday's Law	$\boldsymbol{\nabla} \times \mathbf{E} = -\frac{\partial \mathbf{B}}{\partial t}$	$\oint_{\text{line}} \mathbf{E} \cdot d\mathbf{s} = -\frac{d\mathbf{\Phi}_B}{dt}$
Gauss's Law for Magnetism	$\boldsymbol{\nabla} \cdot \mathbf{B} = 0$	$\oint_{\text{surf}} \mathbf{B} \cdot d\mathbf{a} = 0$
Ampere's Law	$\boldsymbol{\nabla} \times \mathbf{B} =$ $\mu_0 \mathbf{J} + \mu_0 \epsilon_0 \frac{\partial \mathbf{E}}{\partial t}$	$\oint_{\text{line}} \mathbf{B} \cdot d\mathbf{s} =$ $\mu_0 I + \mu_0 \epsilon_0 \frac{\partial}{\partial t} \int_{\text{surf}} \mathbf{E} \cdot d\mathbf{a}$

distance vector **d** have a dipole moment of $q\mathbf{d}$.

Just as an electric dipole moment arises from a spatial distribution of electric charge, a magnetic dipole moment arises from a spatial distribution of electric current. In both cases, the dipole moment is related to the dipole term of the multipole expansion of the appropriate potential—the scalar potential, V, for the electric dipole and the *vector potential*, **A**, for the magnetic dipole.

Since the divergence of the curl of any vector field is zero, Gauss's Law for magnetism permits the definition of a vector potential **A** such that

$$\mathbf{B} = \nabla \times \mathbf{A}\,. \tag{A.9}$$

Inserting this representation of **B** into Ampere's Law in differential form yields

$$\nabla \times (\nabla \times \mathbf{A}) = \mu_0 \mathbf{J}\,, \tag{A.10}$$

which, with the use of a common vector identity, can be written as

$$\nabla(\nabla \cdot \mathbf{A}) - \nabla^2 \mathbf{A} = \mu_0 \mathbf{J}\,. \tag{A.11}$$

The condition of $\nabla \cdot \mathbf{A} = 0$ can then be placed on the vector potential with no effect on Maxwell's equations such that Ampere's Law reads

$$\nabla^2 \mathbf{A} = -\mu_0 \mathbf{J}\,. \tag{A.12}$$

This relationship has the form of Poisson's equation and can once again be solved according to the Helmholtz theorem such that

$$\mathbf{A}(\mathbf{r}) = \frac{\mu_0}{4\pi} \int \frac{\mathbf{J}}{|\mathbf{r} - \mathbf{r}'|} \, d\mathbf{r}' \,, \tag{A.13}$$

as long as there exists no time-dependent electric field (i.e., $\partial \mathbf{E}/\partial t = 0$). In order to put this vector equation in a manageable form for a series expansion, the special case of a current loop with current $\mathbf{I} = I \, d\mathbf{l}$ will be considered. In this representation, the line element $d\mathbf{l}$ lies along the loop and points in the direction of the electric current. For this case, the vector potential takes the form

$$\mathbf{A}(\mathbf{r}) = \frac{\mu_0 I}{4\pi} \oint \frac{1}{|\mathbf{r} - \mathbf{r}'|} \, d\mathbf{l} \tag{A.14}$$

and can be expanded in terms of Legendre polynomials just as the scalar potential was before such that

$$\mathbf{A}(\mathbf{r}) = \frac{\mu_0 I}{4\pi} \sum_{n=0}^{\infty} \frac{1}{r^{n+1}} \oint (r')^n P_n(\cos\theta) \, d\mathbf{l} \,. \tag{A.15}$$

The second term ($n = 1$) of this series,

$$\mathbf{A}_{\mathrm{dipole}}(\mathbf{r}) = \frac{\mu_0 I}{4\pi r^2} \oint r' \cos\theta \, d\mathbf{l} = \frac{\mu_0 I}{4\pi r^2} \oint (\hat{\mathbf{r}} \cdot \mathbf{r}') \cos\theta \, d\mathbf{l} \,, \tag{A.16}$$

is the magnetic dipole term and can be manipulated such that

$$\mathbf{A}_{\text{dipole}}(\mathbf{r}) = \frac{\mu_0 I}{4\pi r^2}\left(-\frac{1}{2}\hat{\mathbf{r}} \times \oint (\mathbf{r}' \times d\mathbf{l})\right) . \tag{A.17}$$

If the magnetic dipole moment, $\boldsymbol{\mu}$, is defined as

$$\boldsymbol{\mu} = \frac{I}{2}\oint (\mathbf{r}' \times d\mathbf{I}) , \tag{A.18}$$

the dipole term can be written as

$$\mathbf{A}_{\text{dipole}} = \frac{\mu_0}{4\pi r^2}(\boldsymbol{\mu} \times \hat{\mathbf{r}}) . \tag{A.19}$$

With this definition of the magnetic dipole moment (or simply the *magnetic moment*) established, it follows that a loop of current lying in a single plane has a magnetic moment of $I\mathbf{a}$ where $\mathbf{a}$ is a vector with magnitude equal to the area of the loop and direction given by the dominant direction of $\mathbf{r}' \times d\mathbf{l}$.

1.2 Quantum Mechanics and Spin

A few fundamental quantum mechanical concepts need to be introduced at this point in order to provide a more accurate description of nuclear magnetic resonance. Just as Maxwell's equations lie at the heart of classical electromagnetism, the Schrödinger equation provides the foundation for quantum mechanics. For a particle of mass m moving in a potential V, the Schrödinger equation takes the form

$$i\hbar\frac{\partial\psi(\mathbf{r},t)}{\partial t} = -\frac{\hbar^2}{2m}\nabla^2\psi(\mathbf{r},t) + V\psi(\mathbf{r},t)\,, \tag{A.1}$$

where $\psi(\mathbf{r},t)$ is the particle's space and time dependent wave function and $\hbar = h/(2\pi) = 1.05457 \times 10^{-34}\,\mathrm{J}\cdot\mathrm{s}$ with h being Planck's constant. Solutions of this wave-like relation are quantized just as are the possible modes of a vibrating string. It is in this way that the Schrödinger equation's wave description of matter explains the observable quantization of fundamental particle properties.

One such fundamental property is angular momentum. A particle can possess orbital angular momentum (e.g., due to rotational motion in a central potential) and/or intrinsic angular momentum known as *spin.* Spin (commonly denoted by **S**) can be thought of as the angular momentum associated with a massive particle rotating on its axis, but spin is actually a far more fundamental property in that point particles such as the electron and massless particles such as the photon also possess a measurable nonzero intrinsic angular momentum. Both types of angular momentum are fundamentally quantized according to the Schrödinger equation. While the possible orbital angular momentum states of a particle can vary with the complexity of the potential experienced by that particle, a particle's spin takes on a range of quantized values independent of the environment. For protons, neutrons, and electrons, the only possible measurable spin values $\pm\hbar/2$ making these particles spin-1/2 particles[†].

[†] Such behavior was first observed in the Stern-Gerlach experiment of 1922.

Such particles that possess spin with half-integer multiples of $\hbar$ define a class of particles known as *fermions*, while particles with spin equal to whole-integer multiples of $\hbar$ are known as *bosons*. All known particles are either bosons or fermions. The possible spin states of spin-1/2 particles along the three orthogonal Cartesian directions, which will be useful in upcoming calculations, can written in terms of the Pauli spin matrices as

$$\mathbf{S}_x = \frac{\hbar}{2}\begin{bmatrix} 0 & 1 \\ 1 & 0 \end{bmatrix} \qquad \mathbf{S}_y = \frac{\hbar}{2}\begin{bmatrix} 0 & -i \\ i & 0 \end{bmatrix} \qquad \mathbf{S}_z = \frac{\hbar}{2}\begin{bmatrix} 1 & 0 \\ 0 & -1 \end{bmatrix}. \tag{A.2}$$

1.3 The Nuclear Magnetic Moment

The previously mentioned case of a simple current loop is highly relevant to a discussion of the magnetic moment of an atomic nucleus, since a nucleus is composed of protons and neutrons[‡] each possessing spin angular momentum. In this way, nucleons can be thought of as a small loop of electric current with an associated magnetic moment. The experimentally determined relationship between a particle's spin and the associated magnetic moment, $\boldsymbol{\mu}$, is

$$\boldsymbol{\mu} = \gamma \mathbf{S}\,, \tag{A.1}$$

where the proportionality factor γ is the gyromagnetic ratio. For the proton, $\gamma = 2.675 \times 10^{8}\,\mathrm{rad/s/T}$, but different particles have different gyromagnetic ratios de-

---

[‡] Although the neutron has a net charge of zero, its component quarks each have nonzero charge and contribute to the nucleon's overall magnetic moment.

pending on their mass, charge, and internal structure. For example, the electron's gyromagnetic ratio is 658 times that of the proton due partly to the electron's drastically smaller mass and partly due to its lack of structure in the form of component quarks.

The spin angular momentum of an atomic nucleus is simply the vector sum of the spin angular momenta of the component nucleons. In this way, the nuclear magnetic moment is related to the component spins through the expression

$$\mu_N = \gamma_N \sum_i \mathbf{S}_i \,. \tag{A.2}$$

Thus, only nuclei with nonzero spin have a nonzero magnetic moment. Since nucleons in the ground state tend to pair by type (proton or neutron) and by opposite spin states (according to the Pauli exclusion principle[†]), it is only nuclei with an odd number of protons and/or an odd number of neutrons that have a nonzero magnetic moment. Only these nuclei (e.g. ^{1}H, ^{17}O, ^{19}F, ^{23}Na, ^{31}P) are capable of participating in the phenomenon of nuclear magnetic resonance.

1.4 A Magnetic Dipole in an External Magnetic Field

The energy of a magnetic dipole in an external magnetic field is determined by the strength of the magnetic moment, the magnitude of the external field, and the orientation of the magnetic dipole with respect to the external field. Since the mag-

---

[†] The Pauli exclusion principle states that no two identical particles in a given system can have the exact same set of quantum numbers. Since nuclear energy states are degenerate in the number of available spin states, ground state nucleons in the same energy level tend to occupy opposite spin states.

netic moment tends to line up with the external field direction just like the needle of a compass, this configuration represents the lowest energy state. The highest energy state occurs when the magnetic moment is anti-parallel to the field. In general, the energy of a magnetic moment in an external field is given by

$$E = \boldsymbol{\mu} \cdot \mathbf{B}_{\text{ext}} \,. \tag{A.1}$$

Expressing this potential energy in terms of a particle's spin gives

$$E = -\gamma \mathbf{S} \cdot \mathbf{B}_{\text{ext}} \,. \tag{A.2}$$

If, for example, the external field is in the z direction such that $\mathbf{B}_{\text{ext}} = B_0 \hat{\mathbf{z}}$, this expression becomes

$$E = -\gamma \mathbf{S} \cdot B_0 \hat{\mathbf{z}} = -\gamma B_0 S_z \,. \tag{A.3}$$

Given only two possible values of S_z for spin-1/2 particles, there are only two possible potential energy states for protons, neutrons and electrons subject only to an external magnetic field:

$$E_{\pm} = \mp \frac{\gamma B_0 \hbar}{2} \,. \tag{A.4}$$

For such a system, the solution to the Schrödinger equation can be written in a matrix representation as

$$\psi(t) = \begin{bmatrix} \cos(\alpha/2) e^{+i\gamma B_0 t/2} \\ \sin(\alpha/2) e^{-i\gamma B_0 t/2} \end{bmatrix} , \tag{A.5}$$

where the coefficients are written in terms of α, an angle with physical significance to be discussed shortly. Given this wave function, the expectation value of the z component of spin is then calculable as follows:

$$\begin{aligned}\langle S_z\rangle &= \left(\psi'(t)\right)^* S_z\psi(t)\\ &= \begin{bmatrix}\cos(\alpha/2)e^{-i\gamma B_0 t/2} & \sin(\alpha/2)e^{+i\gamma B_0 t/2}\end{bmatrix}\frac{\hbar}{2}\begin{bmatrix}1 & 0\\ 0 & -1\end{bmatrix}\begin{bmatrix}\cos(\alpha/2)e^{+i\gamma B_0 t/2}\\ \sin(\alpha/2)e^{-i\gamma B_0 t/2}\end{bmatrix}\\ &= \frac{\hbar}{2}\cos(\alpha)\,,\end{aligned} \tag{A.6}$$

with $\left(\psi'(t)\right)^*$ denoting the transposed complex conjugate of $\psi(t)$. Similarly, the spin expectation values in the x and y directions are

$$\langle S_x\rangle = \left(\psi'(t)\right)^* S_x\psi(t) = \frac{\hbar}{2}\sin(\alpha)\cos(\gamma B_0 t) \tag{A.7}$$

and

$$\langle S_y\rangle = \left(\psi'(t)\right)^* S_y\psi(t) = -\frac{\hbar}{2}\sin(\alpha)\sin(\gamma B_0 t)\,. \tag{A.8}$$

The physical interpretation of these expectation values is that the particle's net spin vector is tilted at a constant angle relative to the z axis and precesses about the z axis with a constant angular frequency

$$\omega_0 = \gamma B_0\,. \tag{A.9}$$

This frequency is known as the Larmor frequency, and the general phenomenon of a particle's magnetic moment precessing about the ambient magnetic field direction is known as Larmor precession—both named after the Irish physicist Joseph Larmor who experimented with the effects of a magnetic field on radiation in the late nineteenth century.

In terms of physical forces, Larmor precession is the result of torque applied to the magnetic moment by the external magnetic field:

$$\boldsymbol{\tau} = \boldsymbol{\mu} \times \mathbf{B}_{\mathrm{ext}}\,. \tag{A.10}$$

The classical equation of motion for the magnetic moment can be derived from this relationship along with the knowledge that torque is equivalent to the time derivative of the angular momentum vector. Formulating the torque equation in terms of angular momentum, generically written as $\mathbf{J}$, results in

$$\frac{d\mathbf{J}}{dt} = \gamma \mathbf{J} \times \mathbf{B}_{\mathrm{ext}}\,. \tag{A.11}$$

Noting that $\mathbf{J} = \boldsymbol{\mu}/\gamma$, this relationship can be written in terms of the magnetic moment vector as

$$\frac{1}{\gamma}\frac{d\boldsymbol{\mu}}{dt} = \gamma\frac{1}{\gamma}\boldsymbol{\mu} \times \mathbf{B}_{\mathrm{ext}} = \boldsymbol{\mu} \times \mathbf{B}_{\mathrm{ext}} \tag{A.12}$$

or

$$\frac{d\boldsymbol{\mu}}{dt} = \gamma \boldsymbol{\mu} \times \mathbf{B}_{\mathrm{ext}}\,. \tag{A.13}$$

This equation of motion for the magnetic moment implies a precession about the direction of $\mathbf{B}_{\text{ext}}$ just as the quantum mechanical expectation values of spin components did before. If the external field is in the z direction, then

$$\frac{d\boldsymbol{\mu}}{dt} = \gamma \mathbf{B}_{\text{ext}}(\boldsymbol{\mu} \times \hat{\mathbf{z}})\,, \tag{A.14}$$

and the three components of this vector equation are

$$\frac{d\mu_x}{dt} = \gamma B_{\text{ext}}\mu_y \qquad \frac{d\mu_y}{dt} = -\gamma B_{\text{ext}}\mu_x \qquad \frac{d\mu_z}{dt} = 0\,. \tag{A.15}$$

In agreement with the quantum mechanical results, μ_z is a constant while μ_x and μ_y imply a circular motion of the transverse magnetic moment where

$$\mu_{\text{transverse}} = \mu_{\perp} = \sqrt{\mu_x^2 + \mu_y^2}\,. \tag{A.16}$$

With the Larmor frequency ω_0 having been defined, the two possible energy levels of spin-1/2 particles in an external magnetic field can be expressed as

$$E_{\pm} = \mp\frac{\omega_0 \hbar}{2}\,. \tag{A.17}$$

The energy difference between the two states is then

$$\Delta E = \gamma B_0 \hbar = \omega_0 \hbar\,, \tag{A.18}$$

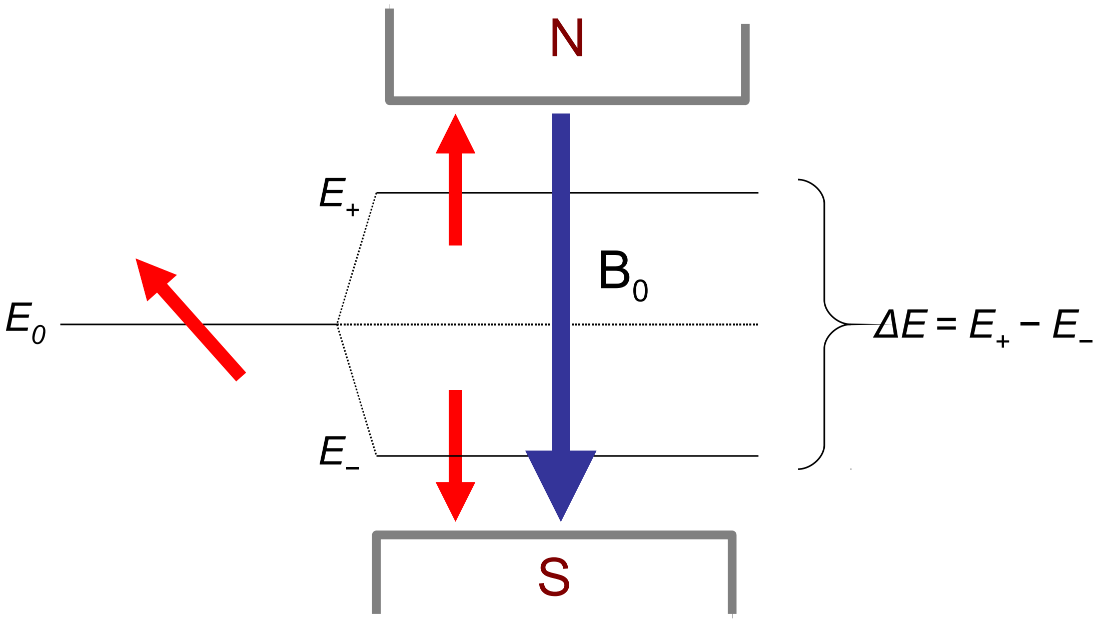

Figure A.1: Energy levels of a nuclear spin in an external magnetic field.

implying that a particle may absorb a photon of frequency ω_0 to transition from the E_+ (spin-aligned) state to the E_- (spin-anti-aligned) state and may emit an identical photon to undergo the opposite transition[†]. A schematic diagram of energy levels is shown in Figure A.1.

1.5 Nuclear Magnetic Resonance

The single electron in the neutral hydrogen atom experiences a magnetic field originating from the magnetic moment of the proton. The presence of this magnetic field causes the division of each electron energy level into two levels with slightly different energies a higher energy state in which the electron magnetic moment is parallel to that of the proton and a lower energy state in which the two magnetic moments are anti-parallel. This division of atomic energy levels due to spin-spin

---

[†] If the photon frequency is ω, the photon energy is $\hbar\omega$.

interaction gives rise to the hyperfine structure of the atomic hydrogen spectrum. The electron can be excited to the higher energy state through means such as thermal collisions with neighboring particles and can return to the lower energy state via the emission of a radio frequency photon with a 21 cm wavelength[†]. The associated photon energy of 5.9×10^{-6} eV corresponds to the energy difference between the two hyperfine states within the electronic ground state of neutral hydrogen.

The hydrogen proton can theoretically undergo a similar *spin-flip* transition to the electron, but it is exceedingly rare that the proton would be the particle excited by atomic collisions. Since the gyromagnetic ratio of the proton is 658 times less than that of the electron, the photon from the proton undergoing a spin-flip would have a proportionally longer wavelength, i.e., 138 m. Needless to say, this radiation would be difficult to detect from an astronomical source, but, in a controlled laboratory setting with the proton subjected to a much higher magnetic field strength, stimulated excitation and radiation detection of the proton's magnetic dipole transitions are quite possible. Such manipulations of the nuclear spin state in fact form the basis of nuclear magnetic resonance.

Suppose a hydrogen nucleus (proton) is subject to an external magnetic field ($\mathbf{B}_{\text{ext}}$) of 1 T in the z direction. The proton's magnetic moment then precesses about the field direction at the Larmor frequency dictated by the field strength and the proton

---

[†] The corresponding 21 cm spectral line is commonly observed in radio astronomy as such radiation is emitted from cool neutral hydrogen regions in interstellar space.

gyromagnetic ratio:

$$\begin{aligned}\omega_0 = \gamma\,|\mathbf{B}_{\text{ext}}| &= (2.675\times10^8\,\text{rad/s})(1\,\text{T}) = 2.675\times10^8\,\text{rad/s}\\ &= 2.675\times10^8\,\text{rad/s}\frac{1\,\text{cycle}}{2\pi\,\text{rad}} = 42.57\,\text{MHz}\,.\end{aligned}\tag{A.1}$$

Since the Larmor frequency is directly proportional to the field strength, the quantity $\gamma/(2\pi)$ is useful for computing the Larmor frequency in Hz for a given field strength:

$$\left(\frac{\gamma}{2\pi}\right)_{\text{proton}} = 42.57\,\text{MHz/T}\,.\tag{A.2}$$

Thus, for a 7 T field, ω_0 for a proton is simply $7\,\text{T}\times 42.57\,\text{MHz/T}$ or 298.0 MHz.

If atomic hydrogen in a 1 T field is subject to radiation of frequency 42.57 MHz, the nucleus will readily absorb a photon and transition to the excited state in which the nuclear magnetic moment and the external field direction are anti-aligned. This phenomenon of a nucleus in a magnetic field absorbing energy from radiation at the resonant (Larmor) frequency is known as nuclear magnetic resonance (NMR). Since each type of nucleus has a unique gyromagnetic ratio, different types of nuclei have different Larmor frequencies at a given magnetic field strength. For this reason, nuclei of only a certain type in a sample can be selectively excited by stimulation with radiation at the Larmor frequency. The precessing magnetization vector of the excited nuclei can then be detected by means of the changing magnetic flux through a radio frequency coil (Faraday's Law). Such tactics can be employed to determine the identity of atoms in an unknown sample by way of probing the resonant frequencies of the sample. This process of identifying elements by their unique Larmor frequencies is known as NMR spectroscopy.

1.6 Bulk Magnetization and the Bloch Equation

For a material in an external magnetic field, the bulk magnetization **M** is simply the volume density of magnetic moments such that

$$\mathbf{M} = \frac{1}{V}\sum_i \boldsymbol{\mu}_i \,. \tag{A.1}$$

This net magnetization vector follows an equation of motion analogous that of a single spin:

$$\frac{d\mathbf{M}}{dt} = \gamma \mathbf{M} \times \mathbf{B}_{\text{ext}} \,. \tag{A.2}$$

Breaking this relation into longitudinal (parallel to the field direction) and transverse (perpendicular to the field direction) components results in

$$\frac{dM_z}{dt} = 0 \qquad\qquad \frac{dM_\perp}{dt} = \gamma \mathbf{M}_\perp \times \mathbf{B}_{\text{ext}} \,. \tag{A.3}$$

This is one representation of the Bloch equation, the relation that govern the behavior of the bulk magnetization vector in an external field. The equation for M_z holds true only if nuclear spins are not allowed to exchange energy with their surroundings. If spins do interact with the lattice of surrounding particles, M_z will eventually return to its equilibrium value M_0 such that

$$\frac{dM_z}{dt} = \frac{1}{T_1}(M_0 - M_z)\,, \tag{A.4}$$

where T_1 is the time constant of the longitudinal magnetization recovery. The solution to this equation can be written in terms of an initial time t_0 as

$$M_z(t) = M_z(t_0)e^{-(t-t_0)/T_1} + M_0\left(1 - e^{-(t-t_0)/T_1}\right)\,. \tag{A.5}$$

While the longitudinal magnetization recovers to equilibrium, the transverse component of magnetization will simply precess about the applied field direction with frequency ω_0 as long as all spins in the material experience the same magnetic field. In reality, different spins have different local magnetic environments due to 1) the magnetic fields of neighboring particles, 2) additional applied external magnetic fields, and 3) external field heterogeneities. Such variations in the net applied field cause the precession frequencies to vary for different spins. The existence of a range of ω_0 values leads to a dephasing and thus reduction of the transverse magnetization that is independent of the effects of longitudinal recovery. The overall rate of $M_\perp$ dephasing is typically characterized by the time constant T_2^* such that in a frame of reference rotating at the mean Larmor frequency of the material (in this frame, the effective magnetic field is zero) the transverse magnetization follows the relationship

$$\frac{d\mathbf{M}_\perp}{dt} = -\frac{1}{T_2^*}\mathbf{M}_\perp\,, \tag{A.6}$$

which has the solution

$$\mathbf{M}_{\perp}(t) = \mathbf{M}_{\perp}(t_0)e^{-t/T_2^*}\,. \tag{A.7}$$

Contributions to dephasing from external field heterogeneities are often thought of separately and characterized by a time constant T_2' while dephasing effects due to the local magnetic environment are characterized by the time constant T_2. The relationship between these three transverse magnetization dephasing time constants is then

$$\frac{1}{T_2^*} = \frac{1}{T_2'} + \frac{1}{T_2}\,. \tag{A.8}$$

The time constant T_1 and the various T_2's can be measured in material and thus provide information about the magnetic properties of the material, its composition, and the local magnetic environment.

1.7 Spin Tipping and NMR Signal Detection

The equations of motion for bulk magnetization in material having been established, the intimate relationship between the direction of the applied field and the direction of the net magnetization vector is obvious. Application of a secondary field $\mathbf{B}_1$ (in the form of a radio frequency (RF) pulse) in addition to the main field $\mathbf{B}_0$ will cause the magnetization vector to precess about a different direction determined by the vector sum of the applied fields. In a frame of reference rotating with the Larmor frequency associated with the $\mathbf{B}_0$ field such that the effective $\mathbf{B}_0$ field is zero, the magnetization vector will precess about the $\mathbf{B}_1$ direction with a frequency $\omega_1 = \gamma|\mathbf{B}_1|$ dependent on the amplitude of the RF field. The angle through which the magnetization vector rotates, called the *flip angle*, is then determined by the time integral of the ω_1 precession frequency such that

$$\theta_{\text{flip}} = \int_0^{\Delta T} \omega_1(t)\, dt = \gamma \int_0^{\Delta T} B_1(t)\, dt\,, \tag{A.1}$$

where the integration limit ΔT corresponds to the duration of the RF pulse. Thus, by controlling the magnitude of the field and the duration of its application, a given flip angle can be experimentally selected. Such manipulations of the magnetization vector are crucial to detecting an NMR signal since only the transverse component of magnetization is detectable.

In the equilibrium state ($\mathbf{M} = M_0\hat{\mathbf{z}}$), the transverse components of magnetization cancel since the phases of individual spins are arbitrary. If the magnetization vector is tipped via an RF pulse so that it has a transverse component, Larmor precession then results in a changing magnetic field at a given point in space. By virtue of Faraday's Law, this changing magnetic field leads to a changing magnetic flux through a strategically positioned RF coil that in turn is subject to a detectable voltage or electromotive force (emf). The size and shape of this detected voltage constitute the NMR signal. In terms of the magnetization vector, which may certainly vary in space, the NMR signal is given by

$$S = \int |M_\perp(\mathbf{r})|\, d\mathbf{r} = \int \rho_M(\mathbf{r}) e^{i\phi(\mathbf{r})}\, d\mathbf{r}\,, \tag{A.2}$$

where ρ_M represents the magnitude of the transverse magnetization and ϕ represents its phase in the complex (i.e., x-y) plane.

1.8 Magnetic Field Gradients and Slice Selection

With the goal of forming 2-D images from the NMR signal, it is requisite to have a method for obtaining signal from only a particular region/slice of space. In magnetic resonance imaging (MRI), this slice selection is accomplished by use of linear magnetic field gradients. Such gradients are typically produced by electrical coils that are mounted on the inside of the bore of the main field magnet. Via Ampere's Law, currents in these coils produce additional magnetic fields that can be engineered to vary linearly in space such that

$$B_{\text{gradient}} = \mathbf{r} \cdot \mathbf{G}\,, \tag{A.1}$$

with $\mathbf{G}$ being the field gradient. Because of the presence of such a gradient, the spins are subject to different Larmor frequencies at different positions in space. In the aforementioned rotating frame, the procession frequency in terms of the field gradient is given by

$$\omega(\mathbf{r}, t) = -\gamma(\mathbf{r} \cdot \mathbf{G}(t))\,. \tag{A.2}$$

Since the phase is simply the time integral of the precession frequency, the phase can be written as

$$\phi(\mathbf{r}, t) = -\gamma \mathbf{r} \cdot \int \mathbf{G}(t)\, dt\,. \tag{A.3}$$

Thus, the phase of magnetization in material can be selected via the amplitude and duration of the applied gradient field.

To selectively excite the magnetization of a slice of material in a given x-y plane, a gradient can be applied in the z direction such that

$$B_z(z,t) = B_0 + zG_z(t)\,. \tag{A.4}$$

Each z coordinate then experiences a unique magnetic field and a unique Larmor frequency. An RF pulse modulated by a $(\sin x)/x$ waveform (known as a texttttsinc waveform) can then be used to excite spins within a finite range of precession frequencies. The `sinc` function is ideal for this purpose since its Fourier transform is a square-shaped function in frequency space. That is to say if

$$B_1(\omega) = \int_{-\infty}^{+\infty} B_1(t)e^{-i\omega t}\,dt = \int_{-\infty}^{+\infty} \frac{\sin t}{t}e^{-i\omega t}\,dt\,, \tag{A.5}$$

then

$$B_1(\omega) = \begin{cases} 1 & \text{if } \omega_0 - \Delta\omega \leq \omega \leq \omega_0 + \Delta\omega \\ 0 & \text{otherwise} \end{cases}\,, \tag{A.6}$$

where ω_0 represents the central precession frequency of the target slice and $2\Delta\omega$ is the thickness of the excited slice. The selected slice cannot be perfectly thin because the RF frequency can not be pure if only applied for a finite duration. Within the selected slice the magnetization is uniformly tipped into the transverse plane; however, the phase across the slice because of the inherent range of Larmor frequencies introduced by the presence of the field gradient. This issue can be corrected simply by applying an equal but opposite field gradient for the same duration as the first but with no RF pulse. This effectively rephrases the magnetization within the selected slice.

1.9 MRI: the Spatial Encoding of the NMR Signal

To form images from NMR signals, field gradients are used to produce a correlation between spatial position and the precession frequency of the local magnetization. This process begins with the slice selection outlined in the preceding section and then continues with spatial encoding in the x and y directions.

If a gradient pulse is produced along the x direction, the phase of transverse magnetization in this same direction is given by

$$\phi(x) = -\gamma \int_0^{\Delta T} G_x(t)\, dt \cdot x = k_x x\,, \tag{A.1}$$

where k_x defines the rate at which spin phase changes with position and thus is known as the spatial frequency. Given that the magnitude of the transverse magnetization can be found from the Fourier transform of the NMR signal:

$$\rho_M = \frac{1}{2\pi} \int_{-\infty}^{+\infty} S(k_x) e^{ik_x x}\, dk_x\,. \tag{A.2}$$

Sampling S at different values of k_x allows for a calculation of magnetization as a function of the x coordinate. Sampling k_x values over a wider range will eventually lead to more image detail in the x direction.

There exist two common schemes for sampling a given range of k_x values: *phase encoding* and frequency encoding. In the phase encoding scheme, a certain gradient is applied for a finite duration in the x direction. The signal is sampled and then the magnetization is allowed to return to equilibrium. This process is then repeated for various gradients, one for each k_x value. It is possible to sample $\mathbf{k}$-space in this way since k_x is related to the time integral of the applied gradient. Thus, changing the duration or intensity of the gradient changes the k_x value. This technique is known as phase encoding because the position of a given magnetization element is encoded in the phase of the transverse magnetization. Frequency encoding is fundamentally not much different from phase encoding. The technique prepares the sample through the initial application of a large negative field gradient. Immediately afterward, a relatively small positive gradient is applied and maintained while the magnetization is sampled at a given time interval. Since the k_x value is constantly changing due to the continuously applied positive gradient, each sample of the NMR signal occurs at a unique k_x value. Thus, frequency encoding is an efficient way of collecting the spatially encoded NMR signal. The name of frequency encoding originates from the fact that sampling the magnetization over a set of ever-changing phases amounts to sampling the magnetization over a set of unique frequencies, each x position being associated with a unique Larmor frequency.

If, following slice selection in the z direction, the phase encoding technique is used along the y direction and the frequency encoding technique is used along the x direction, then each position within the imaging slice has successfully been spatial encoded. This rudimentary method of forming tomographic images from NMR signals is known as 2-D Fourier MRI and is only one of a multitude of techniques for sampling **k**-space. Different techniques introduce different trade-offs involving sampling speed and image quality and must be selected according to the specific application.

APPENDIX B

SIMULATION OF THE BLOCH EQUATION

Calculation the final simulated state of the magnetization vector ($\mathbf{M}^S$) during every iteration of the optimization exploits an analytic solution to a relaxation-independent form of the Bloch equations. Given Bloch equations in the form

$$\begin{aligned}\dot{M}_x(t) &= \Delta\omega M_y(t) - \gamma B_{1y} M_z(t)\\ \dot{M}_y(t) &= -\Delta\omega M_x(t) + \gamma B_{1y} M_z(t)\\ \dot{M}_z(t) &= \gamma(B_{1y} M_x(t) - B_{1x} M_x(t))\end{aligned} \tag{B.3}$$

and an RF field described by

$$\begin{aligned}B_{1x} &= \text{constant} = A_{\text{eff}} \cos\phi\\ B_{1y} &= \text{constant} = A_{\text{eff}} \sin\phi\\ B_{1z} &= \Delta\omega/\gamma\\ \omega_{\text{eff}} &= \sqrt{\Delta\omega^2 + \gamma^2(B_{1x}^2 + B_{1y}^2)}\end{aligned} \quad , \tag{B.4}$$

with A_{eff} representing the RF amplitude of the kth sub-pulse subject as weighted by B_1^+ such that $A_{\text{eff}} = A_k B_1^+ / B_{1,\text{nom}}^+$, the analytic solution $\mathbf{M}^f = (M_x^f, M_y^f, M_z^f)$ for a single block-shaped pulse can be written as

$$\begin{aligned}
M_x^f &= \omega_{\text{eff}}^{-2}[\gamma B_{1x}(1-\cos\omega_{\text{eff}}t)\times \\
&\qquad \times(\Delta\omega M_z^0 + \gamma B_{1y}M_y^0 + \gamma B_{1x}M_x^0) \\
&\quad +\omega_{\text{eff}}^2 M_x^0 \cos\omega_{\text{eff}}t \\
&\quad +\omega_{\text{eff}}(\Delta\omega M_y^0 - \gamma B_{1y}M_z^0)\sin\omega_{\text{eff}}t] \\
\\
M_y^f &= \omega_{\text{eff}}^{-2}[\gamma B_{1y}(1-\cos\omega_{\text{eff}}t)\times \\
&\qquad \times(\Delta\omega M_z^0 + \gamma B_{1y}M_y^0 + \gamma B_{1x}M_x^0)+ \\
&\quad +\omega_{\text{eff}}^2 M_y^0 \cos\omega_{\text{eff}}t- \\
&\quad -\omega_{\text{eff}}(\Delta\omega M_x^0 - \gamma B_{1x}M_z^0)\sin\omega_{\text{eff}}t] \\
\\
M_z^f &= \omega_{\text{eff}}^{-2}[\Delta\omega(1-\cos\omega_{\text{eff}}t)\times \\
&\qquad \times(\Delta\omega M_z^0 + \gamma B_{1y}M_y^0 + \gamma B_{1x}M_x^0)+ \\
&\quad +\omega_{\text{eff}}^2 M_z^0 \cos\omega_{\text{eff}}t- \\
&\quad -\gamma\omega_{\text{eff}}(B_{1x}M_y^0 - B_{1y}M_x^0)\sin\omega_{\text{eff}}t]
\end{aligned}, \tag{B.5}$$

where the initial state is described by $\mathbf{M}^0 = (M_x^0, M_y^0, M_z^0)$. This solution is equivalent to the Cartesian rotation matrix $\tilde{R}$ that transforms $\mathbf{M}^0$ to $\mathbf{M}^f$ in the presence of an RF pulse with constant amplitude A and constant phase $\phi = \tan^{-1}(B_{1y}/B_{1x})$ (3) such that

$$\mathbf{M}^f = \tilde{R}\mathbf{M}^0 \tag{B.6a}$$

or equivalently

$$\begin{bmatrix} M_x^f \\ M_y^f \\ M_z^f \end{bmatrix} = \begin{bmatrix} R_{11} & R_{12} & R_{13} \\ R_{21} & R_{22} & R_{23} \\ R_{31} & R_{32} & R_{33} \end{bmatrix} \begin{bmatrix} M_x^0 \\ M_y^0 \\ M_z^0 \end{bmatrix} . \tag{B.6b}$$

Given the additional definitions

$$\beta = \tan^{-1}\left(\frac{\Delta\omega}{\gamma\sqrt{B_{1x}^2 + B_{1y}^2}}\right) \tag{B.7a}$$

and

$$\theta = \omega_{\text{eff}}\Delta T\,, \tag{B.7b}$$

the matrix elements of $\tilde{R}$ can be written as

$$\begin{aligned}
R_{11} =&\ \sin^2\phi\cos\theta + \cos^2\phi\left(\cos^2\beta + \sin^2\beta\cos\theta\right) \\
R_{12} =&\ \sin\beta\sin\theta - \sin(2\phi)\cos^2\beta\sin^2(\theta/2) \\
R_{13} =&\ \sin\phi\cos\beta\sin\theta + \cos\phi\sin(2\beta)\sin^2(\theta/2) \\
R_{21} =&\ -\sin\beta\sin\theta - \sin(2\phi)\cos^2\beta\sin^2(\theta/2) \\
R_{22} =&\ \cos^2\phi\cos\theta + \sin^2\phi\left(\cos^2\beta + \sin^2\beta\cos\theta\right) \\
R_{23} =&\ \cos\phi\cos\beta\sin\theta - \sin\phi\sin(2\beta)\sin^2(\theta/2) \\
R_{31} =&\ -\sin\phi\cos\beta\sin\theta + \cos\phi\sin(2\beta)\sin^2(\theta/2) \\
R_{32} =&\ -\cos\phi\cos\beta\sin\theta - \sin\phi\sin(2\beta)\sin^2(\theta/2) \\
R_{33} =&\ \sin^2\beta + \cos^2\beta\cos\theta
\end{aligned} \quad . \tag{B.8}$$

Using this rotation representation of the analytic solution, the magnetization response to a composite of constant amplitude sub-pulses can be modeled simply by a series of rotations, each corresponding to one of the k individual sub-pulses such that

$$\mathbf{M}^S = \tilde{R}_k \tilde{R}_{k-1} \tilde{R}_{k-2} \ldots \tilde{R}_1 \mathbf{M}^0 \,. \tag{B.9}$$

The rotation operator for each sub-pulse in Eq. (B.9) can equivalently be replaced by a calculation of the magnetization components via Eq. (B.5) given that the initial conditions $\mathbf{M}_k^0$ for the k-th sub-pulse correspond to the final state $\mathbf{M}_{k-1}^f$ of the magnetization following the previous sub-pulse.

Use of an analytic solution means that computational time is independent of the total duration of the an RF pulse—it is only the number of sub-pulses and the size of the B_1^+-ΔB_0 grid that are relevant. MATLAB-based performance comparisons between the two formulations of the analytic solution (Eqs. (B.5) and (B.6b)) indicated that use of Eq. (B.5) results in computations that are considerably ($\sim$ 10 times) faster. Given that the two methods give identical results, the more time-efficient approach was employed for all simulations in this study with computational times for optimization ranging from several minutes (16 sub-pulses) to several days (128 sub-pulses) per pulse on a 2.0 GHz desktop computer. Simulation of the Bloch equations via analytic solution (either Eq. (B.5) or Eq. (B.6b)) has been found to save considerable computational time as compared to a typical finite difference approach for which the time steps must be sufficiently small. Use of an analytic solution means that computational time is independent of the total duration of the an RF pulse—it is only the number of sub-pulses and the size of the B_1^+-ΔB_0 grid that are relevant. For the RF pulses presented in this work, the analytic solution of Eq. (B.5) was utilized, and computational time for optimization ranged from several minutes (16 sub-pulses) to several days (128 sub-pulses) per pulse on a 2.0 GHz desktop computer. These times would increase by a factor proportional to the number of dwell times per sub-pulse if a typical finite difference simulation were used. Furthermore, MATLAB-based performance comparisons between the two formulations of the analytic solution (Eqs. (B.5) and (B.6b)) indicated that use of Eq. (B.5) results in computations that are considerably ($\sim$ 10 times) faster. Given that the two methods give identical results, the more time-efficient approach was employed for all simulations in this study. After optimization, composite pulses were analysized for susceptibility to relaxation of the transverse magnetization. Since an analytic solution to the Bloch equations exists only for the special case in which longitudinal and transverse relaxation time constants are infinite (i.e., $T_1 = T_2 = \infty$), a finite time difference simulation was employed for this purpose. Specifically, the change in magnetization components during the i-th time step were calculated via

$$\begin{aligned}\Delta M_x^i = {} & [2\pi\gamma\left(M_y^{i-1}B_{1z}^i - M_z^{i-1}B_{1y}^i\right) - \\ & M_x^{i-1}/T_2]\Delta t\end{aligned}$$

$$\begin{aligned}\Delta M_y^i = {} & [2\pi\gamma\,(M_z^{i-1}B_{1x}^i - M_z^{i-1}B_{1z}^i) - \\ & M_y^{i-1}/T_2]\Delta t\end{aligned} \quad , \tag{B.10}$$

$$\begin{aligned}\Delta M_z^i = {} & [2\pi\gamma\left(M_x^{i-1}B_{1y}^i - M_y^{i-1}B_{1x}^i\right) - \\ & M_z^{i-1}/T_1]\Delta t\end{aligned}$$

where ΔT is the length of the time step. As previously mentioned, this approach proved much slower than when using an analytic method, especially given that ΔT must be on the order of $0.1\,\mu$s to achieve reasonable accuracy for composite pulses with wildly varying phases and amplitudes. Each optimized pulse, however, need only be simulated once for each T_2 value, as opposed to the multitude of times a simulation must be carried out in the numerical optimization process. All optimized pulses were evaluated in this way for T_2 values of 5, 10, 15, 20, 30, and 50 ms, while T_1 values were always assumed to be infinite. For each pulse, δ_α (Equation (3.2.2)) and $\delta_{\mathbf{M}}$ (Equation (3.2.2)) were calculated and values compared to those found without consideration for T_2.

APPENDIX C

MODULATION FUNCTIONS FOR ADIABATIC PULSES

Provided here are explicit forms of the hyperbolic secant and BIR-4 amplitude, phase, and frequency modulations as employed at various places in this thesis. Also included are a few details on how modulations are determined and strategies used for simulations in this thesis.

3.1 Hyperbolic Secant Modulations

In the absence of relaxation effects, the Bloch equations can be written as

$$\begin{aligned} \frac{d}{dt}\tilde{M}_\perp + i\Delta\omega\tilde{M}_\perp + M_z\tilde{B}_1(t) = 0 \\ \frac{d}{dt}M_z - \tfrac{1}{2}i\left(\tilde{M}_\perp\tilde{B}_1^*(t) - \tilde{M}_\perp^*\tilde{B}_1(t)\right) = 0 \end{aligned}\,, \tag{C.1}$$

with M_z being the longitudinal magnetization and $\tilde{M}_\perp$ the complex transverse magnetization. In terms of the equilibrium magnetization, M_0, and the substitution $\xi = \tilde{M}_\perp / \left(M_0 + M_z\right)$, Equation 1.3.1 can be written in what's commonly known as the Riccati form:

$$\frac{d}{dt}\xi + i\Delta\omega\xi - \frac{1}{2}i\left(\tilde{B}_1^*(t)\xi^2 + \tilde{B}_1(t)\right) = 0\,. \tag{C.2}$$

Although this Bloch-Riccati equation has no general analytic solution, a solution characterized by population inversion within a certain bandwidth ($\Delta\omega_0$) is possible if the $\tilde{B}_1(t)$ field is described by a hyperbolic secant function (72) such that

$$\tilde{B}_1(t) = \left(A_0 \operatorname{sech}(\beta\, t)\right)^{1+i\mu} . \tag{C.3}$$

The parameters A_0, β, and μ define the amplitude modulation (AM) and phase modulation (PM) (or, equivalently, frequency modulation (FM)) waveforms which are specifically given by (73)

$$\begin{aligned} \mathrm{AM}(t) &= \left|\tilde{B}_1\right| = \sqrt{\tilde{B}_1 \tilde{B}_1^*} = A_0 \operatorname{sech}(\beta t) \\ \mathrm{PM}(t) &= \phi_{\tilde{B}_1} = \mu \ln\left(\operatorname{sech}(\beta t)\right) \\ \mathrm{FM}(t) &= \frac{d}{dt}\phi_{\tilde{B}_1} = -\mu\beta \tanh(\beta t) \end{aligned} \quad . \tag{C.4}$$

Thus, A_0 represents the maximum value of the AM waveform, while β is a frequency describing the width of the PM and FM waveforms. The unitless constant μ may best be interpreted as scaling the range of the frequency sweep or, equivalently, fixing the maximum value of the RF phase. Together, μ and β determine the excitation bandwidth (72) such that

$$\Delta\omega_0 = \pm\mu\beta\,. \tag{C.5}$$

3.2 BIR-4 Modulations

Four-part B_1^+-insensitive rotations (BIR-4) are composites of four adiabatic pulse segments. These pulses are capable of producing arbitrary flip angles and have been shown to improve flip-angle uniformity in the context of volume (non-selective) excitation (76; 23); therefore, BIR-4 pulses provide a suitable basis for comparison when evaluating the performance of the optimized composite pulses produced in this study. Flip-angle maps for 4.096 ms BIR-4 pulses with flip angles of 30°, 60°, 90°, and 180° were simulated for specific comparison with the subset of four 4.096 ms optimized pulses subject to additional analysis in Section 3.3.2. Simulation of the Bloch equations (Section 3.2.8) was carried out in an identical manner to that of optimized pulses; however, BIR-4 pulses were divided into as many 6.4μs block-shaped subpulses as possible ($n = 640$) given the total pulse duration ($\Delta T = 4.096$ ms). This reflects the typical way pulses with continuous waveforms are executed digitally on an amplifier for which the dwell time is 6.4μs.

The components of a BIR-4 pulse are defined by hyperbolic tangent amplitude modulation and tangential frequency sweep in the following form:

$$A(t) = \begin{cases} A_0 \tanh[\lambda(1 - \frac{4t}{\Delta T})] \\ A_0 \tanh[\lambda(\frac{4t}{\Delta T} - 1)] \\ A_0 \tanh[\lambda(3 - \frac{4t}{\Delta T})] \\ A_0 \tanh[\lambda(\frac{4t}{\Delta T} - 3)] \end{cases} \tag{C.1a}$$

$$\nu(t) = \frac{\nu_0}{\tan\beta} \cdot \begin{cases} \tan[\frac{4\beta t}{\Delta T}] \\ \tan[2\beta(\frac{2t}{\Delta T} - 1)] \\ \tan[2\beta(\frac{2t}{\Delta T} - 1)] \\ \tan[4\beta(\frac{t}{\Delta T} - 1)] \end{cases} , \tag{C.1b}$$

$$\phi(t) = \begin{cases} \int_0^t \nu(t)dt \\ \int_0^t \nu(t)dt + \Delta\phi_1 \\ \int_0^t \nu(t)dt + \Delta\phi_1 \\ \int_0^t \nu(t)dt + \Delta\phi_1 + \Delta\phi_2 \end{cases} \tag{C.1c}$$

where each piece corresponds respectively to the four equal time intervals given by

$$\begin{aligned} &\Delta T_1 : 0 \leq t < \Delta T/4 \\ &\Delta T_2 : \Delta T/4 \leq t < \Delta T/2 \\ &\Delta T_3 : \Delta T/2 \leq t < 3\Delta T/4 \\ &\Delta T_4 : 3\Delta T/4 \leq t \leq \Delta T \end{aligned} . \tag{C.2}$$

The constants A_0, λ, and β control the shape of the modulation functions and therefore determine the extent to which adiabatic conditions are maintained. The constants $\Delta\phi_1$ and $\Delta\phi_2$ describe phase shifts at the beginning of the second and fourth pulse segments and are related to the target flip angle. For simulation, A_0 was set to $15\,\mu\text{T}$ to maximize adiabatic performance within the prescribed hardware limits while λ and β are assigned respective values of 10 rad and 1.47 rad, as suggested in (76). The constant ν_0 was given a value of 1.5×10^4 rad/s such that the range of the frequency sweep, determined by $\nu_0/\tan\beta$, was 50% larger than the range of ΔB_0 values on the composite pulse optimization grid. This choice ensured that any undesirable effects from including contributions from the shoulder of the central lobe of the slice profile were minimized. The desired flip angle α_0 constrained the selection of the first phase shift via $\Delta\phi_1 = \pi + \alpha_0/2$ while the efficiency of pulses was maximized by the choice of $\Delta\phi_2 = -\Delta\phi_1$ (76).

APPENDIX D

COMPLETE OPTIMIZATION DATA FOR VOLUME EXCITATION PULSES

Given here are the complete optimization results for all composite pulses generated for the work described in Chapter III and for the hyperbolic secant pulses optimizations reported in Section 6.1.

The non-selective composite pulse optimization data is potentially useful in that specific cost function and minimum T_R values are accessible in Tables D.1 and D.2, the former of which reports information for composites of 16–64 sub-pulses and the latter of which gives the same information for composites of 80–128 sub-pulses. Furthermore, Figure D.1 displays this information such that pulse performance as a function of sub-pulse duration (Δt_s) and the number of sub-pulses (N_s). The corresponding data is presented in Chapter III but as a function of total pulse duration only. Thus, the presentation in this appendix provides some additional insight into factors affecting pulse performance. In general in can be concluded that pulse performance as measured by the cost function improves with increases in both Δt_s and N_s, presumably due to the increased allotted power associated with each trend.

The hyperbolic secant optimization data is presented in Tables D.3 and D.4 and allows for access to the optimal values of parameters μ and β for pulses with target bandwidths ranging from 100–1000 Hz.

Table D.1: Dependence of pulse performance on design parameters: groups of rows represent pulses designed with different numbers of component sub-pulses; columns represent different sub-pulse durations. Given for each combination of sub-pulse number and duration are 1) the total pulse duration (ΔT), 2) the normalized average deviations of the simulated flip-angles from the target values of 30°, 60°, 90°, and 180° (denoted respectively by δ_{30°, δ_{60°, δ_{90°, and δ_{180°) over the B_1^+-ΔB_0 grid, and 3) corresponding SAR-limited minimum repetition times ($T_{R,\mathrm{min}}$ as determined via Equation (3.2.5b)) shown as subscripts and rounded to the nearest millisecond). δ_α values correspond to the quantity subject to minimization in the optimization process and explicitly described by Equation (3.2.2).

sub-pulses	attribute	6.4 μs	12.8 μs	19.2 μs	32.0 μs	64.0 μs	128.0 μs	192.0 μs	320.0 μs
16	ΔT (ms)	0.1024	0.2048	0.3072	0.5120	1.0240	2.0480	3.0720	5.1200
	δ_{30°	0.3933_{10}	0.2783_{14}	0.2757_{18}	0.2707_{21}	0.2785_{29}	0.1154_{15}	0.0948_{42}	0.0739_{11}
	δ_{60°	0.7371_{9}	0.5957_{13}	0.3940_{18}	0.2735_{22}	0.1810_{26}	0.0834_{53}	0.1211_{33}	0.0848_{70}
	δ_{90°	0.8113_{9}	0.7304_{13}	0.5960_{18}	0.2824_{22}	0.2286_{26}	0.1631_{51}	0.1184_{39}	0.0586_{61}
	δ_{180°	0.9124_{9}	0.8652_{13}	0.7980_{18}	0.5656_{22}	0.3266_{26}	0.2667_{40}	0.1026_{39}	0.0498_{42}
32	ΔT (ms)	0.2048	0.4096	0.6144	1.0240	2.0480	4.0960	6.1440	10.2400
	δ_{30°	0.2789_{17}	0.2715_{32}	0.2404_{55}	0.1432_{67}	0.0861_{105}	0.0696_{114}	0.0837_{101}	0.2084_{130}
	δ_{60°	0.6159_{13}	0.2825_{26}	0.2610_{41}	0.1960_{42}	0.0973_{42}	0.0519_{57}	0.0460_{57}	0.0517_{45}
	δ_{90°	0.7439_{13}	0.4086_{29}	0.2824_{36}	0.2502_{71}	0.1185_{88}	0.0887_{85}	0.0493_{83}	0.1097_{111}
	δ_{180°	0.8720_{13}	0.7043_{29}	0.6181_{34}	0.3483_{43}	0.2785_{51}	0.0772_{71}	0.0609_{78}	0.0505_{72}
48	ΔT (ms)	0.3072	0.6144	0.9216	1.5360	3.0720	6.1440	9.2160	15.3600
	δ_{30°	0.2764_{22}	0.2461_{57}	0.2239_{67}	0.0998_{109}	0.0653_{111}	0.0818_{134}	0.0705_{203}	0.1229_{191}
	δ_{60°	0.4545_{20}	0.2646_{47}	0.2511_{63}	0.2449_{101}	0.0512_{142}	0.0444_{109}	0.0503_{189}	0.0903_{113}
	δ_{90°	0.6363_{20}	0.3056_{39}	0.2502_{73}	0.2114_{103}	0.0909_{107}	0.0314_{152}	0.0604_{124}	0.0408_{114}
	δ_{180°	0.8182_{20}	0.6511_{38}	0.4457_{55}	0.3232_{71}	0.1686_{87}	0.1463_{73}	0.0488_{91}	0.0418_{77}
64	ΔT (ms)	0.4096	0.8192	1.2288	2.0480	4.0960	8.1920	12.2880	20.4800
	δ_{30°	0.2758_{30}	0.2348_{92}	0.1381_{138}	0.1108_{128}	0.0488_{201}	0.0483_{228}	0.0495_{237}	0.1543_{274}
	δ_{60°	0.3396_{46}	0.2659_{95}	0.1997_{69}	0.0898_{181}	0.0968_{245}	0.0494_{260}	0.0368_{312}	0.1050_{132}
	δ_{90°	0.5558_{39}	0.2479_{63}	0.2116_{105}	0.1072_{172}	0.0691_{168}	0.0381_{114}	0.0509_{211}	0.0304_{148}
	δ_{180°	0.7779_{43}	0.5591_{69}	0.3410_{86}	0.3213_{86}	0.0994_{96}	0.0762_{194}	0.0380_{188}	0.0487_{132}

Table D.2: Dependence of pulse performance on design parameters: groups of rows represent pulses designed with different numbers of component sub-pulses; columns represent different sub-pulse durations. Given for each combination of sub-pulse number and duration are 1) the total pulse duration (ΔT), 2) the normalized average deviations of the simulated flip-angles from the target values of 30°, 60°, 90°, and 180° (denoted respectively by δ_{30°, δ_{60°, δ_{90°, and δ_{180°) over the B_1^+-ΔB_0 grid, and 3) corresponding SAR-limited minimum repetition times ($T_{R,\min}$ as determined via Equation (3.2.5b)) shown as subscripts and rounded to the nearest millisecond). δ_α values correspond to the quantity subject to minimization in the optimization process and explicitly described by Equation (3.2.2).

sub-pulses	attribute	6.4 μs	12.8 μs	19.2 μs	32.0 μs	64.0 μs	128.0 μs	192.0 μs	320.0 μs
80	ΔT (ms)	0.5120	1.0240	1.5360	2.5600	5.1200	10.240	15.3600	25.6000
	δ_{30°	0.2742_{14}	0.1193_{149}	0.1177_{199}	0.0671_{245}	0.0525_{245}	0.1162_{298}	0.1127_{319}	0.0980_{312}
	δ_{60°	0.2825_{99}	0.2683_{165}	0.1133_{273}	0.0627_{358}	0.0432_{351}	0.0420_{346}	0.0738_{630}	0.0825_{391}
	δ_{90°	0.4620_{86}	0.2348_{158}	0.2039_{191}	0.1101_{256}	0.0486_{433}	0.0296_{497}	0.0358_{403}	0.0329_{480}
	δ_{180°	0.7310_{79}	0.4825_{119}	0.3194_{184}	0.3133_{283}	0.0788_{481}	0.0348_{369}	0.0341_{178}	0.0444_{303}
96	ΔT (ms)	0.6144	1.2288	1.8432	3.0720	6.1440	12.2880	18.4320	30.7200
	δ_{30°	0.2785_{113}	0.1150_{166}	0.1000_{153}	0.0569_{211}	0.0396_{701}	0.1014_{691}	0.1030_{193}	0.1808_{778}
	δ_{60°	0.2676_{181}	0.2627_{261}	0.1707_{274}	0.0573_{532}	0.0339_{659}	0.0432_{651}	0.0538_{720}	0.0913_{580}
	δ_{90°	0.2675_{197}	0.2415_{292}	0.1380_{456}	0.2029_{504}	0.0427_{640}	0.0596_{265}	0.0218_{648}	0.0364_{439}
	δ_{180°	0.5983_{145}	0.3410_{344}	0.3352_{211}	0.1721_{559}	0.1160_{798}	0.0349_{715}	0.0345_{941}	0.0376_{900}
112	ΔT (ms)	0.7168	1.4336	2.1504	3.5840	7.1680	14.3360	21.5040	35.8400
	δ_{30°	0.2695_{106}	0.1816_{119}	0.0651_{146}	0.0553_{175}	0.0418_{733}	0.0419_{769}	0.0712_{802}	0.1445_{1002}
	δ_{60°	0.2726_{209}	0.2594_{289}	0.0858_{491}	0.0491_{438}	0.0544_{484}	0.0386_{694}	0.0473_{860}	0.1213_{861}
	δ_{90°	0.2845_{158}	0.2414_{451}	0.1791_{560}	0.1012_{503}	0.0484_{792}	0.0430_{751}	0.0270_{568}	0.0587_{716}
	δ_{180°	0.6049_{276}	0.3275_{569}	0.3178_{663}	0.1713_{824}	0.1738_{927}	0.0333_{889}	0.0319_{930}	0.0371_{984}
128	ΔT (ms)	0.8192	1.6384	2.4576	4.0960	8.1920	16.3840	24.5760	40.9600
	δ_{30°	0.3250_{133}	0.1089_{541}	0.0715_{143}	0.0450_{624}	0.0301_{693}	0.0623_{668}	0.0600_{522}	0.1704_{1210}
	δ_{60°	0.2429_{154}	0.2635_{350}	0.1659_{347}	0.1244_{466}	0.0249_{473}	0.0705_{706}	0.0298_{548}	0.1220_{301}
	δ_{90°	0.2734_{296}	0.2257_{388}	0.1848_{446}	0.1385_{661}	0.0212_{412}	0.0457_{562}	0.0344_{573}	0.0390_{670}
	δ_{180°	0.5787_{419}	0.3370_{655}	0.3281_{710}	0.2746_{848}	0.1336_{793}	0.0302_{876}	0.0343_{841}	0.0347_{1066}

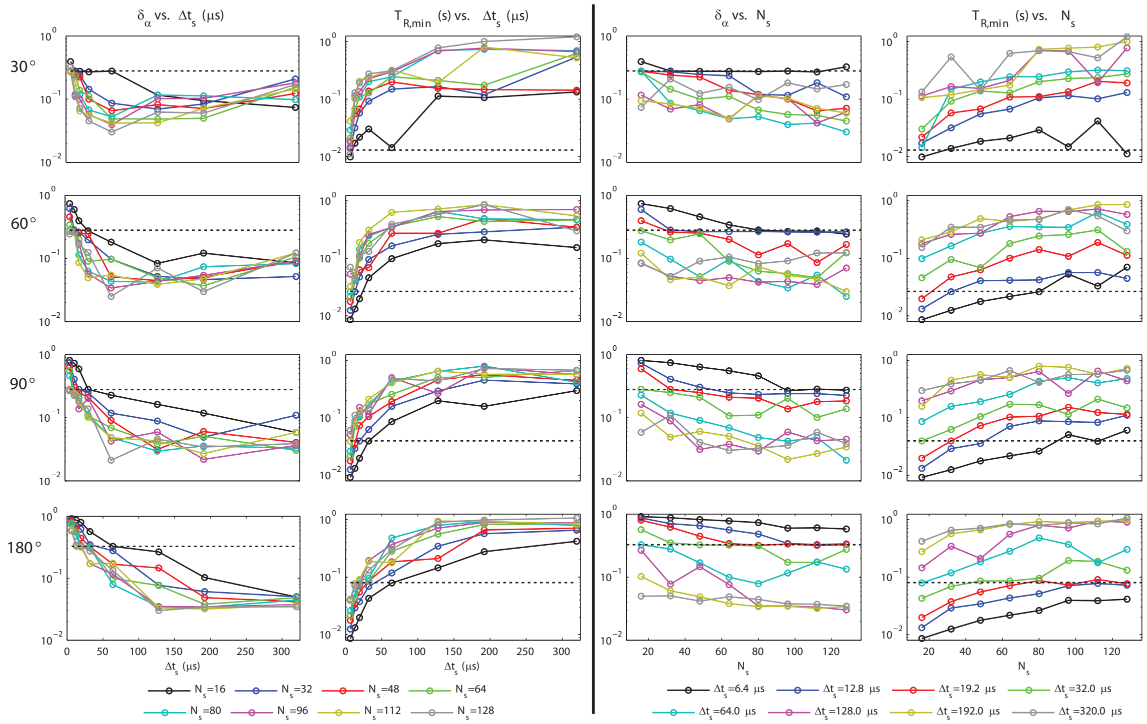

Figure D.1: Optimization results for all 256 composite pulses designed in this study with one row of sub-figures for each nominal flip angle. Minimized function values (δ_α) which are related to flip-angle uniformity (Eq. (3.2.2)) and minimum repetition times ($T_{R,\min}$) which are reflective of SAR (Eq. (3.2.5b)) are given as functions of sub-pulse duration (Δt_s) in the two left columns and as functions of the number of composite elements (N_s) in the right two columns. Colors in the former case denote constant values of N_s and in the latter case denote constant Δt_s. Dotted black lines designate corresponding values of the relevant block pulses described in Fig. 16. In general, data show that reduction in δ_α corresponds to lengthening of $T_{R,\min}$. Relative to maximum bandwidth block pulses, the majority of composite pulses result in increased flip-angle uniformity as measured in the context of the B_1^+-ΔB_0 optimization grid.

Table D.3: Dependence of low-bandwidth hyperbolic secant pulse performance on design parameters. Rows represent pulses with the given optimization bandwidth ($\Delta\omega_{opt}$), and columns correspond to different pulse durations. For each pulse, the average deviation of the flip-angle from the target value of 180° over the entire UPS ($\overline{\sigma}$), the parameter β, the parameter μ, the time-averaged RF power ($\overline{P} = \int A^2\,dt/\Delta T$), and the ratio ($\overline{P}_{ratio}$) of $\overline{P}$ to the corresponding value for a block pulse with equivalent duration and flip angle are given.

$\Delta\omega_{opt}$	atribute	units	5ms	10ms	15ms	20ms	30ms	50ms
±100 Hz	$\overline{\sigma}$	–	0.102	0.047	0.030	0.017	0.007	0.002
	β	rad/s	1240	743	631	514	390	290
	μ	–	2.06	2.56	3.32	3.82	4.40	5.57
	$\Delta\omega_{act}$	Hz	±407	±303	±333	±313	±273	±258
	$\overline{P}$	μT^2	71.4	59.7	46.9	43.1	38.0	30.6
	$\overline{P}_{ratio}$	–	12.9	43.3	76.5	125.1	247.9	554.1
±200 Hz	$\overline{\sigma}$	–	0.117	0.061	0.037	0.026	0.012	0.004
	β	rad/s	1191	765	573	488	374	275
	μ	–	2.35	3.00	3.79	4.80	5.93	7.61
	$\Delta\omega_{act}$	Hz	±446	±365	±346	±372	±353	±333
	$\overline{P}$	μT^2	74.2	57.9	51.6	45.5	39.5	32.3
	$\overline{P}_{ratio}$	–	13.4	42.0	84.2	132.0	258.1	584.8
±300 Hz	$\overline{\sigma}$	–	0.146	0.072	0.047	0.032	0.018	0.007
	β	rad/s	1173	731	555	448	356	252
	μ	–	2.65	3.92	4.88	5.94	7.70	10.19
	$\Delta\omega_{act}$	Hz	±495	±456	±431	±424	±436	±409
	$\overline{P}$	μT^2	75.3	60.6	53.2	49.6	41.6	35.2
	$\overline{P}_{ratio}$	–	13.6	44.0	86.9	143.8	271.3	638.3
±400 Hz	$\overline{\sigma}$	–	0.156	0.088	0.058	0.041	0.024	0.010
	β	rad/s	1015	684	533	438	328	238
	μ	–	4.13	5.16	6.13	7.28	9.42	13.33
	$\Delta\omega_{act}$	Hz	±667	±562	±521	±508	±492	±504
	$\overline{P}$	μT^2	86.5	64.8	55.5	50.6	45.1	37.4
	$\overline{P}_{ratio}$	–	15.7	47.0	90.5	146.8	294.1	677.4
±500 Hz	$\overline{\sigma}$	–	0.169	0.102	0.069	0.050	0.030	0.014
	β	rad/s	1004	671	512	420	314	225
	μ	–	4.40	6.08	7.65	9.02	11.73	16.53
	$\Delta\omega_{act}$	Hz	±703	±649	±623	±602	±586	±593
	$\overline{P}$	μT^2	87.3	66.0	57.7	52.9	47.1	39.4
	$\overline{P}_{ratio}$	–	15.8	47.9	94.3	153.4	307.6	714.1

Table D.4: Dependence of high-bandwidth hyperbolic secant pulse performance on design parameters. Rows represent pulses with the given optimization bandwidth ($\Delta\omega_{opt}$), and columns correspond to different pulse durations. For each pulse, the average deviation of the flip-angle from the target value of 180° over the entire UPS ($\overline{\sigma}$), the parameter β, the parameter μ, the time-averaged RF power ($\overline{P} = \int A^2\,dt/\Delta T$), and the ratio ($\overline{P}_{ratio}$) of $\overline{P}$ to the corresponding value for a block pulse with equivalent duration and flip angle are given.

$\Delta\omega_{opt}$	attribute	units	5ms	10ms	15ms	20ms	30ms	50ms
±600 Hz	$\overline{\sigma}$	–	0.191	0.114	0.079	0.058	0.036	0.017
	β	rad/s	769	629	483	403	302	211
	μ	–	7.87	7.44	9.44	10.90	14.23	19.72
	$\Delta\omega_{act}$	Hz	±964	±745	±726	±700	±685	±662
	$\overline{P}$	μT^2	110.6	70.3	61.1	55.0	48.9	42.1
	$\overline{P}_{ratio}$	–	20.0	51.0	99.8	159.5	319.3	762.4
±700 Hz	$\overline{\sigma}$	–	0.195	0.125	0.088	0.067	0.042	0.021
	β	rad/s	782	565	453	381	290	204
	μ	–	7.97	9.58	11.50	13.22	16.87	23.46
	$\Delta\omega_{act}$	Hz	±992	±862	±828	±801	±779	±761
	$\overline{P}$	μT^2	109.1	780.3	65.2	58.3	51.0	43.6
	$\overline{P}_{ratio}$	–	19.8	56.6	106.5	169.0	332.7	789.8
±800 Hz	$\overline{\sigma}$	–	0.207	0.135	0.097	0.074	0.048	0.025
	β	rad/s	735	534	426	361	278	197
	μ	–	9.09	11.33	13.70	15.69	19.86	27.42
	$\Delta\omega_{act}$	Hz	±1064	±963	±928	±902	±878	±859
	$\overline{P}$	μT^2	114.9	82.3	69.2	61.4	53.2	45.1
	$\overline{P}_{ratio}$	–	20.8	59.7	113.0	178.0	347.5	818.0
±900 Hz	$\overline{\sigma}$	–	0.219	0.143	0.104	0.081	0.054	0.028
	β	rad/s	564	506	399	340	264	189
	μ	–	15.30	13.21	16.27	18.48	23.41	31.82
	$\Delta\omega_{act}$	Hz	±1378	±1065	±1032	±1001	±984	±957
	$\overline{P}$	μT^2	139.7	86.6	73.8	65.10	56.0	47.0
	$\overline{P}_{ratio}$	–	25.3	62.8	120.6	188.8	365.6	851.3
±1000 Hz	$\overline{\sigma}$	–	0.221	0.150	0.113	0.088	0.059	0.032
	β	rad/s	523	449	331	292	234	172
	μ	–	18.80	16.88	24.20	25.94	30.50	39.99
	$\Delta\omega_{act}$	Hz	±1561	±1206	±1274	±1206	±1140	±1096
	$\overline{P}$	μT^2	146.7	96.6	88.3	75.6	63.0	51.6
	$\overline{P}_{ratio}$	–	26.6	70.1	144.1	219.1	411.4	934.5

APPENDIX E

COMPARISON OF DERIVATIVE-BASED AND OPTIMAL CONTROL MINIMIZATION ALGORITHMS

In this appendix, a comparison of the efficacy of derivative-based and optimal control algorithms is presented in the context of composite pulse optimizations. Three different optimization schemes were explored in this study:

I. minimization of deviations between simulated and target flip-angles via the `fmincon` function in Matlab

II. maximization of the dot product between simulated and target magnetization vectors using the same Matlab function

III. maximization of the dot product between simulated and target magnetization vectors using an optimal control algorithm modeled after previous studies (74).

For each optimization scheme, target flip angles over the entire B_1^+-ΔB_0 grid were set to a single value as described in Section 3.2.2. Each minimization scheme was tested for composite pulses with three differing sets of initial conditions: maximum amplitudes and zero phases; random amplitudes and zero phases; random amplitudes and random phases.

In Scheme I, the sub-pulse amplitudes $\mathbf{A} = \{A_1, A_2, \ldots, A_k\}$ and phases $\boldsymbol{\phi} = \{\phi_1, \phi_2, \ldots, \phi_k\}$ of composite pulses are optimized via minimization of the function

$$\overline{\sigma}_\alpha(\mathbf{A}, \boldsymbol{\phi}) = \frac{1}{mn} \sum_{i,j=1}^{m,n} \left| \frac{\alpha^f_{i,j}(\mathbf{A}, \boldsymbol{\phi}) - \alpha^T_{i,j}}{\alpha^T_{i,j}} \right| , \tag{E.3}$$

where i is the B_1^+ index on the B_1^+-ΔB_0 grid, j is the ΔB_0 index on the B_1^+-ΔB_0 grid, and α is the flip angle given by $\cos^{-1}(M_z/M_0)$ with the simulated and target values denoted respectively by the superscripts f and T. The function value $\overline{\sigma}_\alpha$ represents the average deviation of simulated flip angles from the target flip angle over the entire B_1^+-ΔB_0 grid and is expressed as a fraction of the target flip angle. Seeking the global minimum of Equation E.3, the non-linear constrained minimization algorithm (46; 62) (Matlab function `fmincon`) iteratively calculates a numerical estimation of the Hessian matrix defined by the second partial derivatives of Equation E.3 with respect to the k amplitudes and k phases of the RF waveform. The algorithm is seeded via a stochastic pulse in which the k amplitudes and phases conform to an even probability distribution within the prescribed limits of 0–15 μT and $\pm\pi$ rad, respectively. A termination condition is satisfied if the minimization algorithm fails to decrease the value of $\overline{\sigma}_\alpha$ by at least a factor of 10^{-6} over the course of a single iteration.

In Scheme II, $\overline{\sigma}_\alpha$ is replaced by

$$\overline{\sigma}_{\mathbf{M}}(\mathbf{A}, \boldsymbol{\phi}) = \frac{1}{mn} \sum_{i,j=1}^{m,n} \left(1 - \mathbf{M}^f_{i,j}(\mathbf{A}, \boldsymbol{\phi}) \cdot \mathbf{M}^T_{i,j}\right) , \tag{E.4}$$

with $\mathbf{M}$ representing the magnetization vector (M_x, M_y, M_z). Definitions of i, j, f, and T are carried over from Equation E.3. The function $\overline{\sigma}_{\mathbf{M}}$ is minimized via the `fmincon` function, thereby effectively maximizing the dot product between the simulated and target magnetization vectors over the entire B_1^+-ΔB_0 grid. The seeding of the amplitude and phase modulation waveforms as well as the termination criteria for the optimization are identical to those of Scheme I.

Scheme III differs from Scheme II primarily in the minimization algorithm. Instead of using `fmincon`, an optimal control algorithm presented in publications from Skinner et. al. (74; 75) was used to minimize $\overline{\sigma}_{\mathbf{M}}$ as defined in Equation E.4. In summary, the initial magnetization vector $\mathbf{M}^I = (0, 0, 1)$ was propagated forward in time according to the Bloch equations (Section **??**) in the presence of an initial composite RF pulse (i.e. a set of amplitudes A_k and phases ϕ_k). This procedure resulted in a final simulated magnetization vector $\mathbf{M}^F_{i,j}$ for every i-j point on the B_1^+-ΔB_0 grid. The cross product

$$\mathbf{M}^{\times}_{i,j} = \mathbf{M}^F_{i,j} \times \mathbf{M}^T_{i,j} \tag{E.5}$$

was then propagated backward in time for the same composite pulse, resulting in $\mathbf{M}^{\times}_{i,j,k}$ (i.e., a $\mathbf{M}^{\times}_{i,j}$ vector for each of the k time points of the composite pulse). The projection of $\mathbf{M}^{\times}_{i,j,k}$ onto the transverse plane, denoted by $\mathbf{M}^{\times}_{\perp,i,j,k}$, was averaged across the B_1^+-ΔB_0 grid for each k. This step removed the dependence of $\mathbf{M}^{\times}_{\perp,i,j,k}$ on the i-j grid indices leaving

$$\overline{\mathbf{M}}^{\times}_{\perp,k} = \overline{A}^{\times}_{\perp,k}\, e^{i\,\overline{\phi}^{\times}_{\perp,k}}\,. \tag{E.6}$$

With p used to index the iterations of this algorithm, new composite pulse amplitudes (A_k^{p+1}) and phases (ϕ_k^{p+1}) were then computed from the previous values (A_k^p and ϕ_k^p) via the relations

$$A_k^{p+1} = A_k^p + \epsilon \, \overline{A}_{\perp,k}^{\times} \tag{E.7a}$$

and

$$\phi_k^{p+1} = \phi_k^p + \epsilon \, \overline{\phi}_{\perp,k}^{\times} \, , \tag{E.7b}$$

where the parameter ϵ was chosen to maximize the decrease in $\overline{\sigma}_{\mathbf{M}}$ during each iteration. The iterative process was repeated until the termination criterium of Scheme II was satisfied. Because of susceptibility of the optimal control algorithm to the choice of initial A_k and ϕ_k, all A_k^I were set to the maximum allowed value ($15\,\mu$T) and all ϕ_k^I were set to 0. This choice was found to give results comparable to the best results when A_k and ϕ_k were seeded with random values but without the relatively high level of variability.

A fourth optimization scheme in which $\overline{\sigma}_\alpha$ is minimized via the same optimal control algorithm may seem logical; however, application of the optimal control algorithm in this context does not appear straightforward given that the lone condition of flip-angle uniformity does not specify a unique end state for the magnetization vector. This problem may warrant future study.

According to Schemes II and III, the schemes for which a head-to-head comparison between `fmincon` and optimal control algorithms is possible, stability measurements of the `fmincon` and optimal control minimization algorithms were made by repeating optimizations for a 30° composite pulse consisting of 32 sub-pulses each with a 0.1024 ms duration. One hundred repetitions were made for each of the two schemes, with different random initial sub-pulse amplitudes for each repetition. Mean and standard deviations for the resulting distributions of $\overline{\sigma}_{\mathbf{M}}$ were calculated.

Table E.1: Performance of `fmincon` and optimal control algorithms seeded with maximum amplitudes and zero phases. In this case, only the final cost function values are reported. There are no other statistical measures since repetition of the optimization with the same initial amplitude and phase values results in the same composite pulse. The second and third columns give results for Optimization Scheme II. The fourth and fifth columns give results for Optimization Scheme III.

metric	`fmincon` ($\overline{\sigma}_\alpha$)	optimal control ($\overline{\sigma}_\alpha$)	`fmincon` ($\overline{\sigma}_\mathbf{M}$)	optimal control ($\overline{\sigma}_\mathbf{M}$)
min	2.81×10^1	2.01×10^1	1.55×10^{-2}	1.67×10^{-2}

Table E.2: Performance reproducibility of `fmincon` and optimal control algorithms seeded with random amplitudes and zero phases. The second and third columns give results for Optimization Scheme II. The fourth and fifth columns give results for Optimization Scheme III.

metric	`fmincon` ($\overline{\sigma}_\alpha$)	optimal control ($\overline{\sigma}_\alpha$)	`fmincon` ($\overline{\sigma}_\mathbf{M}$)	optimal control ($\overline{\sigma}_\mathbf{M}$)
mean	2.78×10^1	4.03×10^1	1.67×10^{-2}	9.56×10^{-2}
SD	1.98×10^0	1.69×10^1	4.50×10^{-3}	7.45×10^{-2}
RD	7.12×10^{-2}	4.19×10^{-1}	2.55×10^{-1}	7.79×10^{-1}
min	1.46×10^1	1.08×10^1	6.40×10^{-3}	3.71×10^{-3}

Table E.3: Performance reproducibility of `fmincon` and optimal control algorithms seeded with random amplitudes and random phases. The second and third columns give results for Optimization Scheme II. The fourth and fifth columns give results for Optimization Scheme III.

metric	`fmincon` ($\overline{\sigma}_\alpha$)	optimal control ($\overline{\sigma}_\alpha$)	`fmincon` ($\overline{\sigma}_\mathbf{M}$)	optimal control ($\overline{\sigma}_\mathbf{M}$)
mean	2.37×10^1	2.93×10^1	1.44×10^{-2}	1.92×10^{-2}
SD	6.55×10^0	3.40×10^0	1.78×10^{-2}	8.90×10^{-3}
RD	2.76×10^{-1}	1.16×10^{-1}	1.24×10^0	4.64×10^{-1}
min	1.20×10^1	1.77×10^1	4.19×10^{-3}	8.90×10^{-3}

REFERENCES

[1] P. Balchandani, J. Pauly, and D. Spielman. Slice-selective tunable-flip adiabatic low peak-power excitation pulse. *Magnetic Resonance in Medicine*, 59:1072–1078, 2008.

[2] P. Balchandani, J. Pauly, and D. Spielman. Designing adiabatic radio frequency pulses using the shinnar-le roux algorithm. *Magnetic Resonance in Medicine*, 64: 843–851, 2010.

[3] M. R. Bendall and D. T. Pegg. Theoretical description of depth pulse sequences, on and off resonance, including improvements and extensions thereof. *Magnetic Resonance in Medicine.*, 2:91–113, 1985.

[4] M. A. Bernstein, K. F. King, and X. J. Zhou. *Handbook of MRI Pulse Sequences.* Academic Press, 2004.

[5] A. Blamire, D. Rothman, and T. Nixon. Dynamic shimming update: A new approach towards optimized whole brain shimming. *Magnetic Resonance in Medicine*, 36:159–165, 1996.

[6] F. Bloch, W. Hansen, and M. Packard. Nuclear induction. *Physical Review*, 69: 127, 1946.

[7] J.-M. Böhlen, M. Rey, and G. Bodenhausen. Refocusing with chirped pulses for broadband excitation without phase dispersion. *Journal of Magnetic Resonance*, 84:191–197, 1989.

[8] N. Boulant, M. A. Cloos, and A. Amadon. B_1 and B_0 inhomogeneity mitigation in the human brain at 7 T with selective pulses by using hamiltonian theory. *Magnetic Resonance in Medicine*, 65:680–691, 2011.

[9] N. Boulant, D. Le Bihan, and A. Amadon. Strongly modulating pulses for counteracting RF inhomogeneity at high fields. *Magnetic Resonance in Medicine*, 60:701–708, 2008.

[10] N. Boulant, J.-F. Mangin, and A. Amadon. Counteracting radio frequency inhomogeneity in the human brain at 7 Tesla using strongly modulating pulses. *Magnetic Resonance in Medicine*, 61:1165–1172, 2009.

[11] C. R. Bowers and D. P. Weitekamp. Transformation of symmetrization order to nuclear-spin magnetization by chemical reaction and nuclear magnetic resonance. *Physical Review Letters*, 57:2645–2648, 1986.

[12] D. Brunner, N. De Zanche, J. Frölich, J. Paska, and K. Pruessmann. Travelling-wave nuclear magnetic resonance. *Nature*, 457:994–998, 2009.

[13] Center for Devices and Radiologic Health. *Guidance for the submission of pre-market notifications for magnetic resonance diagnostic devices*, 2003. Food and Drug Administration.

[14] S. Conolly, D. Nishimura, and A. Macovski. Variable-rate selective excitation. *Journal of Magnetic Resonance*, 78:440–458, 1989.

[15] C. Counsell, M. Levitt, and R. Ernst. Analytical theory of composite pulses. *Journal of Magnetic Resonance*, 63:133–141, 1985.

[16] C. Cunningham, J. Pauly, and K. Nayak. Saturated double-angle method for rapid B_1^+ mapping. *Magnetic Resonance in Medicine*, 55:1326–1333, 2006.

[17] R. Damadian. Field focusing nuclear magnetic resonance (FONAR): Visualization of a tumor in a live animal. *Science*, 171:1151–1153, 1971.

[18] R. Damadian. Tumor detection by nuclear magnetic resonance. *Science*, 171: 1151–1153, 1971.

[19] R. Damadian, M. Goldsmith, and L. Minkoff. Nmr in cancer .16. FONAR image of live human body. *Physiological Chemistry and Physics*, 9:97, 1977.

[20] B. Dylan. "Shelter From the Storm." *Blood on the Tracks*. Columbia Records, 1975.

[21] D. A. Feinberg and K. Oshio. Grase (gradient- and spin-echo) mr imaging : a new fast clinical imaging technique. *Magnetic Resonance in Medicine*, 181: 597–602, 1991.

[22] A. Garroway, P. Grannell, and P. Mansfield. Image formation in nmr by a selective irradiation process. *Journal of Physics C-Solid State Physics*, 7:L457–L462, 1974.

[23] M. Garwood and Y. Ke. Symmetric pulses to induce arbitrary flip angles with compensation for RF inhomogeneity and resonance offsets. *Journal of Magnetic Resonance*, 94:511–525, 1991.

[24] P. M. Glover. Interaction of mri field gradients with the human body. *Physics in Medicine and Biology*, 54:R99–R115, 2009.

[25] E. L. Hahn. An accurate nuclear magnetic resonance method for measuring spin-lattice relaxation times. *Physical Review*, 76:145, 1949.

[26] E. L. Hahn. Spin echoes. *Physical Review*, 80:580, 1950.

[27] P. A. Hardy, M. P. Recht, and D. W. Piraino. Fat suppressed mri of articular cartilage with a spatial-spectral excitation pulse. *Journal of Magnetic Resonance Imaging*, 8(6):1279–1287, 1998.

[28] A. Henning, A. Fuchs, J. B. Murdoch, and P. Boesiger. Slice-selective fid acquisition, localized by outer volume suppression (fidlovs) for ^{1}H-mrsi of the human brain at 7 T with minimal signal loss. *NMR in Biomedicine*, 83:683–696, 2009.

[29] W. Hinshaw, P. Bottomley, and G. Holland. Radiographic thin-section image of the human wrist by nuclear magnetic resonance. *Nature*, 270:722–723, 1977.

[30] J. Hornak, J. Szumowski, and R. Bryant. Magnetic field mapping. *Magnetic Resonance in Medicine.*, 6:158–163, 1988.

[31] T.-L. Hwang, P. C. M. van Zijl, and M. Garwood. Broadband adiabatic refocusing without phase distortion. *Journal of Magnetic Resonance*, 124:250–254, 1997.

[32] I. Ivan Tkáč, P. Andersen, G. Adriany, H. Merkle, K. Uğurbil, and R. Gruetter. In vivo ^{1}H nmr spectroscopy of the human brain at 7 T. *Magnetic Resonance in Medicine*, 46:251–256, 2001.

[33] J. D. Jackson. *Classical Electrodynamics*. John Wiley & Sons, Inc., New York, third edition, 1999.

[34] M. Jankiewicz, H. Zeng, J. Moore, A. W. Anderson, and J. C. Gore. Practical considerations for the design of sparse-spokes pulses. *Journal of Magnetic Resonance*, 203:294–304, 2010.

[35] P. Jezzard and R. S. Balaban. Correction for geometric distortion in echo planar images from b_0 field variations. *Magnetic Resonance in Medicine*, 34:65–73, 1995.

[36] M. Johnson, AJ Garwood and K. Uğurbil. Slice selection with gradient-modulated adiabatic excitation despite the presence of large b1-inhomogeneities. *Journal of Magnetic Resonance*, 81:653–660, 1989.

[37] U. Katscher, P. Börnert, C. Leussler, and J. S. van den Brink. Transmit SENSE. *Magnetic Resonance in Medicine*, 49:144–150, 2003.

[38] K. Kobzar, T. Skinner, N. Khaneja, S. Glaser, and B. Luy. Exploring the limits of broadband excitation and inversion: II. RF-power optimized pulses. *Journal of Magnetic Resonance*, 194:58–66, 2008.

[39] D. Kunz. Use of frequency-modulated radiofrequency pulses in MR imaging experiments. *Magnetic Resonance in Medicine*, 3:377–384, 1986.

[40] E. Kupče and R. Freeman. Stretched adiabatic pulses for broadband spin inversion. *Journal of Magnetic Resonance Series A*, 117:246–256, 1995.

[41] P. Lauterbur. Image formation by induced local interactions: examples employing nuclear magnetic resonance. *Nature*, 242:190–191, 1973.

[42] M. Levitt. Symmetrical composite pulse sequences for NMR population inversion. I. Compensation of radiofrequency field inhomogeneity. *Journal of Magnetic Resonance*, 48:234–264, 1982.

[43] M. Levitt and R. Ernst. Composite pulses constructed by a recursive expansion procedure. *Journal of Magnetic Resonance*, 55:247–254, 1983.

[44] M. Levitt and R. Freeman. Compensation for pulse imperfections in NMR spin-echo experiments. *Journal of Magnetic Resonance*, 43:65, 1981.

[45] Y. Luo, R. de Graff, L. DelaBarre, A. Tannus, and M. Garwood. The return of the frequency sweep: Designing adiabatic pulses for contemporary NMR. *Journal of Magnetic Resonance*, 153:155–177, 2001.

[46] O. Mangasarian, R. Meyer, and S. Robinson, editors. *Nonlinear Programming 3*. Academic Press, New York, 1978.

[47] P. Mansfield. Multiplanar image formation using nmr spin echoes. *Journal of Physical Chemistry*, 10:L55–L58, 1977.

[48] W. Mao, M. B. Smith, and C. M. Collins. Exploring the limits of RF shimming for high-field MRI of the human head. *Magnetic Resonance in Medicine*, 56: 918–922, 2006.

[49] G. J. Metzger, C. Snyder, C. Akgun, T. Vaughan, K. Uğurbil, and P.-F. Van de Moortele. Local B_1^+ shimming for prostate imaging with transceiver arrays at 7T based on subject-dependent transmit phase measurements. *Magnetic Resonance in Medicine*, 59:396–409, 2008.

[50] C. Meyer, J. Pauly, A. Macovski, and D. Nishimura. Simultaneous spatial and spectral selective excitation. *Magnetic Resonance in Medicine*, 15:287–304, 1990.

[51] S. Michaeli, H. Grohn, O. Grohn, D. J. Sorce, R. Kauppinen, and C. S. Springer Jr. Exchange-influenced $T_{2\rho}$ contrast in human brain images measured with adiabatic radio frequency pulses. *Magnetic Resonance in Medicine*, 53: 823–829, 2005.

[52] S. Michaeli, D. J. Sorce, I. D, and M. Garwood. Transverse relaxation in the rotating frame induced by chemical exchange. *Journal of Magnetic Resonance*, 169:293–299, 2004.

[53] J. Moore, M. Jankiewicz, A. Anderson, and J. Gore. Hyperbolic secant parameter optimization for non-selective inversion at 7 T. *Proceedings of the International Society of Magnetic Resonance in Medicine*, 18:2858, 2010.

[54] J. Moore, M. Jankiewicz, A. Anderson, and J. Gore. An optimized composite refocusing pulse for ultra-high field MRI. *Proceedings of the International Society of Magnetic Resonance in Medicine*, 18:2859, 2010.

[55] J. Moore, M. Jankiewicz, H. Zeng, A. Anderson, M. Avison, E. Welch, and J. Gore. Quantitative comparison of B_1^+ mapping methods for 7 T human imaging. *Proceedings of the International Society of Magnetic Resonance in Medicine*, 17:372, 2009.

[56] J. Moore, M. Jankiewicz, H. Zeng, A. W. Anderson, and J. C. Gore. Composite RF pulses for B_1^+-insensitive volume excitation at 7 Tesla. *Journal of Magnetic Resonance*, 205:50–62, 2010.

[57] J. Pauly et al. A k-space analysis of small-tip-angle excitation. *Journal of Magnetic Resonance*, 81:43, 1989.

[58] J. Pauly, P. Le Roux, D. Nishimura, and A. Macovski. Parameter relations for the shinnar-le roux selective excitation pulse design algorithm. *IEEE Transactions on Medical Imaging*, 10:53–65, 1991.

[59] A. Peters, M. Brookes, F. Hoogenraad, P. Gowland, S. Francis, P. Morris, and R. Bowtell. T_2^* measurements in human brain at 1.5, 3 and 7 T. *Magnetic Resonance Imaging*, 25:748, 2007.

[60] C. S. Poon and R. M. Henkelman. 180° refocusing pulses which are insensitive to static and radiofrequency field inhomogeneity. *Journal of Magnetic Resonance*, 99:45–55, 1992.

[61] C. S. Poon and R. M. Henkelman. Robust refocusing pulses of limited power. *Journal of Magnetic Resonance*, 116:161–180, 1995.

[62] M. Powell. *Nonlinear Programming 3*, chapter The convergence of variable metric methods for nonlinearly constrained optimization calculations. In Mangasarian et al. (46), 1978.

[63] E. Purcell, H. Torrey, and R. Pound. Resonance absorption by nuclear magnetic moments in solids. *Physical Review*, 69:37–38, 1946.

[64] I. Rabi, J. Zacharias, S. Millman, and P. Kusch. A new method of measuring nuclear magnetic moment. *Physical Review*, 53:318, 1938.

[65] S. Rieseberg, J. Frahm, and J. Finsterbusch. Two-dimensional spatially-selective RF excitation pulses in echo-planar imaging. *Magnetic Resonance in Medicine*, 47:1186–1193, 2002.

[66] W. D. Rooney, G. Johnson, X. Li, E. R. Cohen, S.-G. Kim, K. Uğurbil, and C. S. Springer Jr. Magnetic field and tissue dependencies of human brain longitudinal ^1H_2O relaxation in vivo. *Magnetic Resonance in Medicine*, 57:308–318, 2007.

[67] S. Saekho, F. E. Boada, D. C. Noll, and V. A. Stenger. Small tip angle three-dimensional tailored radiofrequency slab-select pulse for reduced B_1 inhomogeneity at 3 T. *Magnetic Resonance in Medicine*, 53:479–484, 2005.

[68] S. Saekho, C.-y. Yip, D. C. Noll, F. E. Boada, and V. A. Stenger. Fast-kz three-dimensional tailored radiofrequency pulse for reduce $\hat{B}_1$ inhomogeneity. *Magnetic Resonance in Medicine*, 55:719–724, 2006.

[69] C. Sagan. *Cosmos*. Random House, Inc., New York, 1980.

[70] F. Schick. Whole-body MRI at high field: technical limits and clinical potential. *European Radiology*, 15:946–959, 2005.

[71] K. Setsompop et al. Sparse spokes slice-selective design for $\hat{B}_1$ inhomogeneity corrections at 7 T. *Magnetic Resonance in Medicine*, 15:256, 2007.

[72] M. Silver, R. Joseph, and D. Hoult. Highly selective $\pi/2$ and π pulse generation. *Journal of Magnetic Resonance*, 59:347–351, 1984.

[73] M. Silver, R. Joseph, and D. Hoult. Selective spin inversion in nuclear magnetic resonance and coherent optics through an exact solution of the bloch-riccati equation. *Physical Review A*, 31:2753–2755, 1985.

[74] T. Skinner, T. Reiss, B. Luy, N. Khaneja, and S. Glaser. Application of optimal control theory to the design of broadband excitation pulses for high-resolution NMR. *Journal of Magnetic Resonance*, 163:8–15, 2003.

[75] T. Skinner, T. Reiss, B. Luy, N. Khaneja, and S. Glaser. Reducing the duration of broadband excitation pulses using optimal control with limited RF amplitude. *Journal of Magnetic Resonance*, 167:68–74, 2004.

[76] R. Staewen, A. Johnson, B. Ross, T. Parrish, H. Merkle, and M. Garwood. 3-D FLASH imaging using a single surface coil and a new adiabatic pulse, BIR-4. *Investigative Radiology*, 25:559–567, 1990.

[77] W. P. Stollberger R. Imaging of the active B_1 field in vivo. *Magnetic Resonance in Medicine*, 35:246–251, 1996.

[78] A. Tannús and M. Garwood. Improved performance of frequency-swept pulses using offset-independent adiabaticity. *Journal of Magnetic Resonance Series A*, 120:133–137, 1996.

[79] A. Tannús and M. Garwood. Adiabatic pulses. *NMR in Biomedicine*, 10:423–434, 1997.

[80] L. Tsu. *Tao Te Ching.* Random House, Inc., New York, 1972.

[81] K. Uğurbil, M. Garwood, and M. Bendall. Amplitude- and frequency-modulated pulses to achieve 90° plane rotations with inhomogeneous B_1 fields. *Journal of Magnetic Resonance*, 72:177–185, 1987.

[82] K. Uğurbil, M. Garwood, and A. R. Rath. Optimization of modulation functions to improve insensitivity of adiabatic pulses to variations in B_1 magnitude. *Journal of Magnetic Resonance*, 80:448–469, 1988.

[83] P.-F. Van de Moortele, C. Akgun, G. Adriany, S. Moeller, J. Ritter, C. M. Collins, M. B. Smith, J. T. Vaughan, and K. Uğurbil. B_1 destructive interferences and spatial phase patterns at 7 T with a head transceiver array coil. *Magnetic Resonance in Medicine*, 54:1503–1518, 2005.

[84] B. van den Bergen, C. A. T. Van den Berg, L. W. Bartels, and J. J. W. Lagendijk. 7 T body MRI: B_1 shimming with simultaneous sar reduction. *Physics in Medicine and Biology*, 52:5429–5441, 2007.

[85] R. van Steenwinkel and K. Hausser. Dynamic nuclear polarisation in liquids at 13 000 gauss. *Physical Letters*, 14:24–25, 1965.

[86] F. Weisinger, P. Boesiger, and K. P. Pruessmann. Electrodynamics and ultimate SNR in parallel MR imaging. *Magnetic Resonance in Medicine*, 52:376–390, 2004.

[87] V. Yarnykh. Actual flip-angle imaging in the pulsed steady state: A method for rapid three-dimensional mapping of the transmitted radiofrequency field. *Magnetic Resonance in Medicine*, 57:192–200, 2007.

[88] V. Yarnykh. Optimal radiofrequency and gradient spoiling for improved accuracy of T_1 and b_1 measurements using fast steady-state techniques. *Magnetic Resonance in Medicine*, 63:1610–1626, 2010.

[89] A. C. Zelinski, L. L. Wald, K. Setsompop, V. Alagappan, B. A. Gagoski, V. K. Goyal, and E. Adalsteinsson. Fast slice-selective radio-frequency excitation pulses for mitigating $\hat{B}_1^+$ inhomogeneity in the human brain at 7 Tesla. *Magnetic Resonance in Medicine*, 59:1355–1364, 2008.